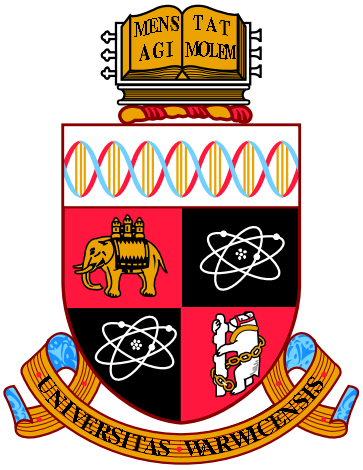

Growth and Structural Characterisation of Spintronic Thin Films Deposited onto III-V Semiconductors

by

Philip Jonathan Mousley

Thesis

Submitted to the University of Warwick

for the degree of

Doctor of Philosophy

Department of Physics

September 2017

THE UNIVERSITY OF WARWICK

Contents

List of Tables

List of Figures

Acknowledgments

I would like to thank my University of Warwick supervisor Dr. Gavin Bell, for passing on both his surface science expertise and his enthusiasm for all things Japanese. My Diamond Light Source supervisor Dr. Chris Nicklin is thanked for his in-depth tutoring on surface x-ray diffraction. A special thank you goes to Dr. Chris Burrows, who taught me both the fundamentals and the vagaries of UHV growth, and also provided much needed support during many beamtime experiments. Dr. Matt Forster and Dr. Jonathan Rawle are thanked for providing expert assistance during these multiple SXRD experiments on the I07 beamline.

I am very grateful to Dr. Masamitu Takahasi and Prof. Shiro Tsukamoto for hosting me during my JSPS research placement, which enabled me to learn more about UHV experiments and synchrotron research, and provided an opportunity to explore Japan. Dr. Hadeel Hussain is thanked for donating time to teaching me the basics of CTR fitting in ROD. My fellow PhD students and officemates, which includes amongst others Stephanie Glover, Haiyuan Wang, Collins Ebiyibo and Alifah Raman, need to be thanked for providing such an enjoyable working environment and company over these past four years.

Finally I would like to thank my family, whose constant support and motivation has enabled me to persevere in the face of the ups and downs encountered over the course of my PhD.

Declarations

I declare that this thesis contains an account of my research work carried out at the Department of Physics, University of Warwick between October 2013 and September 2017 under the supervision of Dr. Gavin. R. Bell and Dr. Chris. Nicklin. The research reported here has not been previously submitted, wholly or in part, at this or any other academic institution for admission to a higher degree.

Dr. Martin Lees is thanked for assistance in collecting VSM measurements presented in chapter 4. Dr. Christopher. W. Burrows provided the MnSb/GaAs(111) samples analysed in chapter 5. Dr. Ana Sanchez produced the TEM images presented in chapters 4 and 6.

Philip Jonathan Mousley

September 2017

Several articles based on this research have been published, are in press, or have been submitted for publication:

P.J.Mousley, C.W.Burrows, M.J.Ashwin, M.Takahasi, T.Sasaki, and G. R. Bell, *In-situ X-ray diffraction of GaAs/MnSb/Ga(In)As heterostructures*, Phya. Status Solidi B. **254**, 1600503 (2017)

P.J.Mousley, A.Sanchez and G.R.Bell, *Growth of MnSb on InGaAs(111)A*, in preparation for submission to J. Cryst. Growth.
P.J.Mousley, C.W.Burrows, C.Nicklin and G.R.Bell, *Ultra-thin Sb film deposition on InAs(111)B*, in preparation for submission.

The work presented in this thesis has been presented at the following national or international conferences.

P.J.Mousley, C.W.Burrows, M.Takahasi, T.Sasaki and G.R.Bell, *Surface X-ray diffraction during GaAs/MnSb/Ga(In) As epitaxial growth* (Poster presentation), Compound Semiconductor Week 2016, Toyama, Japan (June 2016).

Abstract

A surface x-ray diffraction (SXRD) study has been conducted investigating the structural properties of Sb thin-film deposition onto InAs(111)B-(1×1) surfaces via molecular beam epitaxy (MBE). It was found that epitaxy was not possible for deposition at high substrate temperatures (∼220°C), which instead resulted in substitution of the surface As atomic sites. Successful epitaxy required a combination of deposition at room temperature, followed by a short anneal using a substrate temperature of ∼200°C . An increase in film thickness was found to decrease the difference between the intra-bilayer and inter-bilayer distances within the Sb film.

MBE growth of MnSb onto $In_{0.5}Ga_{0.5}As$(111)A-(2×2) surfaces has been investigated, with a focus on the effect of substrate temperature (T_{sub}) and flux ratio $J_{Sb/Mn}$ on thin film growth. It was found that slightly different settings are required compared to growth on GaAs(111) substrates, with intermixing between the overlayer and substrate being observed on multiple samples.

A SXRD study comparing the growth of MnSb on GaAs(111)A and GaAs (111)B surfaces was conducted . Reflection high energy electron diffraction (RHEED) observations during deposition indicate early-stage layer-by-layer growth is only attainable on GaAs(111)A substrates. SXRD measurements confirmed that this difference in early-stage growth process affects the quality of the overall layer, even for thicker films.

A SXRD study of multi-layer heterostructure growth was conducted, focussing on the deposition of GaAs onto MnSb/Ga(In)As(111)A and MnSb/GaAs(001) virtual substrates. Despite poor surface morphology, deposition of crytalline material was achieved. It was found that for (111)A virtual substrates a shift in the central n-MnSb layer was observed, which is attributed to the formation of MnAs at the MnSb surface. For the (001) virtual substrate 3D island growth was observed, and a plausible epitaxial relation between the MnSb($1\bar{1}01$) and GaAs(001) surfaces is presented.

Abbreviations

ADF Annular Dark Field

AFM Atomic Force Microscopy

BEP Beam Equivalent Pressure

BL Bilayer

CTR Crystal Truncation Rod

DFT Density Functional Theory

DW Debye-Waller

EDX Energy Dispersive X-ray

FCC Face-Centered Cubic

GMR Giant Magneto-Resistance

HCP Hexagonal Close-Packed

HMF Half-Metallic Ferromagnet

LEED Low-Energy Electron Diffraction

MBE Molecular Beam Epitaxy

ML Monolayer

MRAM Magnetic Random Access Memory

RHEED Reflection High-Energy Electron Diffraction

RMS Root Mean Square

ROI Region Of Interest

SADP Select-Area Diffraction Pattern

SEM Scanning Electron Microscope

STEM Scanning Transmission Electron Microscope

SXRD Surface X-ray Diffraction

TEM Transmission Electron Microscope

TI Topological Insulator

TMP Transistion Metal Pnictide

TMR Tunnelling Magneto-Resistance

UHV Ultra-High Vacuum

VSM Vibrating Sample Magnetometry

XPS X-ray Photo-electron Spectroscopy

Chapter 1

Introduction

1.1 Spintronics

A large proportion of scientific materials research is devoted to improving both the quality and functionality of information technology (IT). In IT three main actions need to take place: data processing, data storage and data transfer. These actions are predominantly performed with three different carriers of information: electron charge for processing, electron spin for data storage, and photons (via optical connections) for large-distance data transfer. Spintronics is a field of research that focusses on creating devices where these three different types of carriers can be combined [1] [2]. When compared to existing electronics, spintronic devices have both potential and realised benefits. The information storage in spintronic devices is non-volatile, meaning the device can be powered off and the information is preserved [3]. Spintronic devices also have an increased processing speed and decreased power consumption [4][5].

There have been several key stages in the development of spintronics, the first being the discovery of giant magnetoresistance (GMR) in 1988 [6]. This is where two ferromagnetic layers are separated by a non-magnetic spacer layer, and alteration of the relative directions of magnetization in the magnetic layers allows control of the

device's resistance. This breakthrough enabled the creation of technologies such as magnetic field sensors and magnetic information storage. Another important step was the experimental realisation of the tunnelling magnetoresistance (TMR) effect in 1999 [7], which is very similar to the GMR effect, except that the spacer layer is a very thin dielectric tunnel barrier. One main benefit of the TMR is that tunnelling devices carry much lower currents, which is useful for devices with limited power. TMR devices are now incorporated into most hard-disk drives as read-heads, to sense the magnetisation of domains on the disc surface, and allow an increase in the areal density of memory [8]. Magnetic tunnel junctions which utilise the TMR effect have been applied in magnetic random access memory (MRAM)[9], which has the potential to become a universal memory [10][11].

In order for several future spintronic device designs to be implemented a suitable source of spin-polarised current is required. These spin sources will need to have a reliable spin polarisation, and be compatible with standard semiconductors (e.g. GaAs, Si)[12]. In theory a layer of an elemental ferromagnet such as Fe can provide a spin current, however early experiments showed that large elastic deformation at the interface led to the creation of magnetically dead layers which interfere with the spin polarisation [13]. For this reason there are many current research efforts investigating spin functional materials, focusing on their fundamental properties, and how these properties are affected when epitaxially grown onto standard semiconductors. Two of the main types of spin-functional materials being researched that are relevant to this thesis are topological insulators (TIs) and half-metallic ferromagnets (HMFs).

1.1.1 Topological Insulators

Topological insulators (TIs) are materials which are predicted to have topologically protected surface states which cross the energy gap present in the bulk material. This leads to electrons being able to flow at the surface of the material, but this flow is prohibited in the bulk region. These surface states are helical edge states

which occur due to the creation of a Dirac cone between the valence and conduction bands [14]. Example energy dispersion relations for both 2D and 3D TIs are shown in figure 1.1, along with schematic representations of the allowed electron motion. The link between spin and momentum means that if an electron was backscattered from an impurity then it would be required to reverse its spin. The reversal of an electrons spin is not allowed as this would break the time reversal symmetry of the system, and therefore TIs possess dissipationless transport along the surface [15]. This dissipationless transport is one of the main reasons that devices incorporating TIs are proposed to have lower power consumption when compared to standard electronics [2]. TIs could also be used for applications in quantum computing, where they would be used to create novel quasi-particles such as the Majorana fermion [16]. A promising candidate TI material that is of relevance to this thesis is Sb, which is discussed in more detail in section 1.2.1.

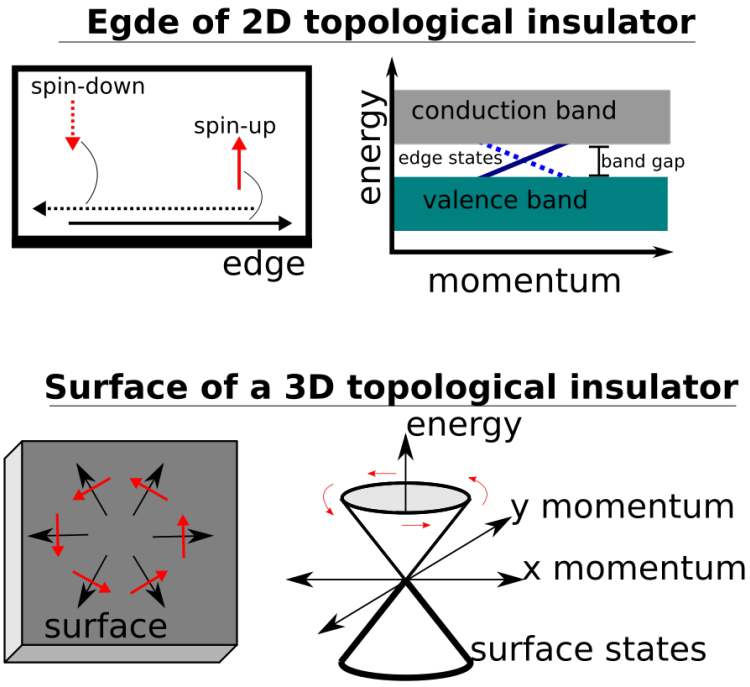

Figure 1.1: Electron motion diagram and energy dispersion plots for (upper) 2D topological insulator, and (lower) 3D topological insulator. Adapted from [14]

1.1.2 Half-metallic ferromagnets

Half metallic ferromagnets (HMFs) are a class of materials that are predicted to display 100% spin polarisation at the Fermi level [17]. This is because unlike standard semiconductors HMFs only possess a band gap in their density of states (DOS) at the Fermi energy for the minority spin direction (figure 1.2). This means HMFs behave as a conductor for one electron spin and as an insulator for the opposite spin.

There are four main classes of materials in which half-metallicity can be found: oxide compounds (e.g. Fe_3O_4 [18]), perovskites (e.g. (La,Sr)MnO_3 [19]), zincblende compounds (e.g. CrAs [20]) and Heusler alloys (e.g. NiMnSb [21]). Despite this wide range of materials predicted to be HMFs , experimentally observing near 100% spin polarisation has proved difficult. One of the best methods for determining half-metallicity is spin-resolved positron annhilation, but as of 2008 only NiMnSb has been proven to be HMF using this experiment technique [22][23]. Spin-resolved x-ray absorption measurements [24], and Andreev reflection spectroscopy [25] have both been used to show high spin polarisation for the transition metal oxide HMF CrO_2. One of the main reasons for the difficulty in observing half-metallicity is the fact that defects at the interface between a HMF and non-HMF materials can easily remove half-metallic behaviour. Therefore studies of these interfaces on the atomic scale are vital for the integration of HMF materials into devices. Currently the search is still on-going for a HMF material that has compatibility with standard semiconductors and that can demonstrate near 100% spin polarisation at room temperature [2]. A promising candidate HMF material that is of relevance to this thesis is the binary transition metal pnictide MnSb, which is discussed in more detail in section 1.2.2.

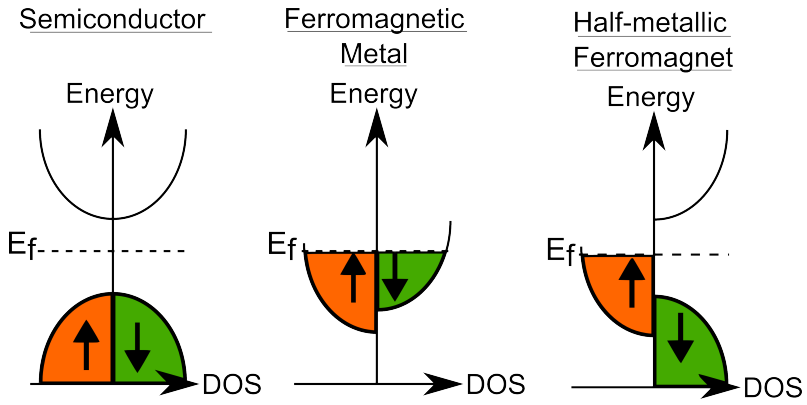

Figure 1.2: Density of states (DOS) near the Fermi energy (E_f) for a semiconductor, ferromagnetic metal and a half-metallic ferromagnet, showing the energy gap which occurs for one of the spin directions.

1.2 Material information

Having provided a brief review of TIs and HMFs, information regarding the specific materials studied in this thesis will be discussed. The work presented in this thesis is mainly concerned with surfaces and interfaces which display three-fold symmetry, specifically (0001) planes of hexagonal materials and (111) planes of cubic materials.

1.2.1 Sb

Sb is a semimetal which adopts a rhombohedral bulk structure. When considering Sb growth on III-V substrates the closest lattice match is often between the [111] directions. Along [111] Sb has a hexagonal unit cell (figure 1.3), which is referred to in the rest of this thesis using the shorthand notation h-Sb. Bulk Sb possesses a Peierls distortion in the h-Sb(0001) direction which causes the Sb atoms to form bilayers (BLs) [26]. The bonding within these BLs is covalent, but the inter-BL bonding is predominantly van der Waals meaning that Sb easily cleaves in the [111] direction. A range of values have been reported for the hexagonal lattice parameters of Sb, these are summarised in table 1.1. Note that the values reported on the Materials Project database [27] are based on first-principle calculations and not experimental

data.

Publication	a	c	H1	H2	Sb-Sb1	Sb-Sb2
Barrett *et al.* [28]	4.3084	11.274	1.506	2.251	2.908	3.355
Bengió *et al.* [29]	4.30	11.340	1.540	2.240	2.921	3.344
Materials Project [30]	4.3853	11.449	1.523	2.294	2.955	3.413

Table 1.1: Values reported for hexagonal Sb bulk crystal lattice parameters. All distances shown are in Å. H1 is the step height between nearest neighbours, H2 is the step height between second nearest neighbours. Sb-Sb1 is the bond distance between nearest neighbours. Sb-Sb2 is the bond distance between second nearest neighbours.

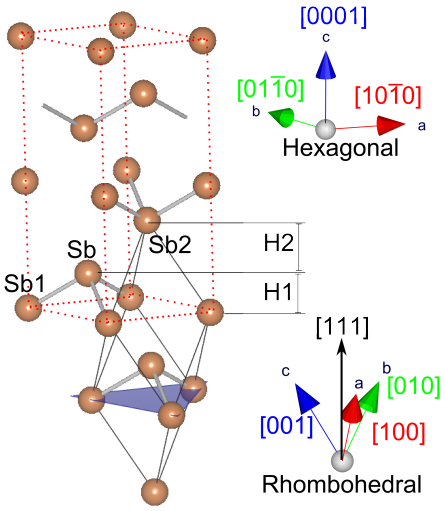

Figure 1.3: Crystal structure of bulk Sb, with the rhombohedral unit cell shown in solid black line and the hexagonal (111) unit cell shown in dotted red line.

There have been many research efforts investigating Sb thin film growth over the past few decades, with a large proportion of this work focussing on the growth of Sb layers with coverages $\leq$1 monolayer (ML) [31] [32] [33]. While some of this research included areas such as optical second harmonic generation [34], the majority of this work had the aim of better understanding the surfactant properties of Sb, and the role of surfactants in epitaxial growth [35][36][37]. It has been shown that Sb monolayers can be successfully grown on III-V (110) surfaces including InAs(110), InP(110), GaAs(110) and GaP(110) [38][39]. Sb monolayers have also been grown

on (111) surfaces including Ge(111) [40] and GaSb(111) [41].

Other work has focussed on the use of Sb pre-deposition steps in the growth of nanostructures. For example, Kaizu *et al.* [42] studied (00L) crystal truncation rods (CTRs) for InAs quantum dot (QD) growth on GaAs(001), and found that an Sb-adsorbed layer led to Sb atoms diffusing into the substrate up to a distance of 8 atomic layers, causing an increase in InAs QD density at the surface. Pillai *et al.* [43] have shown that Sb layers of 0.8-1.4 ML could be used to improve the interface of InAsSb/InAs(111) multi-quantum well structures.

Recent density functional theory (DFT) studies on Sb has focussed on the presence of topological surface states in Sb(111) surfaces [44][45]. Chuang *et al.* [46] showed that a topological insulating state can be induced in a single Sb BL with tensile strain. Wang *et al.* [47] also found that strain played an important role in the transition from 2D TI to trivial semiconductor. Lee *et al.* [48] performed DFT calculations for a 4-BL Sb film and found that doping with non-magnetic impurity atoms could aid in achieving topological conduction. Zhang *et al.* [49] showed that for Sb films ranging from roughly 1 nm to 8 nm, first-principles calculations predict multiple transitions of electronic properties. Films of $\leq$ 1 nm were predicted to be trivial semiconductors, films 1 - 2.7 nm were predicted to exhibit the 2D quantum spin hall state, films 2.7 - 7.8 nm were predicted to have topological insulating states, and films >7.8 nm were predicted to behave as topological semimetals. A recent review of topological semimetals is available by Burkov [50], but this material class will not be discussed further.

These theoretical studies have prompted several experimental investigations of the Sb(111) surfaces, including helium ion scattering [51][52], Fourier-transform scanning tunneling spectroscopy [53] and angle resolved photoemission spectrscopy [54][55] [56][57]. It is clear from the previous research on Sb(111) films detailed above that both theoretically and experimentally there are multiple parameters (e.g. substrate temperature, layer thickness, substrate surface preparation) which strongly

affect the electronic properties of the Sb films. For production of reliable Sb-based spintronic devices it is therefore vital to gain a better understanding of the growth of Sb ultra-thin films $\leq$ 10 nm. Chapter 3 of this thesis presents results from a surface x-ray diffraction (SXRD) investigation on the growth of ultra-thin Sb films on InAs(111)B substrates.

1.2.2 MnSb

MnSb belongs to a group of materials called transition metal pnictides (TMPs), which are compounds made from a transition metal and a group V atom. Some TMPs have been predicted to possess half-metallicity at room temperature for tetrahedrally bonded structures [20]. They are also well suited to growth on standard III-V semiconductor materials via methods such as molecular beam epitaxy (MBE) [58] [59]. MnSb is a promising HMF spintronic candidate due to its high Curie temperature (T_C = 587 K) and epitaxial compatibility with standard semiconductors, which are requirements for a material to be incorporated into devices operated at room temperature [60]. In the bulk ground state MnSb adopts the niccolite (P63/mmc space group) structure, but MnSb can also form two other metastable polymorphs: cubic (c-MnSb) and wurtzite (w-MnSb) (figure 1.4). The space groups for these metastable polymorphs are $F\bar{4}3M$ for c-MnSb, and P63MC for w-MnSb. It is the c-MnSb and w-MnSb polymorphs that are predicted to possess the minority spin energy gap required for half-metallicity [61][62][22]. The c-MnSb polymorph is a metastable structure, but it has been calculated that it is possible for the c-MnSb polymorph to stablise its structure by transitioning into one of two tetragonally distorted phases [63]. Crystallites of the c-MnSb and w-MnSb polymorphs have been observed forming in n-MnSb layers grown on GaAs(111)B [64]. Our research group has conducted several experiments in order to better understand the growth of MnSb layers, and their interactions with standard semiconductor materials. Results from several experiments involving MnSb layers are presented in chapters 4-6 of this thesis.

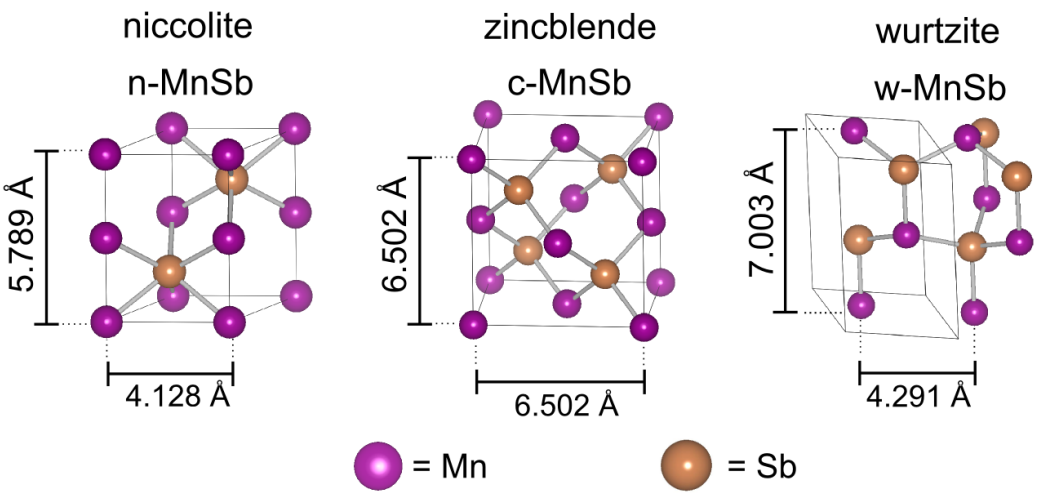

Figure 1.4: Bulk structure of the three different polymorphs of MnSb.

1.2.3 $In_{1-x}Ga_xAs$

InAs and GaAs both adopt the zincblende bulk structure (cubic space group $F\bar{4}3m$), which has a hexagonal unit cell in the [111] direction (figure 1.5). The tetrahedral bonding is asymmetric along the [111] direction, with each atom having three bonds in one direction and only one bond in the opposite direction. When a (111) surface is created the single bond will be preferentially broken which gives rise to two possible surface terminations. If the surface is terminated with the single broken bond on a group III atom then the surface is referred to as (111)A (figure 1.6a). However, if the surface is terminated with the single broken bond on a group V atom then the surface is referred to as (111)B (figure 1.6b). This difference in terminating atomic species leads to large differences in surface bonding chemistry and structure [65].

The identical structure of InAs and GaAs allows the formation of semiconductor alloys of the form $In_xGa_{1-x}As$ for use in the epitaxial growth of thin films. The in-plane lattice constant of these binary alloys can be calculated using Vegard's law (equation 1.1):

$$a_{In_{1-x}Ga_xAs} = (1-x)a_{InAs} + xa_{GaAs} \tag{1.1}$$

where a_i is the in-plane lattice constant of material i. This enables tuning of the lattice mismatch between overlayer and substrate by varying the ratio of In:Ga (i.e. altering the value of x). $In_xGa_{1-x}As$ has been used in several spintronic research efforts including spin distribution studies [66], spin injection efficiency studies [67] [68], and mobility studies for spin transport applications [69]. Work presented in this thesis involves thin film deposition using $In_{1-x}Ga_xAs$ substrates where $x = 0$, 0.5 or 1.

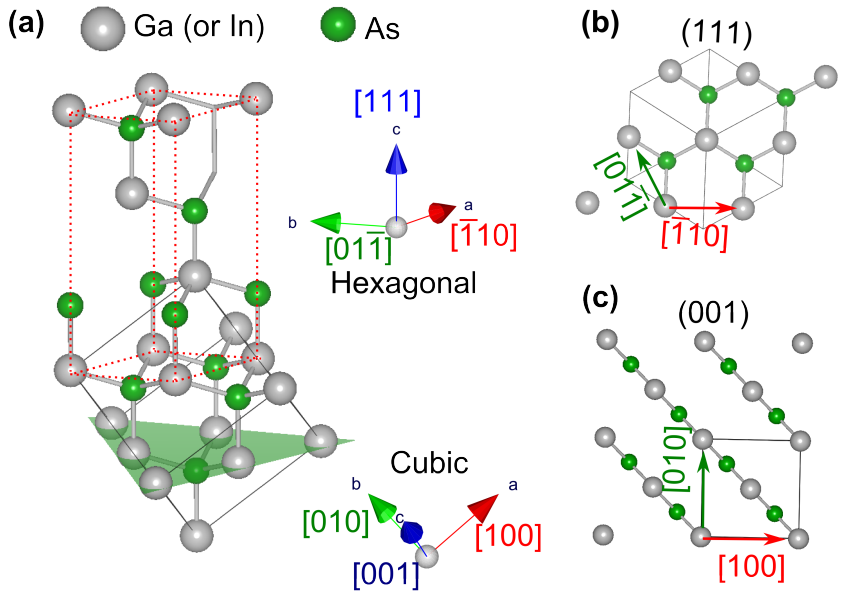

Figure 1.5: (a) Structure of In(Ga)As with the cubic unit cell shown in solid black line, and the hexagonal (111) unit cell shown in dotted red line. Top two layers of the (b) (111)A , and (c) (001) surfaces.

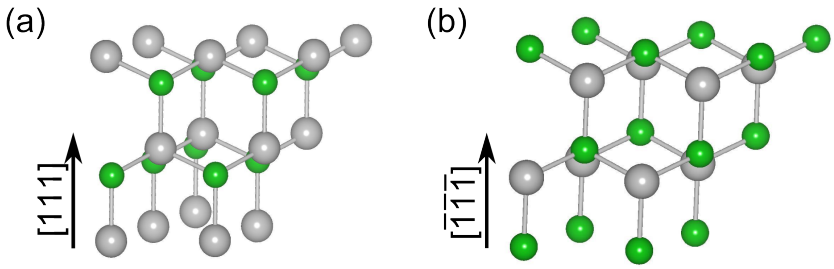

Figure 1.6: (a) Structure of In(Ga)As(111)A surface with Ga(or In) termination, (b) Structure of In(Ga)As(111)B surface with As termination

1.3 Organisation of thesis

Chapter 2 details the experimental techniques used and the theoretical aspects required for the interpretation of results. Chapters 3-6 are experimental results chapters. Chapter 3 is a SXRD study of ultra-thin Sb film epitaxial growth on InAs(111)B surfaces. Chapter 4 is a growth study of MnSb films on InGaAs(111)A. Chapter 5 compares the growth of MnSb films on GaAs(111)A and GaAs(111)B. Chapter 6 is an investigation into the growth of GaAs onto MnSb virtual substrates to form multi-layer heterostructures. Chapter 7 summarises the results presented and outlines possibilities for further work.

Chapter 2

Theory and Experimental Methods

2.1 Molecular Beam Epitaxy

In solid-source solid molecular beam epitaxy (MBE) pieces of the deposition materials are heated up inside effusion cells which are directed towards the target substrate (figure 2.1) [70]. The deposition process is carried out under ultra-high vacuum (UHV) conditions, with pressures less than 10^{-7} Pa. This means the molecules ejected from the effusion cells possess a mean free path larger than the size of the UHV chamber, creating a beam of unscattered atoms or molecules. This allows the beam to be efficiently intercepted by shutters blocking each effusion cell, enabling on/off control of deposition and beam-flux measurements. To quantify the amount of material being output from the effusion cell, measurements with the shutter both open and closed are taken. The difference between the two measurements is defined as the beam equivalent pressure (BEP), and is used to calculated flux ratios when co-depositing elements. Material growth occurs when the shutters are opened and the beams are allowed to impinge on the target crystal. When growth occurs in an ordered manner it is referred to as epitaxy, and can be either of the same material

as the substrate (homoepitaxy) or a different material (heteroepitaxy).

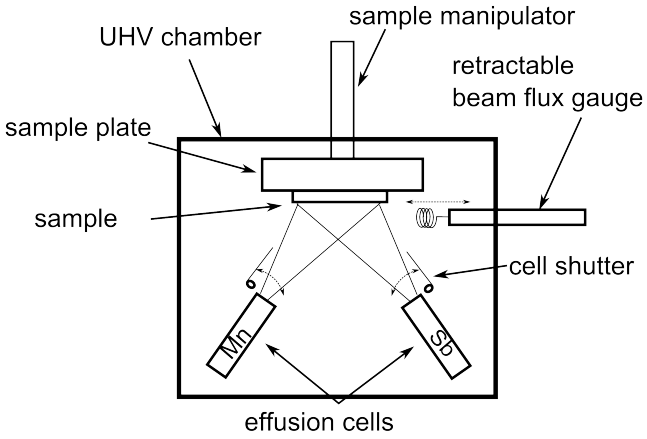

Figure 2.1: Schematic representation of an MBE chamber. Dotted arrows are used to show motion paths of moveable components.

MBE allows the growth to be controlled to atomic layer precision. The growth of each atomic layer can be understood by considering a model of atomic processes (figure 2.2). In this model there are several interactions an adatom on the surface can undergo, it may join with other adatoms to form unstable subcritical clusters which can break apart back into individual atoms. The adatom can join critical clusters which only require one more atom to become a stable cluster. The adatom could also be captured by stable clusters already formed on the surface, or it could evaporate from the surface.

In heteroepitaxial growth (e.g. MnSb on GaAs) there may be a difference in the lattice constant for the substrate (a_{sub}) and the layer (a_{layer}). This defines the lattice mismatch or misfit strain (ϵ_0) of the system using the following equation [71]:

$$\epsilon_0 = \frac{a_{sub} - a_{layer}}{a_{sub}} \tag{2.1}$$

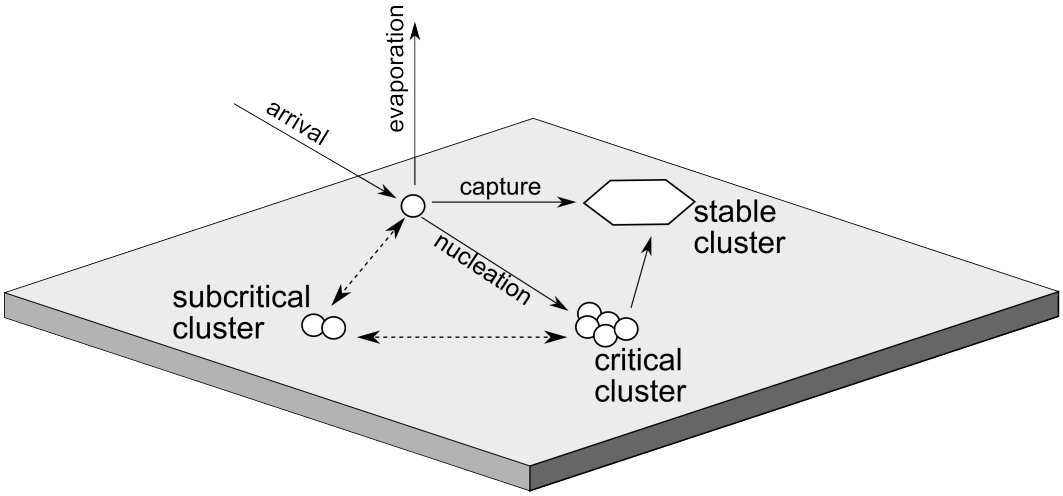

Figure 2.2: Steps of heterogeneous nucleation which occur in gas phase epitaxy (adapted from [72])

The elastic strain energy for a 2D layer of surface area S can be related to ϵ_0 as a function of the layer thickness (h) [73]:

$$W_{2D} = \frac{E}{1-\nu}\epsilon_0^2 Sh \tag{2.2}$$

where E and ν are the layer's Young's modulus and Poisson ratio respectively.

For small layer thicknesses the thin film structure can match the in-plane lattice spacing of the substrate, even if ϵ_0 is large (several %). A strained lattice-matched layer is often referred to as a pseudomorphic layer. Above a certain critical thickness the increase in elastic strain energy will become too large and strain relaxation is required. This usually involves the introduction of misfit dislocations into the growing film. Another method of relaxing the elastic strain is the formation of 3D islands, where free surfaces allow a decrease in the elastic energy [73].

With these strain considerations in mind, heteroepitaxial growth can be modelled with three idealised cases [72], the first is the Frank-van der Merwe model where the overlayer is deposited in a strictly layer-by-layer manner (figure 2.3a). The second is the Volmer-Weber model where the overlayer is initially formed of 3D islands

which then coalesce (figure 2.3b). The third is the Stranski-Krastanov model where there is initially layer-by-layer growth, and then after a critical thickness the growth proceeds via 3D islands (figure 2.3c).

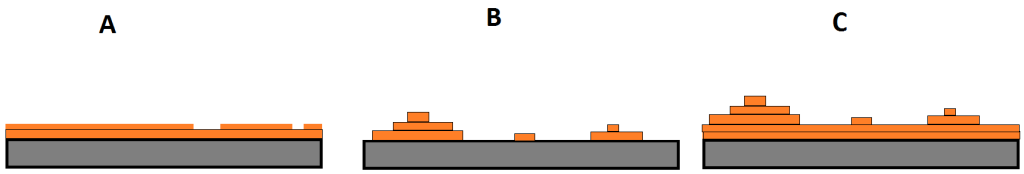

Figure 2.3: Growth models for deposition during MBE. (a)layer-by-layer growth (Frank-van der Merwe) (b)3D island growth (Volmer-Weber) (c) Initially layer-by-layer followed by 3D islands (Stranski-Krastanov)

A key parameter for growing compounds via MBE is the flux ratio J, which for binary compounds can be defined as the ratio of the beam equivalent pressures (BEPs) of the two materials. For example, in the growth of MnSb J is calculated with the following equation:

$$J_{Sb/Mn} = \frac{BEP_{Sb}}{BEP_{Mn}} \tag{2.3}$$

Due to the cell configuration used on the MBE system at Warwick used in this work, when the Sb effusion cell shutters are initially opened there is a spike in Sb pressure which goes above the calibration pressure measured with the beam flux gauge. This can have a significant effect on the flux ratio when growing thin samples with growth times $t_g \leq 3\tau$, where τ is the time constant of the exponential decay for the Sb effusion cell pressure. In order to account for this pressure burst a corrected flux ratio $J^{corr}_{Sb/Mn}$ can be calculated using equation 2.4 [74].

$$J^{Corr}_{Sb/Mn} = J_{Sb/Mn}\left(\frac{t_g + 32.929\ s}{t_g}\right) \tag{2.4}$$

2.2 Surface reconstruction notation

For a material with directional, covalent bulk bonds, the atoms present in the surface atomic layer possess dangling bonds which can cause the atoms to rearrange, adopting a different structure to the underlying bulk. This is called a surface reconstruction, and can involve movement of the surface atoms both perpendicular and parallel to the surface in order for new bonds to be formed between atoms [75] In contrast, a surface relaxation is where atomic layers just have a change in their positions along the out-of-plane direction, with their in-plane positions remaining fixed. In both cases, atomic re-arrangement acts to minimise the surface energy.

Surface reconstructions can be described using Wood notation, which defines the lengths of the surface mesh unit vectors for the reconstructed surface $\mathbf{a}'$ and $\mathbf{b}'$ relative to the lengths of the unit vectors for the underlying bulk-terminated surface mesh $\mathbf{a}$ and $\mathbf{b}$. If the scaling between the unit vectors is given as $|\mathbf{a}'| = p|\mathbf{a}|$ and $|\mathbf{b}'| = q|\mathbf{b}|$, then the general form of Wood notation is:

$$X\{hkl\}(p \times q)R\phi - A$$

where X is the surface material, ϕ is the angle between the two sets of surface mesh unit vectors and A is the adsorbate material (this term is only included if the surface atoms are adsorbates which differ from the surface material). Examples of Wood notation are shown in figure 2.4, highlighting the use of p to label primitive unit meshes and c to label centred unit meshes.

In the case where the directions of unit vectors $\mathbf{a}'$ and $\mathbf{b}'$ cannot be related to $\mathbf{a}$ and $\mathbf{b}$ with a simple rotation and scaling, the matrix notation G must be used as follows:

$$\mathbf{a}' = G_{11}\mathbf{a} + G_{12}\mathbf{b}$$
$$\mathbf{b}' = G_{21}\mathbf{a} + G_{22}\mathbf{b}$$

$$G = \begin{pmatrix} G_{11} & G_{12} \\ G_{21} & G_{22} \end{pmatrix}$$

Note that a similar matrix notation can be used to describe the interface between two materials of different symmetry [76].

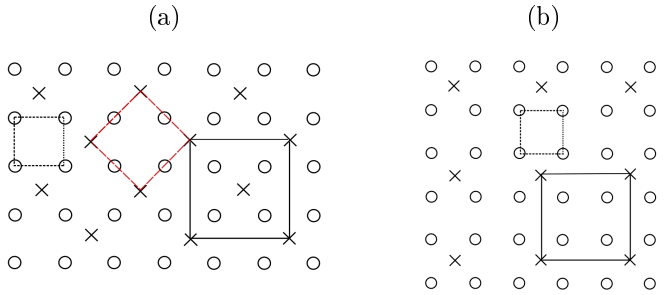

Figure 2.4: Example surface reconstructions where circles represent the periodicity of the unreconstructed bulk, and crosses represent the periodicity in the reconstructed surface. (a) The surface mesh for the unreconstructed bulk is shown as a dotted line, the red dashed line shows the $(\sqrt{2} \times \sqrt{2})R45^\circ$ surface mesh, which can also be described with the centered $c(2 \times 2)$ surface mesh shown as a solid black line. (b) The surface mesh for the unreconstructed bulk is shown as a dotted line, due to having no atom at the centre the reconstruction is described as the primitive $p(2 \times 2)$ surface. Adapted from [77]

2.3 Crystallographic direction notation

For cubic crystal systems all planes and corresponding directions within the crystal can be defined through the use of the Miller indices *h, k* and *l*. The value of *h/k/l* is given by taking the reciprocal of the value where the (*hkl*) plane intercepts the a/b/c axis, in units of the lattice constant for that axis. For cubic symmetry the (001) and (100) planes are identical, and belong to the family of planes {100}. For hexagonal systems the symmetry is different, and therefore an extra index is required to correctly group and distinguish between symmetrical directions. For this the Miller-Bravais index notation (*hkil*) is used, where $i = -(h + k)$ [72]. A comparison between Miller and Miller-Bravais notation is shown in figure 2.5.

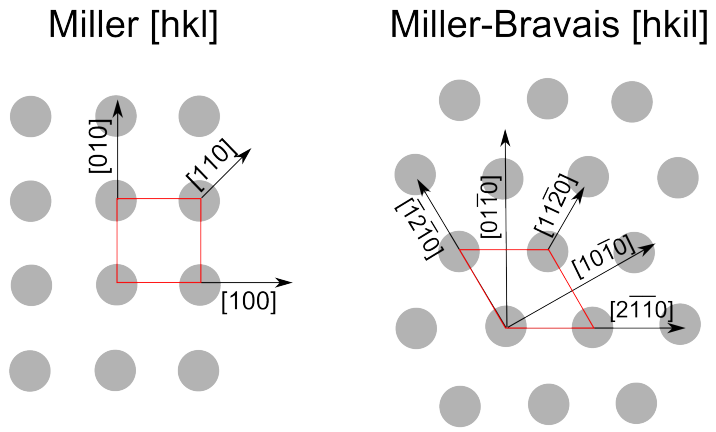

Figure 2.5: A comparison between cubic Miller notation [*hkl*] and hexagonal Miller-Bravais notation [*hkil*]. Unit cells for the surfaces are shown in red solid lines.

2.4 Bulk diffraction

A bulk crystal can be described using a combination of lattice vectors $\mathbf{R}_n$ which connect unit cells, and the atom positions $\mathbf{r}_j$ within the unit cell. When X-rays with an incident wavevector $\mathbf{k}_i$ are diffracted by a bulk crystal that has lattice unit vectors ($\mathbf{a}$,$\mathbf{b}$,$\mathbf{c}$) there are only certain values of diffracted wavevector $\mathbf{k}_f$ that give rise to constructive interference, and therefore measured intensity. The scattering vector $\mathbf{Q}$=$\mathbf{k}_f - \mathbf{k}_i$ is commonly used to describe diffraction. The scattering amplitude from the crystal can be written as the product of two summations: a sum over the unit cell and a sum over the lattice (equation 2.5). Here $f_j(\mathbf{Q})$ is the atomic scattering factor of the jth atom in the unit cell.

$$F^{crystal}(\mathbf{Q}) = \sum_j f_j(\mathbf{Q}) \exp(i\mathbf{Q}.\mathbf{r}_j) \sum_n \exp(i\mathbf{Q}.\mathbf{R}_n) \tag{2.5}$$

For intensity to be measured Q must have a value defined by the following Laue conditions:

$$\mathbf{Q}\cdot\ \mathbf{a} = 2\pi h \quad \mathbf{Q}\ \cdot\ \mathbf{b} = 2\pi k \quad \mathbf{Q}\cdot\ \mathbf{c} = 2\pi l$$

where h,k and l are integers. These conditions are derived from a summation of scattering amplitude contributions from all atoms in the crystal lattice, and this will be explained in more detail in section 2.5.2. The values of $\mathbf{Q}$ that satisfy these conditions make up a lattice of points referred to as the reciprocal lattice, with each point being the result of three δ functions (one δ function for each lattice vector). The reciprocal lattice is defined by the three reciprocal lattice unit vectors $\mathbf{a}^*, \mathbf{b}^*, \mathbf{c}^*$, which are related to the real lattice vectors by the following equations [77]:

$$\mathbf{a}^* = 2\pi\frac{(\mathbf{b}\times\mathbf{c})}{\mathbf{a}.(\mathbf{b}\times\mathbf{c})} \quad \mathbf{b}^* = 2\pi\frac{(\mathbf{c}\times\mathbf{a})}{\mathbf{a}.(\mathbf{b}\times\mathbf{c})} \quad \mathbf{c}^* = 2\pi\frac{(\mathbf{a}\times\mathbf{b})}{\mathbf{a}.(\mathbf{b}\times\mathbf{c})}$$

Therefore constructive interference will only occur when $\mathbf{Q}$ is equal to a reciprocal lattice vector $\mathbf{g}_{hkl}$. This condition is summarised with the following equations:

$$\mathbf{k}_f = \mathbf{k}_i + \mathbf{g}_{hkl} \tag{2.6}$$

$$\mathbf{g}_{hkl} = h\mathbf{a}^* + k\mathbf{b}^* + l\mathbf{c}^* \tag{2.7}$$

From knowing solutions to equations 2.6 and 2.7, the expected diffraction pattern can be calculated graphically by constructing the Ewald sphere (Figure 2.6). The Ewald sphere has a radius $|\mathbf{k}_i|$ and is centred on the tail of $\mathbf{k}_i$ when the head of $\mathbf{k}_i$ is placed at the origin of reciprocal space. All points on the sphere's surface represent values of $\mathbf{k}_f$, and there will only be diffracted intensity when a point on the surface of the Ewald sphere intersects with a point on the reciprocal lattice. Therefore the expected diffraction pattern can be calculated if the section of the Ewald sphere being accessed by an experiment is known.

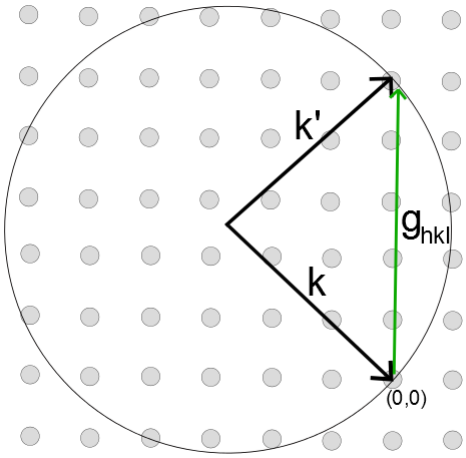

Figure 2.6: 2D representation of the construction of the Ewald sphere, with grey circles representing the reciprocal lattice. An example reciprocal lattice vector $\mathbf{g}_{hkl}$ is also shown.

2.5 Surface X-ray diffraction

X-rays offer a very useful technique for probing the structure of materials due to having much weaker interactions with atoms compared to other probes such as electrons. This weak interacting nature allows X-rays to provide information on bulk materials and buried interfaces of samples. Surface sensitivity can be obtained by using an incident angle very close to the critical angle of the material being investigated. The critical angle (α_c) of a material is linked to its refractive index through equations 2.8 and 2.9 using the simplification that β=0.

$$n = 1 - \delta + i\beta \qquad \alpha_c = \sqrt{2\delta} \tag{2.8}$$

$$\delta = \frac{2\pi\rho f^0(0) r_0}{k^2} \qquad \beta = \frac{\mu}{2k} \tag{2.9}$$

Where n is the refractive index, δ and β are refractive constants related to the scattering and absorption properties of the material respectively. When an incident

angle below α_c is used, an evanescent wave is setup which propagates parallel to the surface and decays rapidly into the sample. This can decrease the penetration depth of the X-rays to a few nanometers, boosting the signal from the sample surface [78]. When a low incident angle is used in scattering geometry the amount of active material being probed, and concomitantly the diffracted signal strength, is significantly decreased. For this reason surface X-ray diffraction (SXRD) experiments using low incident angles require the use of synchrotron radiation X-ray sources that provide high enough intensities to obtain reliable counting statistics.

When considering X-rays being diffracted by a 2D monolayer, the Laue condition in the direction perpendicular to the sample surface is relaxed. This means that only the component of $\mathbf{k}_i$ parallel to the surface is conserved, and the equations summarising the conditions on diffraction become:

$$\mathbf{k}_{f\parallel} = \mathbf{k}_{i\parallel} + \mathbf{g}_{hk} \tag{2.10}$$

$$\mathbf{g}_{hk} = h\mathbf{a}^* + k\mathbf{b}^* \tag{2.11}$$

$$\mathbf{a}^* = 2\pi\frac{(\mathbf{b}\times\mathbf{n})}{\mathbf{a}.(\mathbf{b}\times\mathbf{n})} \quad \mathbf{b}^* = 2\pi\frac{(\mathbf{n}\times\mathbf{a})}{\mathbf{a}.(\mathbf{b}\times\mathbf{n})}$$

where $\mathbf{n}$ is a unit vector normal to the surface. This gives rise to rods of allowed diffraction in reciprocal space, defined as δ functions in the two in-plane directions parallel to the surface, but continuous in the out-of-plane direction.[77][75]

A truncated crystal can be thought of as similar to the combination of a bulk crystal and a monolayer, although the reciprocal lattice is not simply a combination of the bulk points and monolayer rods, because all layers of the crystal contribute to the diffraction. The resulting rods in reciprocal space are called crystal truncation rods (CTRs) and have changing intensity as you vary the value of the out-of-plane parameter (Figure 2.7). The shape of the CTR intensity between Bragg points can provide information about the surface structure. For example the asymmetry of

a plot of intensity versus Q_z is related to the interfacial parameter between the overlayer and substrate [75]. Examples of the effect that lattice displacements and surface roughness have on the shape of the [01L] CTR for a GaAs(111)B model are shown in figure 2.8.

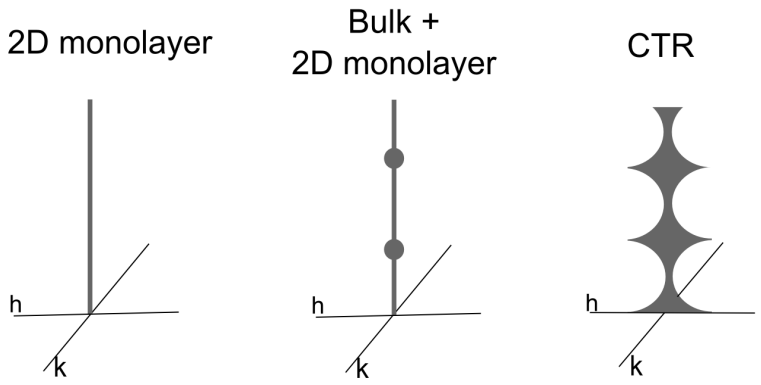

Figure 2.7: Example reciprocal lattices for a 2D monolayer, a bulk crystal with a monolayer, and a real truncated crystal.

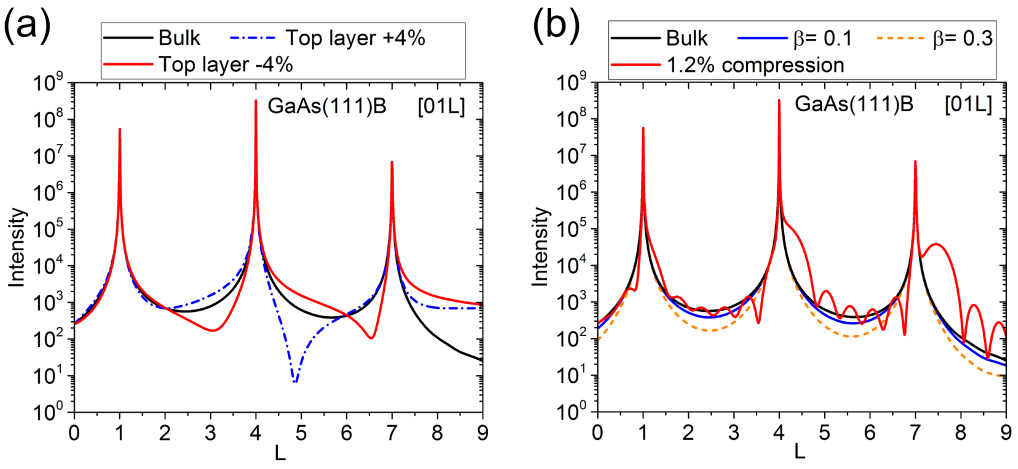

Figure 2.8: Changes in GaAs(111)B [01L] CTR as a result of (a) top layer displacement, and (b)surface model roughness or compression of top 12 atomic layers.

2.5.1 SXRD Data collection

Diffractometers used in SXRD experiments are generally described as being (a + b)-type, where a is the number of degrees of freedom for the sample, and b is the number

of degrees of freedom for the detector [79]. SXRD experiments presented in this thesis were carried out at either the I07 bealime at Diamond Light Source (UK) [80] or the BL11XU beamline at SPring-8 (Japan) [81]. Experiments at the I07 beamline were performed in the second experimental hutch (EH2), using a (2+3) diffractometer (figure 2.9). The UHV chamber in EH2 is made up of three separate sections; a turbo-pumped load lock, a turbo-pumped and ion-pumped buffer chamber, and a turbo-pumped and ion-pumped analysis chamber. Experiments performed at BL11XU used a (2+4) diffractometer with the azimuthal rotation of the detector fixed, so it approximates a (2+3) diffractometer setup. The UHV system on BL11XU has two chambers separated by a gate valve; a sample loading chamber, and a growth and analysis chamber. In both SXRD systems the sample was mounted in vertical scattering geometry, with the sample normal parallel to the floor.

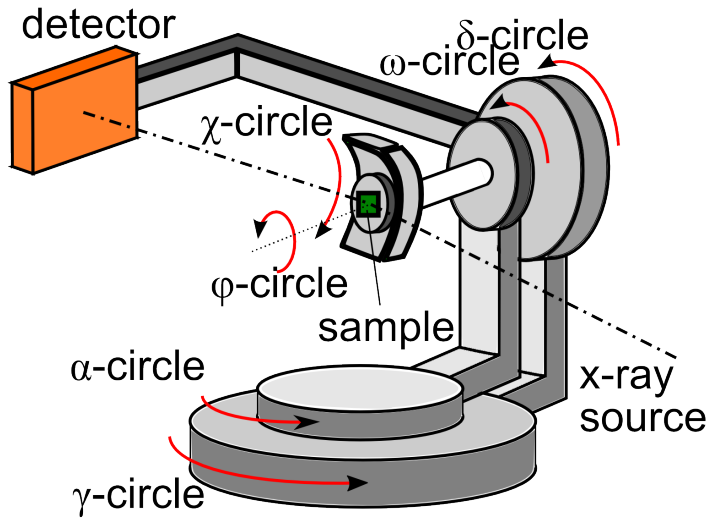

Figure 2.9: Schematic representation of the diffractometer at I07, Diamond light source (UK).

At the beginning of a SXRD experiment the sample needs to be leveled flat. This can be done either optically or crystallographically. The optical leveling method involves making adjustments of sample position based on measurements of

how the sample blocks the direct X-ray beam with all diffractometer angles set to 0. For the crystallographic method, the sample is initially flattened the same way but then a test reflection is measured while the sample is rotated. Any slight offset due to sample miscut will be seen as a movement of the signal upon azimuthal rotation of 180° about the surface normal, and can be corrected accordingly. Once the sample is level a UB matrix needs to be assigned in order to allow navigation in reciprocal space. The UB matrix is a combination of two matrices; U and B. The B matrix is used to convert the reciprocal lattice of the sample to a Cartesian frame, and is obtained directly from the samples real space lattice (a_i, α_i) and reciprocal space lattice (b_i, β_i) (equation 2.12). The U matrix is called the orientation matrix, and accounts for the movement of the various diffractometer circles and the sample positioning relative to the diffractometer axis. This means that the value of the U matrix is dependent upon the diffractometer type, as well as on what position the sample has been mounted in. The UB matrix is determined experimentally by measuring the positions of several reflections. If the lattice parameters are known then only two reflections from non-parallel planes are required. However, if the lattice parameters are unknown then the calculation requires measuring three reflections which have reciprocal lattice vectors that are not co-planar [82].

$$B = \begin{bmatrix} b_1 & b_2 \cos\beta_3 & b_3 \cos\beta_2 \\ 0 & b_2 \sin\beta_3 & -b_3 \sin\beta_2 \cos\alpha_1 \\ 0 & 0 & 2\pi/a_3 \end{bmatrix} \tag{2.12}$$

There are several different types of SXRD scans which can be performed in order to gain information about a sample. An out-of-plane symmetric diffraction scan is obtained by ensuring that the incident and exit angles of the scattered beam are equal. In this type of scan if the sample is tilted by an angle θ, then the detector is required to move an angle equal to 2θ, therefore this scan is referred to as a $\theta - 2\theta$ scan. This scan is used to obtain information about the lattice spacings present in

the out-of-plane direction, and has contributions from all material in the sample. $\theta - 2\theta$ scans can be performed without a UB matrix, and only require the sample surface to be level. The UB matrix enables multiple other types of scans to be conducted, the most common types are crystal truncation rod (CTR) scans and HK-plane scans. CTR scans measure the change in intensity along the out-of-plane L direction when positioned at a specific HK value. CTRs only provide information on materials whose in-plane spacing is close to that of the material used to define the UB matrix. HK-plane scans measure the change in intensity along any direction which lies in the HK plane, and provide information on the in-plane lattice spacings. HK-plane scans can only provide information on materials with similar symmetry to the material used to define the UB matrix.

2.5.2 SXRD Data analysis

Once SXRD CTR data has been collected it needs to undergo data reduction and have correction factors applied before it can be fitted to structural models. For SXRD analysis reported in this thesis a modified version of the matlab programme *Scananlysis* [83] was used to read in the Pilatus images collected during each scan and extract the integrated intensities. The analysis of an image can be quite a subjective process depending on the experience of the data analyst and the quality of the image. The general procedure followed for the datasets analysed in this thesis was as follows:

1. An appropriate region of interest (ROI) for the CTR signal was chosen, and it was ensured that the signal was centred within the ROI as this was necessary for implementation of L-shift corrections (detailed later in this section).

2. A background ROI that was slightly larger than the signal ROI was chosen so that just enough pixels were used to give a good representation of the background

3. The simplest background fitting function which achieved a reasonable fit was chosen. Often this was a linear function when away from Bragg peaks and 2D gaussian function plus a constant when near to Bragg peaks.

4. Once a suitable background substraction was obtained the data point was marked as good and the analysis moved to next image repeating the procedure from step 1

For the data analysis presented in this thesis there were a few instances where there were some exceptions to the standard protocol required, and these will be mentioned later on in this section.

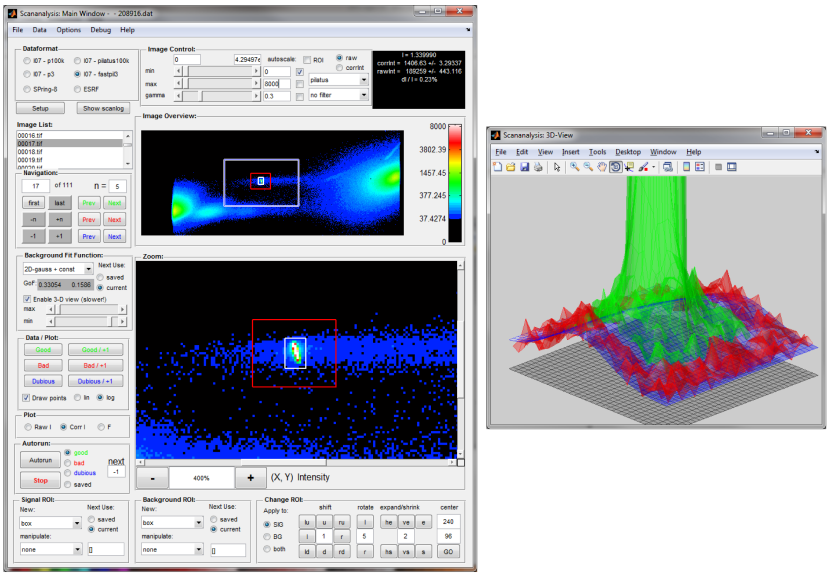

Figure 2.10: Example printscreen from Scananalysis program, showing the main analysis window and the 3D plot of background fitting.

Images that were taken very close to Bragg peaks ($L_{Bragg} \pm 0.01$) were excluded from the dataset for two reasons; firstly the background subtraction functions do not handle the high intensity points well, and secondly the CTR fitting equations are based on the kinematical (single scattering) approximation which is known to inadequately describe the scattered intensity close to Bragg points [84]. Images that

were further away from Bragg peaks but still in the vicinity (± 0.05), whilst not being very surface sensitive, still provided useful information for the scaling of CTRs.

The modified Scananalysis software applied three correction factors to the data before saving the integrated intensity [83]. Firstly there is the polarisation factor which accounts for the polarisation of the incident X-ray beam given by:

$$C_p = p_h(1 - \cos^2\delta \sin^2\gamma) + (1 - p_h)(1 - \sin^2\delta) \tag{2.13}$$

where p_h is the horizontal polarisation of the synchrotron beam. The second is a correction factor (C_I) to account for the amount of CTR intercepting the Ewald sphere given by:

$$C_I = \cos\delta \sin(\gamma - \alpha) \tag{2.14}$$

Thirdly there is a correction factor to account for the active area of the sample [85]:

$$C_{beam} = \begin{cases} \dfrac{1}{\sin\delta \cos(\alpha - \beta_{in})} & \text{for non-specular CTR scans} \\ \sin\alpha & \text{for specular CTR scans} \end{cases}$$

These three correction factors are then used to calculate the corrected intensity I_{corr} from the recorded intensity I_{rec} using:

$$I_{corr} = I_{rec} C_I \frac{1}{C_p} \frac{1}{C_{beam}} \tag{2.15}$$

Ideally the CTR signal should not change its position on the detector during the scan; however imperfect sample alignment can lead to the signal not remaining centred on the detector. Other factors such as sample movement or lattice strain can also alter the position of the CTR signal on the detector during the scan. For these displaced signals the Ewald sphere intercepts the CTR at an L position that differs from the value recorded for the scan image. To correct for this movement a shifted L value (L_{shift}) was calculated based on the amount of pixels that the signal was away

from the detector centre (figure 2.11). For most scans the direction of increasing L aligned with the horizontal line of the detector, however for a small number of scans the L direction was a diagonal direction in the detector reference frame. Therefore for these scans both the vertical and horizontal pixel distances from the centre were used. The pixel spacing was converted to an angular spacing (θ_{shift}) which was used to calculate the Q_z value at the signal position (equation 2.17). This Q_z position was then used to calculate the shifted L-value using the equations 2.16 and 2.18.

$$Q_z^{centre} = k(\sin(\theta_{inc}) + \sin(\theta_{exit})) \tag{2.16}$$

$$Q_z^{signal} = k(\sin(\theta_{inc}) + \sin(\theta_{exit} + \theta_{shift})) \tag{2.17}$$

$$L_{shift} = \frac{Q_z^{signal}}{Q_z^{centre}} \times L_{centre} \tag{2.18}$$

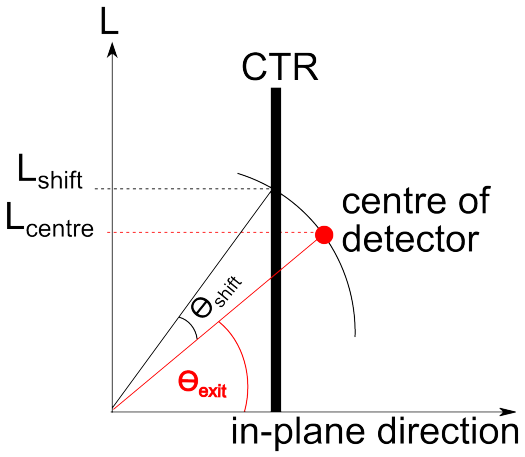

Figure 2.11: Diagram of L-shift calculations. The Matlab code used to implement this correction is included in Appendix A

Effects of crystallographic miscut

When a sample surface has a significant amount of miscut the Bragg points are no longer elongated along the L direction, but are instead elongated along a diagonal to

the L direction (figure 2.12). This altered direction of elongation results in a splitting of the CTR intensity so that there are two signals of intensity on the detector at the anti-Bragg positions. An example of this is shown in the lower panel of figure 2.12, showing the miscut CTR signal of a clean InAs(111)B surface at the (0 1 2.5) position. For samples with an off-cut a slightly altered approach to selecting the ROI and background boxes were needed due to there being two CTR signals present on the detector for the majority of the scan. For images where the two signals were close together a ROI box large enough to encompass both signals was selected and the pixel half-way between the two was used to calculate the L value. However when the two signals were further apart the background fitting procedure struggled to correctly fit the larger background area. Therefore for images that had two signals far apart a ROI box was selected that just encompassed the stronger of the two signals. Note that the off-cut affects quadrants of reciprocal space differently, resulting in an inequivalence for CTRs which are usually symmetrically identical.

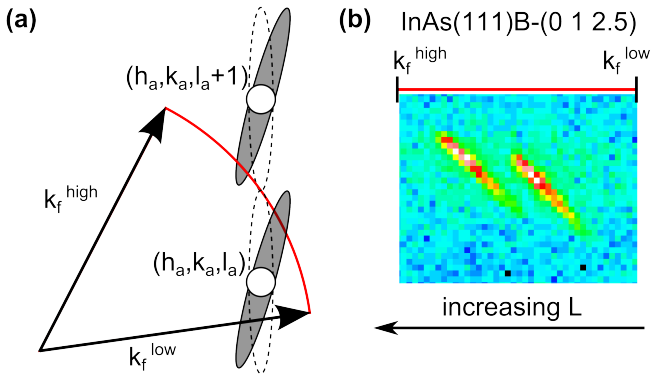

Figure 2.12: (a) Diagram of reciprocal lattice for a miscut surface, (b) an example detector image of a split signal. k_f^{high} (k_f^{low}) is the upper (lower) limit of scattered wavevector reaching the detector. The dotted elipses in (a) represent the elongation from a surface with no miscut.

CTR line profile fitting programs

Once CTR data has been reduced into line profiles, the dataset is loaded into a fitting program to compare the line profiles to modelled profiles. For CTR profile fitting pre-

sented in this thesis the program WinRod [86] was used. The theoretical model for SXRD can be derived using a kinematical approximation, where secondary diffraction events are neglected. The overall scattered intensity measured from a sample material for a specific *hkl* reflection can be found by a succession of summations. This starts off by considering the X-ray intensity scattered from a single electron, goes on to sum these electron contributions over a single atom and then sums these atomic contribution over all the atoms present in the unit cell. Once the scattered intensity is obtained for a single unit cell, it is combined with the sample lattice type to obtain the *hkl* structure factor F_{hkl} (equation 2.19). Here f_j is the atomic scattering factor of atom j, B is the Debye-Waller parameter, Q is the total momentum transfer, (hkl) are the Miller indices, and (xyz) are the fractional co-ordinates representing the position of atom j. This structure factor is then used to calculate the overall scattered intensity $|F_{hkl}|^2$.

$$F_{hkl} = \sum_j f_j \exp(\frac{-B_j Q^2}{16\pi^2}) \exp(2\pi i(hx_j + ky_j + lz_j)) \tag{2.19}$$

For the model used in the fitting program WinROD a combination of a bulk slab defined by a bulk unit cell (B.U.C) and a surface slab defined by a surface unit cell (S.U.C) is used [87]. The structure factors of these two slabs are summed together to give the overall structure factor from the total sample (equation 2.20). The surface structure factor equation has an extra parameter for occupancy (θ_j) because the surface atomic layers are not necessarily 100% occupied.

$$F_{hkl} = F_{sum} = F_{surf} + F_{bulk} \tag{2.20}$$

$$F_{surf} = \sum_j^{\text{S.U.C}} f_j \theta_j \exp(\frac{-B_j Q^2}{16\pi^2}) \exp(2\pi i(hx_j + ky_j + lz_j)) \tag{2.21}$$

$$F_{bulk} = \sum_{j=-\infty}^{0} \exp(2\pi i l j) \exp(j\alpha) \left[\sum_{j}^{\text{B.U.C}} f_j \exp(\frac{-B_j Q^2}{16\pi^2}) \exp(2\pi i (hx_j + ky_j + lz_j)) \right] \tag{2.22}$$

Bulk parameters were used to create an initial model with suitable starting atomic positions. The L-shifted CTR dataset was then loaded into the winROD program and compared to the calculated profiles from a single bulk slab. Each CTR was individually scaled so that the intensities closest to the substrate Bragg points matched as closely as possible to the calculated profiles from the bulk slab. Once all CTRs had been appropriately scaled, an initial surface slab using the appropriate bulk material atomic positions was added to the model and used as a starting point for structure refinement. The structure refinement process is carried out by using the simulated annealing χ^2 minimisation procedure available in ROD. This returns a χ^2 value (equation 2.23) which is used to quantify the goodness-of-fit between the current model and experimental data. Here N is the number of data points in the dataset, p is the number of independent fitting parameters used in the model, and σ_{hkl} is the experimental uncertainty.

$$\chi^2 = \frac{1}{\sqrt{N-p}} \sum_{hkl} \frac{|F_{hkl}^{calc}|^2 - |F_{hkl}^{exp}|^2}{\sigma_{hkl}} \tag{2.23}$$

Real world samples will most likely deviate from the simplified model presented above. ROD has several modifications which can be made to the interference sum in order to account for some of these non-ideal characteristics [87]. A roughness parameter R is included to account for surface roughness, which is calculated from the fitted value of β, the value of the nearest Bragg peak (l_{Bragg}) and the number of equidistant layers within the unit cell (N_{layers}) (equation 2.24). For samples where there are two different types of surface layer present ROD can have a second surface model loaded in as a set fraction (f_{s2}) of the first surface (f_s). The modified equation for F_{sum} is given in equation 2.25, where S is an overall scale factor and α_j is the occupancy of the jth domain.

$$R = \frac{1-\beta}{\sqrt{(1-\beta)^2 + 4\beta \sin^2\left(\frac{\pi(l - l_{Bragg})}{N_{layers}}\right)}} \tag{2.24}$$

$$F_{sum} = SR\Big[(1-f_s)\sum_j \alpha_j F_{b,j}^2 + f_s(1-f_{s2})\sum_j \alpha_j (F_{s,j} + F_{b,j})^2 + f_s f_{s2}\sum_j \alpha_j (F_{s2,j} + F_{b,j})^2\Big]^{1/2} \tag{2.25}$$

3D visualisation

3D visualisation of the CTR datasets was conducted using a combination of BINoculars software [88] and Mayavi software [89]. While these software provided a useful method of visualising the dataset, it should be noted that their representation of the HK plane is not completely accurate as the HK axes should be separated by 60° rather than 90°. Example Matlab code used to convert '.hdf5' files into '.VTK' files is included in appendix A.

2.6 Reflection high energy electron diffraction

Reflection high energy electron diffraction (RHEED) is a UHV technique for surface diffraction. In RHEED, electrons with kinetic energy 5 - 30 keV are directed towards the sample at low grazing angles ($< 5°$), which provides surface specificty as the electrons are travelling nearly parallel to the surface and cannot penetrate far into the sample. The use of grazing angles also means it is possible to conduct RHEED measurements during MBE growth, providing real time information on the growth process. The analysis of electron diffraction patterns from a surface can be conducted in a similar manner to X-ray diffraction, with the use of the Ewald sphere showing which parts of the accessible area of reciprocal space contribute to diffraction.

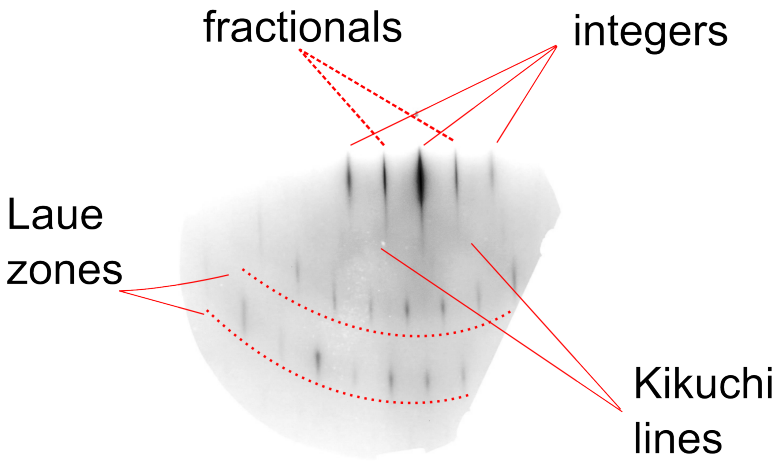

Figure 2.13: An annotated example of a RHEED pattern showing integer peaks, fractional peaks, Laue zones and Kikuchi lines

The RHEED pattern is displayed on a phosphor screen and provides information on the structure of the overlayer. An example RHEED pattern obtained from a highly crystalline (2×2) reconstructed surface is shown in figure 2.13. Both the integer and fractional signals are streaks, which arises from the intersection of the Ewald sphere by reciprocal rods of finite width (figure 2.14). These rods possess a finite width due to the imperfect periodicity of the sample surface and atomic vibrations [90]. The width of the reciprocal rod can also be affected by the spread in energies (ΔE) of the electron beam, but a common tungsten filament produces $\Delta E \leq 1$ eV which is negligible in the energy ranges used.

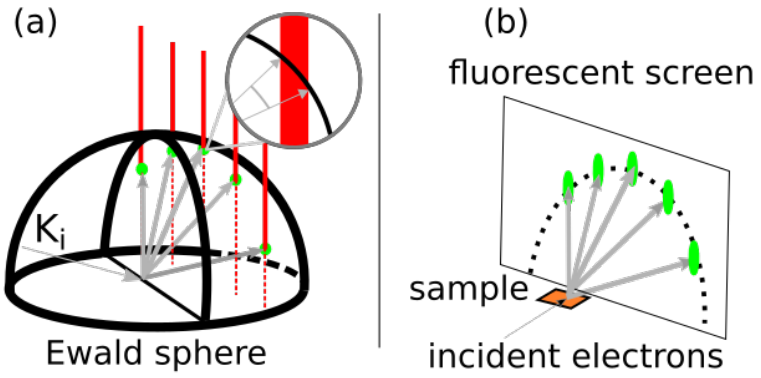

Figure 2.14: (a) Intersection of Ewald sphere with reciprocal rods of finite width, and (b) Corresponding streaks in real space on the RHEED phosphor screen.

The strong integer streaks correspond to distances of periodicity present in both the reconstructed surface and the unreconstructed layers beneath. The fractional order streaks between the integer order streaks correspond to the larger distance of periodicity present in just the reconstructed surface. The example RHEED pattern (figure 2.13) also exhibits other common features including Laue zones and Kikuchi lines. Laue zones are extra bands of diffracted intensity that arise from the Ewald sphere cutting through multiple planes of reciprocal rods. Kikuchi lines are a set of lines that intersect the central integer streak at roughly 45 ° that arise due to secondary scattering effects. This is where inelastically scattered electrons within the crystal contribute to the diffraction pattern by undergoing elastic scattering from bulk planes. Therefore Kikuchi lines indicate high crystalline quality of the overlayer.[90]

For surfaces which are almost perfectly periodic the reciprocal rods approach δ functions, and produce a diffraction pattern consisting of spots. This high level of periodicity occurs for surfaces which possess terraces of material $\geq$100 nm in width. A second, more common, type of spots are produced if the surface contains 3D islands of material through which the incident electrons can undergo transmission diffraction rather than grazing reflection. The presence of these patterns indicate

growth is occurring via either Volmer-Weber or Stranski-Krastanov growth modes. If the transmission spots share the same spacing as the integer streaks then they are termed commensurate, but if they have a spacing that differs from the integer streak spacing then they are termed incommensurate.

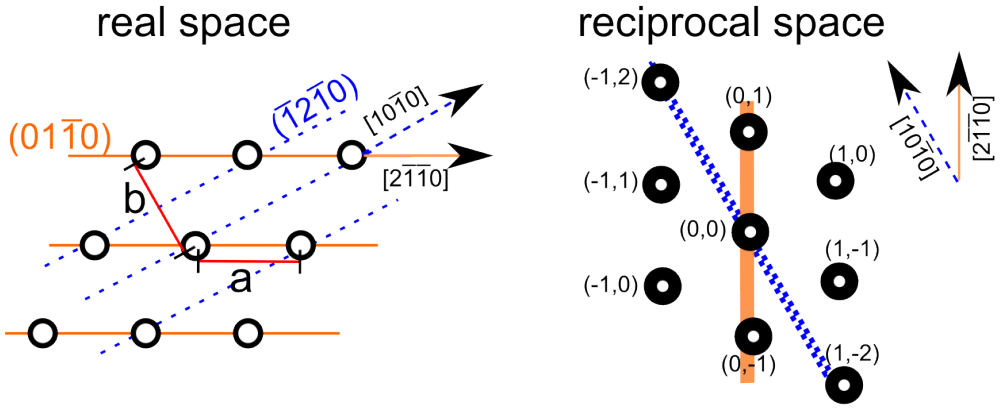

Figure 2.15: Real space and reciprocal space diagrams for hexagonal surfaces, highlighting the distances probed when used different RHEED directions.

For a hexagonal surface there are two different magnitudes of spacing, in directions which are 30° apart. To collect full two dimensional RHEED information from these surfaces it is necessary to rotate the sample about its normal, due to the fact that any periodicity present in the plane of incidence will not affect the periodicity of the RHEED pattern [77]. The relationship between the real and reciprocal lattices for a hexagonal surface are shown in figure 2.15, with the RHEED pattern either being wide [10$\bar{1}$0] or narrow [2$\bar{1}$10]. The spacings of the real lattice can be calculated from either the wide or narrow patterns. For the wide RHEED pattern a simple factor of two is needed to transform the spacing d into the lattice constant a. For the narrow RHEED pattern a factor of $1/cos(\phi)$ is needed where ϕ is the angle between the spacing being probed and the lattice parameter (e.g. 30° for a hexagonal lattice)[90][91].

For samples grown at Warwick the streak separations were calculated using the fixed separation of fluorescent squares attached to either side of the RHEED

screen as calibration. From this relationship the real space distances being probed (d) can be calculated using the following equation:

$$d = \frac{2\pi L}{k_i s}, \tag{2.26}$$

where L is the distance from sample to the RHEED screen (camera length), s is the separation of the integer streaks in the RHEED pattern, and k_i is the wavevector of the incident electrons.

2.7 Low energy electron diffraction

Low energy electron diffraction (LEED) is a different UHV electron diffraction technique for measuring reciprocal space, which is conducted in backscattering geometry (figure 2.16). LEED is usually conducted with an electron beam accelerated with 10-500 V, which is incident normal to the surface with a fluorescent screen collecting the elastically backscattered electrons [92]. Rotation of the sample is not required during LEED because each pattern provides a measurement of reciprocal space in two-dimensions, which are approximately in the HK plane.

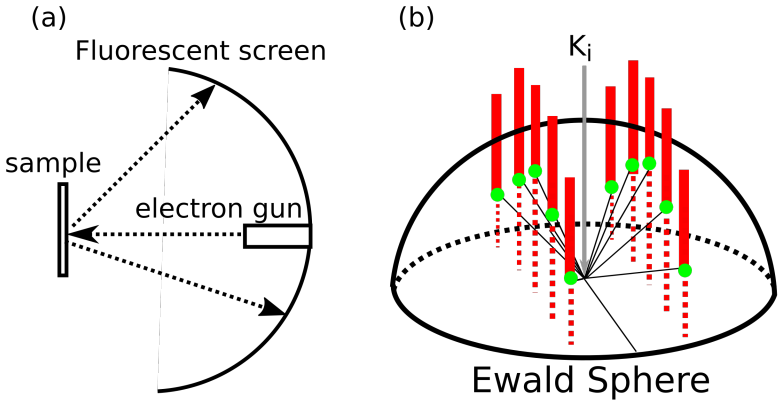

Figure 2.16: (a) Schematic representation of LEED setup (b) Ewald sphere for LEED

2.8 X-ray Photoelectron Spectroscopy

X-ray photoelectron spectroscopy (XPS) is a technique which allows the identification of atomic species and chemical environments present near a sample's surface. In XPS a monochromatic X-ray beam is incident on a sample surface resulting in the photoemission of electrons. The spectrum of photoelectron energies is measured, typically with a concentric hemispherical analyser. From knowing the initial energy of the X-ray photons ($h\nu$), the work function of the material (ϕ) and the kinetic energy (E_K) of the measured electrons, then the binding energy (E_B) of the measured electron can be calculated using the relation $E_K = h\nu - E_B - \phi$. A typical X-ray source is Al K_α , which has a $h\nu$ value of 1486.7 eV. The exact values of E_B provides information on both the atomic species present in a sample, as well as the chemical bonding environments of the atoms. Whilst the X-rays can penetrate $\geq$1 mm into the sample, the photoelectrons produced have an inelastic mean free path of $\sim$1nm. This means that typically XPS measures photoelectrons from only the top few nm of a sample.

2.9 Atomic Force Microscopy

Atomic force microscopy (AFM) is an imaging technique which allows the measurement of local surface topography. In AFM a cantilever with a sharp tip is moved over a sample surface, and the interactions between the surface atoms and the tip cause changes in the deflection of the cantilever (figure 2.17). The tip is scanned across the sample surface using piezo electric motors, and the movements of the cantilever are measured by the change in position of a laser beam reflected onto a photo diode. These cantilever movements are then processed and used to build up a map of the surface topography, an example image is shown in the right panel of figure 2.17.

There are two main types of imaging modes for AFM. The first is contact mode where the tip makes contact with the surface and is scanned whilst maintaining

contact. The second is tapping mode where the cantilever is driven to oscillate at a set frequency, then the tip is scanned over the surface without making prolonged contact. The frequency of oscillation is altered by a magnitude determined by the interactions of the tip and the sample surface. In both modes a feedback system ensures that either the cantilever deflection or frequency shift is kept constant as the tip is rastered, generating a surface topography z(x,y). The majority of AFM images in this thesis were collected using contact mode, and exceptions to this will be identified as they are presented. Typical image sizes are of the order 1μm, and typical root mean square (RMS) roughnesses are 1 - 10 nm

The program Gwyddion [93] was used to analyse all AFM images presented in this thesis. All images had a second order polynomical background removed to account for sample tilt and thermal drift.

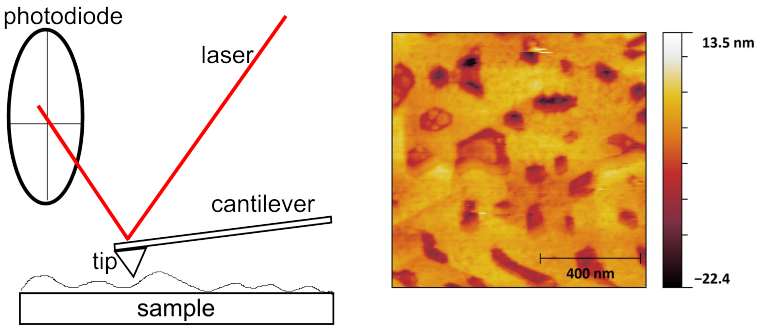

Figure 2.17: (left) Schematic representation of an AFM (right) Example AFM image obtained using contact mode AFM.

2.10 Scanning Electron Microscopy

In scanning electron microscopy (SEM) an electron beam is rastered across a sample surface and the intensity of backscattered or secondary electrons is measured. SEM is complementary to techniques such as AFM, because it gives a measure of the relative scattering strength of areas on the surface rather than topography. SEM also enables the rapid imaging of much larger surface areas, allowing for improved

statistical information on the occurrence of surface features such as crystallites. In this work SEM is only used to assess the prevalence of particular features on MBE-grown samples. A full review of SEM methods can be found in [94].

2.11 Transmission Electron Microscopy

In transmission electron microscopy (TEM) an incident electron beam is transmitted through a very thin region of a specimen, and the transmitted electrons are detected. The thinned sample can be created by fabricating a specimen perpendicular to the sample surface, which allows the full depth of an MBE layer structure to be investigated. This can provide information on the structure such as interface quality and layer homogeneity. High resolution imaging can readily provide information on individual atomic columns present in different layers of the substrate, as well as the formation of structures at interface e.g. steps.

When no optics are used to treat the transmitted electron beam a collection of diffraction spots will be recorded, creating a selected area diffraction pattern (SADP). These spots correspond to allowed diffraction conditions, and can be analysed in a similar way to other diffraction techniques. SADPs can complement other techniques by providing local information on crystal structures present within areas of the order 100 nm in size.

When the incident electron beam strikes the surface, X-rays are also emitted from the sample. Energy dispersive X-ray (EDX) spectroscopy can be performed on these X-rays to determine which atomic species they originated from. EDX is used to provide an elemental compositional analysis of the sample. In this work TEM and EDX were used to assess the structure of thin films and interfaces, complementing the other studies.

2.12 Vibrating sample magnetometry

To assess the magnetic properties of MBE-grown thin films, vibrating sample magnetometry (VSM) was employed. In VSM a sample is placed between two coils of wire and subjected to an external magnetic field (H). The sample is then oscillated perpendicular to the common axis of the coils. The movement of the sample will induce a current in the coils determined by the samples magnetisation (M). Measuring changes to the current induced in the coils when the value of H is altered will provide information on the magnetic behaviour of the sample. A M-H loop is the change in M measured when H undergoes one full oscillation between an upper and lower limit(figure 2.18). There are several key values which can be obtained from M-H loops. The saturation magnetisation (M_s) is the maximum value of M obtained through the loop. The remnant magnetisation (M_r) is the magnetisation which remains after the external field is returned to 0. The coerceive field (H_c) is the field required to return the magnetisation of the sample back to 0. M_s gives information on the overall magnetic quality of the sample, whereas M_r and H_c provide information on the ease of magnetisation of the sample. Typically thin-film samples show very different coercive fields and remnant magnetisation when the external field is applied in-plane or out-of-plane.

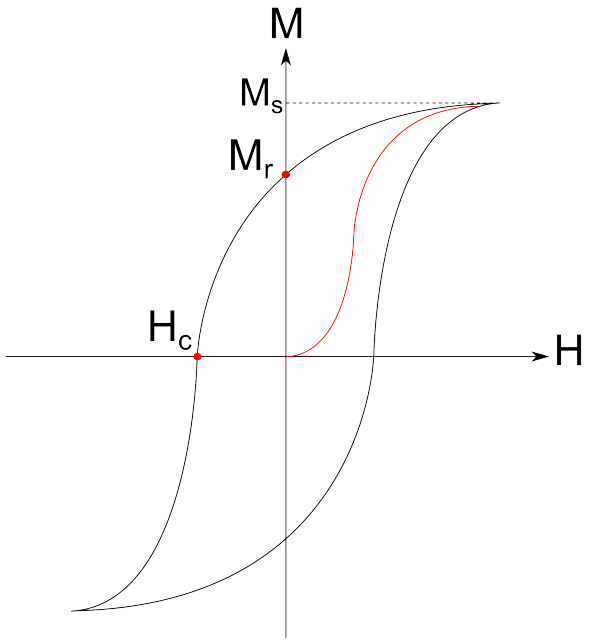

Figure 2.18: Schematic M-H loop with annotations showing the saturation magnetisation M_s, remnant magnetisation M_r and coercive field H_c. The red line shows the initial magnetisation of the sample, which is sometimes omitted from loops.

Chapter 3

Ultra-thin Sb film growth on InAs(111)B

3.1 Introduction

Due to the theoretical predictions of possible topological surface states in Sb (see section 1.2.1), there has been renewed interest in understanding the growth of ultra-thin Sb films with thicknesses $\leq$10 nm. Depositions of Sb onto Si(001) have shown a strong dependence on substrate temperature [95], with substrate temperatures below 300°C producing a 2D Sb layer with clusters forming for coverages above 0.9 ML. Use of higher substrate temperatures lead to the formation of just 2D layers with coverages 0.7-0.9 monolayers (ML), where the value of coverage depended on the substrate temperature and adsorbing species used (Sb_4 or dissociated Sb_4).

Deposition of Sb onto a cleaned Si(111) surface showed that nucleation of Sb islands occurs for film thicknesses above one monolayer [96]. Smooth Sb(111) films have been successfully grown on a variety of Si(111) surfaces, either through the use of a Bi buffer layer [97], or by inducing a surface reconstruction such as the Bi-terminated Si(111)-$\sqrt{3} \times \sqrt{3} - R30°$ [57] or Si(111)-(6×6)Au [98]. For the latter surface Strozak *et al.* found that consecutive bilayers (BLs) did not grow in

the same manner. The first Sb BL deposited in a crystalline manner, the second to fourth BLs were amorphous, and the films transitioned back to the crystalline phase on completion of the fifth BL. Growth of thicker Sb(111) films (10 - 500 Å) have been reported on Bi(111) through the use of Sb_xBi_{1-x} buffer layers formed by Sb deposition at elevated temperatures [99].

Growth of Sb films on III-V semiconductor surfaces has also been investigated, with initial research focussed on Sb growth on GaAs(110) finding that deposition at 300 K proceeds via monolayer-plus-multilayer simulataneous growth [100]. Cafolla *et al.* [101] used XPS studies to show that Sb deposition onto GaAs(111)B at room temperature follows Volmer-Weber growth characteristics. Carelli *et al.* [102] have also reported the creation of 2D Sb layers for Sb adsorption on GaAs(110), where a single Sb ML remained after a post-deposition anneal between 240-360°C, highlighting the strong bonding present between the first Sb ML and the substrate.

Initial studies on Sb thin films grown at Warwick have looked at deposition of Sb onto various substrates including glass, InAs(111)B, GaAs(111)B and GaSb(111). It was found that InAs(111)B substrates have an excellent epitaxial match to Sb films, with the thin films also exhibiting anomalously high transport measurements. The increased mobility measured on these samples could be linked to topological surface states present in the Sb film. An estimate of the critical thickness for the Sb/InAs(111)B system was calculated to be approximately 75 nm, and was obtained using the Matthews-Blakeslee model with a $\{11\bar{2}2\}$ slip plane in the $<11\bar{2}3>$ slip direction. This slip system was selected due to previous work by Srinivasan et al on similar hexagonal systems [103]. This critical thickness value shows that the system is well suited for ultra-thin film growth studies.

In order to gain a better understanding of these conductivity measurements more detailed information was required regarding the structure, growth dynamics and interface development for ultra-thin film Sb epitaxy. To obtain this key information a SXRD investigation into the early stage growth of ultra-thin Sb films on

InAs(111)B(1×1) surfaces was carried out. The results of this SXRD study will be presented in this chapter as follows; experimental details of sample growth and characterisation will be given in sec. 3.2, results including XPS, SXRD and AFM will be presented in sec. 3.3, and a summary is then given in sec. 3.4.

3.2 Experimental details

SXRD experiments were performed on the I07 beamline at the Diamond Light Source synchrotron, Oxford UK. Deposition of Sb was achieved using an Sb Knudsen effusion cell originally from Warwick attached onto the main XRD chamber of EH2. This Sb cell was calibrated using XPS and low energy electron diffraction (LEED) measurements from a Ge(111) substrate test sample.

InAs(111)B samples 10 mm × 10 mm in size were mounted onto stainless steel plates using Indium eutectic bonding. Once loaded into UHV the samples were degassed and then cleaned with cycles of argon ion bombardment (500 eV , discharge current 3mA, 8 minutes) and annealing (T_{sub}=410-440 °C for 30 minutes). This cleaning process produced a strong, sharp hexagonal LEED pattern (figure 3.1) which is consistent with LEED patterns from clean InAs(111)B reported in literature [104].

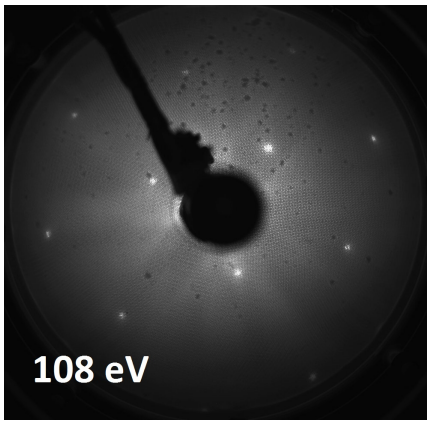

Figure 3.1: LEED pattern from a clean InAs(111)B-(1×1) surface, obtained using the cleaning procedure detailed in text

Three samples were grown using the experimental settings and procedures detailed in table 3.1. For the first sample (sample 1) repeated depositions were conducted with the high substrate temperature $T_{sub} = 220°C$. For the second sample (sample 2) an increased Sb beam flux was used, and two stages of growth were carried out. The first deposition on sample 2 was aiming for a similar growth rate to sample 1, consequently both the substrate temperature (T_{sub}) and the Sb effusion cell temperature (T_{cell}) were increased. For the second deposition on sample 2 the substrate temperature was reduced to room temperature. Sample 2 then underwent a post-deposition annealing stage for 20 minutes at $T_{sub} = 210°C$. The final sample (sample 3) had only a single deposition stage using $T_{cell} = 430°C$, with the substrate kept at room temperature. Following this single stage deposition sample 3 was annealed at $T_{sub} = 205°C$ for 20 minutes.

	Duration (minutes)	T_{cell}(°C)	T_{sub}(°C)
	Sample 1		
Sb deposition 1	1	390	220
Sb deposition 2	5	390	220
Sb deposition 3	24	390	220
Anneal	15	-	300
Sb deposition 4	10	390	220
	Sample 2		
Sb deposition 1	20	430	260
Sb deposition 2	20	430	25
Anneal	20	-	210
	Sample 3		
Sb deposition 1	5	430	25
Anneal	20	-	205

Table 3.1: Growth settings and procedures for all Sb/InAs(111)B samples. T_{cell} is the temperature of the Sb effusion cell, and T_{sub} is the temperature of the InAs(111)B substrate.

3.3 Results

3.3.1 XPS

XPS data from sample 1 (figure 3.2) shows a strong Sb 3d signal appearing after growth, signalling successful Sb deposition onto the InAs(111) surface. There is also still a strong signal from In 3d and As 2p present after Sb deposition which suggest two possibilities; either a very thin monolayer with high surface coverage or a thicker layer with lower amount of surface coverage. XPS data from sample 2 (figure 3.3) shows that after deposition 1 there is a strong Sb 3d signal along with substrate In 3d and As 2p signals. This means that when compared to sample 1 there are the same two possibilities of surface coverage for deposition 1 on sample 2. XPS data from sample 3 (figure 3.4) shows a much stronger Sb 3d signal, and a complete loss of substrate In 3d and As 2p signals. This indicates that the lower substrate temperatures used achieved complete surface coverage. A complete surface coverage of Sb was assumed for sample 2 after deposition 2, due to the use of identical deposition settings compared to sample 3 for a longer growth time. Higher resolution scans around the Sb 3d region (figure 3.5) show the presence of an O 1s peak for sample 1, but both sample 2 and sample 3 show no sign of an O 1s signal. The presence of oxygen in the sample is therefore most likely due to the effusion cell not being fully degassed before deposition onto sample 1.

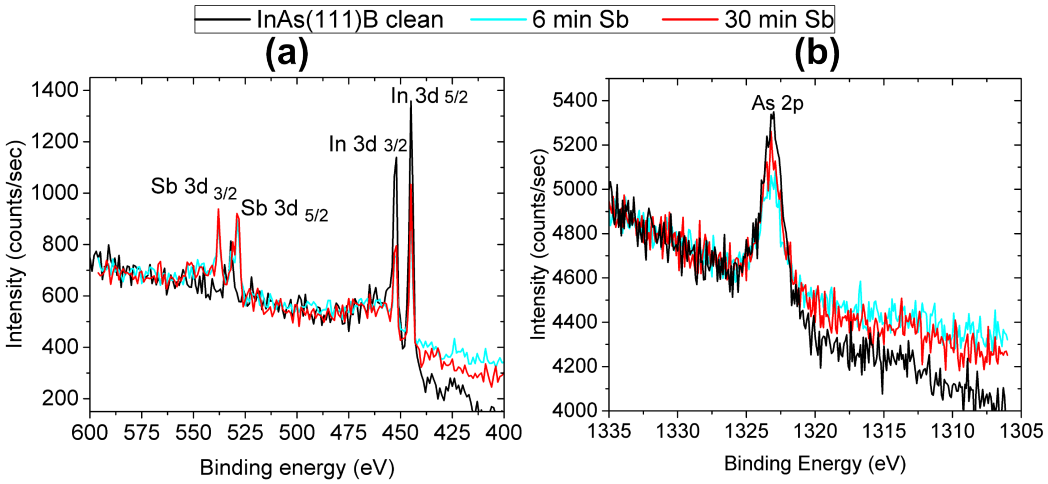

Figure 3.2: XPS data collected from sample 1 after multiple depositions in the energy ranges of (left) Sb 3d signal, and (right) As 2p signal

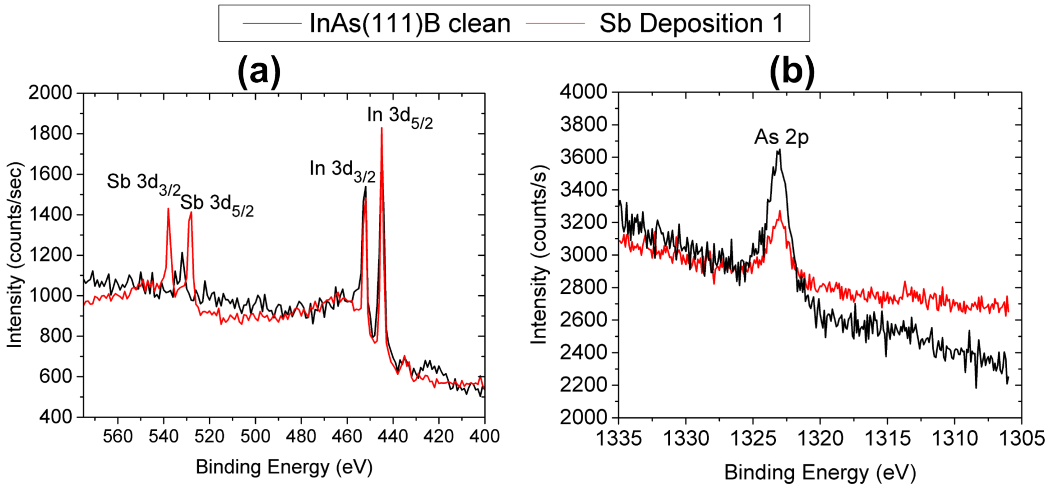

Figure 3.3: XPS data collected from sample 2 after deposition 1 in the energy ranges of (left) Sb 3d signal, and (right) As 2p signal. Clean InAs(111)B data from sample 1 has been plotted for comparison.

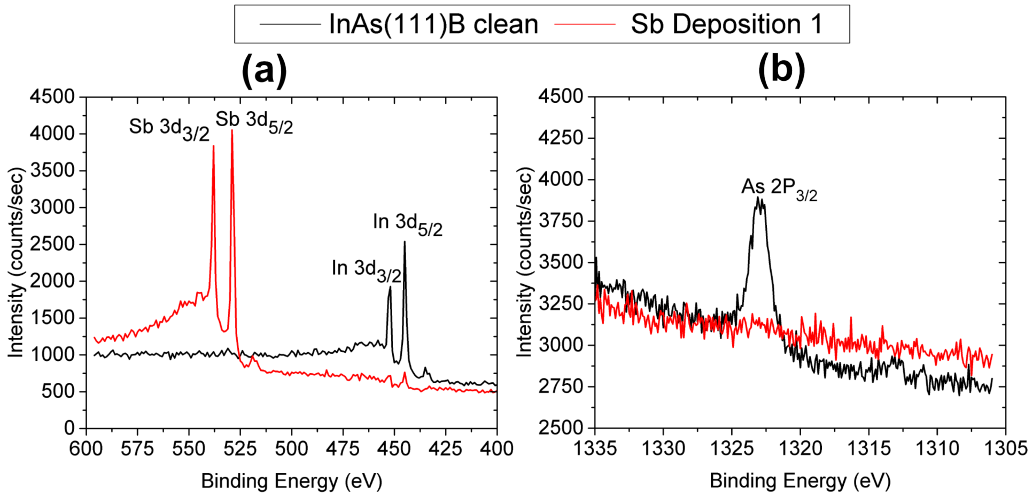

Figure 3.4: XPS collected from sample 3 after cleaning, and after deposition 1 in the energy ranges of (left) Sb 3d signal, and (right) As 2p signal

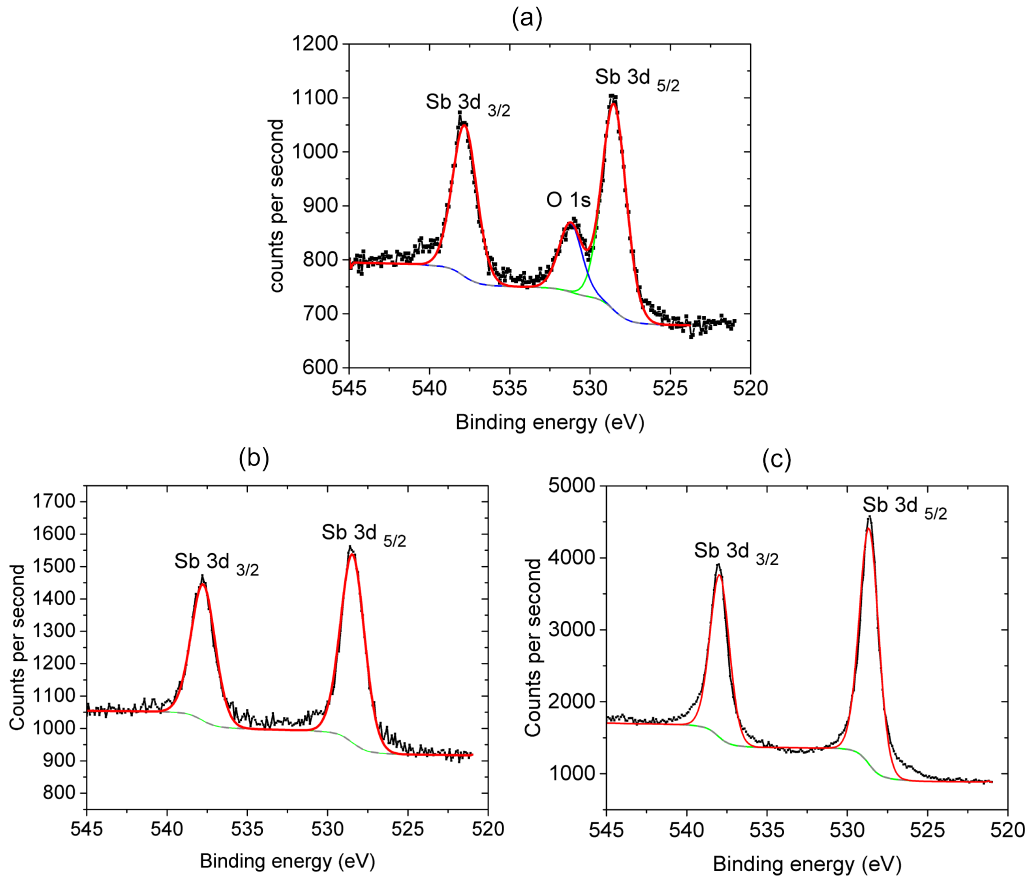

Figure 3.5: XPS data collected from around the Sb 3d region for samples (a) S1 after deposition 3, (b) S2 after deposition 1, and (c) S3 after deposition 1. Red lines show full fit profile, dashed grey lines show background function, and other colours of solid lines indicate pairs of doublet peaks fitted to Sb 3d.

3.3.2 SXRD

All XRD data presented in this chapter was measured at the I07 beamline (Diamond Light Source, UK) using a photon energy of 12.5 keV (0.99Å), and recorded using a PILATUS 100K detector [105].

Out-of-plane symmetric XRD sample 1

Out-of-plane symmetric $\theta - 2\theta$ scans collected from sample 1 after deposition stages 2-4 are shown in figure 3.6. These scans were taken in sections either side of the

strong InAs(111) Bragg peaks in order to avoid saturation of the detector. All scans taken after the initial Sb deposition (stages 2-4) are almost identical, which indicates that repeated depositions at high substrate temperature did not significantly alter the sample surface. There is a broad feature labelled '1' present in all scans at approximately $2\theta = 19.3°$ (lattice spacing 2.959Å), which becomes more pronounced in scans taken after the initial Sb deposition. A possible identity for this signal is the h-In(0001) reflection (spacing of 2.964Å). Extra In at the surface is plausible due to the formation of excess group III atoms on III-V surfaces being well documented in literature [106] [107], where heating the substrate above the congruent temperature leads to a larger loss of the group V species. However, the signal's broadness and a lack of higher order reflections means that a definitive identification is not possible.

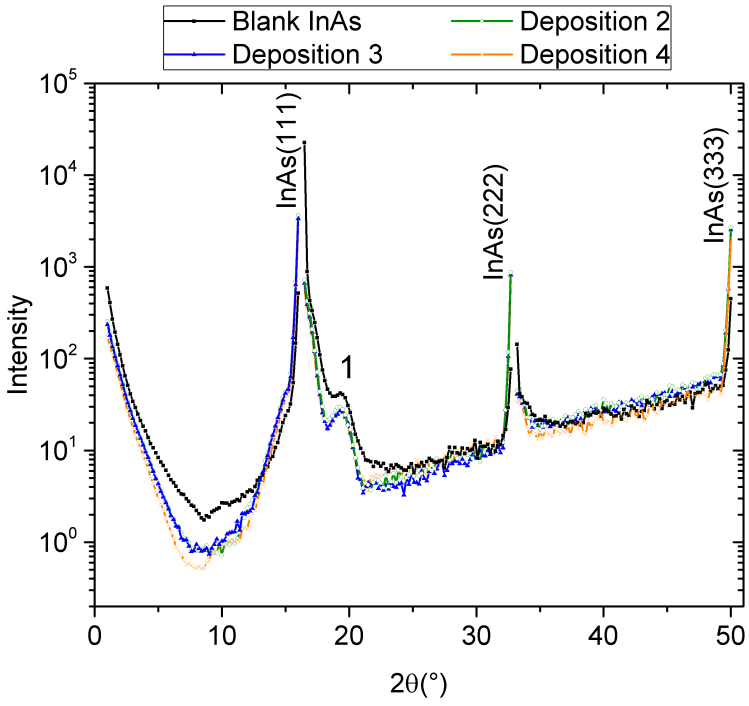

Figure 3.6: Out-of-plane symmetric XRD data collected from sample 1 before Sb deposition, and after depositions 2,3 and 4. The peak labelled with '1' is discussed in the text.

Out-of-plane symmetric XRD sample 2

Out-of-plane $\theta - 2\theta$ data from sample 2 was collected after both depositions and also following the post-growth anneal (figure 3.7). The scans taken after deposition 2 on sample 2 show the appearance of h-Sb(000n) Bragg peaks (n=3,6,9) signalling successful deposition of h-Sb. After the 20 minute post-growth anneal to T_{sub} = 430°C, an increase in Sb peak intensity occurred along with the appearance of Kiessig interference fringes. This appearance of fringes indicates that a post-deposition annealing step can smooth out the substrate-film and film-vacuum interfaces (figure 3.7). This is similar to behaviour reported previously for post growth annealing of Sb films. Hu *et al.* [108] showed that for Sb deposition onto GaAs(110) post growth annealing to 475 K leads to the smoothing out of the Sb surface due to the flattening of 3D clusters. Park *et al.* [109] showed that for Sb films grown on Si surfaces annealing to approximately T_{sub} = 500°C was shown to create ordered interfaces on Si(111). This ordering was attributed to the dissociation of metastable clusters of Sb_4 which formed during room temperature deposition. Surface flattening has also been demonstrated for Sb layers on Si(113), where LEED patterns have been recovered by annealing to T_{sub} = 400°C [110] [111].

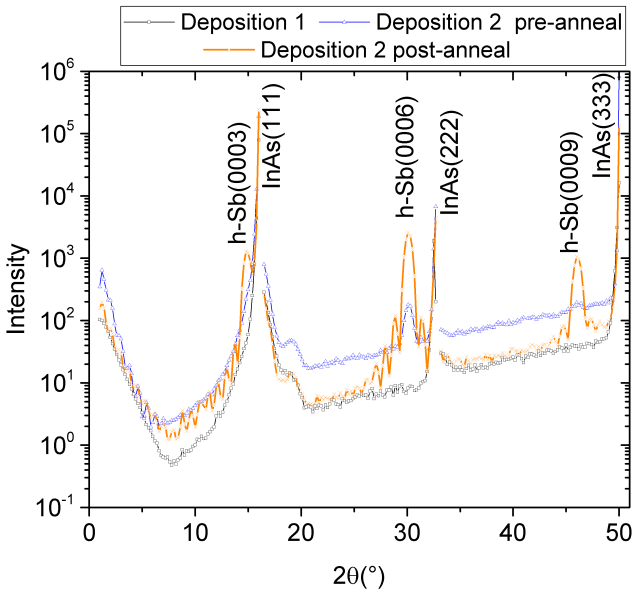

Figure 3.7: Out-of-plane symmetric XRD data collected from sample 2, highlighting the appearance of intensity oscillations following annealing.

The separation between maxima values of the fringes present in the post-anneal data can be used to calculate the film thickness (d) using the equation:

$$d = \frac{\lambda}{2(\sin\theta_{n+1} - \sin\theta_n)} \tag{3.1}$$

where λ is the wavelength of incident x-ray radiation and θ_n is the angle at which the n^{th} maxima peak occurs. In order to obtain angle values for each peak maxima the Kiessig fringes were fitted individually with functions of the form $y = ax^2+bx+c$ (figure 3.8). These maxima for four consecutive peaks were combined with equation 3.1 to give a calculated mean film thickness of 7.04 $\pm$ 0.18 nm .

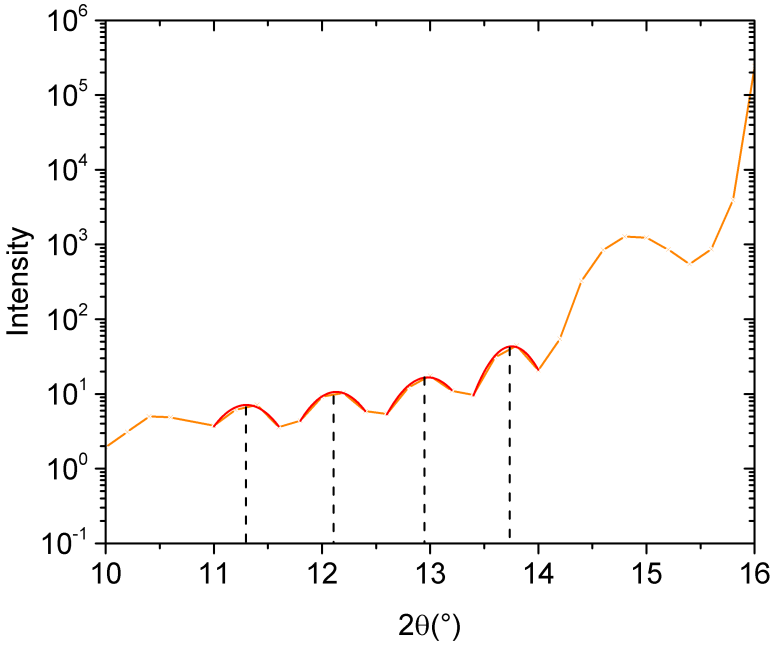

Figure 3.8: Enlarged section of the post-anneal out-of-plane symmetric XRD data from sample 2 shown in figure 3.7, highlighting oscillations in data. Fits to peaks are shown with solid red lines, vertical dotted black lines indicate the rough location of each peak maxima.

Out-of-plane symmetric XRD sample 3

For sample 3 out-of-plane $\theta-2\theta$ data collected after Sb deposition shows broad peaks from h-Sb(000n) Bragg peaks for n=3,6,9 (figure 3.9). However no clear intensity oscillations can be seen in the scan, so no estimate of the thickness could be made using the $\theta - 2\theta$ data from this sample.

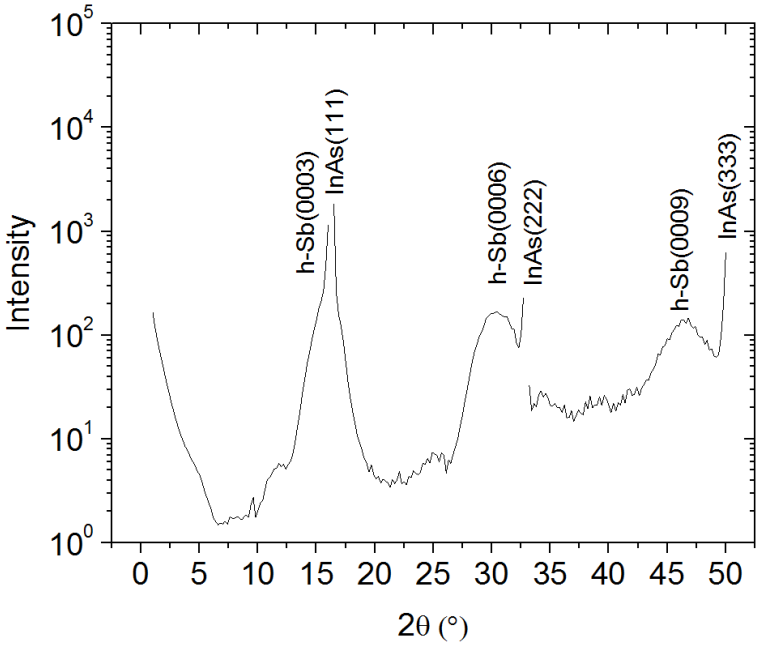

Figure 3.9: Out-of-plane symmetric XRD data collected after the single Sb deposition stage onto sample 3.

CTR fitting sample 1 - Clean

To aid in interpreting the effects of layer thickness on sample structural properties, CTR fitting results will be presented in order of thickness of the deposited Sb layer going from thinnest to thickest (table 3.2). Due to the error obtained from counting statistics being much smaller than error contributions from the SXRD equipment, error bars for the CTR datasets were increased. Each CTR dataset was fitted by modelling intensities in WinROD, and each CTR scan had errors set to 30% unless stated otherwise. This large error is a result of the CTR profiles being fitted as intensities and not structure factors, and correspond the equivalent of a 15% error when fitting structure factors which is consistent with common literature values. Uncertainties on individual fitting parameters were calculated by measuring the change required to increase the value of χ^2 by $1/(N-p)$ times its minimum value, while keeping all other parameters fixed. N is the number of data points included in the

dataset, and p is the number of independent variables used in the fitting model.

Sample	Sb Thickness
Sample 1 clean	-
Sample 1 deposition 3	surface substitution
Sample 2 deposition 1	surface substitution
Sample 3 deposition 1	∼1.5 nm
Sample 2 deposition 2	∼7 nm

Table 3.2: CTR datasets in order of Sb layer thickness.

In total 15 CTRs were measured from the clean surface of sample 1, as well as after deposition stages 1-3, as shown in the reciprocal space HK plot in figure 3.10. As outlined in chapter 2, the mis-cut of the InAs(111)B surface affects symmetrically equivalent CTRs in different ways depending on which section of reciprocal space they are located. This effectively breaks the 120^o symmetry, therefore no symmetry averaging of CTRs was conducted for all datasets presented in this chapter. Following data reduction the final dataset for clean InAs(111)B contained 9 symmetrically distinct CTRs indicated with the bold outlines in figure 3.10, which gave a total of 476 reflections.

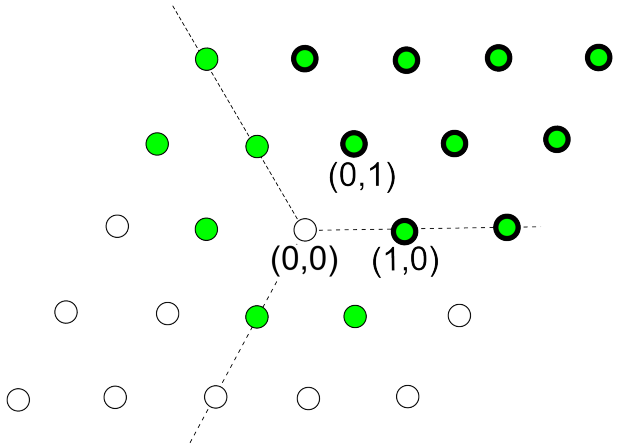

Figure 3.10: HK plot of CTR scans measured from sample 1 after cleaning, and also after depositions 1-3. Collected CTR positions are indicated with green filled circles. The 120° symmetry is indicated with the three dotted lines, and the symmetrically independent CTRs used in fitting are indicated with a bold outline.

The clean InAs(111)B dataset was fitted using an InAs(111)B-(1×1) bulk model, with individual displacement parameters for the top 4 atomic layers, and a scaling factor. Surface roughness and top layer occupancy were trialled in the fitting procedure, but it was found that 100% occupancy and $\beta = 0$ gave the best fit therefore these parameters were removed from the model. The best fit model was an As terminated surface (χ^2=1.363) which showed a small outward expansion of the top BL coupled with an inward contraction of the second BL (figure 3.12). Exact values of these layer shifts are presented in table 3.3. The measured and simulated CTR profiles are shown in figure 3.11, and for comparison the dashed blue lines show CTRs from the best fit obtained with a model using an In terminated surface (χ^2=3.322). Horizontal lines show the level of each atomic layer in the (111) direction, with the z-displacement parameter used for each atomic layer shown to the left of each line. The arrows next to the z-fitting parameter number represents the direction of movement for the layer when compared to the bulk lattice positions which are shown with dotted red lines.

Outward expansions of the top surface layer are common in III-V semiconductors (111)B surfaces, due to rehybridisation of the group V valence orbitals leading to a weakening of the backbonding between the surface group V atoms and the underlying group III atoms [65]. This termination result agrees with previous studies of InAs(111)B surface preparation where cycles of sputtering and annealing produced an atomically flat unreconstructed surface of As atoms each with a single dangling bond [112].

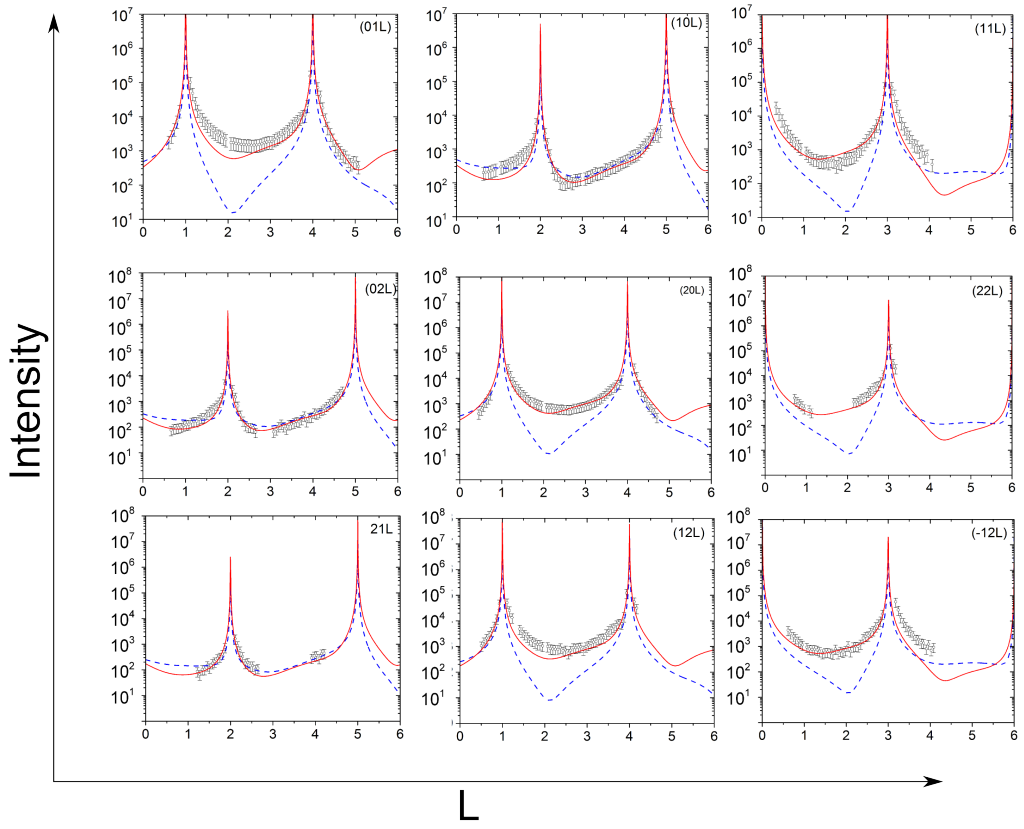

Figure 3.11: CTR profiles measured from cleaned InAs(111)B-(1×1) surface, along with profiles from best fits models obtained for either In terminated (dotted blue line) or As terminated (solid red line) surfaces. The As terminated model is shown in figure 3.12.

Layer	Bulk position	Fit Position	Displacement(%)
1	1.0000	1.0026 ± 0.0009	0.26
2	0.9167	0.9188 ± 0.0006	0.21
3	0.6667	0.6576 ± 0.0010	-0.91
4	0.5833	0.5802 ± 0.0008	-0.31

Table 3.3: Layer positions for the InAs layers in the best fit model for clean InAs(111)-(1×1) shown in figure 3.12. Layer positions are given as ratios of InAs c-lattice parameter (10.4547 Å), displacements are given as a percentage of InAs c-lattice parameter.

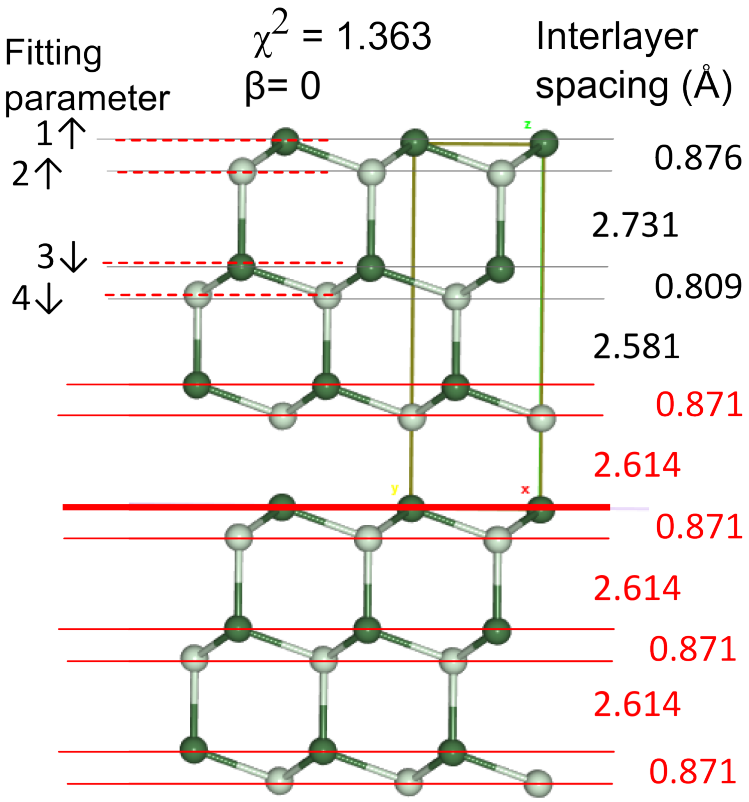

Figure 3.12: Best fit model for cleaned InAs(111)B-(1×1) surface. Solid red lines indicate atomic layers which were fixed at bulk positions during fitting, with the thick solid red line indicating the top of the bulk file. Solid black lines show positions of layers for best fit model and dotted red lines show the bulk positions for layers moved during fitting.

CTR fitting sample 1 - Deposition 3

A summary of the deposition stages used on sample 1, which had a CTR dataset recorded afterwards, is given in table 3.4. Figure 3.13 shows CTR profiles taken from sample 1 after each deposition at $T_{sub} = 220°$C. The loss of signal at the anti-Bragg positions following the initial Sb deposition shows that surface roughening has occurred. The fact that the shape of the CTRs remain the same following subsequent Sb depositions agrees with the out-of-plane diffraction data presented earlier. Together these observations indicate that after 1 minute of deposition an

equilibrium is developed between the rate of Sb adatoms incident on the surface and the rate of desorption of Sb surface atoms. This is similar to the behaviour found in previous studies of Sb thin films deposition onto III-V (110) surfaces at high temperatures. In these studies following the deposition of several monolayers of Sb, an annealing step of either 330°C [39] or 347°C [38] lead to the removal of excess Sb forming a well ordered Sb monolayer. Due to the shape of the CTRs collected after each deposition on sample 1 being virtually identical, only the CTRs collected after deposition 3 were used for CTR line profile fitting.

Sample 1	Duration (minutes)	T_{cell}(°C)	T_{sub}(°C)
*Sb deposition 1	1	390	220
*Sb deposition 2	5	390	220
*Sb deposition 3	24	390	220
Anneal	15	-	300
Sb deposition 4	10	390	220

Table 3.4: Growth settings and timings for sample 1. Stages labelled with '*' are those which had CTR datasets collected directly afterwards. T_{cell} is the temperature of the Sb effusion cell, and T_{sub} is the temperature of the InAs(111)B substrate.

The model used to fit InAs(111) CTR data measured after deposition 3 on sample 1 was a bulk InAs(111)B model with Sb substitution of the surface As atoms. This substitution was achieved through adding an additional Sb atom to the fit file at the exact same position as the top As atom, and varying their relative occupancies. Fitting the As and Sb occupancies freely within the χ^2 minimisation routine could lead to an unphysical fit result i.e. a combined occupancy at the top InAs layer site which is larger than 100%. Therefore the occupancies of these two atoms were altered manually prior to each fitting run to ensure the occupancies of both atom species sum to a physically realistic value i.e. $\leq 100\%$.

The best fit to deposition 3 on sample 1 involved a mixture of layer movements, with some layers expanding outwards away from the substrate, and some contracting inwards towards the substrate (figure 3.15). The top BL had an overall atomic site occupancy of 60%, and in its top atomic layer 50% of the occupied sites

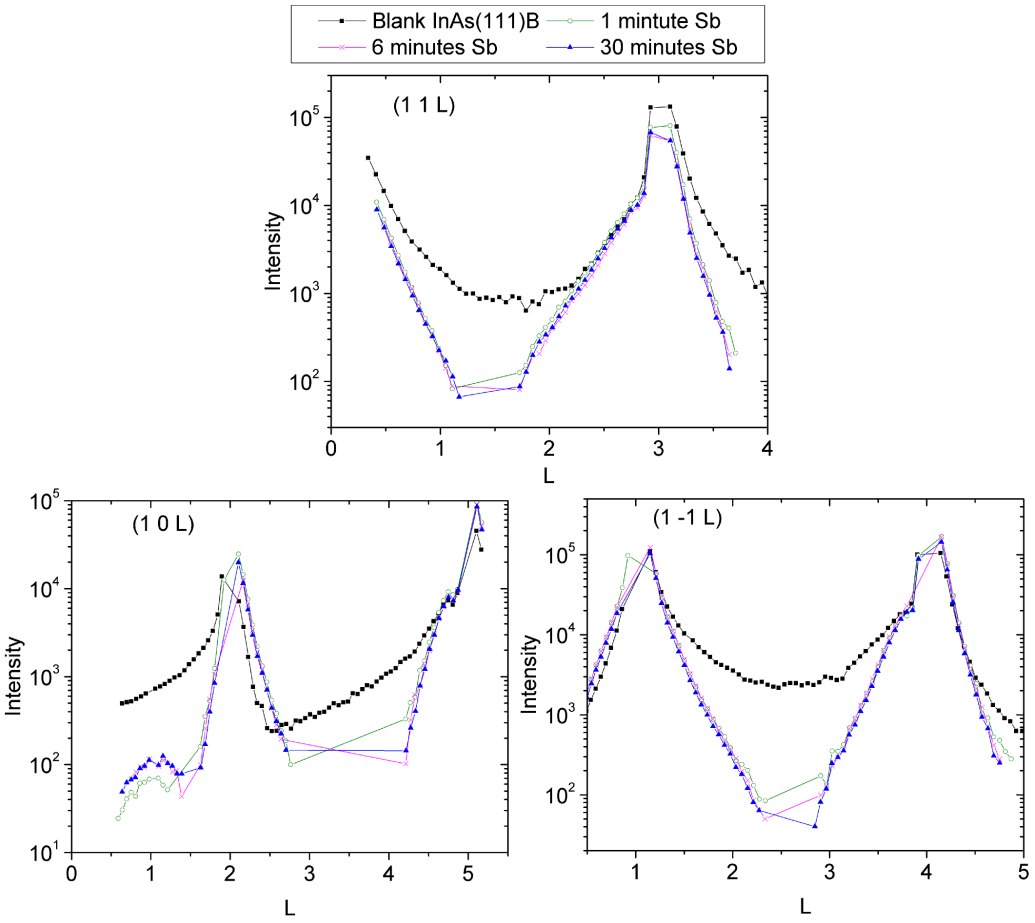

Figure 3.13: Example CTR profiles measured from sample 1 after depositions 1-3.

(30% of total surface) were Sb atoms substituted onto the As atomic sites. This substitution in the best fit model agrees with similar behaviour in literature, with Sb substitution onto As surface sites being reported for Sb deposition onto GaAs(001) [113] and InAs(001) [114]. Maeda *et al.* [115] assumed that, due to high substitution energy required for a direct substitution, the Sb overlayer observed was caused by a two-step replacement process occurring due to the different evaporation pressures of As and Sb. The low occupancy of the top BL in the best fit model suggests that multiple cycles of deposition at high temperature caused roughening of the surface.

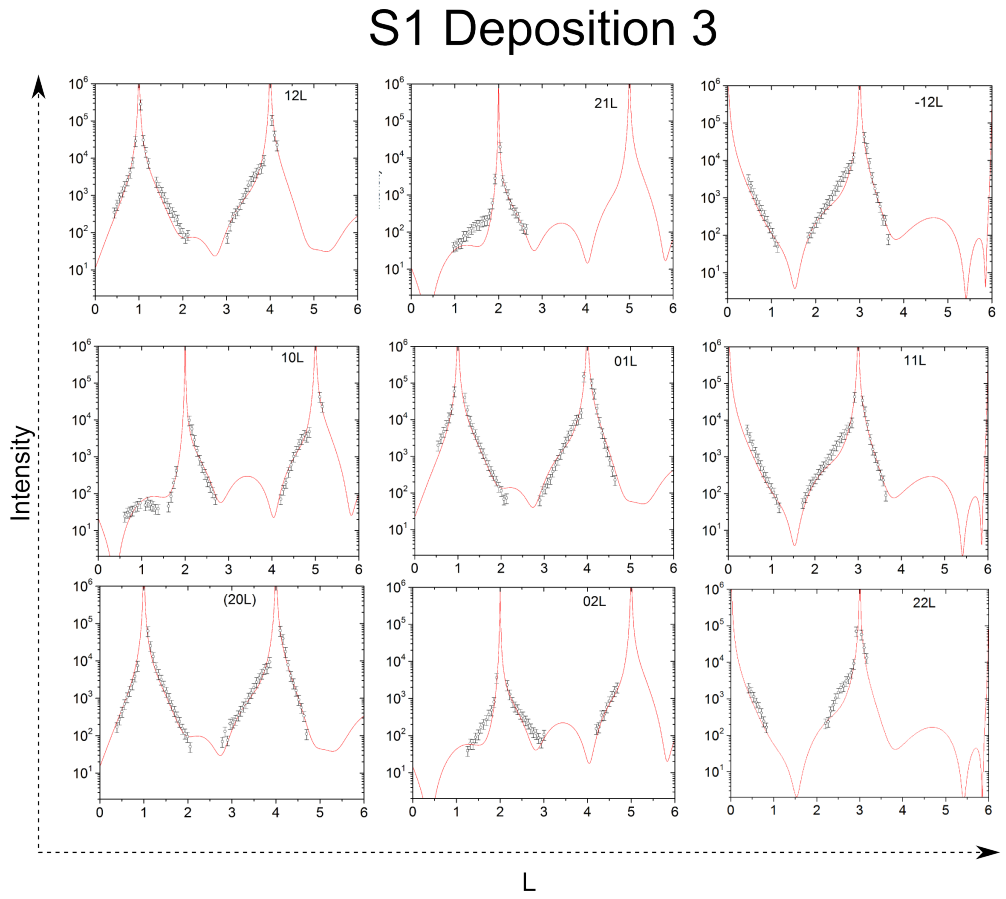

Figure 3.14: CTR profiles measured from sample 1 after deposition 3, with fitting profiles (solid red lines) calculated from the model shown in figure 3.15

Layer	Bulk position	Fit Position	Displacement(%)
1	1.0000	1.0190 ± 0.0009	1.90
2	0.9167	0.8992 ±0.0010	-1.75
3	0.6667	0.6592 ± 0.0005	-0.75
4	0.5833	0.5805 ± 0.0006	-0.28
5	0.3333	0.3378 ± 0.0011	0.45
6	0.2500	0.2376 ± 0.0008	-1.24

Table 3.5: Layer positions for the InAs layers in the best fit model for deposition 3 on sample 1 shown in figure 3.15. Layer positions are given as ratios of InAs c-lattice parameter (10.4547 Å), displacements are given as a percentage of InAs c-lattice parameter.

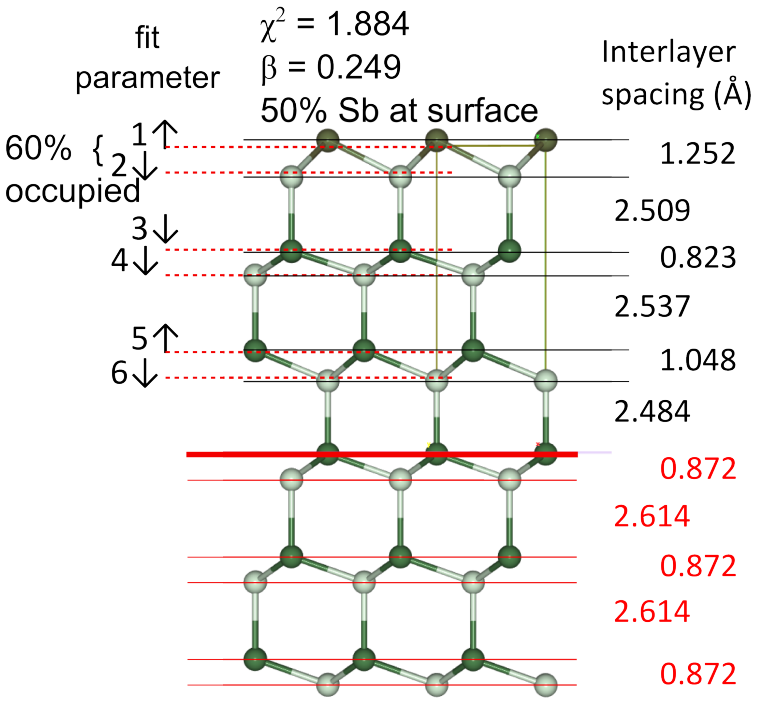

Figure 3.15: Best fit model for CTR data collected from sample 1 following deposition 3. Solid red lines indicate atomic layers which were fixed at bulk positions during fitting, with the thick solid red line indicating the top of the bulk file. Solid black lines show positions of layers for best fit model and dotted red lines show the bulk positions for layers moved during fitting.

CTR fitting sample 2 - Deposition 1

A summary of the deposition stages used on sample 2 is given in table 3.6. CTRs collected after deposition 1 on sample 2 are summarised in the HK plot in figure 3.16. In total 15 CTRs were measured, which after data reduction gave 9 symmetrically independent CTRs made up of 385 reflections.

Sample 2	Duration (minutes)	T_{cell}(°C)	T_{sub}(°C)
*Sb deposition 1	20	430	260
Sb deposition 2	20	430	25
*Anneal	20	-	210

Table 3.6: Growth settings and timings for sample 2. Stages labelled with '*' are those which had CTR datasets collected directly afterwards. T_{cell} is the temperature of the Sb effusion cell, and T_{sub} is the temperature of the InAs(111)B substrate.

The best fit model obtained for this surface was a bulk structure with 60% occupancy of the top BL, and for the top atomic layer 15% of this was Sb substituted at the surface As positions. This model had a combination of outward expansions and inward contracts similar to sample 1 (figure 3.18). The occupancy of the first InAs BL in the best fit models for the deposition at high substrate temperatures were identical for both sample 1 and sample 2 (60%). If a two step substitution mechanism is assumed, then the different percentages of Sb in the best fit models show that a larger amount of As was removed from sample 1. The lower amount of Sb substitution for the higher temperature deposition onto sample 2 has two likely causes. The first is that deposition 1 on sample 2 had a shorter duration, which decreases the amount of time over which Sb substitution can occur. Also this deposition had an increased substrate temperature, which would have increased the rate of Sb re-evaporation from the surface, consequently decreasing the rate of substitution.

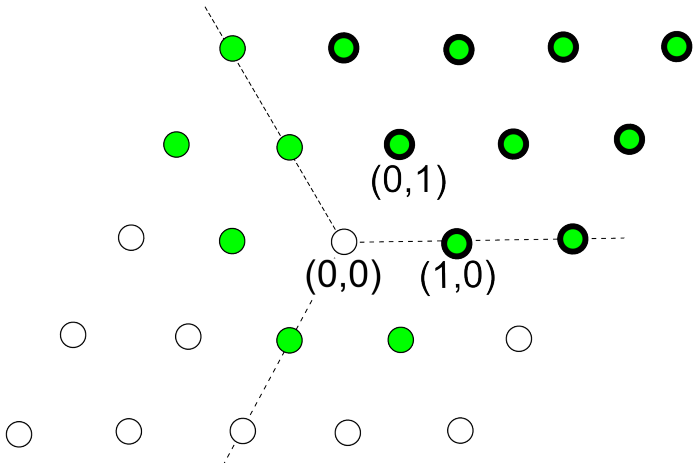

Figure 3.16: HK plot of CTR data collected from sample 2 after deposition 1, with collected CTR positions indicated with green filled circles. The 120° symmetry is indicated with the three dotted lines, and the symmetrically independent CTRs used in fitting are indicated with a bold outline.

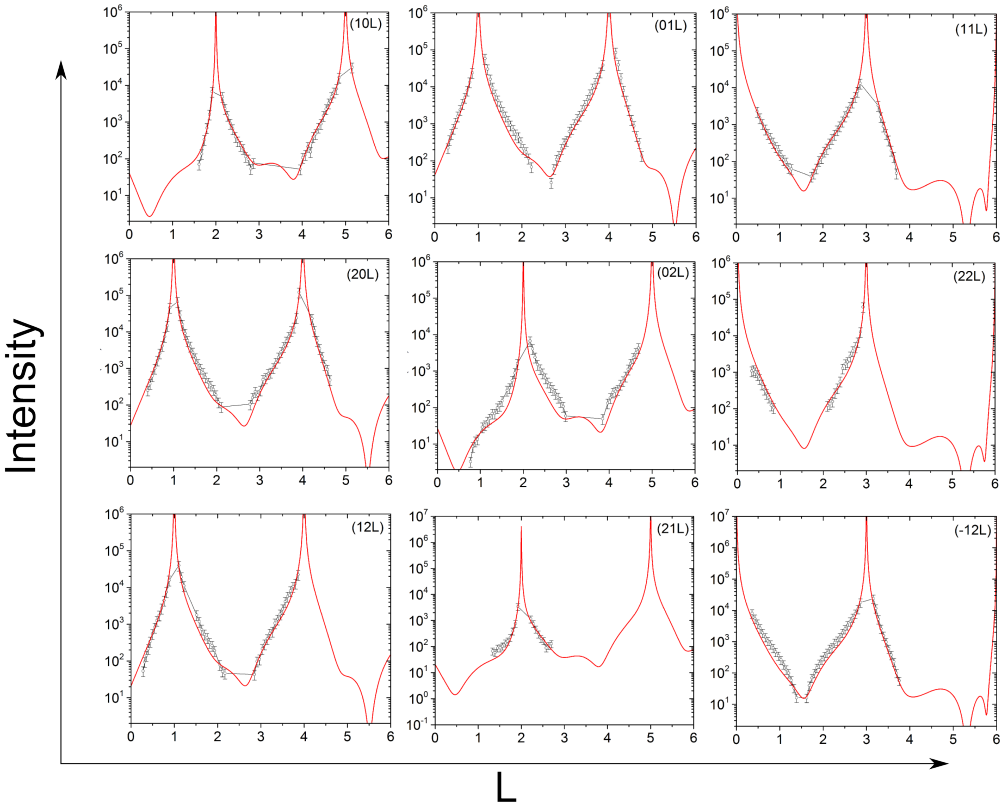

Figure 3.17: CTR profiles measured from sample 2 after deposition 1, with fitting profiles (solid red lines) calculated from model shown in 3.18

Layer	Bulk position	Fit Position	Displacement(%)
1	1.0000	1.0180 ± 0.0008	1.80
2	0.9167	0.9144 ± 0.0006	-0.53
3	0.6667	0.6685 ± 0.0005	0.18
4	0.5833	0.5808 ± 0.0004	-0.25
5	0.3333	0.3318 ± 0.0006	-0.15
6	0.2500	0.2438 ± 0.0007	-0.62

Table 3.7: Layer positions for the InAs layers in the best fit model for deposition 1 on sample 2 shown in figure 3.18. Layer positions are given as ratios of InAs c-lattice parameter, displacements are given as a percentage of InAs c-lattice parameter.

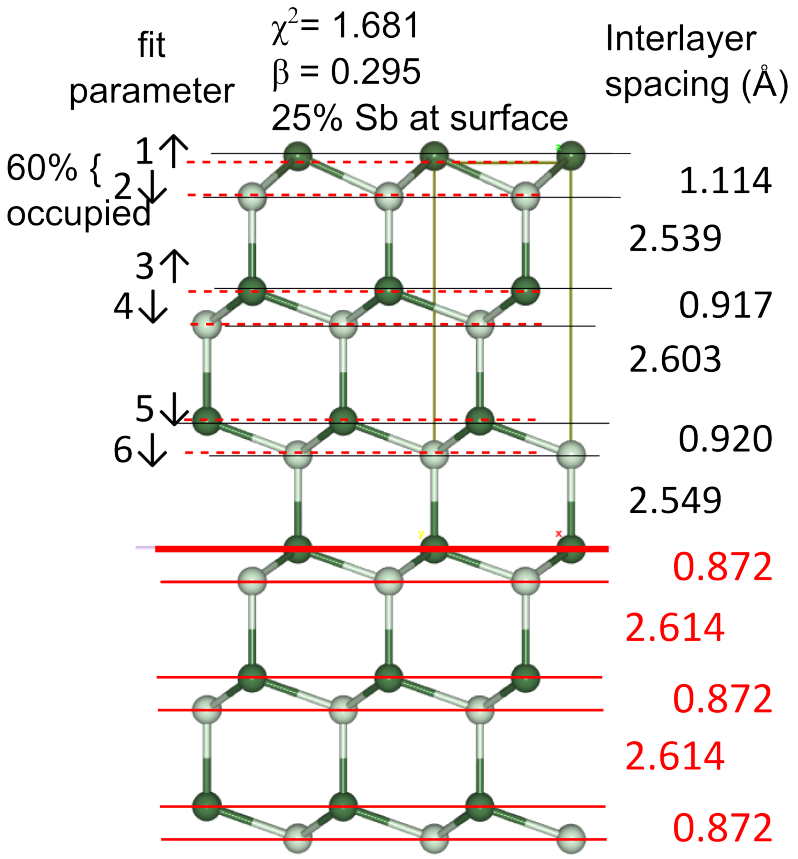

Figure 3.18: Best fit model for CTR data collected from sample 2 after deposition 1. Solid red lines indicate atomic layers which were fixed at bulk positions during fitting, with the thick solid red line indicating the top of the bulk file. Solid black lines show positions of layers for best fit model and dotted red lines show the bulk positions for layers moved during fitting.

The results obtained from fitting to CTR datasets collected following high temperature (≥300°C) depositions onto samples 1 and 2 show that substitution on the surface As atomic sites occurs. It has also been shown that this substitution is reduced with an increased substrate temperature. This lack of layer growth was found to be similar to previous results reported in literature for the annealing of thin Sb films.

CTR fitting sample 3 - Deposition 1

A summary of the deposition stages used on sample 2 is given in table 3.8. CTR data collected after Sb deposition and annealing on sample 3 are summarised in the HK plot in figure 3.19. A total of 13 CTRs were collected, which after data reduction gave 9 symmetrically non-equivalent CTRs providing a dataset of 927 reflections. Due to a strong CTR signal being present in all scans, background subtraction and L-shift correction were more reliable, therefore a lower error of 20% was given to CTRs in this dataset.

Sample 3	Duration (minutes)	T_{cell}(°C)	T_{sub}(°C)
Sb deposition 1	5	430	25
*Anneal	20	-	205

Table 3.8: Growth settings and timings for deposition on sample 3. T_{cell} is the temperature of the Sb effusion cell, and T_{sub} is the temperature of the InAs(111)B substrate. Stages labelled with '*' are those which had a CTR dataset collected directly afterwards.

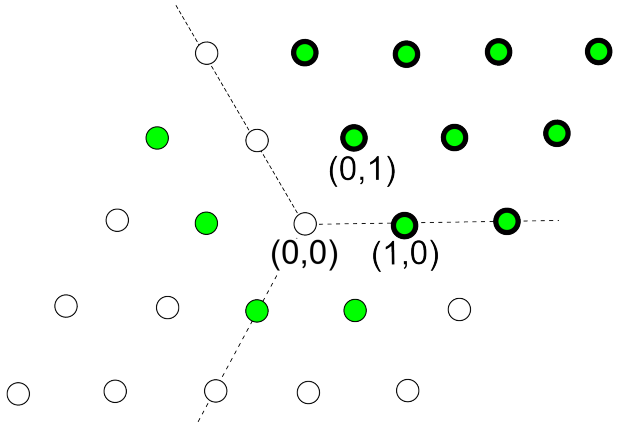

Figure 3.19: HK plot of CTR data collected from the single deposition onto sample 3, with collected CTR positions indicated with green filled circles. The 120° symmetry is indicated with the three dotted lines, and the symmetrically independent CTRs used in fitting are indicated with a bold outline

Initially a model using bulk InAs and Sb positions was roughly fitted to the data using the positions of the main Sb peaks as a guide. Once the width of these

oscillation peaks had been matched with the appropriate model layer thickness, a single z-displacement parameter was used to determine the compression or expansion of the Sb layer lattice. This was done by giving each Sb layer a scaling factor to apply to the shared displacement parameter according to its distance from the substrate (e.g. 1 for the first Sb layer above substrate, 2 for the second layer above substrate, etc). This fitting method gave the closest fits to sample 3 using a model of four Sb BLs, which was then used to further investigate the interface structure.

For the epitaxial growth of Sb onto InAs(111)B surfaces there are two different stacking orders possible for the Sb overlayer: continuing the ordering of the InAs layer (AaBbCc-ABCABC) or alternating the order to create a twinned domain (AaBbCc-BACBAC) (figure 3.20). In this notation the type of letter represents the surface site, and the use of upper and lower case indicate differing atomic species within the InAs structure. WinROD has a symmetry function which can model symmetry related domains, however this creates twinned domains for all atoms in the surface file, which is unsuitable for models where some of the substrate atoms are included in the surface file. Therefore modelling twinning was achieved through the use of the multi-surface function in WinROD which enables two surface models to be defined. In this setup, the second surface replaces a set percentage of the first surface. For the Sb models used in this experiment the first surface was the structure which had layer stacking the same as the InAs substrate, and the second surface structure had the twinned layer stacking.

The results from initial CTR profile fitting revealed that there is a low amount of twinning, with a clear preference for the majority of the Sb film to retain the stacking order of the InAs substrate. The lowest χ^2 values were obtained using 10% twinned domains (figure 3.21a). Twinning behaviour is not unusual for deposition of Sb films, with twinned signals previously measured from 250 nm thick Sb films grown on GaSb(111) [41].

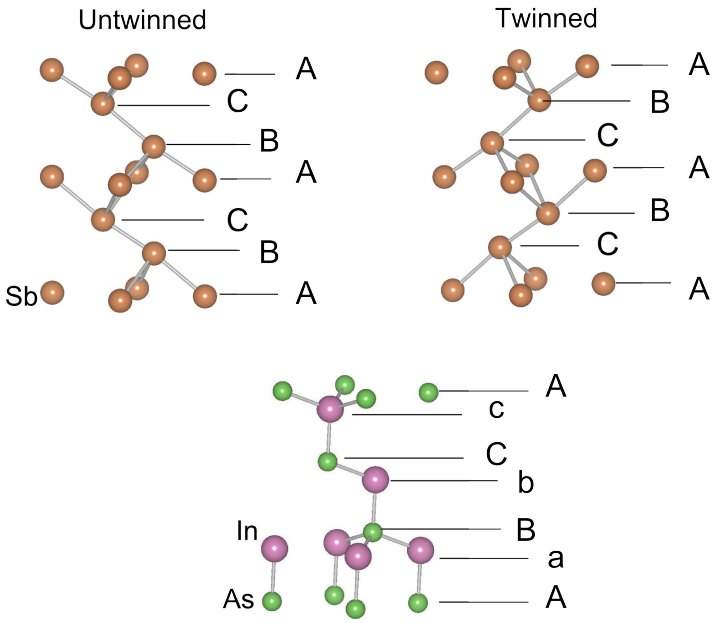

Figure 3.20: Crystal structure layer positions of twinned and untwinned Sb layers relative to an underlying InAs(111)B substrate. Different letters refer to different in-plane positions, with the case of the letter representing the element species within the InAs structure.

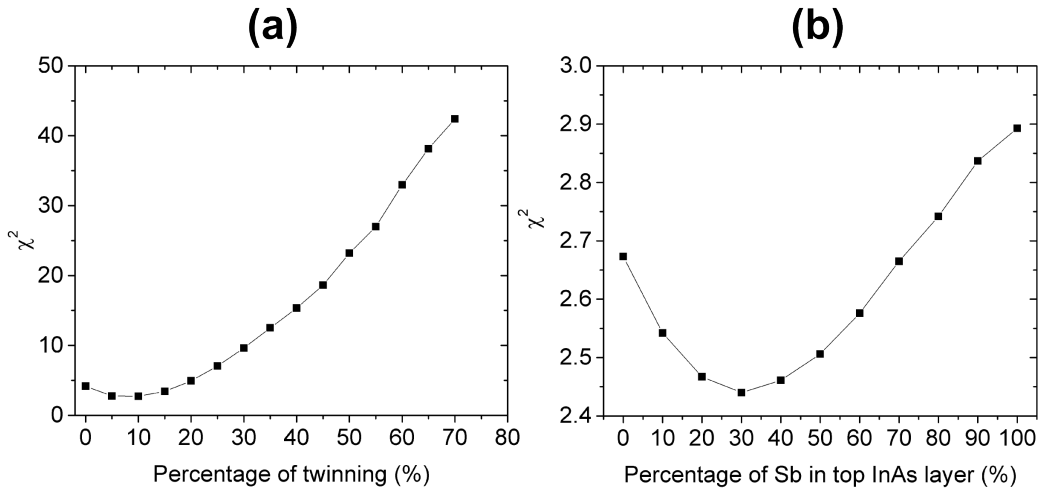

Figure 3.21: Change in CTR χ^2 fitting values for sample 3 due to (a) twinning of Sb surface model, and (b) Sb substitution of top substrate atomic layer.

Models with 10% twinning were then further refined by varying the amount of Sb substitution within the top As layer. Models where the top InAs(111) layer is

predominantly As gave consistently lower χ^2 values, with the best fits achieved for a top InAs(111) layer of 30% Sb (figure 3.21b).

During Sb epitaxial growth on the InAs(111)B there are three possible adsorption sites for the initial layer of Sb adatoms to adsorb to: hexagonal close-packed (HCP) hollowsite, face-centred cubic (FCC) hollowsite and on-top site (figure 3.22). Trial models gave twinned and untwinned domains separate adsorption sites, and used the following fitting parameters: a scale factor, a roughness factor β, 14 individual z-displacements, 20 Debye-Waller (DW) factors (combination of DW1 and DW2), and a surface layer occupancy. A combination of DW factors was used so that all atoms had an out-of-plane DW factor (DW2), and an extra in plane DW factor (DW1) was given to atoms which were located in the surface layer or in either of the interface layers. Combinations involving the on-top positions mixed with a hollowsite were not considered, as this would lead to unphysical atomic positions at the twin domain boundaries. These models gave best fit values shown in table 3.9.

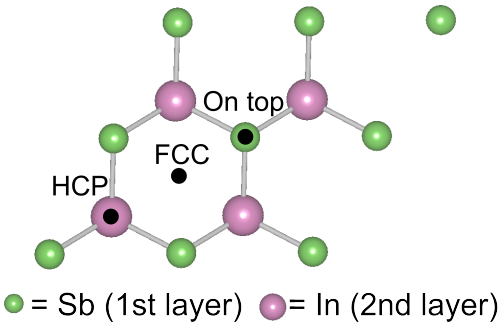

Figure 3.22: Surface adsorption sites for the InAs(111)B surface.

The adsorption position which produced the best fit was FCC (HCP) for the untwinned (twinned) domain. The individual layer separations are summarised in figure 3.24. This final fit shows that all of the InAs layers below the film-substrate interface undergo a contraction away from the interface towards the bulk, whereas the top InAs atomic layer moves away from the interface towards the surface. This can be explained by the fact that the atoms within the top atomic layer of the interface

are now in an octahedral bonding state rather than the tetrahedral bonding state of the bulk. This introduction of stronger bonding to the atom plane above will decrease the strength of bonding to the atomic plane below, causing the expansion away from the bulk.

Adsorption site(Untwinned/Twinned)	χ^2
FCC/HCP	2.017
FCC/FCC	3.183
HCP/HCP	5.086
On top /On top	5.203
HCP/FCC	6.532

Table 3.9: χ^2 values for fits to CTR data collected after single deposition onto sample 1, using various combinations of adsorption sites for twinned and untwinned domains

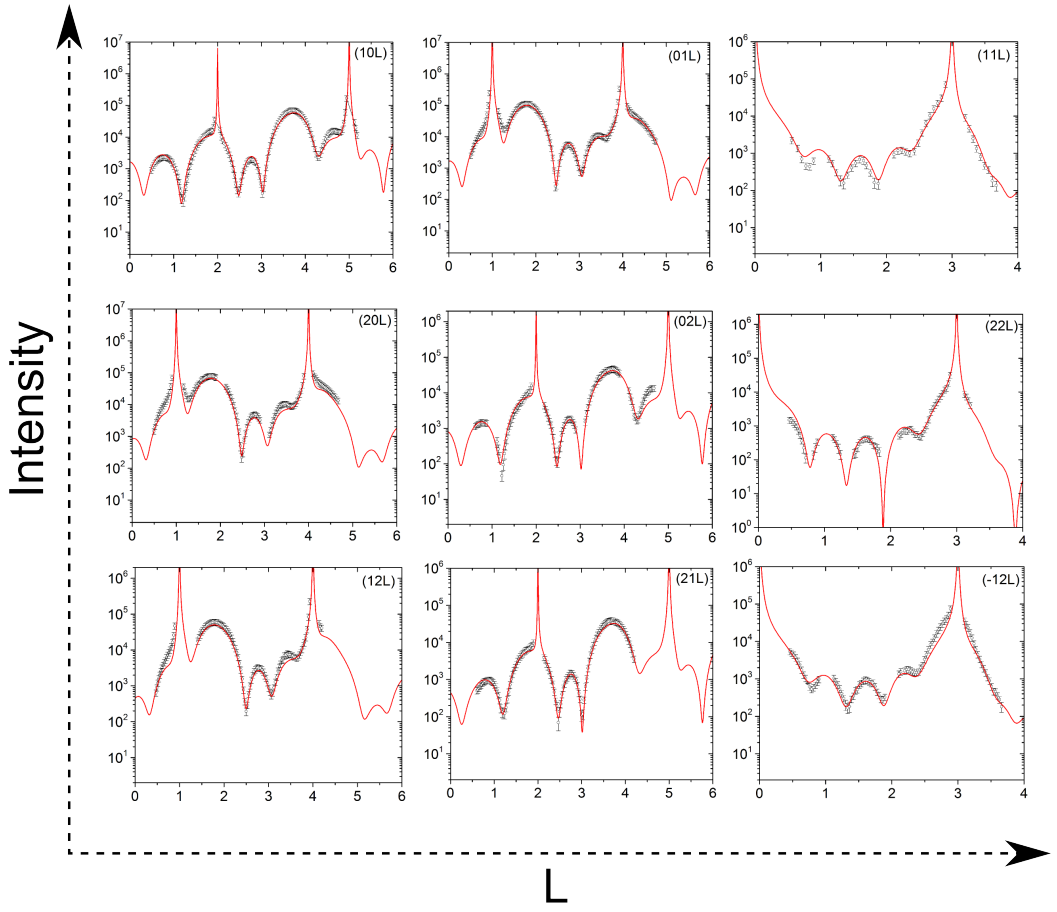

Figure 3.23: CTR profiles measured after the single deposition onto sample 3, with fitting profiles calculated from model shown in figure 3.24.

Layer	Bulk position	Fit Position	Displacement(%)
9	1.0000	1.0185 ± 0.0013	1.85
10	0.9167	0.9087 ± 0.0009	-0.80
11	0.6667	0.6593 ± 0.0015	-0.74
12	0.5833	0.5763 ± 0.0008	-0.70
13	0.3333	0.3290 ± 0.0009	-0.43
14	0.2500	0.2489 ± 0.0004	-0.11

Table 3.10: Layer positions for the InAs layers in the best fit model for deposition 1 on sample 3 shown in figure 3.24. Layer positions are given as ratios of InAs c-lattice parameter, displacements are given as a percentage of InAs c-lattice parameter.

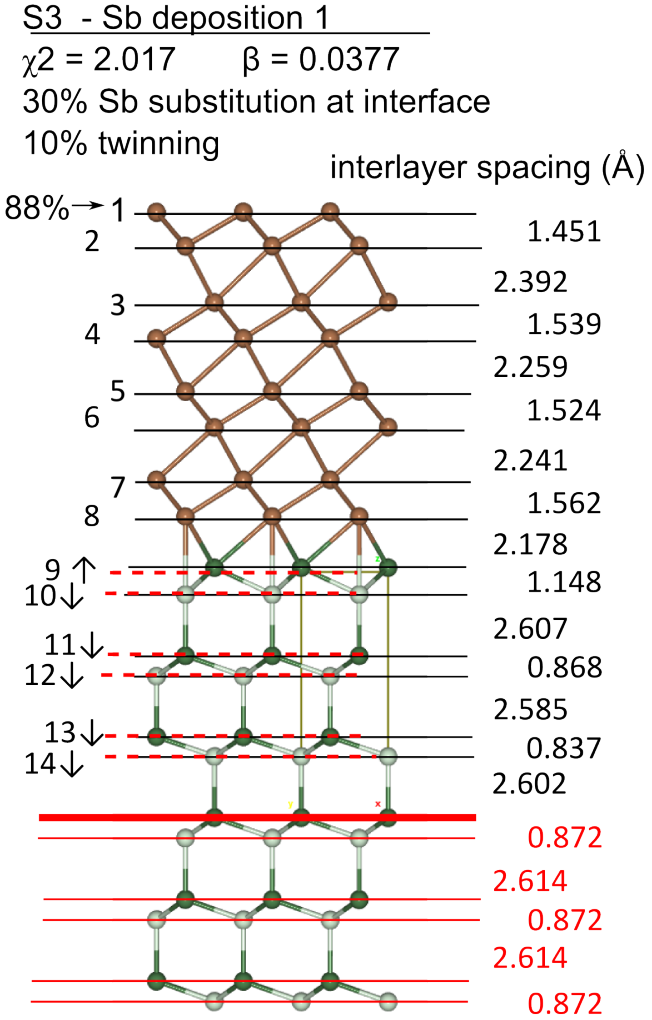

Figure 3.24: Best fit model for single deposition onto sample 3. Solid red lines indicate atomic layers which were fixed at bulk positions during fitting, with the thick solid red line indicating the top of the bulk file. Solid black lines show positions of layers for best fit model and dotted red lines show the bulk positions for InAs layers moved during fitting.

CTR fitting sample 2 - Deposition 2

A summary of the deposition stages used on sample 2 is given in table 3.11. Finally the thickest Sb film is considered, which was deposition 2 on sample 2. CTR data collected after this deposition are summarised in the HK plot in figure 3.25. 13

CTRs were measured, of which there were 7 symmetrically non-equivalent CTRs. The data reduction for this dataset was complicated by the fact that the spacing of thickness oscillations in the intensity was of a similar size to the spacing created by the substrate miscut. This led to difficulties in background subtraction as well as extra uncertainty in the overall measured intensities. As a result of these complications, larger errors of 40% were given to all CTR scans and only 6 CTRs were used in the final dataset, giving a total of 664 reflections.

Sample 2	Duration (minutes)	T_{cell}(°C)	T_{sub}(°C)
*Sb deposition 1	20	430	260
Sb deposition 2	20	430	25
*Anneal	20	-	210

Table 3.11: Growth settings and timings for sample 2. T_{cell} is the temperature of the Sb effusion cell, and T_{sub} is the temperature of the InAs(111)B substrate. Stages labelled with '*' are those which had a CTR dataset collected directly afterwards.

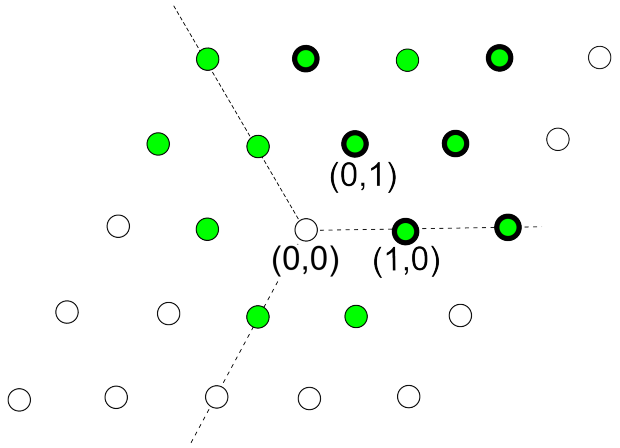

Figure 3.25: HK plot of CTR data measured after deposition 2 onto sample 2, with collected CTR positions indicated with green filled circles. The 120°C symmetry is indicated with the three dotted lines, and the symmetrically independent CTRs used in fitting are indicated with a bold outline.

Fitting was conducted following the same procedure used for sample 3. To begin with the amount of Sb layers and initial interlayer spacing were found from matching the model peaks to the Sb peak positions in the data. This gave best fits for

36 atomic layers of Sb with a thickness of 6.9 nm, which agrees well with the thickness estimate from the out-of-plane $\theta - 2\theta$ oscillations presented earlier. Matching the relative peak heights of signals from twinned and untwinned domains gave best fits with 5% twinning. DW factors were included in an identical method to sample 3 with most atoms having only an out-of-plane DW factor (DW2), but atomic layers at the surface or the interface had both an in-plane and out-of-plane DW factor (DW1 and DW2). In order to reduce the total number of fitting parameters the central Sb BLs (BLs more than three atomic layers away from either the surface or the interface) were fitted with identical z-displacement parameters. Fitting Sb substitution of surface As showed a preference for 90% Sb substitution in the top As layer (figure 3.26). This increased level of substitution when compared with the single deposition used on sample 3 indicates that the initial deposition at high temperature promotes the Sb substitution of surface As atoms.

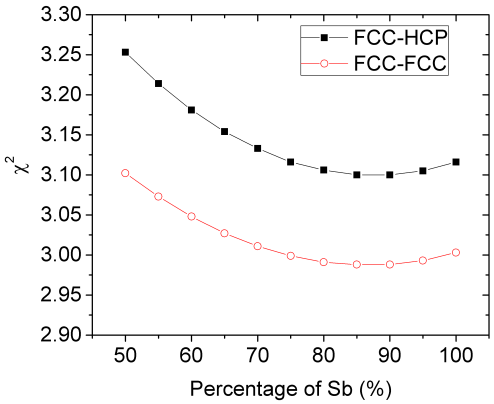

Figure 3.26: Effect of Sb substitution on fitting CTR data collected from sample 2 after Sb deposition 2.

Adsorption site(Untwinned/Twinned)	χ^2
FCC/FCC	2.988
FCC/HCP	3.100
On top/ On top	3.793

Table 3.12: Values of fits to CTR data collected after deposition 2 onto sample 2, using various combinations of adsorption sites for twinned and untwinned domains

Models using 5% twinning and 90% Sb substitution were then refined using various adsorption sites for the twinned and untwinned Sb overlayers. The fit values from the best three adsorption site models are shown in table 3.12. These results indicate that the twinned domains show a slight preference for the FCC hollowsite compared to the HCP hollowsite. This suggests that the initial high temperature deposition leads to a more uniform adsorption, and that this is the thermodynamically preferred site. The best fit model is shown in figure 3.28, with the displacements of InAs layers presented in table 3.13. Note that a compacted representation has been used for this diagram, where 13 of the similarly spaced central Sb BLs have been omitted as indicated by the dashed orange box. The movement of the InAs layers indicates that the interface bonding has become more like InSb. The higher electron mobility of InSb suggests that this could potentially be linked to the increased transport properties observed on previous thin Sb films.

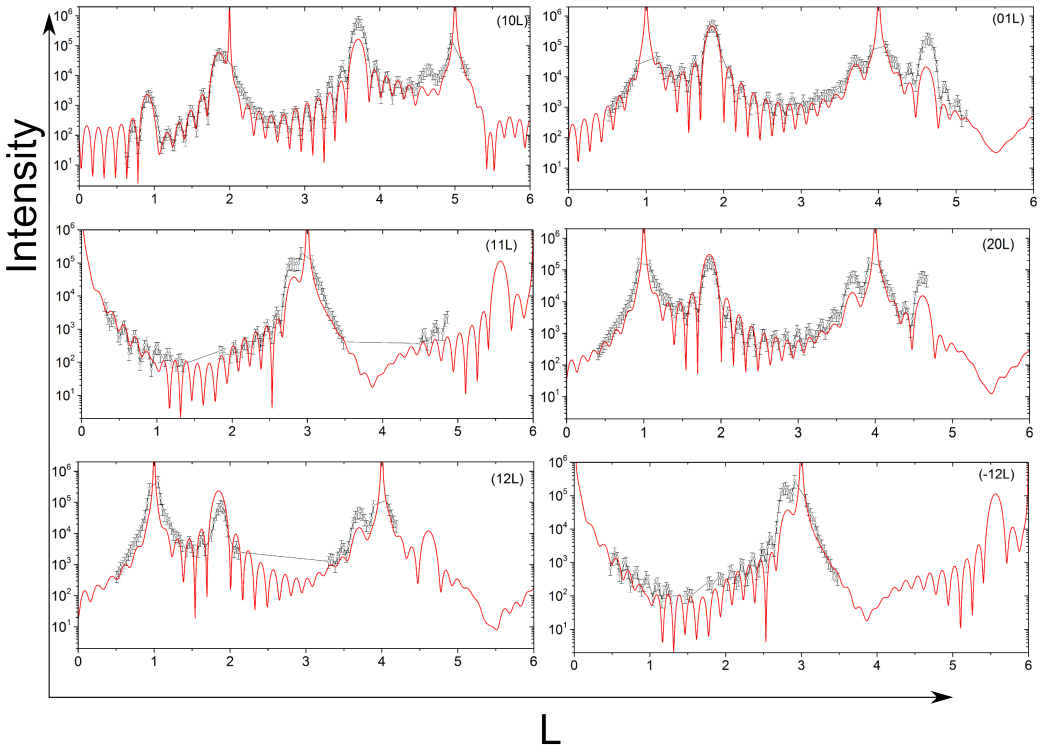

Figure 3.27: CTR profiles measured after Sb deposition 2 on sample 2, with fitting profiles calculated from the model shown in figure 3.28.

Layer	Bulk position	Fit Position	Displacement(%)
9	1.0000	1.0185 ± 0.0015	1.85
10	0.9167	0.9265 ± 0.0023	0.98
11	0.6667	0.6600 ±0.0030	-0.67
12	0.5833	0.5746 ± 0.0033	-0.90
13	0.3333	0.3035 ± 0.0035	-2.98
14	0.2500	0.2430 ± 0.0025	-0.70

Table 3.13: Layer positions for the InAs layers in the best fit model for deposition 2 on sample 2 shown in figure 3.28. Layer positions are given as ratios of InAs c-lattice parameter, displacements are given as a percentage of InAs c-lattice parameter.

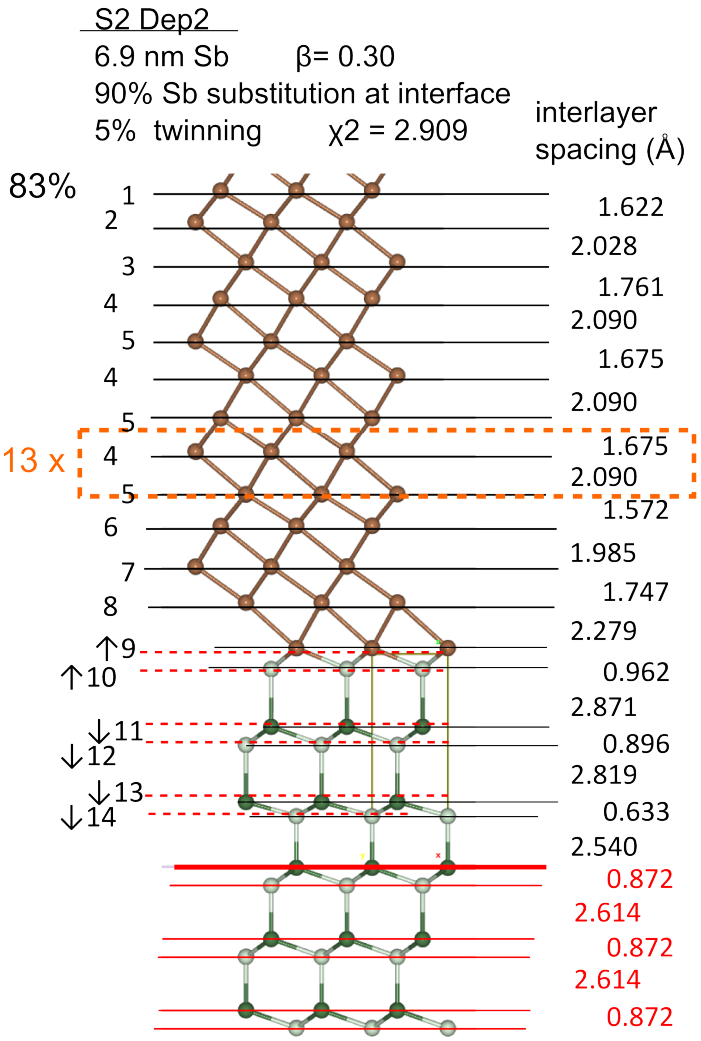

Figure 3.28: Best fit model for CTR data collected after deposition 2 onto sample 2. Solid red lines indicate atomic layers which were fixed at bulk positions during fitting, with the thick solid red line indicating the top of the bulk file. Solid black lines show positions of layers for best fit model and dotted red lines show the bulk positions for InAs layers moved during fitting. The dotted orange box represents a compacted representation of identical Sb layers which were repeated at the centre of the layer, the full model contains 36 atomic layers of Sb.

The fitting to datasets collected after room temperature (25 °C) depositions onto sample 2 and 3 show that layer-by-layer growth of Sb thin films can be achieved on InAs(111)B surfaces. Sb substitution was found to occur at the surface As atomic sites, although this was a much lower amount of substitution compared to the depo-

sitions at elevated temperatures. The Sb layers were found to have a small amount of twinning (5-10%). The large amount of substitution present in sample 2 led to the whole top BL of the InAs substrate moving outwards away from the bulk.

3.3.3 AFM

Post-growth ex-situ tapping mode AFM data collected by Dr. Christopher Burrows is shown in figures 3.29 and 3.30. These show ex-situ images from a 50 nm Sb/InAs(111)B sample grown previously at Warwick using T_{sub}=200°C, and images from sample 2 and 3 of this SXRD study. Similar to the triangular features seen on the previously grown 50 nm thick sample, both ultra-thin samples show small crystallites forming with a clear triangular structure. However, there are also larger crystallites which lose this triangular morphology and become unstructured. The heights of both triangular and unstructured crystallites are shown in 3.31, with the counts being the total from two $5\mu m \times 5\mu m$ scan areas for both samples. These counts show that for sample 2 the triangular crystallites grow higher before transitioning to unstructured growth. This crystallite height cut-off limit for triangular morphology is approximately 5 nm for sample 2, and 2 nm for sample 3. The surface areas between crystallites show almost identical low RMS roughness values for sample 2 and sample 3 (0.181 nm and 0.173 nm respectively).

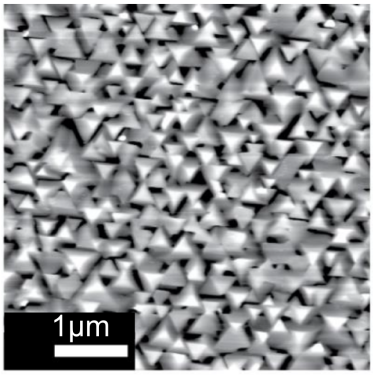

Figure 3.29: Tapping mode AFM collected from a 50 nm Sb/InAs(111)B sample grown previously at Warwick using $T_{sub} = 200°C$, showing the triangular morphology present in thicker films.

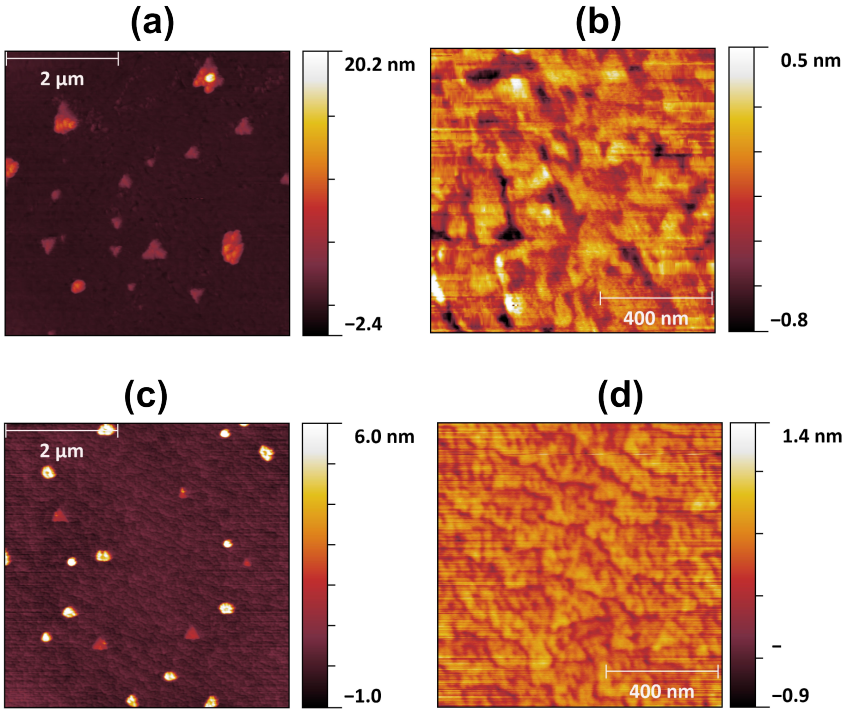

Figure 3.30: Ex-situ post-growth tapping mode AFM data collected from (a,b) sample 2, and (c,d) sample 3. Both samples show two types of crystallites; triangular and unstructured.

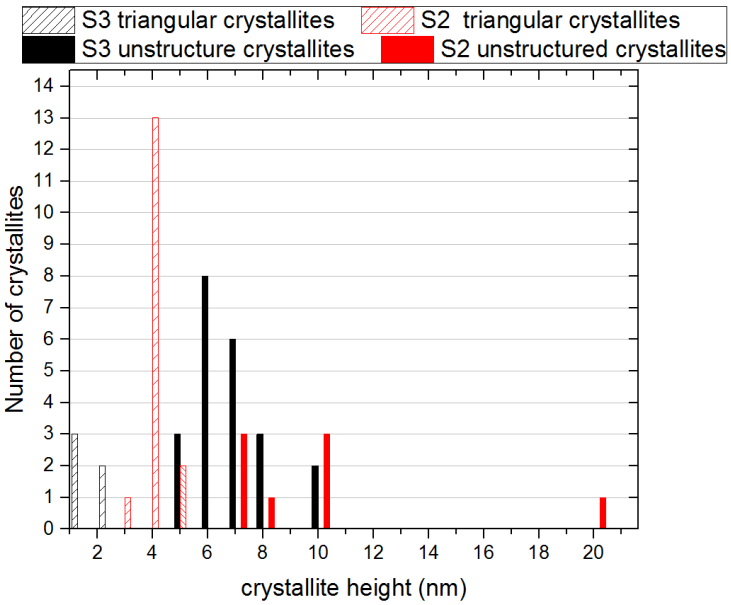

Figure 3.31: Size distribution of both triangular and unstructured crystallites on sample 2 and samples 3, calculated from two $5\mu m \times 5\mu m$ areas on each sample

3.4 Summary

From the results presented in this chapter it has been shown that Sb can be successfully grown epitaxially on InAs(111)B. The main adsorption site was found to be the FCC hollowsite, with a small amount adsorption occurring at the HCP hollowsite for a single deposition stage at room temperature. The use of an extra initial high temperature deposition stage showed an increase in Sb substitution on the surface As sites, as well as a decrease in twinning in the Sb overlayer. The Sb substitution was found to cause an expansion of the top InAs atomic layer away from the substrate, with a substitution of 70% causing an expansion of the whole of the first InAs BL away from the substrate. An increase in Sb layer thickness was found to cause a decrease in the difference between inter-BL (H1) and intra-BL (H2) distances. AFM showed that although most of the surface has very low RMS roughness values, there are crystallites which form on the surface which have a triangular structure at the beginning of their growth. These crystallites were found to lose their triangular

morphology after a certain size limit. This size limit was found to increase with the use of an initial high temperature deposition step, which creates a monolayer of Sb substituted onto the InAs surface. These results will provide valuable inputs for future density function theory simulations, as well as aiding further experiments investigating Sb thin film deposition.

Chapter 4

MnSb/InGaAs(111)A growth study

4.1 Introduction

Several research groups have investigated the growth of MnSb onto technologically relevant substrates, especially III-V semiconductor materials. The ternary alloy substrate $In_xGa_{1-x}As$ has several beneficial properties for use in spintronic applications including high electron mobility, high Lande g-factor, and formation of low Schottky-barriers at metal-semiconductor interfaces [116] [69]. A group III ratio of $In_{0.5}Ga_{0.5}As(111)$ provides a very good in-plane lattice match to n-MnSb(0001) (0.12% mismatch). This makes the MnSb/$In_{0.5}Ga_{0.5}As(111)$ system an excellent candidate to examine the epitaxial growth of MnSb.

Successful epitaxial growth of MnSb onto $In_xGa_{1-x}As$ has been reported by Amemiya *et al.* during the fabrication of waveguide optical isolators [117]. The devices grown were shown to be functional, but detailed information about the growth of the MnSb layers was not reported. Epitaxial growth of MnSb on $In_{0.5}Ga_{0.5}As(111)A$ was recently conducted at Warwick using the same growth conditions as used for GaAs(111) substrates, and showed evidence of c-MnSb formation

[118]. However a detailed MBE parameter space study for epitaxial growth of MnSb onto InGaAs(111)A has not been previously carried out, which means these may not necessarily be the optimum conditions. Therefore, to investigate the effect of flux ratio ($J_{Sb/Mn}$) and substrate temperature (T_{sub}) on the epitaxial growth of MnSb onto $In_{0.5}Ga_{0.5}As$(111)A substrates, a growth study has been carried out. The results are presented in this chapter as follows. Sec. 4.2 provides the experimental details of sample growth and characterisation. In Sec. 4.3 experimental data is presented in the following order RHEED, AFM and SEM, TEM, XRD, and VSM. Sec. 4.4 then provides a summary of all experimental results.

4.2 Experimental Details

Samples of approximately 10mm $\times$ 8mm in size were cleaved from $In_{0.5}Ga_{0.5}As$(111)A virtual substrates. These are 400nm thick $In_{0.5}Ga_{0.5}As$ layers grown at Warwick in a Varian MBE system on 50mm GaAs(111)A wafers. Previous characterisation of these virtual substrates has shown that the surface roughness and crystalline mosaic values for InGaAs were higher than those of the GaAs wafers due to the considerable lattice mismatch of 3.2% between them [118]. The cleaved samples were then spot welded onto stainless steel plates with tantalum wires before being ultrasonicated and then rinsed with a series of solvent washes (acetone, isopropanol, and then deionised water). After the solvent rinse the samples were blown dry with nitrogen and loaded immediately into the UHV system. Sample substrates then underwent an argon ion bombardment and annealing (IBA) process as follows:

1. Degas sample for 1 hour at $420 \pm 10°C$
2. Ion bombardment at 500 eV for 8 minutes
3. Anneal at $490 \pm 10°C$ for 1 hour

Following this procedure all of the $In_{0.5}Ga_{0.5}As$(111)A substrates gave a

(2×2) RHEED pattern (figure 4.1). While an As trimer termination is possible for III-V(111)A surfaces [119], it requires excess As flux to give complete As coverage of the surface. In this study As flux was not used in the surface preparation of samples, therefore the (2×2) reconstruction observed on $In_{0.5}Ga_{0.5}As$(111)A is most likely a missing group III atom reconstruction similar to reconstructions seen on GaAs(111)A [120][121] and InAs(111)A [122] [123]. The RHEED patterns were observed during growth and the final patterns were recorded. In order to investigate the surface morphology, roughness and layer crystallinity, ex-situ SEM, AFM and XRD measurements were obtained for all samples. TEM and VSM magnetometry measurements were obtained from a few representative samples. The samples were removed from UHV without any special precaution such as an Sb capping layer. This was to aid in the analysis of XRD data and identification of the presence of the cubic MnSb polymorph (c-MnSb), because the h-Sb(0003) reflection from an Sb cap would occur at $Q_z = 1.672$ Å^{-1} which is almost an identical position to the c-MnSb(111) reflection at $Q_z = 1.674$ Å^{-1}.

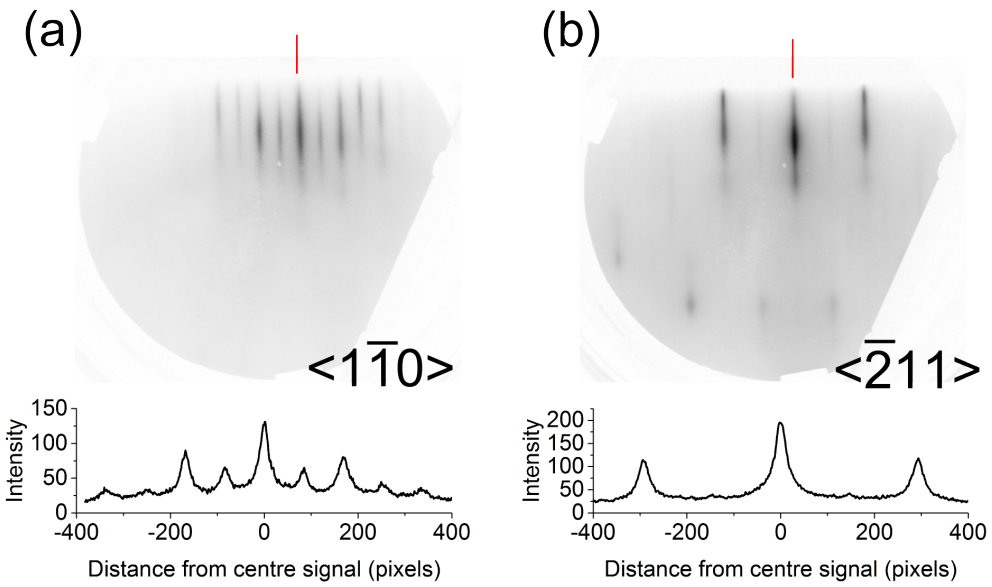

Figure 4.1: RHEED patterns from a clean InGaAs(111)A-(2 × 2) surface, in two azimuthal directions of the (111) surface (a) $<1\bar{1}0>$, and (b)$<\bar{2}11>$. Red lines indicate the origin of the line profiles. The surface was prepared using the ion-bombardment and annealing cleaning procedure detailed in the text.

MnSb films approximately 120 nm thick were then deposited using a range of flux ratios ($J_{Sb/Mn} = 3.5 - 9.5$) and substrate temperatures ($T_{sub} = 350 - 450°C$) (figure 4.2) . The growth rate used for all samples was approximately 2 nm.min^{-1}. The critical thickness for MnSb deposition onto $In_{0.5}Ga_{0.5}As(111)$ was calculated in a similar manner to the previous chapter, using the Matthews-Blakeslee model [124] for misfit dislocations on the hexagonal $\{11\bar{2}2\}$ slip plane in the $<11\bar{2}3>$ slip direction. Using this method the critical thickness was calculated to be approximately 220 nm, therefore all sample thicknesses were below the critical thickness value.

Most samples were grown using a single-stage growth method where the substrate was maintained at constant temperature for the whole growth period. In this case, the parameter space was explored using 3 values of $J_{Sb/Mn}$ (3.5, 6.5, 9.5) and 3 values of T_{sub} (350, 415, 450°C). A second set of fewer samples was grown using a two-stage growth method where the substrate was initially held at $T_{sub} = 350°C$ for

60 seconds, the growth was then interrupted while the substrate temperature was increased to $T_{sub} = 415°C$, and then the substrate was kept at this temperature for the remainder of the deposition. For this set of samples 3 values of T_{sub} (350, 415, 450°C) were used with the single value of $J_{Sb/Mn} = 6.5$.

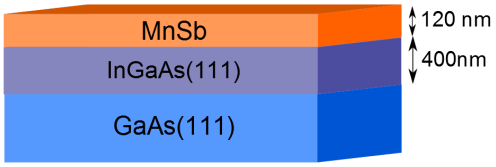

Figure 4.2: Schematic diagram showing layer types and thicknesses of MnSb/InGaAs(111)A samples

All RHEED images presented in this chapter were collected using an accelerating voltage of 12.5 keV. All AFM images presented in this chapter were collected using a Veeco multimode AFM in contact mode. All SEM images presented in this chapter were collected using a Zeiss SUPRA 55-VP SEM with a 10kV accelerating voltage. All symmetric out-of-plane XRD $\theta - 2\theta$ data was collected using the in-house Panalytical X'Pert Pro diffractometer with an x-ray wavelength $\lambda = 1.5406$Å. All VSM data presented in this thesis was collected at 10 K, with H directed in the plane of the sample surface. TEM data was collected by Dr. Ana Sanchez using a Jeol 2100 LaB6 microscope in scanning mode (STEM), and EDX data was collected using an Oxford Instruments windowless EDX detector attached to a Jeol ARM 200F STEM. Two different image types were obtained: low magnification annular dark field (ADF) STEM images with corresponding EDX compositional analysis, and atomic resolution ADF-STEM with selected area diffraction patterns (SADP).

4.3 Results

4.3.1 RHEED

Single-stage samples

For all samples grown at T_{sub} = 350°C the (2×) fractional streaks of the substrate disappeared in the first 10 seconds of growth. At this temperature for $J_{Sb/Mn} = 3.5$ and 6.5 the substrate integer streaks also disappeared completely after 20 seconds of growth. For $J_{Sb/Mn}$ = 9.5 the integer streaks did not disappear, but they did become highly modulated into elongated commensurate transmission spots. For $J_{Sb/Mn}$ = 3.5, after 2 minutes of deposition blurry modulated integer streaks appeared. For $J_{Sb/Mn} = 6.5$ a modulated (2×) streak pattern appeared after 30 seconds of deposition, with a faint (2×) pattern appearing after 60 seconds. For $J_{Sb/Mn}$ =9.5 after 2 minutes of deposition (2×) fractional order streaks were present, although all streaks had modulated intensities. These observations indicate that at T_{sub}=350°C low flux ratios do not allow MnSb to form highly crystalline layers, indicated by the lack of (2×) reconstructions and poor integer streak quality. For higher flux ratios the MnSb (2×) reconstruction indicates good ordered layers forming, but the transmission spots present at $J_{Sb/Mn}$ = 9.5 shows 3D growth processes are also occurring.

For T_{sub} = 415°C a similar RHEED pattern transition was observed at $J_{Sb/Mn}$ = 3.5, with substrate integer order streaks and fractional order streaks disappearing after 10 seconds, and only a blurry (1×) pattern appearing after 4 minutes. These observations indicate that at $T_{sub} = 415$°C, low $J_{Sb/Mn}$ values lead to poor epitaxy and the formation of MnSb layers with low crystalline quality. For $J_{Sb/Mn}$ = 6.5 the substrate (2×) fractional order streaks disappeared after only 2 seconds indicating a good level of surface coverage. The substrate integer streaks disappeared after 40 seconds, with a modulated (2×) pattern appearing after 1 minute 30 seconds. This fast loss of fractional streaks, along with retention of the integer

streaks for most of the deposition, indicates a maintained ordered surface signalling epitaxial 2D layer-by-layer growth. For $J_{Sb/Mn} = 9.5$ the substrate (2×) fractional order streaks also disappeared almost instantly after 2s, whereas the integer order streaks faded after 5 seconds. Modulated integer order streaks appeared after 30 seconds, which later smoothed out in intensity after 2 minutes. The longer time taken for integer streaks to appear, and the modulation in their intensity for $J_{Sb/Mn} = 9.5$ indicates that these conditions are moving more towards 3D island growth.

For T_{sub}=450°C growth at $J_{Sb/Mn} = 3.5$ showed the disappearance of the substrate (2×) fractional order streaks after 30 seconds, and the substrate integer order streaks became diffuse after 1 minute. This long transition time at the start of growth indicates that for these conditions there is a much lower rate of deposition. This is to be expected due to the rate of Sb sublimation increasing exponentially for temperatures above 400°C [125]. This leads to a further reduction in the already limited Sb incorporation for Sb-limited deposition at low $J_{Sb/Mn}$ values. For $J_{Sb/Mn} = 6.5$ the substrate (2×) fractional order streaks disappeared after 3 seconds, and the integer streaks became faint after 10 seconds. After 30 seconds the integer streaks increased in intensity, and at 1 minute 30 seconds a faint (2×) pattern emerged. This indicates that, similar to growths at lower temperatures, the MnSb layer grew epitaxially in a 2D fashion when using $J_{Sb/Mn} = 6.5$. The similar timescale for streak appearences at the start of growth for $J_{Sb/Mn} = 6.5$ at different T_{sub} values agrees with previous studies that for $J_{Sb/Mn} \geq 6$ layer deposition is Mn-limited [125]. For $J_{Sb/Mn} = 9.5$ both fractional and integer streaks had disappeared within 10 seconds, with strong spot like integer order streaks appearing after 30 seconds and smoothing out in intensity after 2 minutes. This indicates that the growth at these settings is initially 3D island growth, which transitions to 2D growth mode after a certain thickness.

RHEED observations made in this growth study show that growth of MnSb on InGaAs(111)A follows a similar trend to growth on GaAs(111)A, showing best

layer epitaxy when settings are between Sb-limited growth at low $J_{Sb/Mn}$ (and high T_{sub}), and Mn-limited growth at high $J_{Sb/Mn}$.

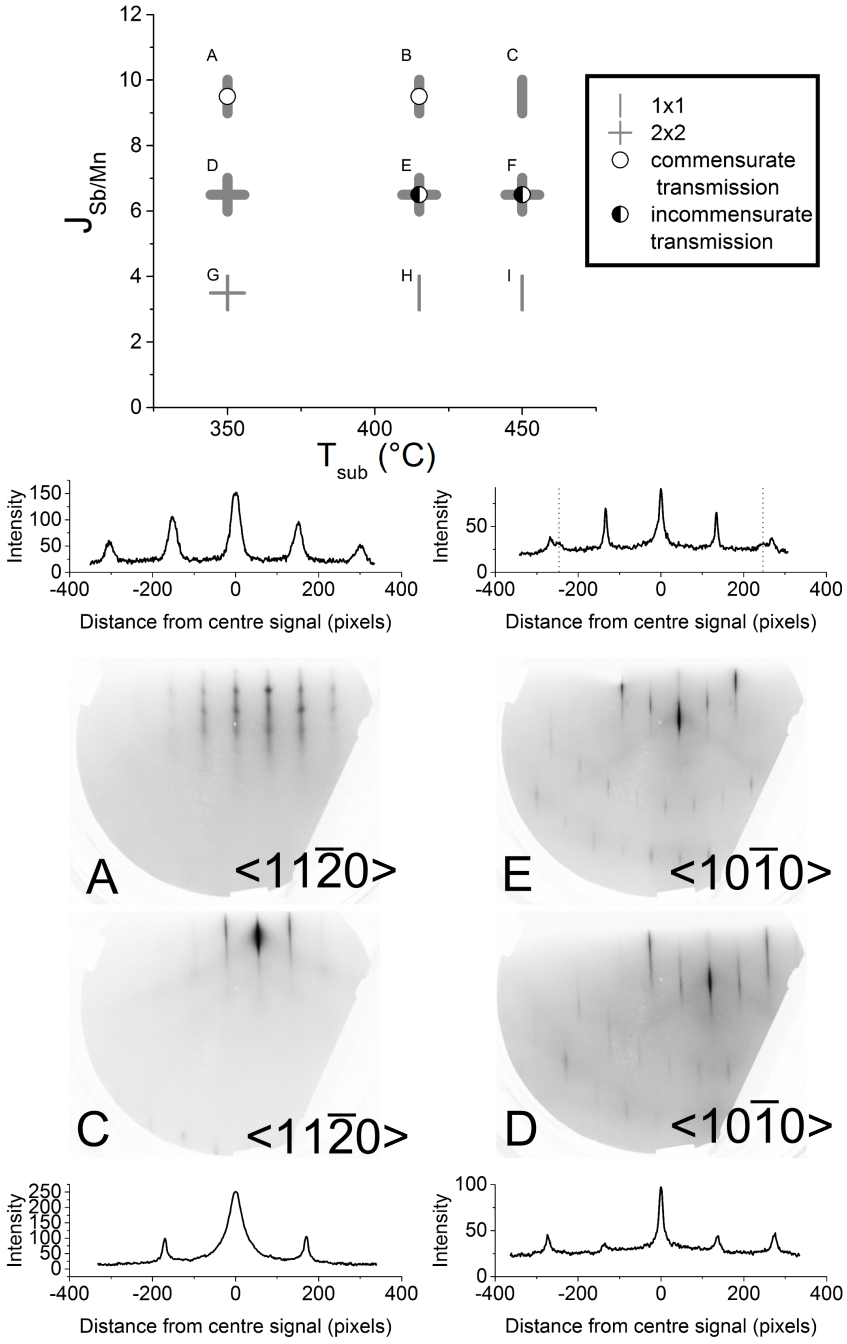

Figure 4.3: Parameter space plot showing RHEED patterns observations. Strong(weak) signals are indicated with the use of thick(thin) lines. Examples of the main types of features are shown in below, with accompanying line profiles, as follows. A - (1×1) with commensurate transmission, E - (2×2) with incommensurate transmission, C - (1×1) , D - (2×2) The dashed grey lines in the line profile for sample E mark the position of the incommensurate transmission spots.

The RHEED patterns obtained at the end of MnSb growth are detailed in the parameter space diagram in the upper section of figure 4.3, with images of example patterns for the individual features shown in the lower section. Note that the use of bold lines indicates that the pattern observed had a very high intensity compared to the background level.

All MnSb samples grown with $J_{Sb/Mn} = 6.5$ were found to adopt a (2×2) surface reconstruction exhibiting strong sharp integer and fractional order signals.The final RHEED patterns also contained multiple Laue zones and Kikuchi lines, which indicate that the MnSb layers are highly crystalline and have ordered smooth surfaces. For the $J_{Sb/Mn} = 6.5$ samples grown at the higher temperatures of $T_{sub} \geq 415$°C very faint incommensurate transmission spots can be seen. When compared to the integer streaks these spots have an ∼10% smaller spacing in the RHEED pattern, indicating that the material in the 3D islands has an in-plane lattice parameter approximately 10% larger than the main MnSb layer. This corresponds to an in-plane lattice parameter of roughly 4.54 Å, which is most likely a different material to MnSb. Some potential materials which might have formed are InSb(111) (4.569 Å), c-MnSb(111)(4.598 Å), or an alloy such as $InGa_{0.5}Sb_{0.5}$(111)(4.447 Å).

For the higher and lower flux ratios $J_{Sb/Mn} = 9.5$ and 3.5 the quality of the MnSb layer was found to decrease in smoothness and crystallinity when compared with MnSb layers grown using $J_{Sb/Mn} = 6.5$. The use of the high flux ratio $J_{Sb/Mn} = 9.5$ formed RHEED patterns which showed a (1×1) surface reconstruction with very faint fractional signals, and transmission spots present for growth at $T_{sub} = 350$°C and 415°C. Only a single Laue zone was present in the RHEED patterns and kikuchi lines were not present for the low growth temperature of $T_{sub} = 350$°C. For growth conditions using a low flux ratio of $J_{Sb/Mn} = 3.5$ the RHEED patterns became very weak, with the higher temperatures $T_{sub} \geq 415$°C producing very weak and modulated signals. No clear Laue zones or kikuchi lines were present in RHEED patterns from MnSb layers grown at $J_{Sb/Mn} = 3.5$.

The in-plane lattice spacing of the n-MnSb overlayers at the end of growth was calculated using the integer streak separation extracted using line profiles from RHEED images. The lattice spacings also required an extra correction factor obtained from using the measurement of the clean $In_{0.5}Ga_{0.5}As(111)A$ substrate as calibration. The in-plane lattice spacings calculated using this technique are shown in figure 4.4. The values for the in-plane lattice parameters were roughly centred around the bulk in-plane lattice spacing 4.128 Å, but there was a considerable range of values. This result will be revisited later on in this chapter.

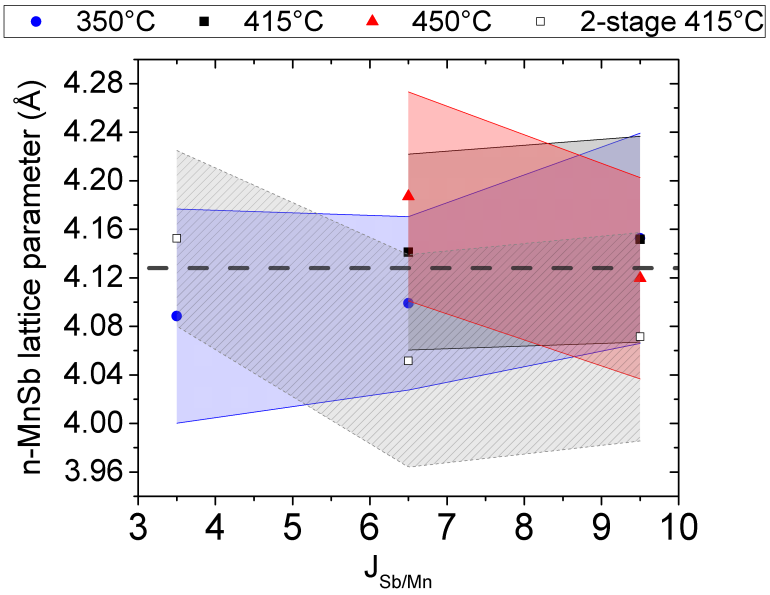

Figure 4.4: The n-MnSb lattice parameters calculated from RHEED integer streak spacings, with errors represented by colour coded shaded areas. The grey dotted horizontal line indicates the in-plane lattice constant of bulk n-MnSb 4.128 Å.

Two-stage Samples

The final RHEED patterns from the samples grown using the two-stage methodology are summarised in figure 4.5. These show that for $J_{Sb/Mn} = 3.5$ a (2×) pattern with incommensurate transmission spots is obtained, indicating that the growth is mostly epitaxial in nature but still has a small amount of 3D island growth. For $J_{Sb/Mn} = 6.5$ and 9.5 the transmission signals are no longer present using a two-

stage growth process, indicating that this promotes smoother 2D epitaxial growth. This agrees with similar findings for deposition of MnSb onto GaAs(111)B, where the two-stage growth methodology was shown to prevent the formation of surfaces with incomplete coverage [126].

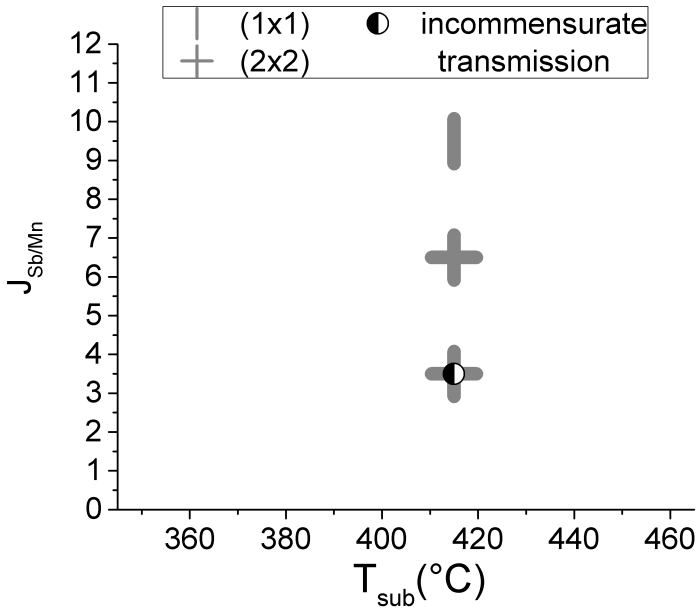

Figure 4.5: Characteristics of RHEED patterns observed for samples grown using two-stage growth method. The substrate temperature plotted on the graph is the temperature used during the second stage of deposition. Strong(weak) signals are indicated with the use of thick(thin) lines.

4.3.2 AFM and SEM

Single-stage Samples

SEM images of single-stage growth samples are shown in figure 4.6. All samples show small crystallites on the surface which are between 0.1 - 1 μm in size (figure 4.7). The shape of the crystallites is highly dependent upon flux ratio, with an increase in $J_{Sb/Mn}$ increasing the amount of protrusions on the crystallite. This suggests that the crystallites are capturing the excess Sb, and are likely to be $MnSb_2$ or Sb. The areal density of these crystallites was calculated for each sample from large area

SEM images (figure 4.8). The areal crystallite densities are shown in figure 4.9, with the errors on each value represented by the colour coded shaded regions. These errors were calculated based on simple counting statistics where the error on the number of crystallites counted in each image (N) is given by $\sigma_N = \sqrt{N}/N$. From this data it can be seen that $J_{Sb/Mn} = 6.5$ shows the lowest crystallite density for all growth temperatures apart from 350°C. Growth at this temperature gave crystallite densities at $J_{Sb/Mn} = 6.5$ and $J_{Sb/Mn} = 9.5$ with roughly equivalent areal densities within error. This is due to these surfaces being highly disrupted and having crystallites which were only in the initial stages of formation. A possible cause of these crystallites is nucleation at threading dislocations originating from the defects on the InGaAs(111)A substrate surface. This explanation agrees with calculated areal densities matching the dislocation densities (roughly 10^6 cm^{-2}) reported in literature, obtained from etch pit analysis on heterostructures involving highly strained $In_xGa_{1-x}As$ layers grown on GaAs [127] [128] [129][130].

The SEM images in figure 4.6 show that for $T_{sub} = 415$°C with $J_{Sb/Mn} = 6.5$ the surface between crystallites is relatively uniform compared to other growth conditions, which shows that this surface has the most homogeneous composition when compared to the other single-stage growth samples.

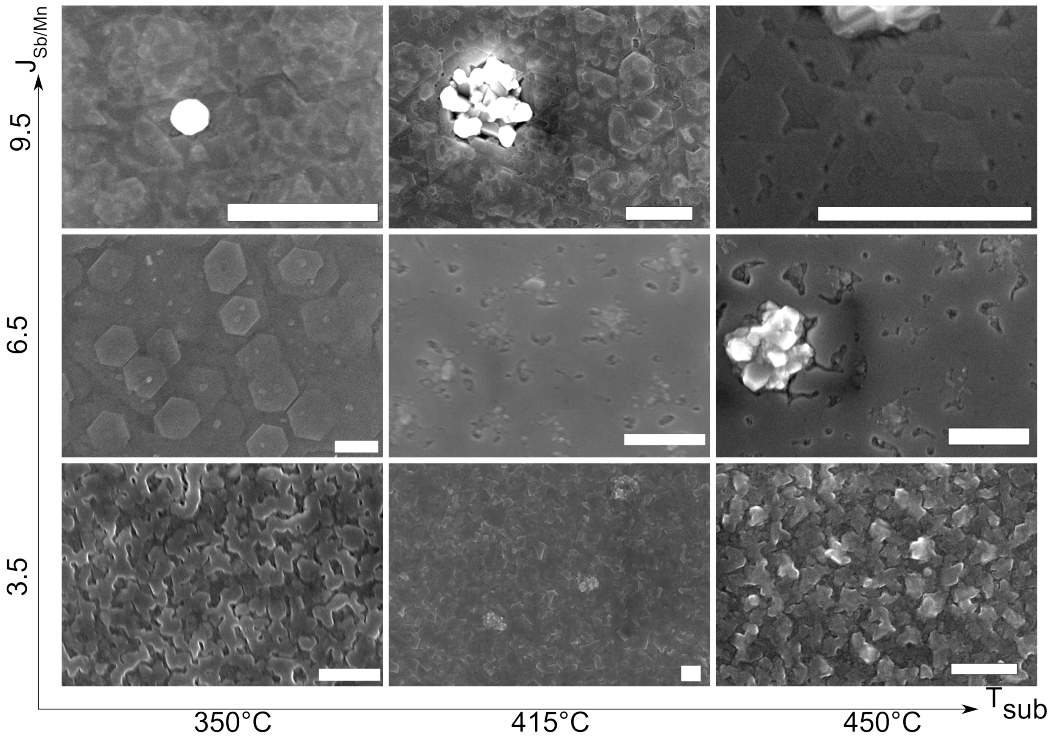

Figure 4.6: SEM images obtained from samples MnSb/InGaAs(111)A samples grown using single-stage growth method, highlighting the key features found on each surface. The white scale bar in each image corresponds to 1μm. One representative image is shown for each point in parameter space.

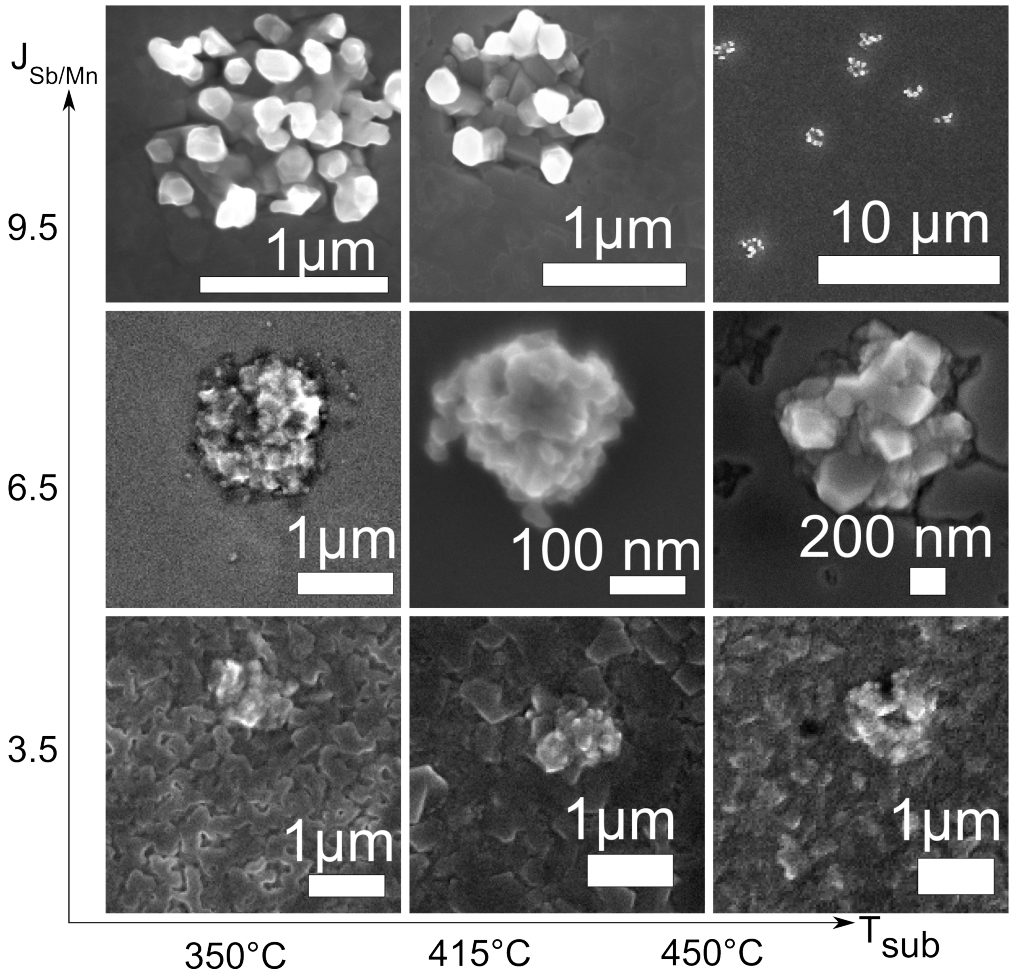

Figure 4.7: SEM images focussing on crystallites formed on the surface of samples grown using single-stage growth method. One representative image is shown for each point in parameter space.

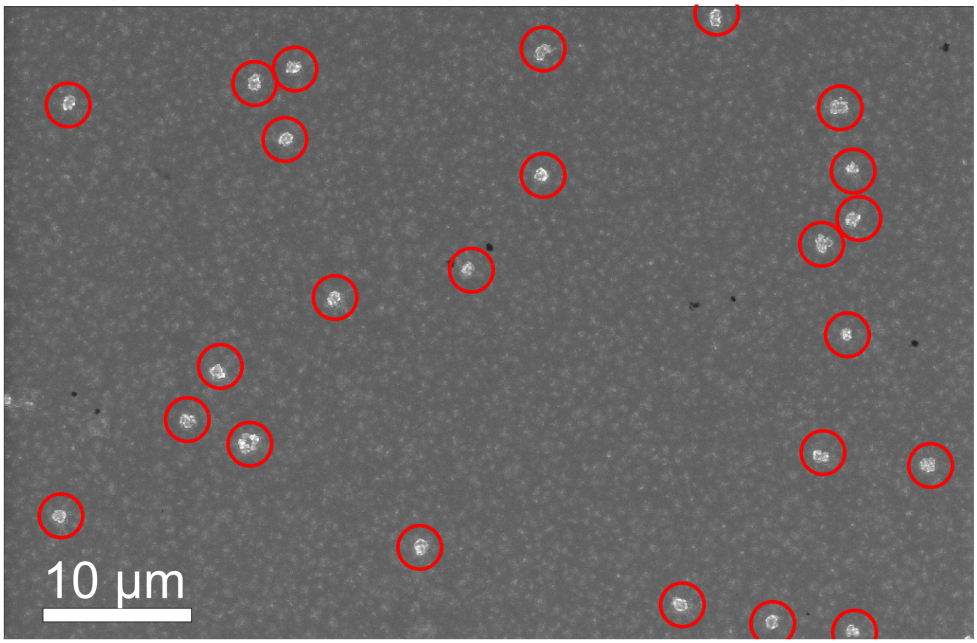

Figure 4.8: Example of a large area SEM image used to calculate the areal density of the surface crystallites. Each crystallite that was included in the surface count has been circled in red.

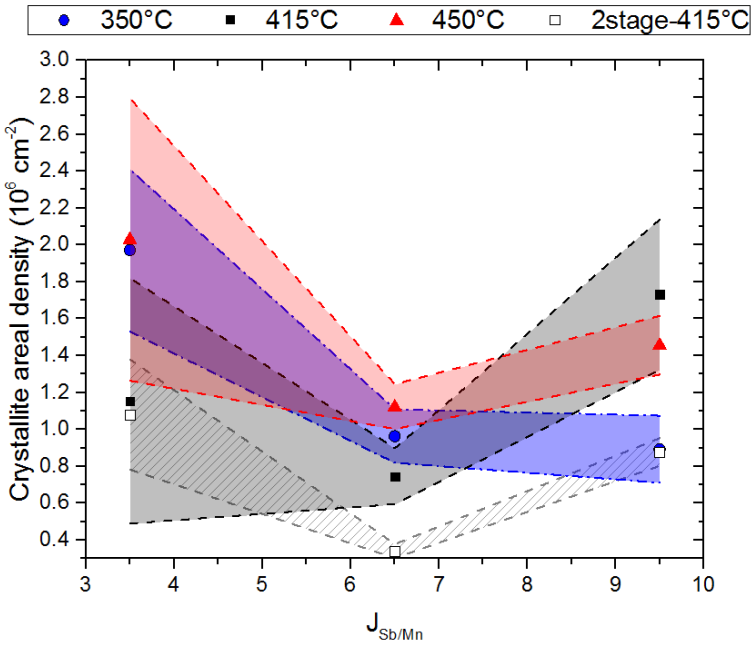

Figure 4.9: Areal densities of surface crystallites found for different growth conditions, with errors represented with colour coded shaded regions. These errors were calculated assuming simple counting statistics as described in the text.

AFM images $5\mu m \times 5\mu m$ in size are shown in figure 4.10, and the RMS roughness values calculated from $1\mu m \times 1\mu m$ images are shown in figure 4.11. All samples grown with $J_{Sb/Mn} = 3.5$ showed highly disrupted surfaces in the SEM and possess the highest AFM RMS roughness values out of all samples grown, which was consistent with the poor post-growth RHEED patterns observed for these samples.

AFM measurements of the sample grown using $T_{sub} = 415°$C with $J_{Sb/Mn} = 6.5$ gave an RMS value of 1.29 nm, which shows that the 100 nm sized crystallites are spread out on top of a flat surface. For the growth conditions $J_{Sb/Mn} = 6.5$ and $T_{sub} = 350°$C hexagonal structures can be seen that are approximately 400 nm in width, along with very small clusters spread across the surface. The AFM shows these hexagonal pillars to be roughly 10 - 15 nm in height, and all of these are rotationally aligned with one another showing preferential epitaxy to the substrate.

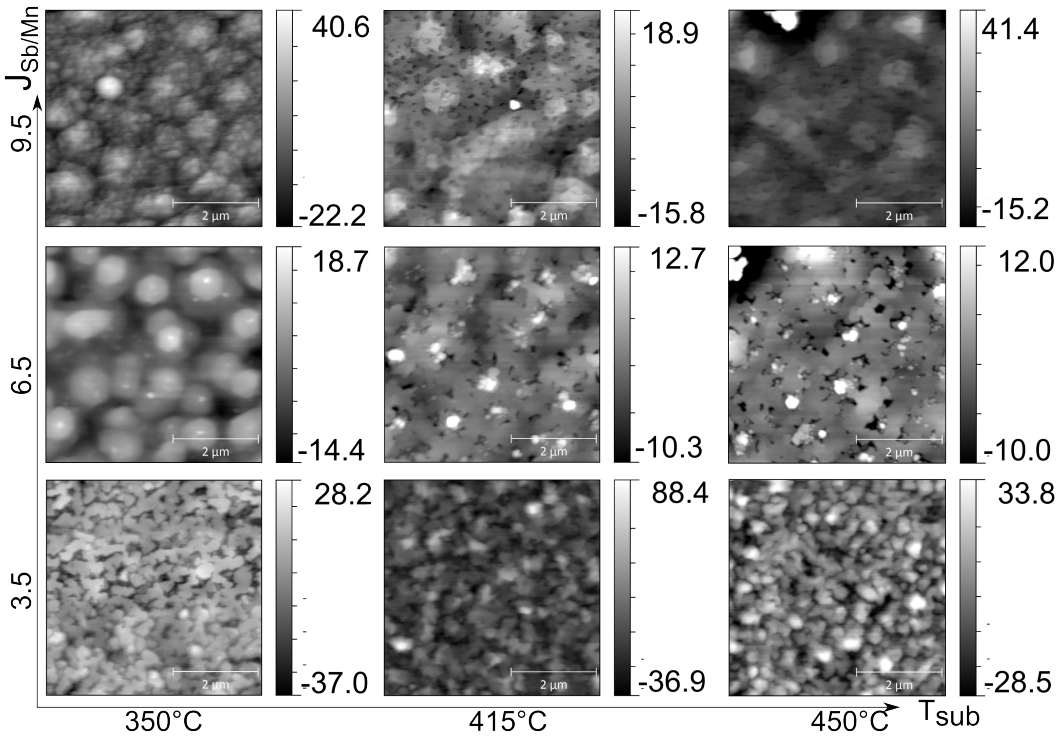

Figure 4.10: $5\mu m \times 5\mu m$ AFM images showing key surface features observed on samples grown under different conditions.

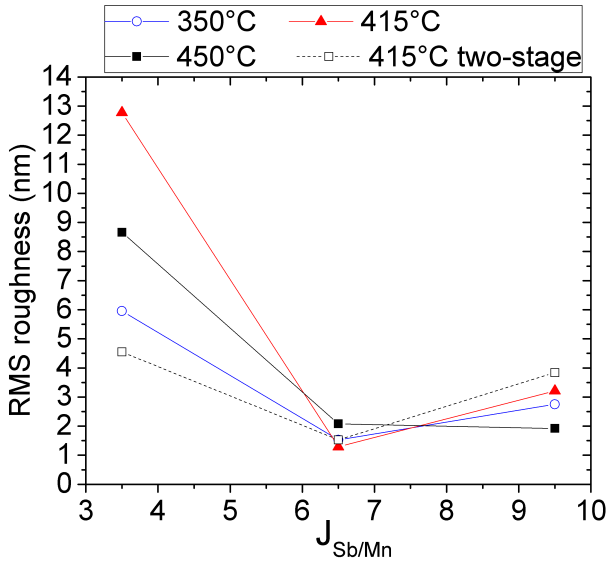

Figure 4.11: RMS roughness values calculated from 1 μm $\times 1\mu$m AFM images, taken on areas without any crystallites present.

Two-stage samples

SEM and AFM data collected from the two-stage growth samples are shown in figure 4.12. When compared to the single-stage samples, the two-stage samples exhibit a similar trend with $J_{Sb/Mn}$ in terms of areal density of surface clusters, and AFM RMS roughness values. Comparing absolute values to the single-stage data (figures 4.9 and 4.11) shows that the two-stage samples have lower areal cluster densities, and a much lower RMS roughness for growth at $J_{Sb/Mn} = 3.5$ and T_{sub} =415°C. These comparisons show that the two-stage growth methodology leads to smoother, higher quality MnSb surfaces.

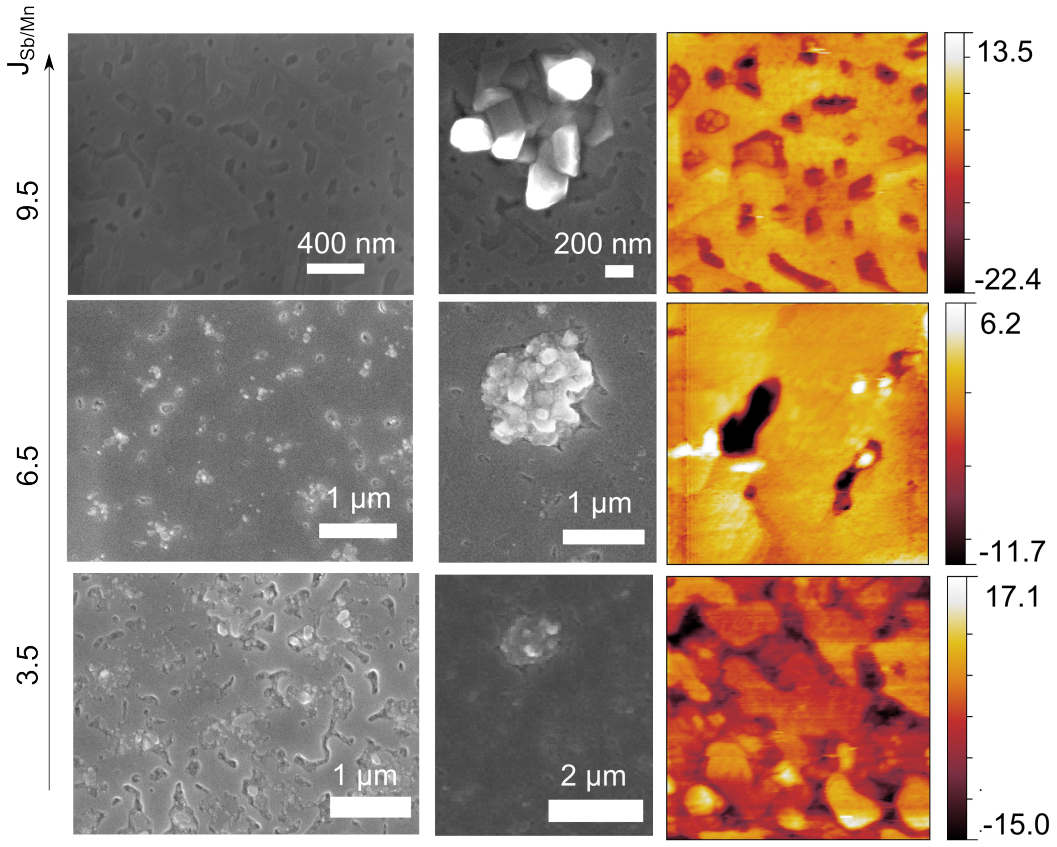

Figure 4.12: Collection of microscopy images for two-stage samples growth using T_{sub} =415°C . (Left column) main features found in SEM images, (middle column) focus on shape of surface crystallites (right column) $1\mu m \times 1\mu m$ AFM images, with height ranges in nm.

4.3.3 TEM

Single-stage Samples

TEM data, along with EDX compositional analysis, was obtained from a selection of samples (figures 4.13 - 4.20). These show a large amount of intermixing, between the MnSb layer and the $In_{0.5}Ga_{0.5}As$ substrate, for samples grown using $J_{Sb/Mn} = 3.5$ (figures 4.13 and 4.14). Segregation of In and Ga into the over layer formed $In_xGa_{1-x}Sb$ sections, and this coincided with the formation of a layer of MnAs beneath the interface. Segregation of In and Ga indicates that the IBA cycles may not be the optimum method of surface preparation, and could be causing In and Ga droplets at the surface which leads to the formation of $In_xGa_{1-x}Sb$ alloys. Indium has also been shown previously to segregate to the surface in $In_xGa_{1-x}As$ thin films grown on GaAs(001) [131].

Mn diffusion into the substrate and formation of MnAs at the surface region is similar to the behaviour documented previously for Mn deposition onto In terminated InAs(001) surfaces [132]. However, for that work MnAs was only observed at substrate temperatures $\leq$300 K, and it was shown that the amount of Mn diffusion into the substrate increased at higher substrate temperatures. Ga segregation has been observed previously during MnSb growth at similar settings ($J_{Sb/Mn} = 2$, T_{sub}=300°C) on GaAs(111)B substrates [58]. However in contrast to the results presented in this chapter, only 1 ML layer of Ga was present at the surface, and it was suggested that Ga segregation to the surface acted as a surfactant and promoted layer-by-layer growth. In segregation has also been observed for MnSb layers grown on InP(001)[133], where the substrate added an additional effective In flux to the growing layer.

In addition to formation of $In_xGa_{1-x}Sb$ in the overlayer, the formation of pure In inclusions is evident in the TEM for $J_{Sb/Mn} = 3.5$ at T_{sub}=350°C. However, no In inclusions are present in the TEM data for $J_{Sb/Mn} = 3.5$ with increased

temperature T_{sub}=415°C, which suggests that higher temperatures drive the segregation of In towards the surface leading to incorporation into the $In_xGa_{1-x}Sb$ alloyed sections. It should be noted though that TEM only provides information about a small section of the sample therefore similar pure In inclusions occurring at higher substrate temperatures cannot be completely ruled out.

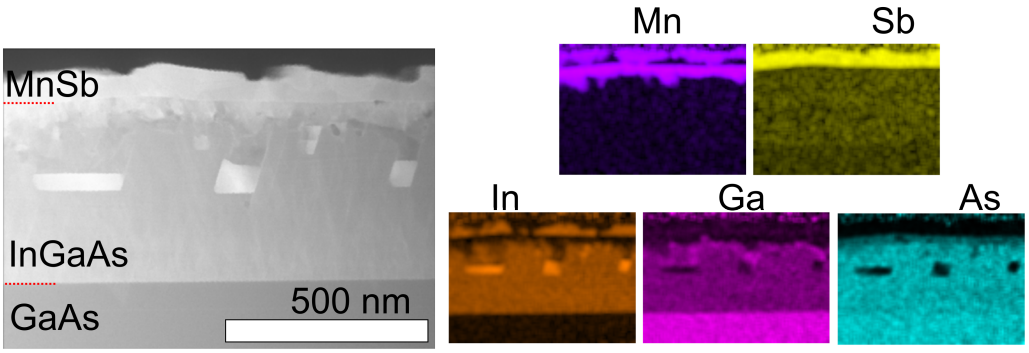

Figure 4.13: (left) TEM image of full layer structure for sample grown using $J_{Sb/Mn} = 3.5$ and $T_{sub} = 350$°C (right) EDX analysis of layers shown in the TEM image. Mn diffusion into the substrate can be seen, as well as formation of In inclusions within the substrate, and Segregation of In to the MnSb layer.

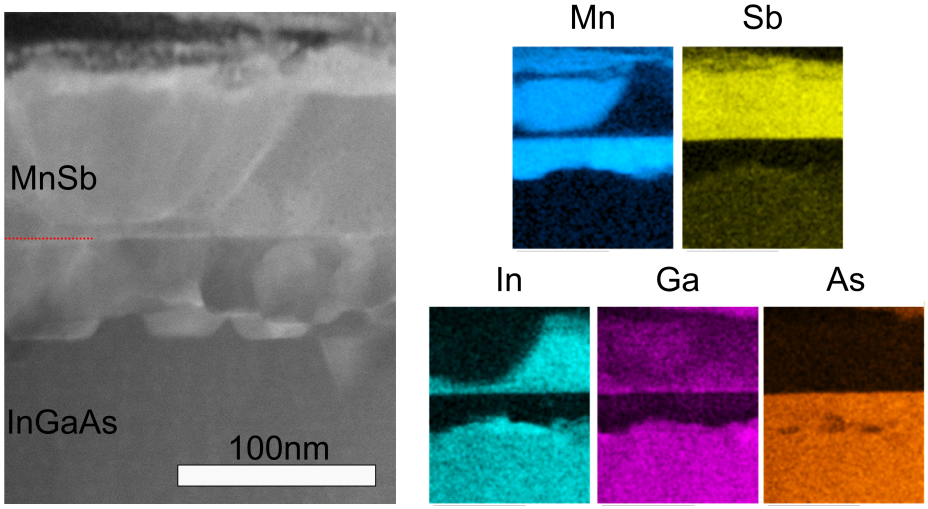

Figure 4.14: (left) TEM image of full layer structure for sample grown using $J_{Sb/Mn} = 3.5$ and $T_{sub} = 415$°C (right) EDX analysis of layers shown in the TEM image. Mn diffusion into the substrate can be seen, as well as the segregation of both In and Ga into the MnSb layer.

For growth using $J_{Sb/Mn} = 6.5$ and $T_{sub} = 350°C$ a sharp interface formed with the InGaAs(111)A substrate, showing a relatively flat interface with only a very small amount of intermixing (figure 4.15). For $J_{Sb/Mn} = 6.5$ and $T_{sub} = 415°C$ a similarly flat interface was formed, however a substantial amount of intermixing occurred (figure 4.16). The compositional analysis presented in table 4.1 show In,Ga and As segregated into the MnSb layer forming a large inclusion of mostly $In_{1-x}Ga_xSb$. The fact that these $In_{1-x}Ga_xSb$ inclusions, with larger in-plane lattice spacing, reach the surface offers a possible origin for the incommensurate RHEED patterns noted earlier. The position of the RHEED spots (10% less than MnSb) corresponds to an in-plane lattice spacing of 4.541 Å, and therefore an alloy composition of approximately $In_{0.9}Ga_{0.1}Sb$. GaSb has previously been found to form at the n-MnSb/GaAs interface during growth of MnSb at similar growth settings [118]. This was attributed to Sb flux reacting with Ga droplets formed on the surface during sputtering, but this cannot explain the large amounts of segregation seen for these MnSb/InGaAs samples. Therefore this segregation is attributed to In and Ga diffusion mechanisms from the substrate bulk. Also MnAs was formed within the InGaAs substrate, similar to the $J_{Sb/Mn} = 3.5$ samples but in smaller amounts.

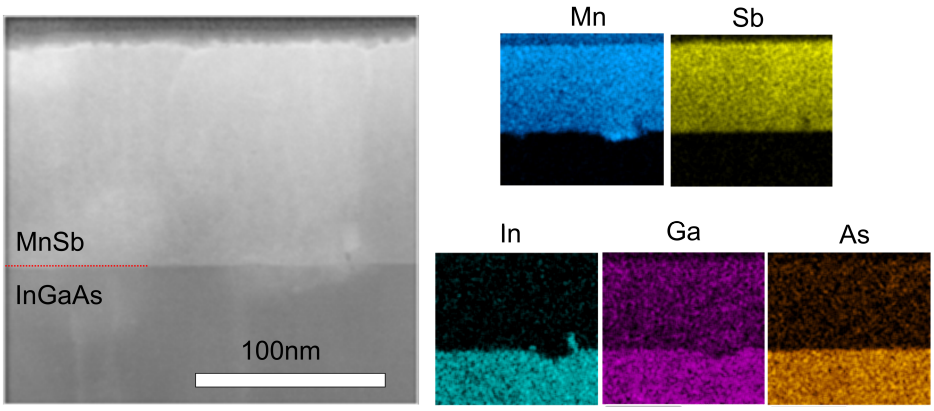

Figure 4.15: (left) TEM image of full layer structure for sample grown using $J_{Sb/Mn} = 6.5$ and $T_{sub} = 350°C$ (right) EDX analysis of layers shown in the TEM image. Composition of layers show only a very small amount of intermixing between InGaAs substrate and MnSb overlayer at the interface.

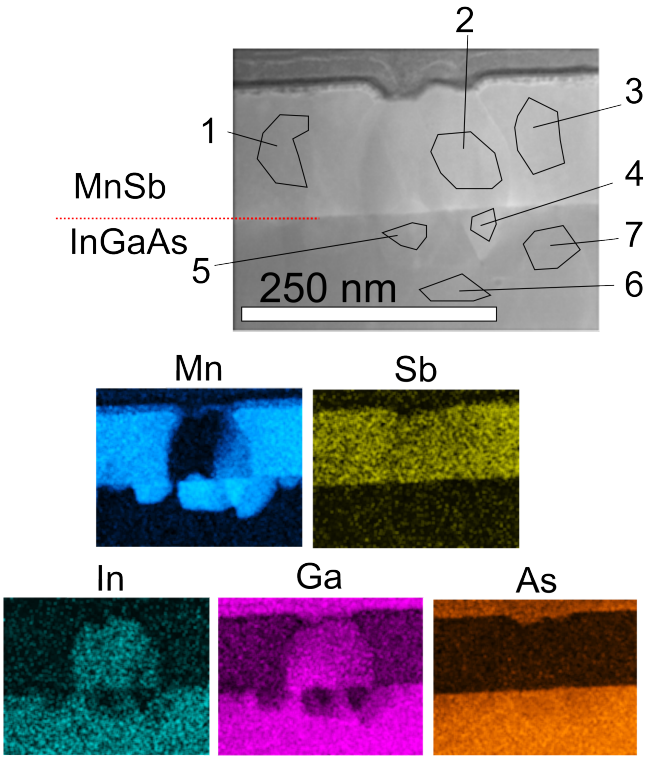

Figure 4.16: (Left) TEM image of sample grown using $J_{Sb/Mn} = 6.5$ and $T_{sub} = 415°C$, with numbered areas corresponding to compositional analysis detailed in table 4.1 (Right) EDX analysis of layers shown in the TEM image.

Area	Mn%	Ga%	In%		Sb%	As%
1	82	18	0		91	9
2	12	46	42		89	11
3	83	17	0		91	9
4	87	11	2		2	98
5	80	15	6		3	97
6	0	56	44		0	100
7	4	53	43		0	100

Table 4.1: Compositional analysis for the areas labelled in figure 4.16.

Figure 4.17 shows selected area diffraction patterns (SADPs) taken along the $<\bar{1}10>$ InGaAs zone axis, from two samples grown using $J_{Sb/Mn} = 6.5$. Figures 4.17a and 4.17b show the characteristic atomic column patterns of n-MnSb(0001) and cubic InGaAs(111), confirming the epitaxial relationship between the two materials.

However the SADP in figure 4.17b shows a slight tilt in the diffraction spots for both n-MnSb and InGaAs sections, which indicates that T_{sub} =415°C produces a worse epitaxial relation at the MnSb/InGaAs interface. Figure 4.17c shows an overlay of the n-MnSb and InGaAs(111) crystal structures along the <110> and <$\bar{1}$10> zone axes respectively. However the samples were not completely uniform, with some areas from the sample grown using T_{sub} = 350°C showing mixed SADPs (figure 4.17d).

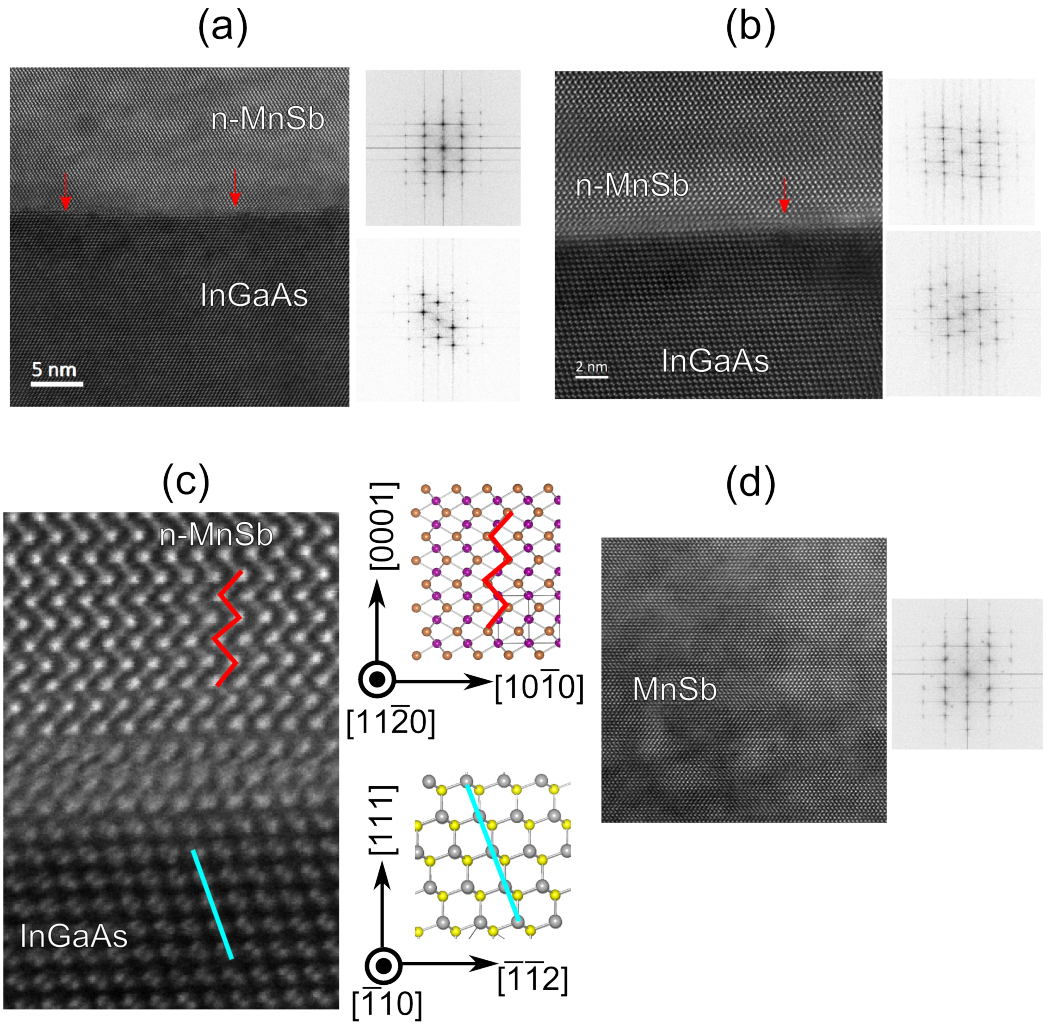

Figure 4.17: TEM images and SADPs of MnSb/InGaAs interface for samples grown at $J_{Sb/Mn}$=6.5, with (a)T_{sub}=350°C, and (b)T_{sub}=415°C. Red arrows indicate steps observed at the MnSb/InGaAs interface. (c) overlay of crystal structure showing <110> n-MnSb zone axis, and <$\bar{1}$10> InGaAs zone axis. (d) Area within sample grown at $J_{Sb/Mn}$ = 6.5 and T_{sub}=350°C showing mixed SADP patterns.

TEM from samples grown using $J_{Sb/Mn}$ = 9.5 (figures 4.18 and 4.20) show a fairly sharp and abrupt interface, with no signs of Ga and In segregation into the overlayer. However, large inclusions of Sb can be seen formed in the MnSb layers, which are more pronounced in the layer grown at the low temperature 350°C (figure 4.18). This is understandable as previously the sublimation of Sb has been found to increase by an order of magnitude over this temperature range, and for MnSb

depositon on GaAs(111)B a substrate temperature of at least 400°C is required for growth of stoichiometric material [125]. The existence of these Sb inclusions suggest that the surface preparation used for all samples did not lead to a significant amount of Ga or In droplets, and that segregation observed is due to diffusion processes. TEM of the MnSb sections (figures 4.19 and 4.21) show that for the $J_{Sb/Mn} = 9.5$ samples there is an uneven composition in the MnSb sections for both substrate temperatures.

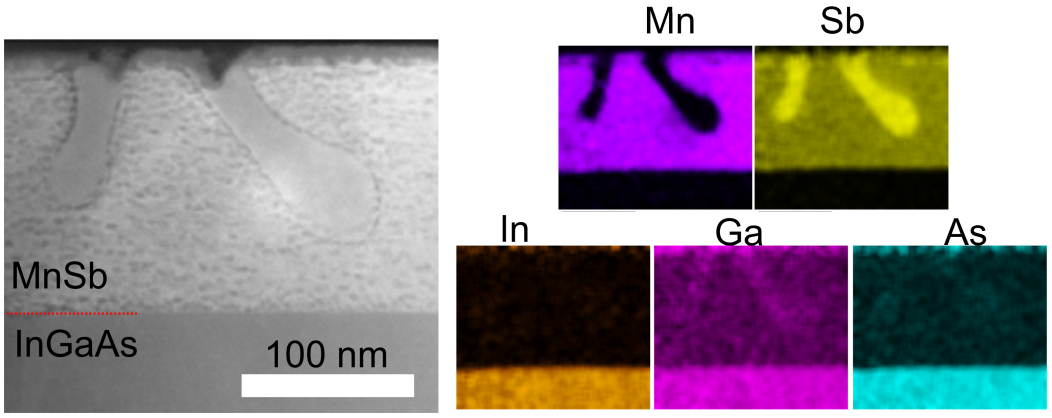

Figure 4.18: (left) TEM image of full layer structure for sample grown using $J_{Sb/Mn} = 9.5$ and $T_{sub} = 350$°C (right) EDX analysis of layers shown in TEM image. A sharp interface is present between the MnSb and InGaAs layers, but large inclusions of Sb can be seen within the MnSb layer.

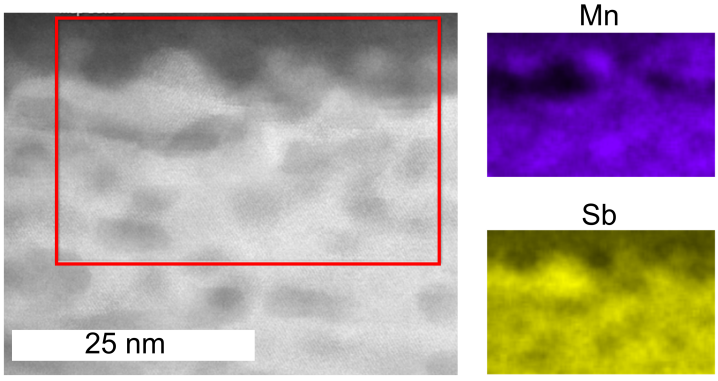

Figure 4.19: (left) TEM image from top 30 nm of MnSb layer for sample grown using $J_{Sb/Mn} = 9.5$ and $T_{sub} = 350$°C (right) EDX analysis of red boxed area showing compositional variations present within film.

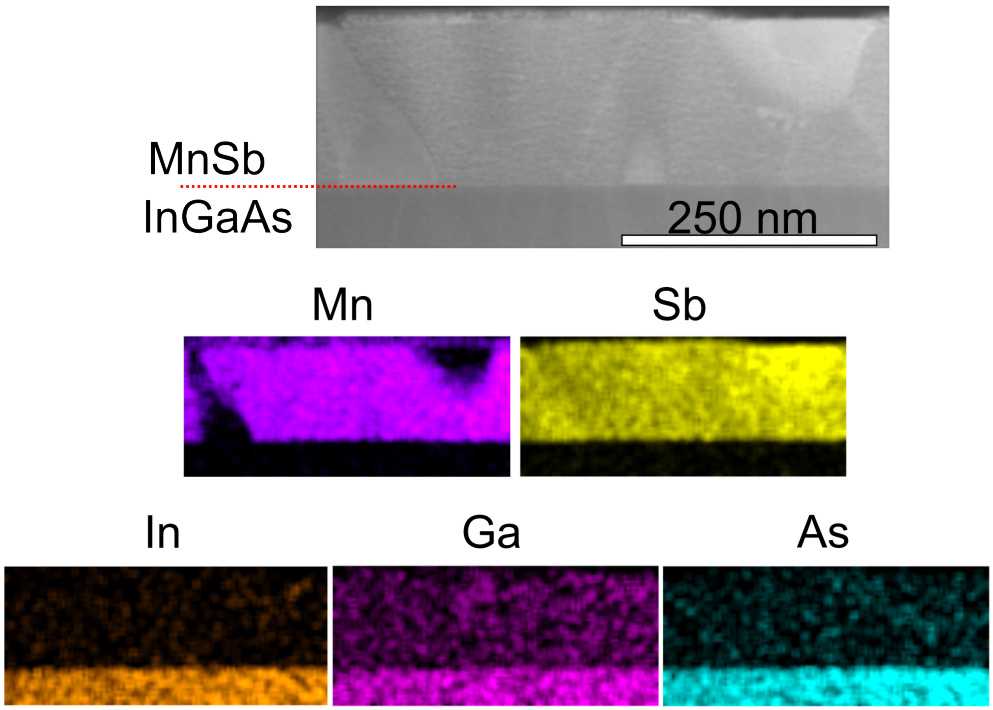

Figure 4.20: (upper) TEM image of full layer structure for sample grown using $J_{Sb/Mn} = 9.5$ and $T_{sub} = 415°C$ (lower) EDX analysis of layers shown in TEM image. A sharp interface is present between the MnSb and InGaAs layers, but inclusions of Sb can be seen within the MnSb layer.

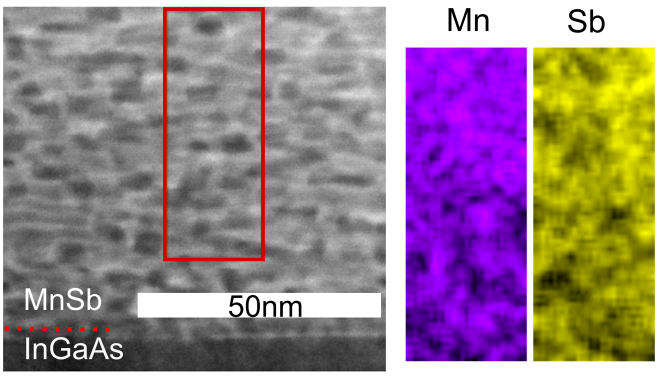

Figure 4.21: (left) TEM image from centre of MnSb layer for sample grown using $J_{Sb/Mn} = 9.5$ and $T_{sub} = 415°C$ (right) EDX analysis of red boxed area showing compositional variations present within film.

Thicknesses calculated from TEM images are summarised in table 4.2. The

lower thickness values for $J_{Sb/Mn}$=3.5 agree with the MnSb growth being Sb-limited, so excess Mn leads to the large amount of intermixing shown in TEM. When there is a large amount of intermixing, incident adatoms will diffuse into the substrate rather than building up the overlayer, leading to a thinner overall film. The larger thicknesses seen for $J_{Sb/Mn}$=9.5 agree with the MnSb growth being Mn-limited, leading to the Sb inclusions seen in TEM. This means that an increase in Sb flux leads to an overall increase in layer thickness.

T_{sub}(°C)	$J_{Sb/Mn}$	Thickness (nm)
350	3.5	81
350	6.5	115
350	9.5	149
415	3.5	96
415	6.5	123
415	9.5	169

Table 4.2: MnSb layer thicknesses calculated from TEM images. Errors on all thicknesses are ± 5 nm.

Two-stage Samples

TEM from the two-stage growth samples is in the process of being obtained, but it is not currently available at time of writing.

4.3.4 XRD

Single-stage Samples

Out-of-plane $\theta - 2\theta$ XRD data collected from all single-stage samples is shown in figure 4.22. As expected, strong signals from the substrate materials GaAs(111) and InGaAs(111) are present in all scans. Strong peaks from n-MnSb(0002) are present in all samples grown using $J_{Sb/Mn}$ ≥6.5. For $J_{Sb/Mn}$=3.5 a weaker n-MnSb(0002) is present only for a substrate temperature T_{sub}=350°C. Fitting of the strong n-MnSb(0002) signals found that samples grown using $J_{Sb/Mn}$ = 9.5 could be fitted

with a single peak, but a minimum of two peak was required for a suitable fit to scans from all samples grown at $J_{Sb/Mn}$=6.5 (figure 4.23). This indicates that there are multiple strain states for n-MnSb present for the samples grown at $J_{Sb/Mn} = 6.5$. Note that for T_{sub}=350°C this second strain state appears at higher Q_z , whereas for T_{sub}>350°C it appears at lower Q_z. This indicates that there are two different mechanisms driving the formation of multiple strain states in the MnSb.

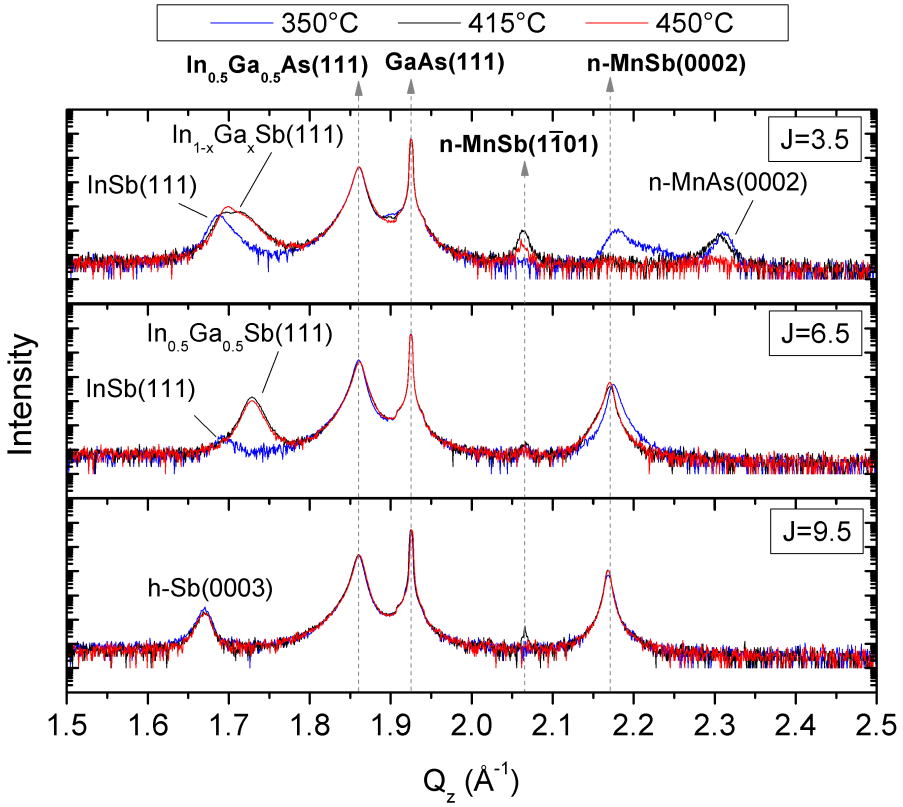

Figure 4.22: Symmetric X-ray diffraction data for all single-stage MnSb samples. Each panel shows data at different T_{sub} values superimposed for a single value of $J_{Sb/Mn}$. Major peaks found in at least one scan from each $J_{Sb/Mn}$ value are identified by the dotted arrows to bold text at the top of the figure. Other features are labelled individually.

Samples grown with $J_{Sb/Mn} = 3.5$ and 6.5 show peaks at low Q_z values close to Q_z=1.674 Å^{-1} where a peak from c-MnSb(111) would appear. However, due to the significant segregation or intermixing evidenced in the TEM, these peaks are

attributed to various combinations of signals from InSb(111) and $In_{(1-x)}Ga_xSb(111)$.

For samples grown with $J_{Sb/Mn} = 3.5$ a growth temperature of $T_{sub} \geq 415°C$ causes the appearance of a peak around Q_z=1.7 Å^{-1} (figure 4.24). From comparison to TEM data, this can be attributed to $In_xGa_{1-x}Sb$, with In content ranging between 65-80%. This indicates that Ga segregation has been promoted causing the formation of $In_xGa_{1-x}Sb$ rather than InSb. There are also signals near Q_z=2.3 Å^{-1} for $T_{sub}<450°$. From comparison with TEM data, there are two potential identities for the signals: MnAs(0002) expected at Q_z= 2.200 Å^{-1}, or cubic-In(111) expected at Q_z =2.269 Å^{-1}. Despite having the larger difference to the observed signal position, MnAs(0002) is the more probable cause due to TEM only showing In inclusions within the substrate for $T_{sub} = 350°C$. Also it is highly unlikely that any In segregated into the overlayer would fail to react with Sb, even at $J_{Sb/Mn} = 3.5$.

A similar trend of Ga segregation with substrate temperature can be seen at $J_{Sb/Mn} = 6.5$, but the change is from a single InSb(111) peak to a single $In_xGa_{1-x}Sb$ (111) peak. This indicates that Ga segregation occurs a lot more readily at this flux ratio, and therefore lone InSb inclusions are less likely to form. The observation of the single $In_xGa_{1-x}Sb(111)$ peaks for $T_{sub} = 350°C$ coincide with the existence of a second strain state at lower Q_z. This shows that the second weaker strain state in these samples is most likely due to sections of n-MnSb close to the $In_xGa_{1-x}Sb(111)$ areas.

For the highest Sb flux with $J_{Sb/Mn} = 9.5$ there is an individual signal at Q_z=1.67 Å^{-1} for all growth temperatures, which is attributed to h-Sb due to Sb inclusions imaged in TEM. This shows that higher Sb fluxes decrease the amount of segregation at the interface, due to the formation of Sb inclusions preventing the amount of free Sb available for formation of $In_xGa_{1-x}Sb$.

Out-of-plane strain values for the n-MnSb layers are shown in figure 4.25a, which were calculated using the n-MnSb(0002) peak positions and have FWHM values shown in 4.25b. The lowest out-of-plane strain values were observed in samples

grown using $J_{Sb/Mn} = 6.5$. Growth substrate temperatures 350°C and 415°C showed slight compressive out-of-plane strains for the n-MnSb, as expected from an epitaxial relation to the larger in-plane lattice parameter of the $In_0.5Ga_0.5As(111)$ substrate. The lowest FWHM values were found in the samples grown using $J_{Sb/Mn} = 9.5$, which can be linked to the lack of In and Ga intermixing observed for samples grown using $J_{Sb/Mn} = 6.5$.

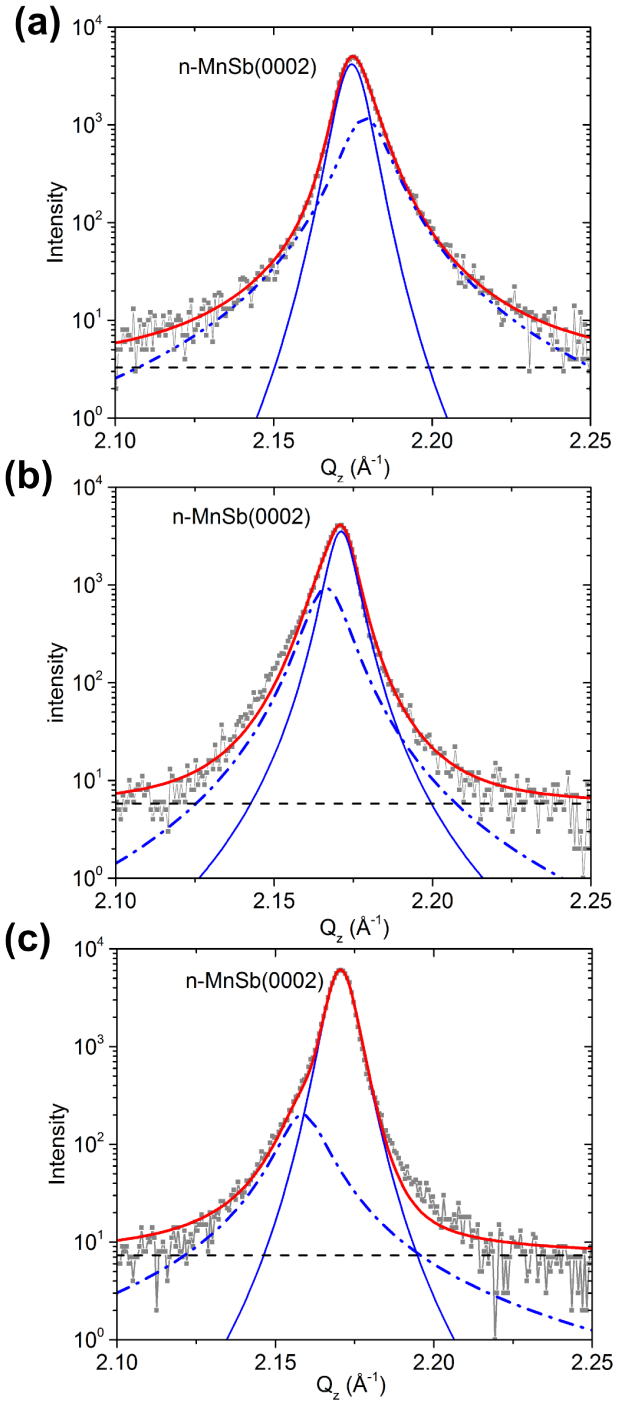

Figure 4.23: Out-of-plane symmetric XRD data near Q_z=2.20 Å^{-1}, for samples grown using $J_{Sb/Mn} = 6.5$ and T_{sub}= (a) 350°C, (b) 415°C, (c) 450°C. In all cases XRD peaks must be fitted with two components. Red lines show the overall fit profile, blue lines show the contributing peaks, and dashed grey lines show the background function used in fit.

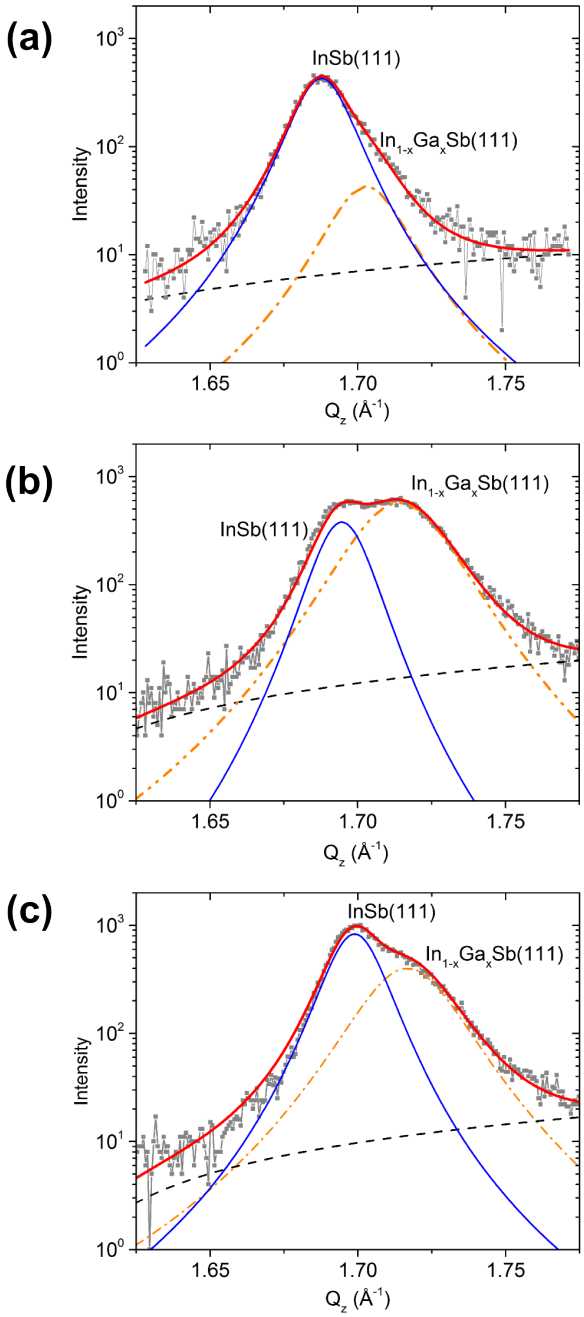

Figure 4.24: Out-of-plane symmetric XRD data near Q_z=1.70 Å^{-1} for single-stage samples grown using $J_{Sb/Mn} = 3.5$ and T_{sub}= (a) 350°C, (b) 415°C, (c) 450°C. In all cases XRD peaks must be fitted with two components. Red lines show the overall fits, blue lines show the peaks attributed to InSb, Orange lines show the peaks attributed to $In_{1-x}Ga_xSb$, and grey dashed lines show the background function used in the fit.

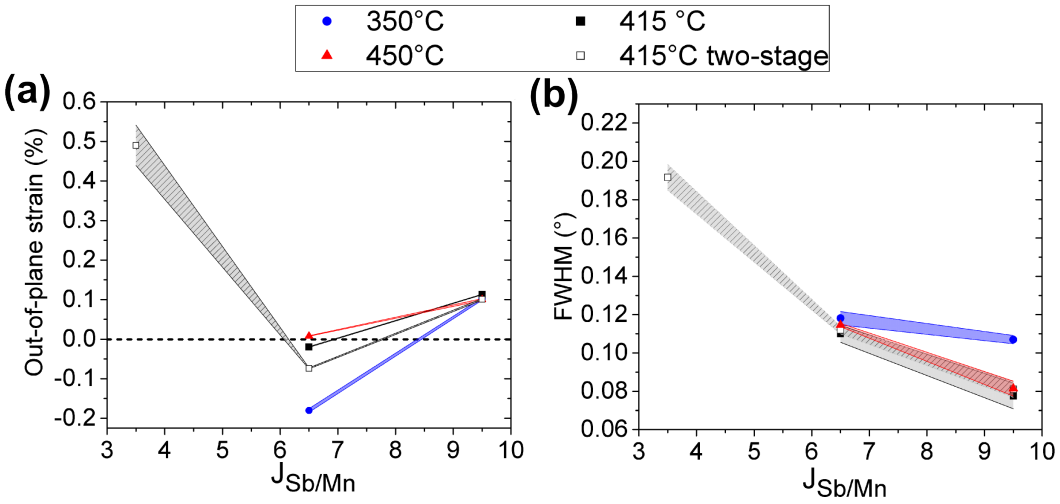

Figure 4.25: (a) Out-of-plane strain for the n-MnSb layer relative to the bulk n-MnSb lattice 5.789 Å, calculated from positions of the n-MnSb(0002) peaks. (b) FWHM values for the n-MnSb(0002) peaks

Two-stage samples

XRD data collected from two-stage growth samples (figure 4.26) shows very similar features to the single-stage samples. All two-stage scans show strong InGaAs(111) and GaAs(111) substrate signals, and in contrast to the single-stage samples n-MnSb(0002) signals were present at all $J_{Sb/Mn}$ values. This improvement in the n-MnSb for $J_{Sb/Mn}$=3.5 when using two-stage growth method is most likely due to the effect of annealing the ultra-thin film during the heating step between deposition stages. The growth rate of 2 nm.min^{-1} means that the first deposition of 60 seconds only gives a 2 nm film which, when compared to lengthscales of diffusion observed in TEM, is not enough to successfully prevent interactions between the interface region and the rest of the film.

A high flux ratio value of $J_{Sb/Mn}$ = 9.5 gave a signal near Q$_z$=1.67 Å^{-1} which could only be fitted adequately with a minimum of two peaks (figure 4.28). These relate to two different strain states which could be both of Sb, or possibly a combination of Sb and strained c-MnSb. However two strain states of Sb appears more likely due to the large amount of Sb inclusions observed in TEM from the

single-stage samples grown at $J_{Sb/Mn} = 9.5$. The lower flux ratios $J_{Sb/Mn} = 3.5$ and 6.5 both gave a single peak near Q_z=1.72 Å^{-1}, which on comparison to the single-stage sample data was attributed to $In_{1-x}Ga_xSb(111)$. The lack of InSb(111) signals for the two-stage growth samples show that whilst Sb diffusion into the substrate is occurring, it is to a lesser degree when compared to the single-stage growth samples.

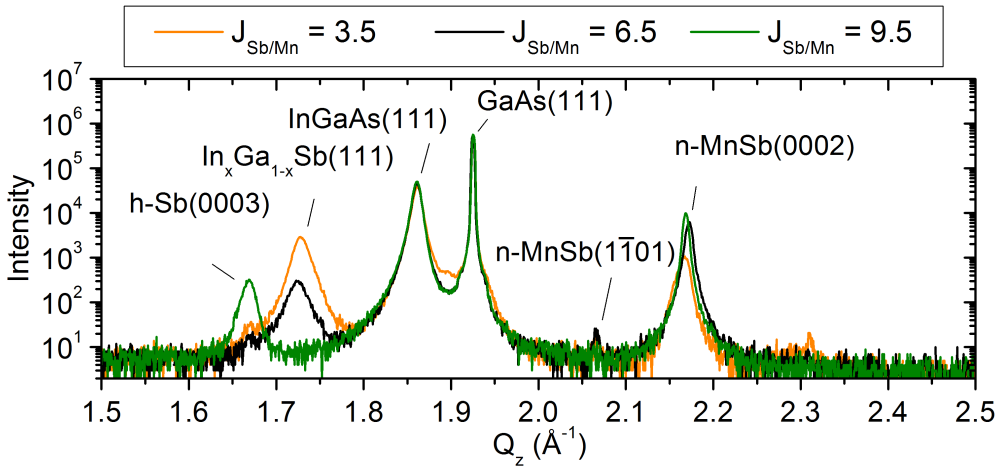

Figure 4.26: Out-of-plane symmetric X-ray diffraction data for all two-stage growth samples. Data at different T_{sub} values have been superimposed to aid comparison.

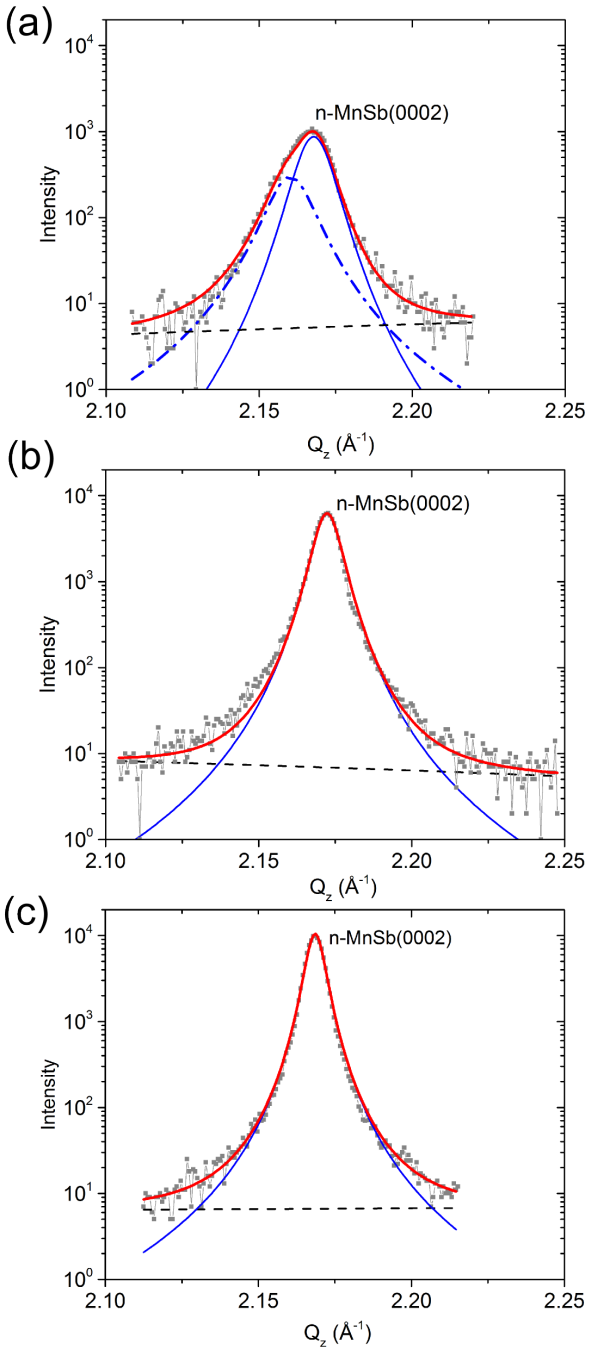

Figure 4.27: Out-of-plane symmetric XRD data near Q_z=1.70 Å^{-1} for two-stage MnSb/InGaAs(111)A samples grown using T_{sub}=415°C and $J_{Sb/Mn}$ = (a) 3.5, (b) 6.5 and (c) 9.5. Only $J_{Sb/Mn} = 3.5$ required multiple fitting components. Red lines show the overall fit profile, blue lines show the contributing peaks, and dashed grey lines show the background function used in fit.

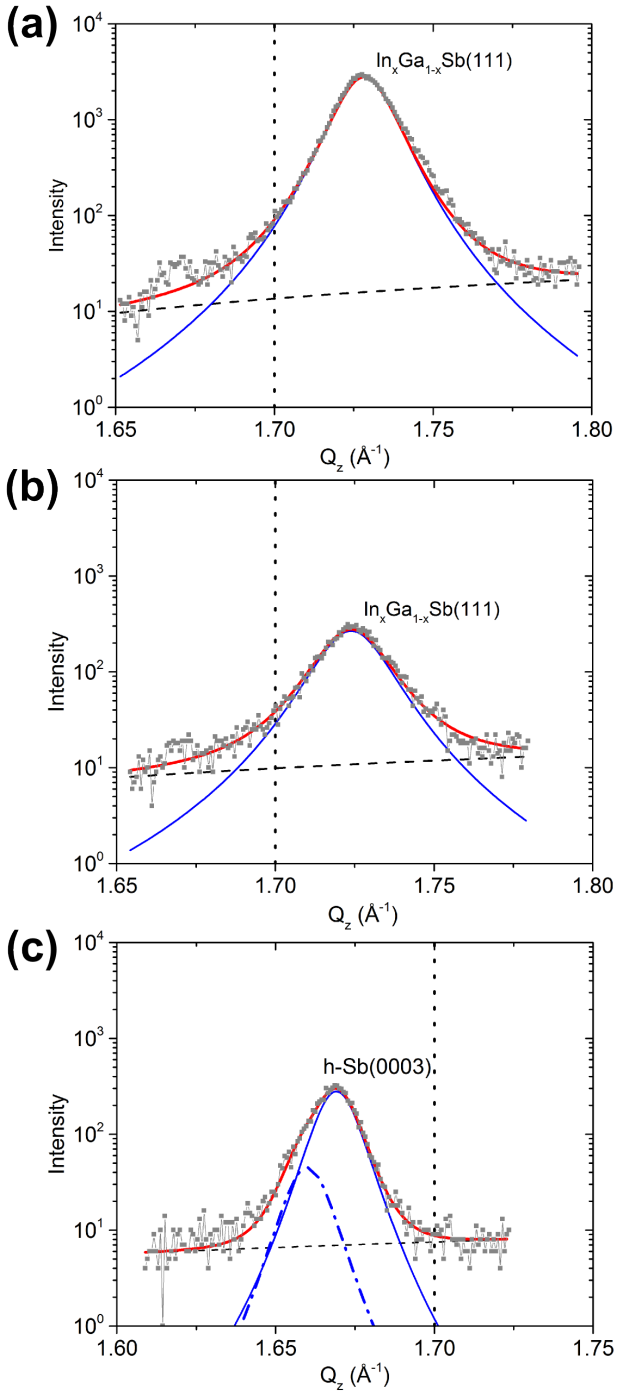

Figure 4.28: Out-of-plane symmetric XRD data near Q_z=1.70 Å^{-1} for two-stage samples grown using T_{sub}=415°C and $J_{Sb/Mn}$ = (a) 3.5, (b) 6.5 and (c) 9.5. Only $J_{Sb/Mn}$ = 9.5 required multiple fitting components. Red lines show the overall fit profile, blue lines show the contributing peaks, and dashed grey lines show the background function used in fit. The vertical dotted lines at Q$_z$=1.70 are to aid comparison between plots.

4.3.5 Magnetometry

Single-stage samples

In-plane VSM data was collected from three representative single-stage samples to compare the magnetic properties of MnSb layers grown under different conditions. There was a clear difference shown between the $M-H$ loops collected from samples grown with $J_{Sb/Mn} = 6.5$ and the $M-H$ loop collected from the sample grown using $J_{Sb/Mn} = 3.5$ and T_{sub}= 415°C (figure 4.29). The $M-H$ loops for $J_{Sb/Mn} = 6.5$ were adjusted to account for a small trapped field (∼50 Oe) in the VSM magnet, and the negative gradient seen at the ends of the scans is due to the diamagnetic response of the InGaAs substrate, as well as contributions from the sample container. Saturation magnetisation (M_S), remnant magnetisation (M_R) and coercive field (H_C) values taken from the $M-H$ loops are shown in table 4.3. The two samples grown at $J_{Sb/Mn} = 6.5$ show a much smaller H_C and a much larger M_S. The magnetisation will be affected by both the size and film thickness of the samples, however such a large difference can only be explained by an improved magnetic quality of the layer, which correlates well with the crystallinity and improved surface morphology detailed in the previous sections of this chapter.

There is also a noticeable difference between the two $J_{Sb/Mn} = 6.5$ samples, with the sample grown at T_{sub}=350°C giving the smallest coercive field (103 Oe) and the largest saturation magnetisation (0.001245 emu)(figure 4.30). These improved values for $J_{Sb/Mn} = 6.5$ $T_{sub} = 350$°C agree with the TEM findings which show it has the lowest level of intermixing in the MnSb layer. The sample grown at $J_{Sb/Mn} = 6.5$ and $T_{sub} = 350$°C also exhibits a stepped shape in its loop (figure 4.30) which is present on both the up and down sweeps of the scan. These steps are caused by the magnetic switching of the differently sized hexagonal domains seen in AFM and SEM.

$J_{Sb/Mn}$	T_{sub}	MnSb volume (cm^3)	M_S (emu)	M_R (emu)	H_C (Oe)
6.5	350°C	1.38 E-6	1.245 E-3	1.098 E-3	103
6.5	415°C	1.85 E-6	1.075 E-3	0.905 E-3	211
3.5	415°C	1.92 E-6	0.486 E-3	0.312 E-3	683

Table 4.3: Saturation magnetisation (M_S), remnant magnetisation (M_R) and coercive field (H_C) values for M-H loops shown in figure 4.29. Volumes were calculated using thicknesses obtained from TEM images.

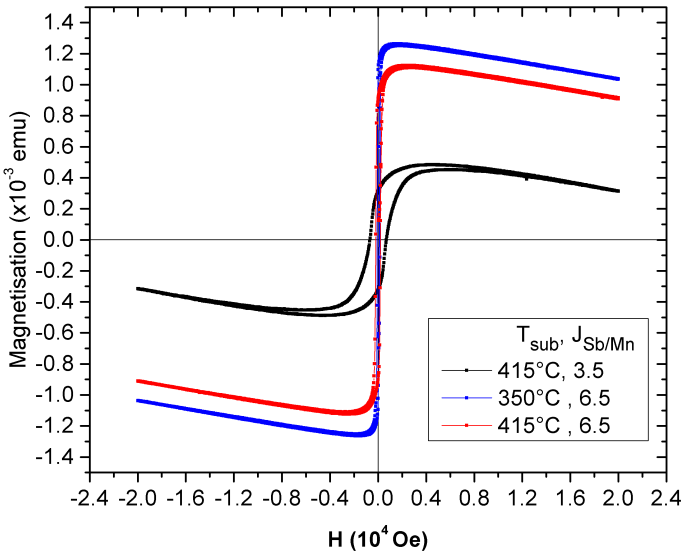

Figure 4.29: M-H measurements obtained using a VSM at 10 K for MnSb/InGaAs(111)A grown using favourable ($J_{Sb/Mn}$=6.5) and non-favourable ($J_{Sb/Mn}$=3.5) growth conditions, with the magnetic field aligned in-plane.

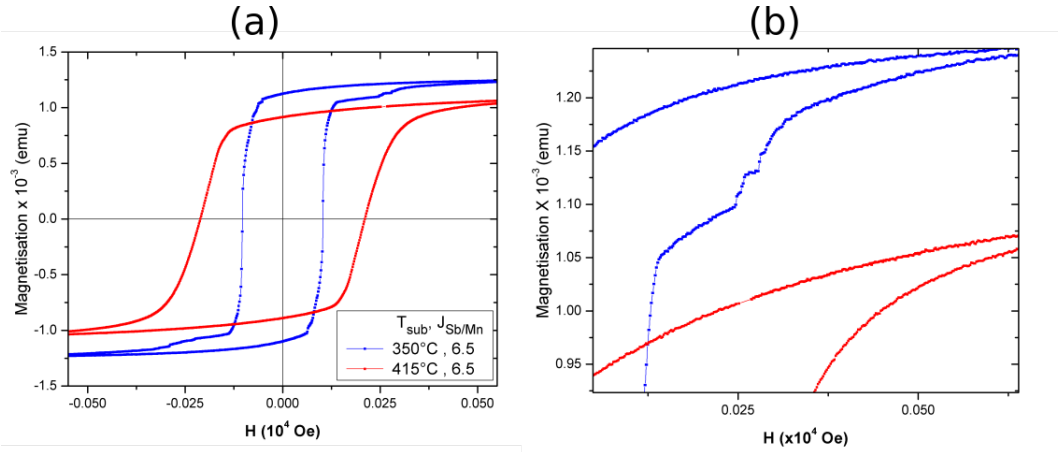

Figure 4.30: (a) A close-up comparison of M-H measurements for samples grown using $J_{Sb/Mn}$=6.5, obtained using a VSM at 10 K with the magnetic field aligned in-plane. (b) Zoom in of top section of loop revealing stepped structure for the sample grown using T_{sub} = 350°C

4.4 Summary

Results presented in the previous sections of this chapter show that for MnSb growth on $In_{1-x}Ga_xAs$(111)A, both $J_{Sb/Mn}$ and T_{sub} play an important role in the layer growth. Sb-limited growth occurs at $J_{Sb/Mn}$=3.5, with excess Mn diffusing into the substrate as it will not re-evaporate within the substrate temperature range used. Growth is dominated with Sb inclusions for $J_{Sb/Mn}$=9.5. For growth which does not have an excess of Sb ($J_{Sb/Mn} \leq 6.5$), an increase in substrate temperature leads to an increase in out-diffusion of In and Ga into the overlayer. A flux ratio of $J_{Sb/Mn}$ = 6.5 gave the optimum layer growth. This was shown by $J_{Sb/Mn}$ = 6.5 samples having the lowest amount of surface crystallites, lowest RMS roughness, and improved magnetic properties. There was found to be a differing preference of substrate temperature for either a smooth surface or a sharp interface. A lower substrate temperature of 350°C was found to produce the best interface between overlayer and substrate, containing the least amount of intermixing. However these settings also produced nanosized hexagonal structures protruding from the surface.

The higher substrate temperature of 415°C produced the smoothest surfaces with the lowest RMS roughness values, but also a large amount of intermixing at the interface. This suggests that the optimum growth temperature, which would produce samples with both a smooth surface and an abrupt interface, lies somewhere between these two values.

The use of a two-stage growth process led to higher quality n-MnSb layer, evidenced by n-MnSb(0002) signals being present for all sample including $J_{Sb/Mn}$=3.5. However the diffusion lengths observed suggest that a longer initial stage of deposition is required to decrease the effect of interface structure on the growing layer. Surface crystallites were found to form during growth, which increased in size at higher $J_{Sb/Mn}$ values. These crystallites could be linked to nucleation at surface threading dislocations which originate in the InGaAs substrate. The size increase at higher $J_{Sb/Mn}$ values suggests that they are either mainly $MnSb_2$ or h-Sb.

Chapter 5

MnSb/GaAs(111)A Vs MnSb/GaAs(111)B

5.1 Introduction

An important factor to consider when growing thin films by MBE, other than the substrate temperature and flux ratio, is the substrate surface chemistry. This plays an important role in determining the structural and electronic properties of the epitaxial layer [72]. The polar (111) surfaces of III-V semiconductors demonstrate differences in both electronic [134] and structural properties [65]. Nishida *et al.* found that for Ga-V substrates the (111)A surfaces undergo a relaxation towards the bulk, whereas (111)B surfaces expand away from the bulk. These differences mean that the orientation of (111) substrates can affect the growth processes occurring during MBE thin film deposition [70]. TEM studies of the growth of zincblende (zb) GaN onto GaAs(111) substrates using organometallic vapour phase epitaxy have shown that samples grown on GaAs(111)A displayed an improved quality of both interface structure and crystallinity of the zb-GaN layer [135][136]. The choice of substrate termination has also been found to affect the properties of sulfur passivation of GaAs(111) surfaces [137] [138]. Murphy *et al.* found that a full surface layer of

sulfur forms on GaAs(111)A surfaces, however a mixed As and sulfur termination is formed on GaAs(111)B surfaces.

There have been a substantial number of MBE studies of MnSb deposition onto GaAs(111)B [139][58][140][141] [142] [143] [144], but there have been relatively few for MBE growth of MnSb on GaAs(111)A [118]. Lawniczak-Jablonska *et al.* [145] investigated the formation of MnSb inclusions within a GaSb matrix, deposited on a GaAs(111)A substrates. Hot wall epitaxy studies of MnSb films grown on GaAs(111)A were conducted by Tatsuoka *et al.* [146], and it was concluded from MnSb(0002) XRD FWHM values that layers grown on GaAs(111)B were of higher crystalline quality. This was explained by the fact that the Ga termination of the (111)A surface meant that bonding to both Mn and Sb could occur, which affects the structural quality of the growing layer. Research comparing the MBE growth of the related half-metallic ferromagnet NiMnSb on both GaAs(111)A and GaAs(111)B surfaces was conducted by Van Roy *et al.* [147], and interestingly it was reported that there were only small differences in growth on the two substrate orientations.

It is clear that the polarity of GaAs(111) substrates can strongly affect the outcome of thin film growth, but despite this fact there has not yet been a similar polarity comparison study for the growth of MnSb via MBE onto GaAs(111) surfaces. Therefore a polarity comparison study of MnSb films grown onto GaAs(111)A and GaAs(111)B surfaces was carried out. Results will be presented as follows: experimental details of sample growth and characterisation will be given in sec. 5.2, experimental data including RHEED, XPS, SXRD and AFM is presented in sec. 5.3, and a summary is then given in sec. 5.4.

5.2 Experimental Details

To investigate the effect of surface polarity on the epitaxial growth of MnSb on GaAs(111) substrates, an SXRD experiment was conducted at the I07 beamline

at DLS. Prior to the experiment at Diamond (UK), some out-of-plane symmetric XRD data was also collected from a few samples on the XMaS beamline at the ESRF (France). Sample growth conditions used at Warwick, and sample preparation performed at I07, are summarised in table 5.1. The sample set included ultra-thin films of approximately 5 nm, and thick films of approximately 100 nm grown on both GaAs(111)A and GaAs(111)B substrates. For 100 nm thick samples the standard two-stage growth procedure was used, with a 60 second deposition at $T_{sub} = 350°C$ and the remainder of the growth time at $T_{sub} = 415°C$. Due to the very short growth time required for the 5 nm films, only a single deposition stage was used at $T_{sub} = 415°C$. The shortened deposition times meant that the effective flux ratio for the 5 nm films was approximately $J^{Corr}_{Sb/Mn}$=7.5. All CTR data presented in this chapter was taken without a fixed incident angle, therefore the diffraction is from the entire sample.

Sample	**Substrate**	**MnSb film thickness (nm)**	**J corr**	**T_{sub} (°C)**	**Sb cap**	**surface preparation (I07)**	**UB matrix**(I07)
5-A1	GaAs(111)A	5	7.51	415	Yes	In bonded in air, UHV annealed	GaAs(111)
5-A2	GaAs(111)A	5	7.28	410	Yes	-	-
5-B	GaAS(111)B	5	7.50	410	Yes	In bonded in air, UHV annealed	GaAs(111)
100-A	GaAs(111)A	100	6.62	350/415	No	In bonded in air, UHV annealed	GaAs(111)
100-B1	GaAs(111)B	100	6.60	350/415	No	In bonded in air, etched in HCl, UHV annealed	GaAs(111)
100-B2	GaAs(111)B	100	6.70	350/410	Yes	In bonded in argon atmosphere, UHV annealed	n-MnSb(0001)

Table 5.1: List of sample growth and surface preparation techniques for MnSb/GaAs(111)A and MnSb/GaAs(111)B

5.3 Results

5.3.1 RHEED

Prior to deposition clean GaAs(111)A and GaAs(111)B surfaces were prepared using Ar sputtering and annealing. After cleaning RHEED patterns where measured along two principle in-plane directions as shown in figure 5.1. These gave surface reconstructions as expected from previous work [148][101], with the GaAs(111)A substrate showing a (2×2) surface (figure 5.2), and the GaAs(111)B substrate showing a weak Sb background induced triple domain (1×3) surface (figure 5.4).

5 nm samples

For sample 5-A1 the substrate pattern faded within 3 seconds of opening the cell shutters, with (2×) fractionals and transmission spots appearing after 10 seconds. After the full deposition time the RHEED pattern had become a strong and sharp (2×2), without any transmission spots. For sample 5-B the substrate streaks faded within 6 seconds, with blurred integer streaks and weak (2×) fractionals appearing after 10 seconds. There was also a large amount of modulation in the intensity of the streaks, as well as the appearance of transmission spots on the integer streaks. After the full deposition the RHEED pattern was a (2×2) with weak fractional streaks. For single-stage deposition of MnSb at $T_{sub} = 415$°C, the presence of transmission spots shows that both substrates have initially 3D island growth. However the sharper clearer pattern for sample 5-A1 shows that deposition on GaAs(111)A led to layers with higher crystalline quality layers.

100 nm samples

RHEED patterns collected after the first and second stages of deposition onto sample 100-A are shown in figure 5.2. The substrate fractional streaks had disappeared within 3 seconds, and the integer streaks faded after 20 seconds. A (2×) in the

[11$\bar{2}$0] direction formed after 25 seconds, and the pattern remained (2×2) throughout the remainder of the film growth. The RHEED patterns at the end of growth of sample 100-A (figure 5.2c) show a strong and sharp (2×2) pattern, with faint Kikuchi features and multiple Laue zones present. The line profile shown in figure 5.3 is taken along the red line in figure 5.2, and shows the presence of a faint (2×) signal, along with an additional weaker signal. Dotted vertical lines at the approximate centres of the each peak indicate that this additional signal is closer to the positions of the fractional (2×) streaks than the integer positions. This shows that surface has a mixture of reconstructions, including a (2×) and a (3×) with the 1/3 fractional missing. This (3×) is most likely due to a $\sqrt{3} \times \sqrt{3}$-R30° reconstruction, which has previously been seen to co-exist with other reconstructions on MnSb(0001) surfaces [125].

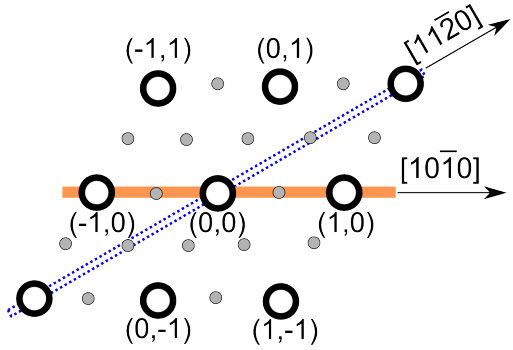

Figure 5.1: RHEED reciprocal space directions for a (2×2) reconstruction on a hexagonal lattice. Integer signals are shown in large open circles, and fractional signals are shown in small filled grey circles.

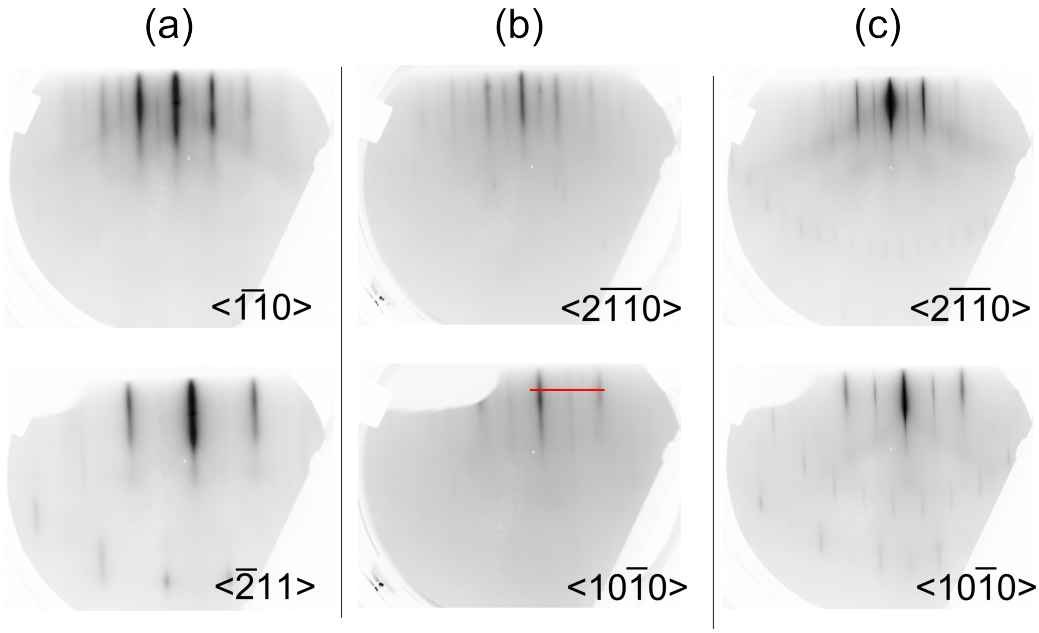

Figure 5.2: RHEED patterns from sample 100A measured along the [2$\bar{1}$10] and [10$\bar{1}$0] direction (a) on clean GaAs(111)A substrate (b) after 1st stage deposition (c) after full deposition. The red line shows the section of image used for the line profile shown in figure 5.3.

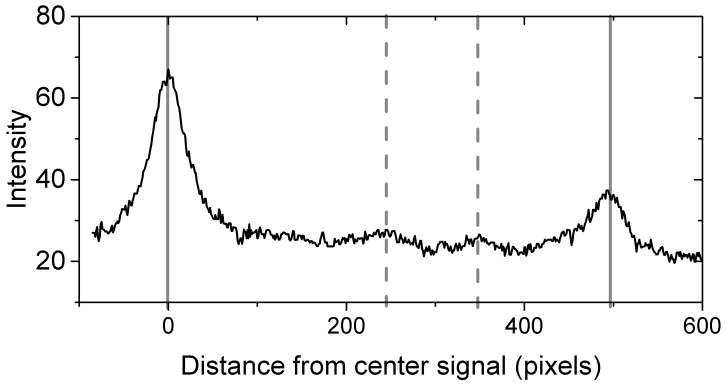

Figure 5.3: Line profile from sample 100-A after 1st stage deposition taken from red line shown in figure 5.2, highlighting the existence of a mixture of reconstructions on the surface. Solid vertical lines indicate positions of integer signals, dotted lines indicate positions of fractional signals.

RHEED patterns collected from sample 100-B1 after the first and second stages of MnSb deposition are shown in figure 5.4. RHEED observations during

growth showed that initially the substrate fractional streaks faded within 7 seconds, with a blurry (1×) pattern emerging after 25 seconds. RHEED patterns collected after the end of the first deposition stage (figure 5.4b) show a faint (2×2) pattern with transmission spot features commensurate with the substrate streaks. RHEED patterns collected after the second growth stage (figure 5.4c) show a sharp 2×2 pattern. This pattern was weaker than the pattern from sample 100-A, and showed weaker integer and fractional order streaks compared to background. This indicates that for (111)B substrates the initial deposition proceeds via 3D island growth. Sample 100-B1 also had less pronounced Laue zones and Kikuchi features when compared with sample 100-A, meaning the n-MnSb film of sample 100-B is of poorer crystalline quality. These observations indicate that, for two-stage growth of MnSb, GaAs(111)A substrate promotes better 2D epitaxial growth of MnSb when compared to the GaAs(111)B substrate.

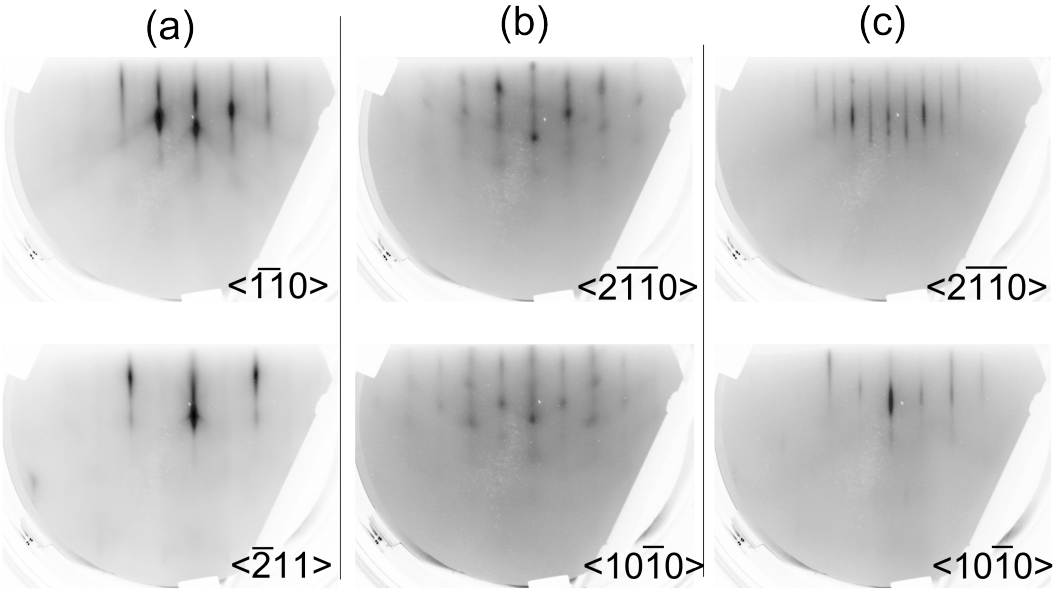

Figure 5.4: RHEED patterns from sample 100-B1 measured along the [2$\bar{1}$10] and [10$\bar{1}$0] direction (a) on clean GaAs(111)A substrate (b) after 1st stage deposition (c) after full deposition.

In-plane lattice parameters calculated from RHEED integer streak spacings are shown in table 5.2. Both substrates show a decrease in lattice constant following the second deposition stage, and the values from 100-B are slightly higher at both growth stages. However all values are within error of each other, so no definitive conclusions can be drawn about in-plane differences due to polarity.

Sample	Deposition stage	a lattice parameter (Å)
100-A	1st	4.13
	2nd	4.12
100-B1	1st	4.17
	2nd	4.12

Table 5.2: In-plane n-MnSb lattice constants for 100 nm samples, calculated from RHEED integer streak spacing. Values were calibrated to integer spacing from GaAs(111) substrate. Errors on all values are ±0.07 Å.

5.3.2 Decapping monitoring

After MnSb film deposition most samples had a protective Sb capping layer deposited prior to removal from the Warwick UHV system, and therefore required a decapping step once inside the UHV chamber at Diamond. Note that Sample 100-B2 was indium bonded to the sample plate in a protective Ar atmosphere, with the aim of minimising the probability that the heating step required for bonding would disrupt the Sb protective cap. Once loaded into the UHV chamber at I07, the capped samples underwent a decapping stage by annealing to T_{sub}= 300-350°C for approximately 30 minutes. Changes to the substrate temperature (monitored with a thermocouple attached to the sample stage), as well as the variations in chamber pressure were measured during the decapping process. Plots of substrate temperature and pressure are shown in figure 5.5. These show very similar behaviour for all decapped samples, with a peak in chamber pressure occurring once the heater had reached approximately 300°C. Note that for sample 5-A1 there was lag in time between when the heater power was increased and when the thermocouple registered the change. This is why the peak in pressure for the 5-A1 sample appears to be oc-

curring at a slightly lower temperature when compared to the other samples. LEED patterns observed after decapping showed blurry hexagonal (1×1) patterns for both 5-A1 and 100-B2. No LEED pattern was obtained from the decapped 5-B sample.

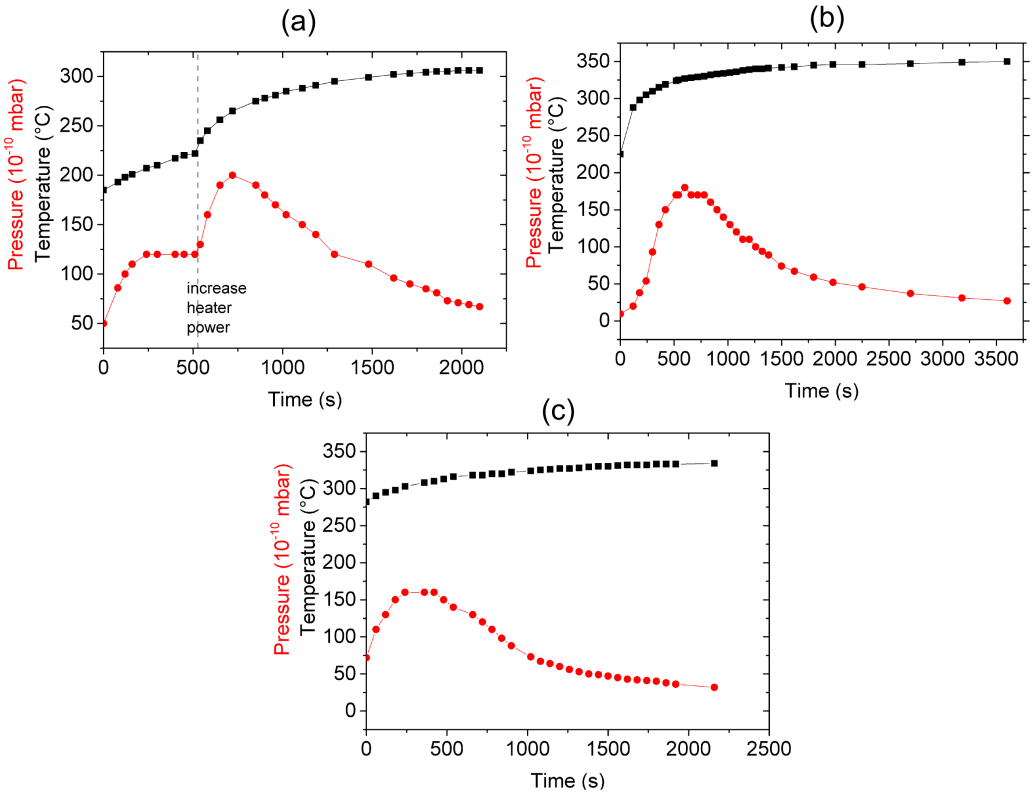

Figure 5.5: Plots of buffer chamber pressure (red circles) and substrate thermocouple temperature (black squares) measured during the Sb decapping process for sample (a) 5-A1, (b) 5-B, and (c) 100-B2.

5.3.3 XPS

To gain more information about the cleanliness of the decapped surfaces, XPS data from the Sb 3d and Mn 2p regions was collected from all decapped samples (figure 5.6). Scans around the Sb 3d peak positions (figures 5.6a,c,e) show the presence of the Sb 3d doublet, as well as an O 1s peak for all samples. However the Sb signal is considerably weaker for sample 5-B, indicating less Sb content at the surface. The scans from samples with strong Sb signal (5-A1 and 100-B2) were fitted with two Sb

doublets, indicating two environments for Sb. The stronger doublets are attributed to Sb-Mn bonding, and the weaker doublets are most likely due to bonding within an intermixed area near the interface.

Scans around the Mn 2p region (figures 5.6 b,d,f) indicate the presence of two Mn doublets for all three samples. The stronger doublets are assigned to Mn-Sb bonding, and the weaker doublets are assigned to Mn-O bonding. These results indicate that the standard Sb capping method was not effective for preserving clean surfaces of the MnSb films, which agree with the LEED patterns observed for the decapped samples. The heating step, used for indium bonding of samples to the holder prior to loading into UHV, is the most likely cause of the surface oxidation. One possible explanation for the 5 nm film on GaAs(111)B being more susceptible to oxidation could be that it possessed a lower quality Sb cap to begin with, meaning that the heating during indium bonding had a larger disruptive effect.

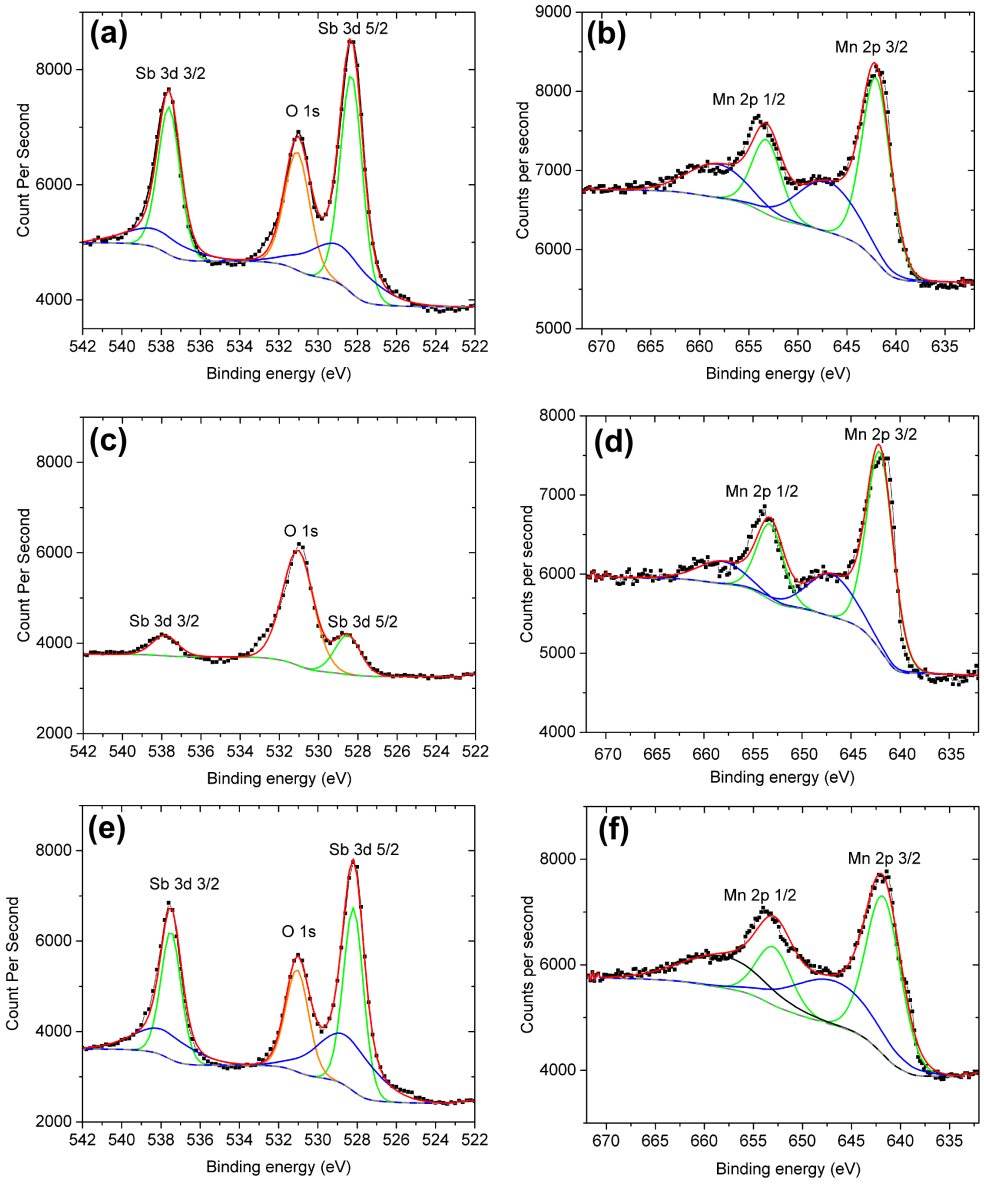

Figure 5.6: XPS data measured after the Sb decapping process for sample (a,b) 5-A1, (c,d) 5-B, and (e,f) 100-B2. Red lines show full fit profile, dashed grey lines show background function, and other colours of solid lines indicate pairs of doublet peaks fitted to either Sb 3d or Mn 2p.

5.3.4 In-plane XRD

Figure 5.7 shows a HK plot of the various in-plane scan directions, along with the expected in-plane signals from GaAs and MnSb. All samples contained signals from GaAs(111), n-MnSb(0002) and GaSb(111). There were also additional types of signals seen in some scans (figure 5.8) and these have been labelled as follows: powder ring style signals are labelled P and extremely diffuse signals are labelled D. Some signals did not match peak positions for any oxides (Sb_2O_3, Sb_2O_5, MnO), or any of the usual materials that arise from segregation or interdiffusion (MnAs, GaSb, h-Sb). These unidentified peaks have been marked with an asterisk (*) in figures 5.9 - 5.12.

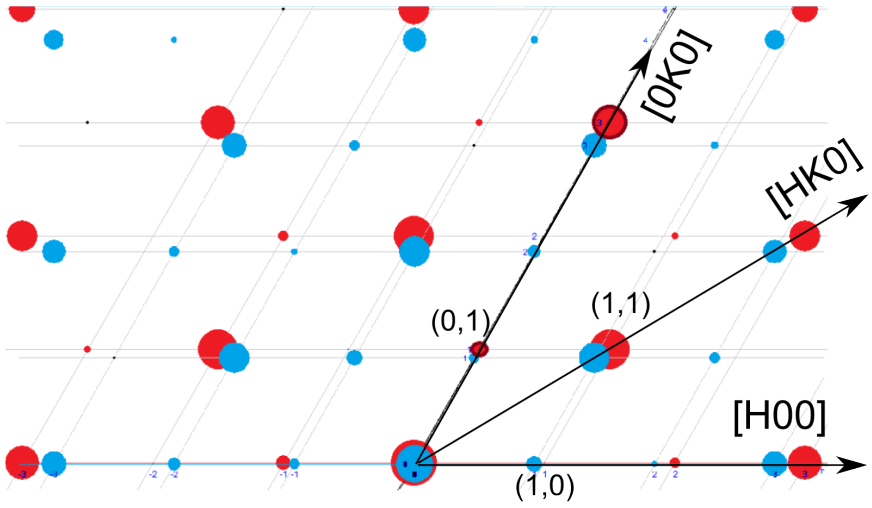

Figure 5.7: HK plot of expected reflections for GaAs(red circles) and MnSb(blue circles). The sizes of circles with the same colour indicate the relative intensities of reflections for that material, but circle sizes do not give any information of intensity comparisons between materials. Arrows indicate the in-plane scan directions.

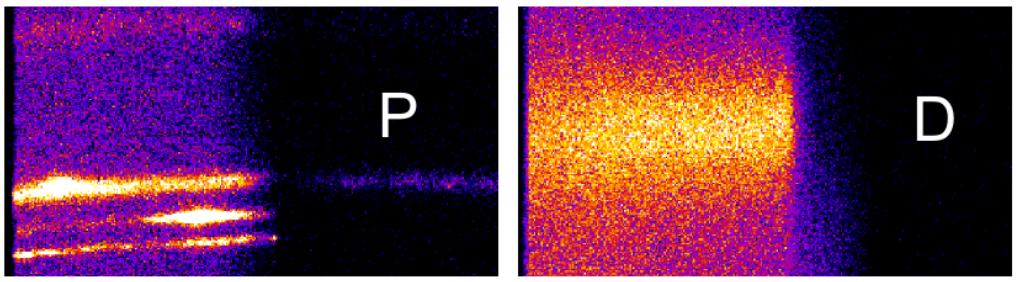

Figure 5.8: Example detector images of additional signals seen for in-plane scans. (a) Powder ring style signal, and (b) very diffuse intensity.

HK scans 5 nm samples

In-plane scans collected from samples 5-A1 and 5-B are shown in figures 5.9 and 5.10. These scans show that sample 5-B shows a stronger in-plane GaSb signal, which demonstrates that GaSb forms more readily during the early stages of MnSb deposition on GaAs(111)B. For these 5nm samples, in-plane strain values relative to bulk lattice constants were calculated from fitting peak positions of the GaSb and n-MnSb signals present at H (or K) = 3. The calculated strain values are shown in table 5.3, and from these it can be seen that the strain of the n-MnSb is lower for the (111)A substrate. The strong signal labelled 1 in scans shown in figure 5.10 could potentially be due to c-MnO(111) (a = 3.178Å) expected at H(or K)= 1.258. However similar signals are not seen in the individual [H00] and [0K0] scans, and the signals in the [HK0] scans are weak and broad, meaning a definitive identification is not possible.

Sample	n-MnSb in-plane strain (%)	GaSb in-plane strain (%)
5-A1	-0.33 ± 0.01	-0.85 ± 0.01
5-B	-0.58 ± 0.02	-0.64 ± 0.01

Table 5.3: In-plane strain values for n-MnSb and GaSb present in the 5nm MnSb samples relative to the bulk lattice parameters MnSb 4.128 Å, and GaSb 4.326 Å

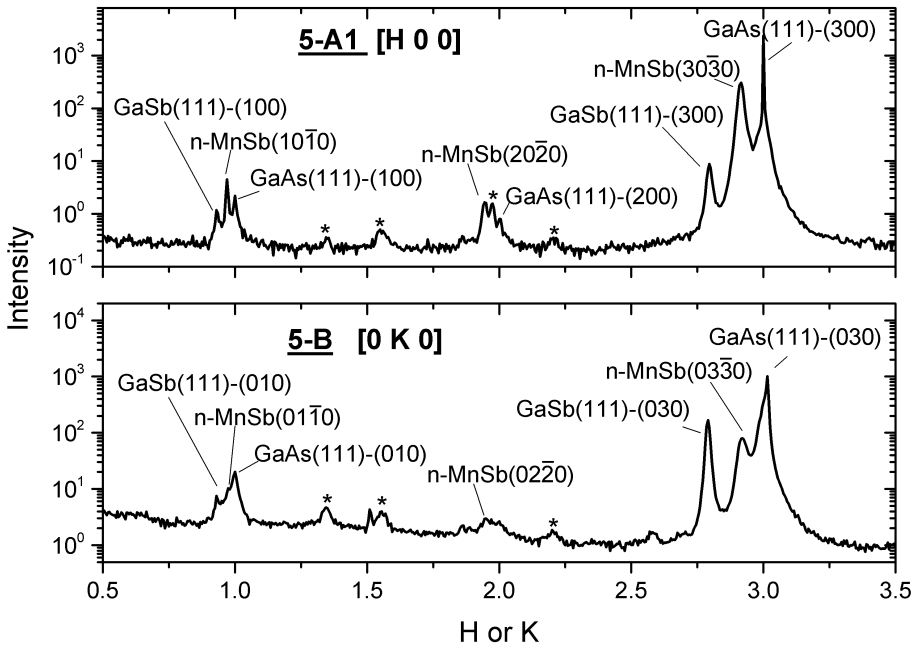

Figure 5.9: In-plane H or K scans measured on sample (*Top*) 5-A1, (*Bottom*) 5-B.

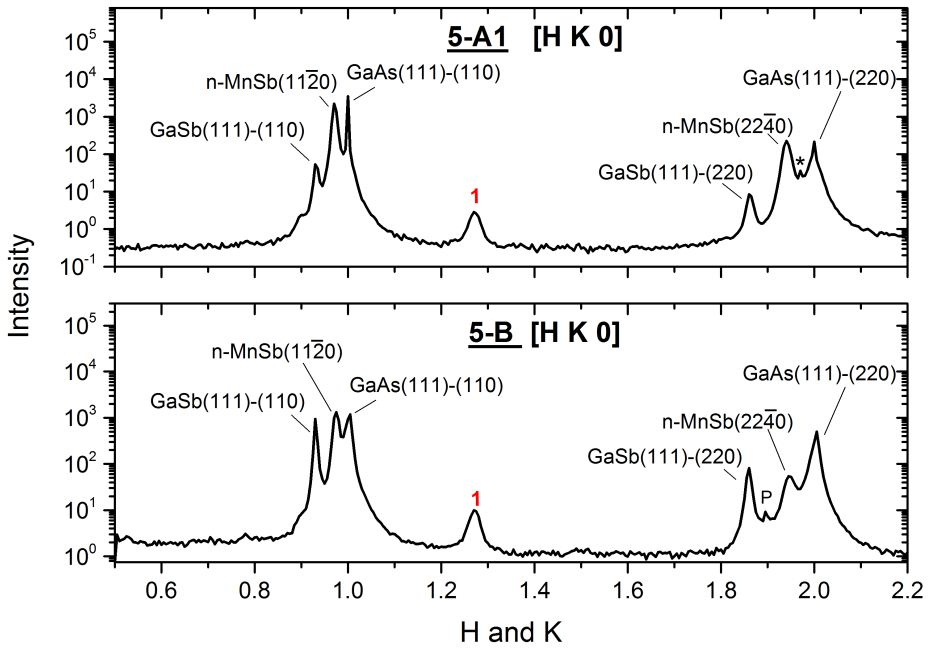

Figure 5.10: In-plane HK scans measured on sample (*Top*) 5-A1, (*Bottom*) 5-B.

HK scans 100 nm samples

In-plane scans for the 100nm samples are shown in figures 5.11 and 5.12. The in-plane strain values calculated from peak fitting for [H00] scans are shown in table 5.4. For both substrates, when considering changes for going from 5 nm to 100 nm films, the n-MnSb in-plane strain has changed from an in-plane contraction to an in-plane expansion. This relaxation is to be expected from previous studies on this highly strained (3.26% mismatch) system [74], which showed that the critical thickness for MnSb films on GaAs(111)B is approximately 3 nm. When compared to the 5 nm films, the 100 nm films on both substrates also show a reduction in compressive strain for the GaSb(111) signals, with sample 100-B1 showing the lowest in-plane strain. This agrees with a growth model where GaSb(111) inclusions form mostly at the interface. In this model the subsequent layers of MnSb, with larger in-plane lattice parameter than the substrate, can counteract the compressive strain that

the GaAs(111) substrate enacts on the GaSb inclusions. A similar reduction in compressive strain would occur for GaSb sections which form within alloyed areas of $GaSb_{1-x}As_x$.

Sample	n-MnSb in-plane strain (%)	GaSb in-plane strain (%)
100-A	0.11±0.01	-0.54 ±0.02
100-B1	0.24 ±0.01	-0.12 ±0.02

Table 5.4: In-plane strain values for n-MnSb and GaSb present in the 100 nm MnSb samples, relative to the bulk in-plane n-MnSb lattice parameter 4.128 Å.

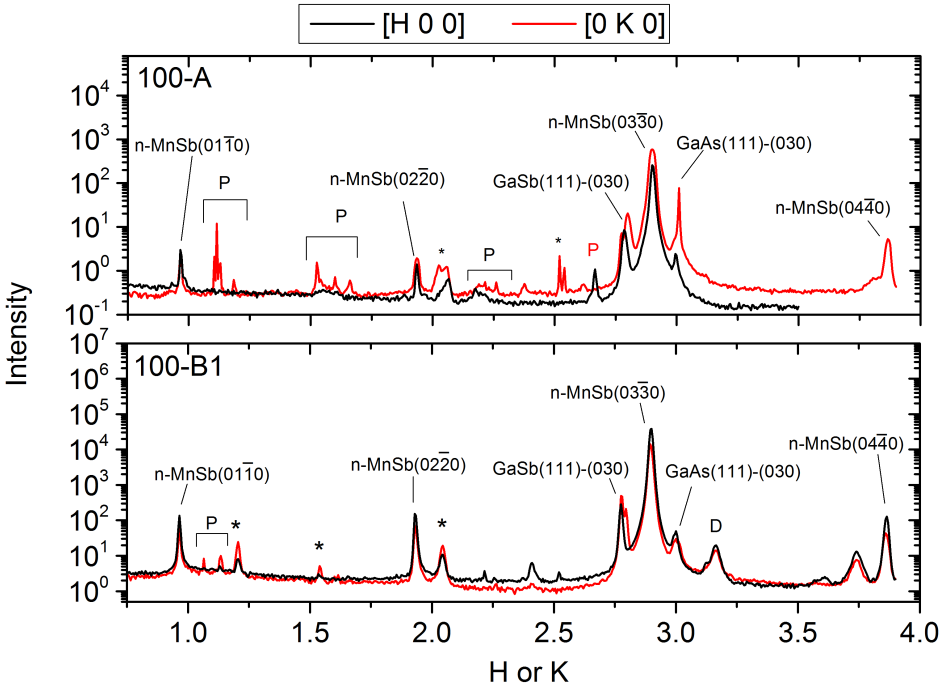

Figure 5.11: In-plane H or K scans measured on sample (*Top*) 100-A, (*Bottom*) 100-B1.

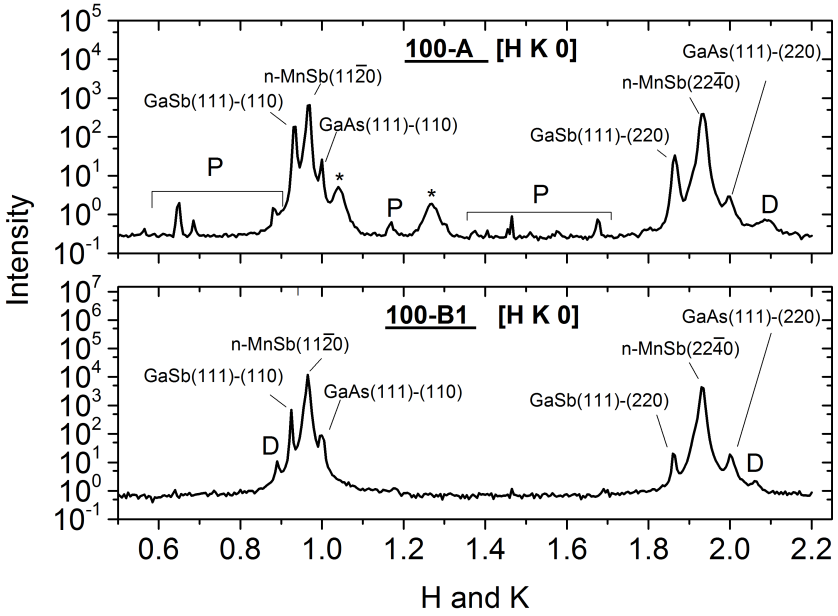

Figure 5.12: In-plane [H K 0] scans measured on samples (*Top*) 100-A, and (*Bottom*) 100-B1

A higher magnification plot of [0K0] scans from samples 100-A and 100-B1 shows double peaks near the GaSb(111)-030 peak (figure 5.13). On inspection of the individual detector images, clear double signals can be seen for the GaAs and GaSb signals (figure 5.14). The fact that the splitting is seen on two different samples which were mounted at random azimuths, as well as the lack of splitting in the n-MnSb signal, shows that this splitting is a feature of the sample and not a spurious signal from any diffractometer equipment. The fact that this splitting is seen in both the GaAs(111) and GaSb(111) signals shows that the GaSb is heavily influenced by the GaAs. The broadness of the MnSb(0002) signals indicates that it is still affected by the underlying GaAs, but to a lesser degree than the GaSb. These observations agree with a model that has GaSb predominantly formed at the interface, acting as a spacer between GaAs and MnSb. Interestingly the splitting is only present for the in-plane [0K0] direction, and is not observed for in-plane scans in the [H00] direction. Splitting of signals can be seen in samples where there are two separate

domains slightly rotated relative to one another. However, this has been ruled out because if this was the case then there would be splitting seen for both the [H00] and [0K0] scan directions.

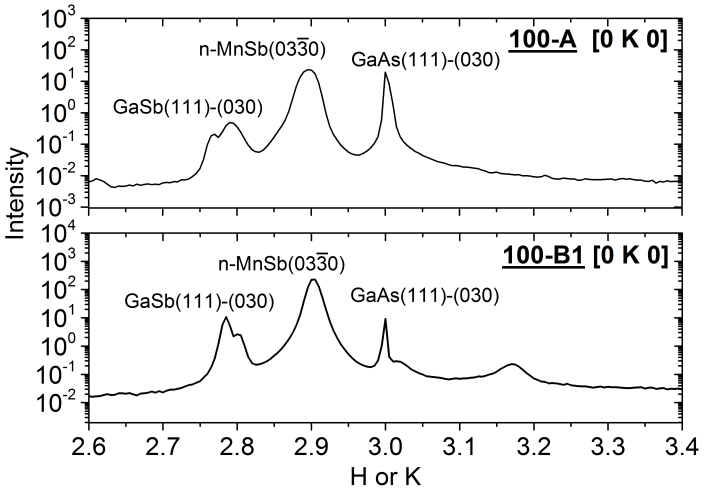

Figure 5.13: Zoomed in plot K scans shown in figure 5.11, highlighting double signals present for GaSb signals

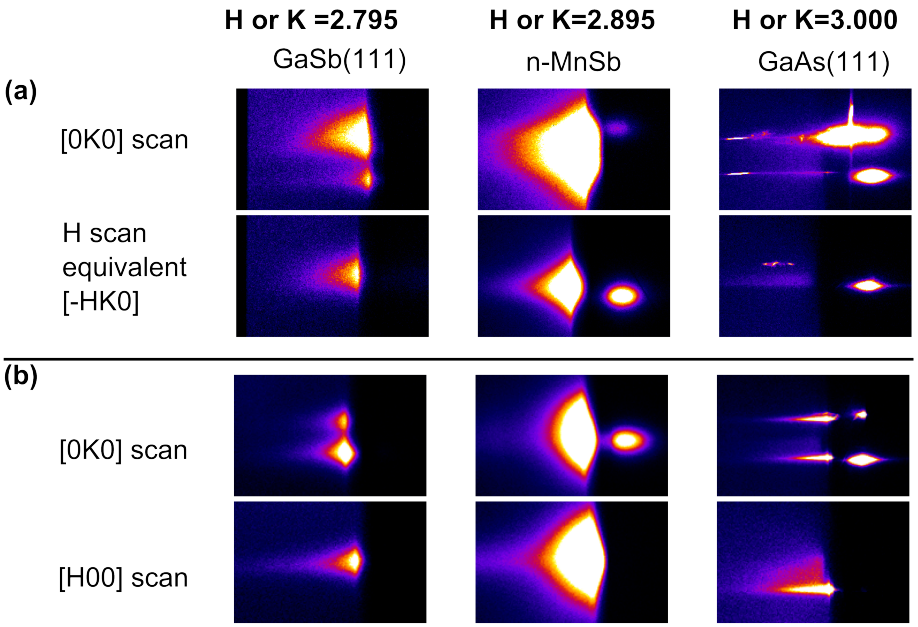

Figure 5.14: Detector images from [H00] and [0K0] scans from sample (a) 100-A, and (b) 100-B1. A double signal can be seen for GaSb and GaAs signals in both [0K0] scans, but not in [H00] scans.

5.3.5 Out-of-plane XRD

[00L] line profile fitting - 5 nm samples

Out-of-plane $\theta - 2\theta$ data collected from 5 nm samples before decapping (ESRF) and after decapping (I07) is shown in figures 5.15 and 5.16. It can be seen that for the 5 nm samples a much stronger n-MnSb(0002) signal is present for the (111)A samples, which is in agreement with the early stage RHEED observations detailed earlier. Broad signals can be seen near $Q_z = 2.1$ Å^{-1} indicated by the grey shaded region in figure 5.15. These are attributed to surface Sb oxides since these signals were no longer present in the scans from decapped samples (figure 5.16).

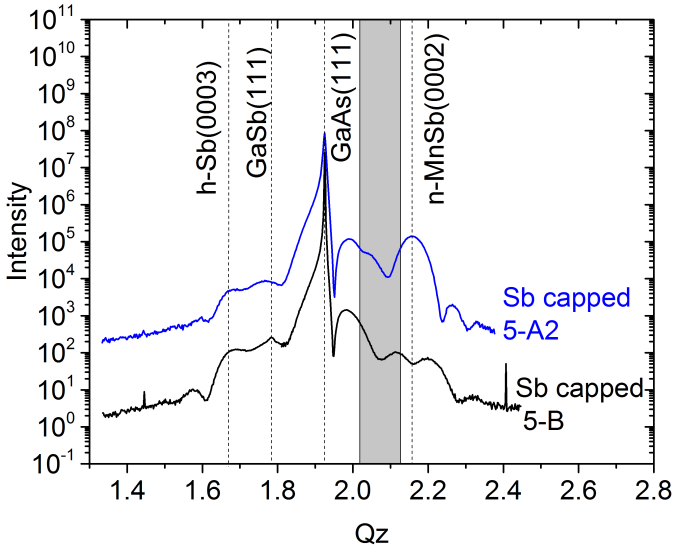

Figure 5.15: Out-of-plane symmetric diffraction data collected from capped 5nm MnSb samples

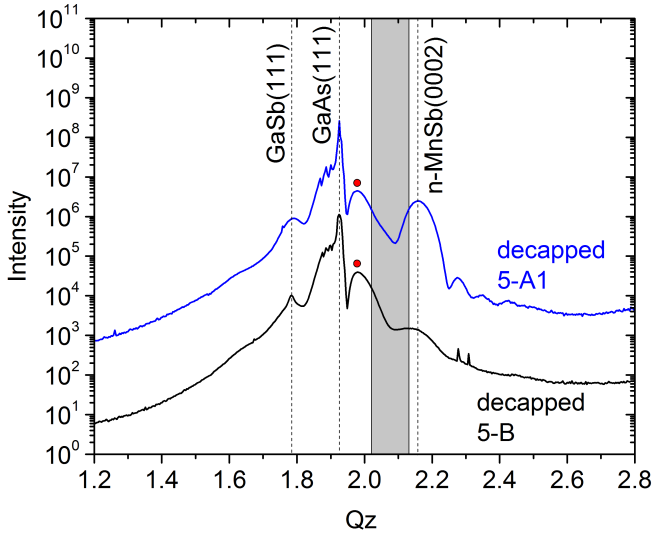

Figure 5.16: Out-of-plane symmetric diffraction data collected from decapped 5nm MnSb samples

To gain more information from the out-of-plane symmetric diffraction for the 5 nm samples presented in figures 5.15 and 5.16 , the scans were converted into CTR

00L format to allow for profile fitting. For both samples there is a peak in intensity to the right of the GaAs(111) signal at roughly $Q_z = 2.0$ Å^{-1} , indicated with red dots in figure 5.16. This type of peak has previously been attributed to MnSb($1\bar{1}01$), but it is actually part of a much broader peak centred on the GaAs(111) peak. It was found that this broader peak can be fitted with a mixed alloy interfacial region of $GaAs_{1-x}Sb_x$, which has a slightly expanded c-lattice compared to the underlying bulk.

For both samples two types of surface models were tested, with each type having a GaAsSb layer and a MnSb layer (figures 5.19 and 5.20). In the type-I models the GaAsSb layer and MnSb layer were stacked on top of one another. For the type-II models individual surface models were used for the GaAsSb layer and the MnSb layer, both being directly on top of the bulk GaAs. The best fits to profiles from samples 5-A1 and 5-B are shown in figures 5.17 and 5.18 respectively. Due to the fitting only using a section of one CTR, a full χ^2 fit was not suitable, but a visual inspection shows that for both samples a better fit is obtained from the type-II model. This shows that diffusion of Sb into the bulk, and the growth of MnSb occur on different areas of the surface. This style of deposition is consistent with the Sb diffusion being initiated by Ga droplets on the surface, which can be caused by IBA surface preparation. A comparison of the composition for the $GaAs_{1-x}Sb_x$ layers in these type-II fit models (figures 5.19 and 5.20) shows that sample 5-A1 had less Sb substitution occurring at the As sites, but the overall diffusion depth of the Sb was larger. The large out-of-plane MnSb lattice constant for sample 5-B is most likely an overestimate, as the effect of the MnSb layer on fitting was very small.

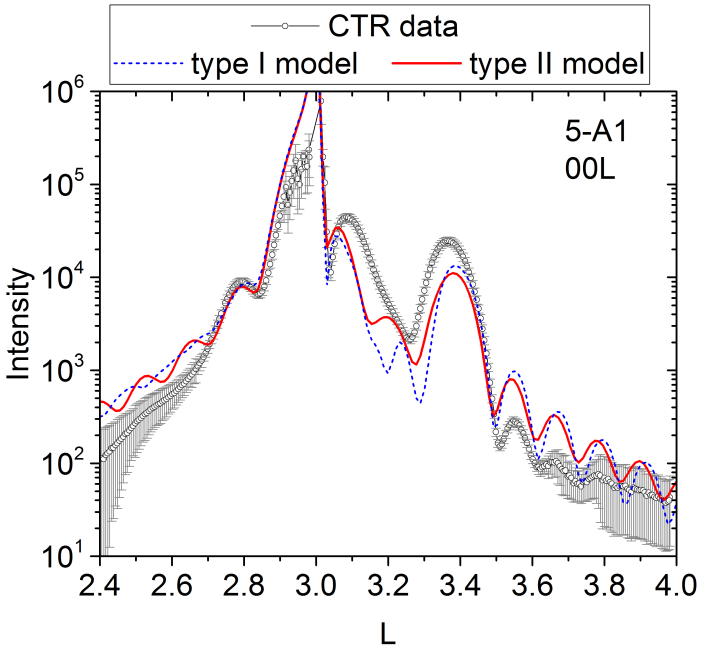

Figure 5.17: Line profile of the (00L) CTR for sample 5-A1, with best fit model for (a)one surface model (dashed blue line) and (b) two surface model (solid red line)

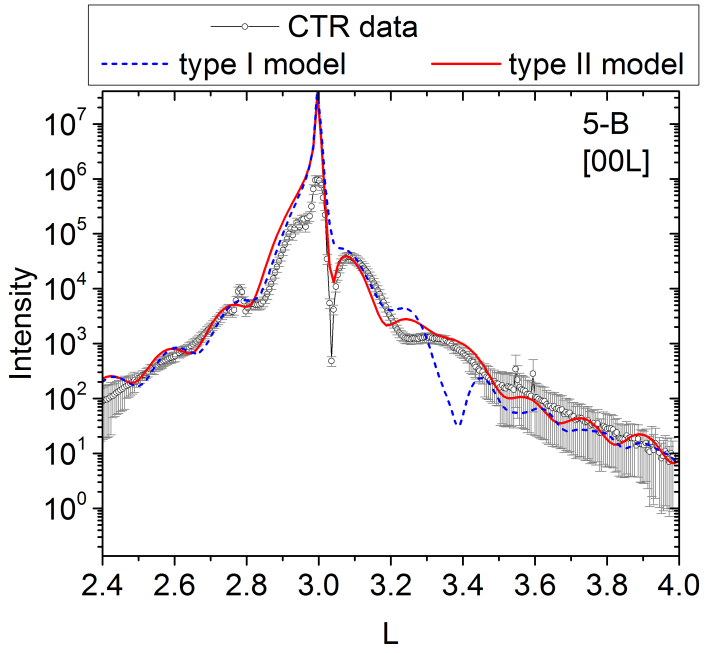

Figure 5.18: Line profile of the (00L) CTR for sample 5-B, with best fit model for (a)one surface model (dashed blue line) and (b) two surface model (solid red line)

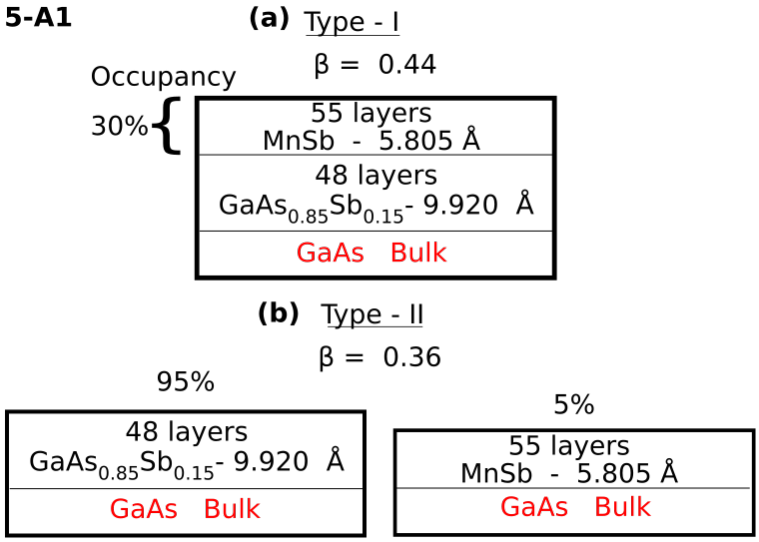

Figure 5.19: Schematic representation of the two models types used for fitting [00L] data for sample 5-A1. (a) Type-I surface model where layers are stacked ontop of one another, and (b) type-II surface model where mixed alloy interfacial layer and the MnSb layer are separate surfaces.

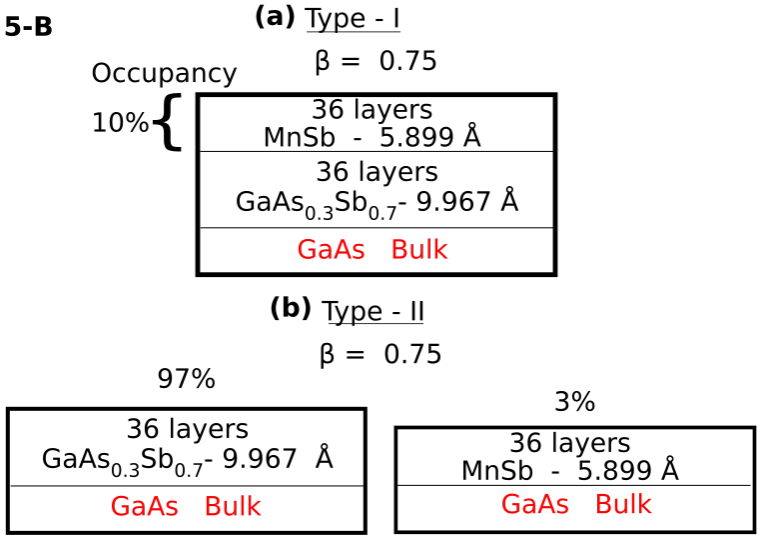

Figure 5.20: Schematic representation of the two models types used for fitting [00L] data for sample 5-B. (a) Type-I surface model where both surface layers are stacked on top of one another, and (b) type-II surface model where the mixed alloy interfacial layer and the MnSb layer are separate surfaces.

[00L] line profile fitting - 100 nm samples

Out-of-plane symmetric diffraction data collected from the 100nm samples after decapping (figure 5.21) shows the presence of strong peaks for both GaAs(111) and n-MnSb(0002). In individual detector images oscillations can be seen for the n-MnSb(0002) signal from sample 100-A1 (figure 5.22), which gives an estimated thickness of 60 $\pm$ 15 nm. Similar to the 5nm samples there is also a broad $GaAs_{1-x}Sb_x$ peak present in both 100 nm samples, showing that the two-stage growth process also produces an alloyed interface layer for both substrates.

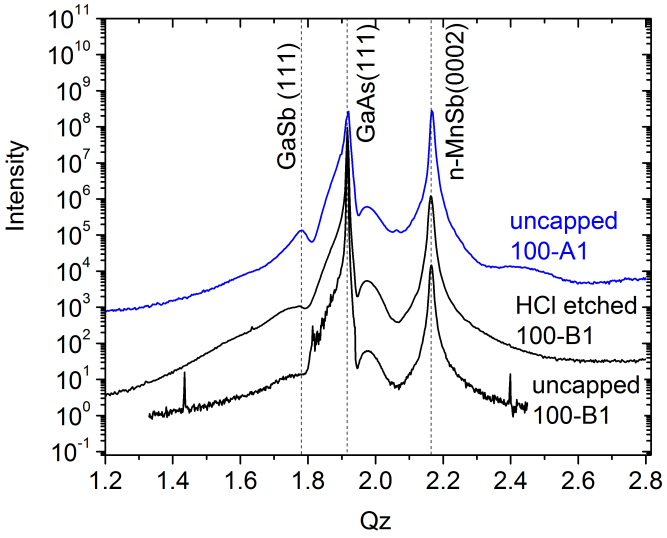

Figure 5.21: Out-of-plane symmetric diffraction data collected from decapped 100 nm samples.

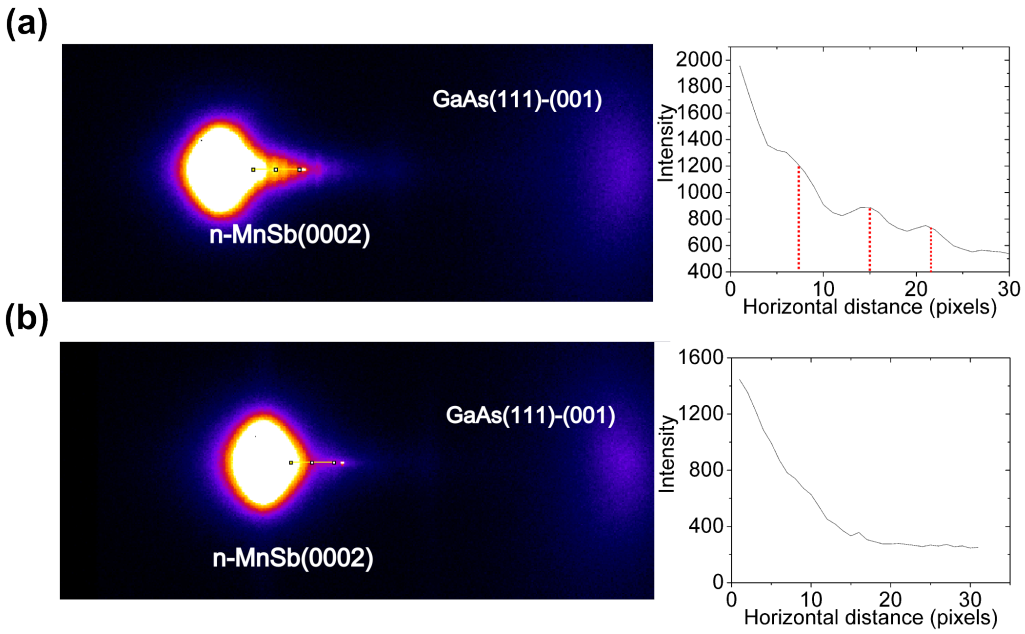

Figure 5.22: Single detector images taken from out-of-plane symmetric diffraction scans, and corresponding line profiles for sample (a) 100-A and (b) 100-B1. Red dotted lines indicate the rough positions of maxima for oscillations observed from sample 100-A.

To gain information about these alloyed interface layers the out-of-plane symmetric diffraction scans from the 100 nm samples were converted to 00L CTRs (figure 5.23). Due to the MnSb layers being too thick to model, only a rough fitting to these CTRs was possibly using surface models containing just a $GaAs_{1-x}Sb_x$ layer (figure 5.24). The best fit models to the 100 nm samples show the same trends as with the 5 nm samples, with the GaAs(111)A sample having a larger depth of Sb interdiffusion but a smaller level of Sb substitution. This diffusion behaviour is similar to work by Akinaga *et al.* [142] who showed that the use of As flux, during both annealing and a subsequent GaAs buffer layer stages, aids the MBE deposition of MnSb onto GaAs(111)B surfaces. The improvement was attributed to the formation of a perfect As-terminated surface which prevents both Ga-Sb bonding at the surface and Sb interdiffusion. In comparison, the results presented in this chapter suggest that As termination does hinder the interdiffusion of Sb, but it does not prevent

interdiffusion entirely. The level of Sb substitution at the As sites was found to increase on GaAs(111)B substrates. The existence of substitution on GaAs(111)B can be explained by the fact that a much higher substrate temperature was used when compared to Akinaga *et al.*, and this higher substrate temperature promotes Sb substitution at the As sites. The larger amount of Sb substitution on GaAs(111)B is understandable, because if the substrate temperature is high enough to make Sb substitution energetically favourable, then the GaAs(111)B surface will have more As sites readily available to incident Sb atoms.

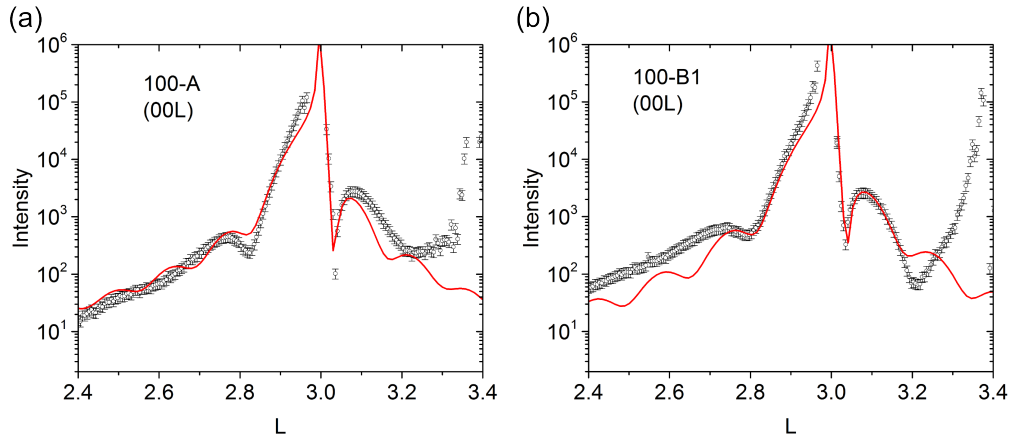

Figure 5.23: Line profiles of the (00L) CTRs for sample (a) 100-A and (b) 100-B1. Red lines are best fits from models shown in figure 5.24.

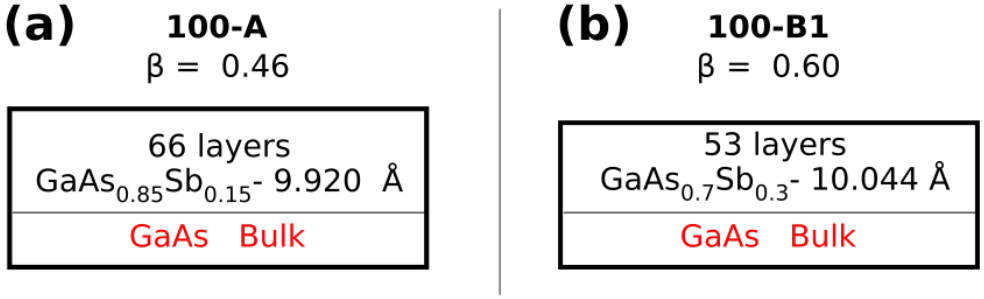

Figure 5.24: Schematic representation of the models used to obtain fits to the broad $GaAs_{1-x}Sb_x$ signals in (00L) data shown in figure 5.23, for sample (a) 100-A , and (b) 100-B1.

CTR separate line analysis

CTR data collected from samples showed that even the 5nm MnSb layers are relaxed in-plane, and therefore offset in the HK plane (figure 5.25). This agrees with previous work on MnSb/GaAs thin films, where films were found to relax for thicknesses larger than 3 nm [74]. The offset in the HK plane makes standard CTR profile analysis unsuitable because normal CTR profile fitting assumes an identical in-plane spacing for all layers. An extension for ROD has been previously created to model relaxed surface adsorbates, however currently this software only works with square in-plane unit cells which have "cube-on-cube" epitaxy [149]. Therefore a different method of analysis was implemented for this dataset, which involved comparing the intensities measured using three different positions for the region of interest box (figure 5.26). The middle box position (black) is centred on the GaAs CTR position, the lower box position (red) is centred on the MnSb CTR, and the upper box position (blue) is centered on a background signal located away from both CTRs. The box positions only differed in the y-direction of the detector image in order to maintain the same L value across all ROI positions. This separate line analysis shows that the CTR signals from sample 5-A1 (figure 5.26 d,e) have much higher signal-to-background ratio than those from sample 5-B (figure 5.26 b,c). This indicates a higher crystalline quality for layers on (111)A, which is in good agreement with the previous data presented. Thickness oscillations can be seen for sample 5-A1 (figure 5.27), analysis of these peaks gave an estimated thickness of 5 ± 0.5 nm.

Out-of-plane strain values for n-MnSb calculated from peak fitting of line profiles obtained from separate line analysis are shown in table 5.5. When compared with the in-plane strain values these do not agree with a volume conserving model, which predicts a larger out-of-plane strain for (111)B. However this is a very simplified model, and does not take into account extra factors such as material intermixing and elemental segregation.

Sample	n-MnSb out-of-plane strain (%)
5-A1	0.360 ± 0.064
5-B	0.210 ± 0.046
100-A	0.282 ± 0.018
100-B1	0.297 ± 0.050

Table 5.5: Out-of-plane strain values for n-MnSb relative to the bulk lattice spacing 5.789 Å, calculated from fitting peaks obtained in separate line analysis.

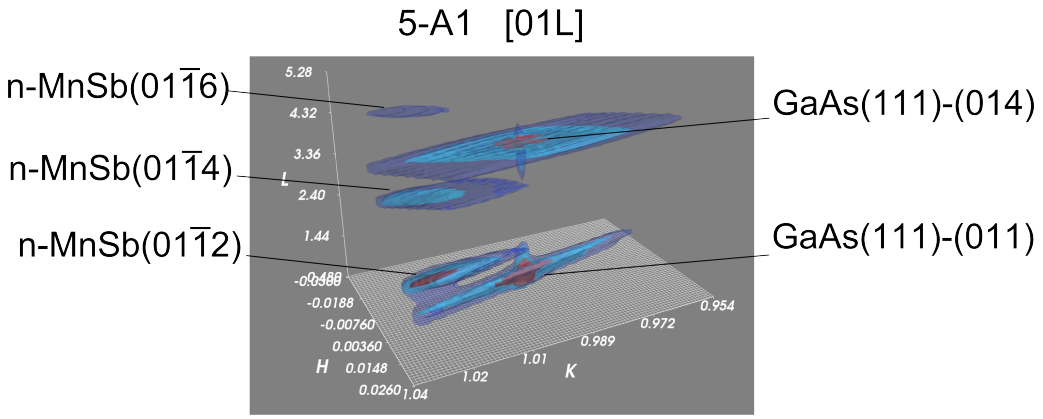

Figure 5.25: 3D visualisation of the 01L CTR for sample 5-A1, showing the off-set in the HK plane for the n-MnSb signals relative to the GaAs(111) substrate signals.

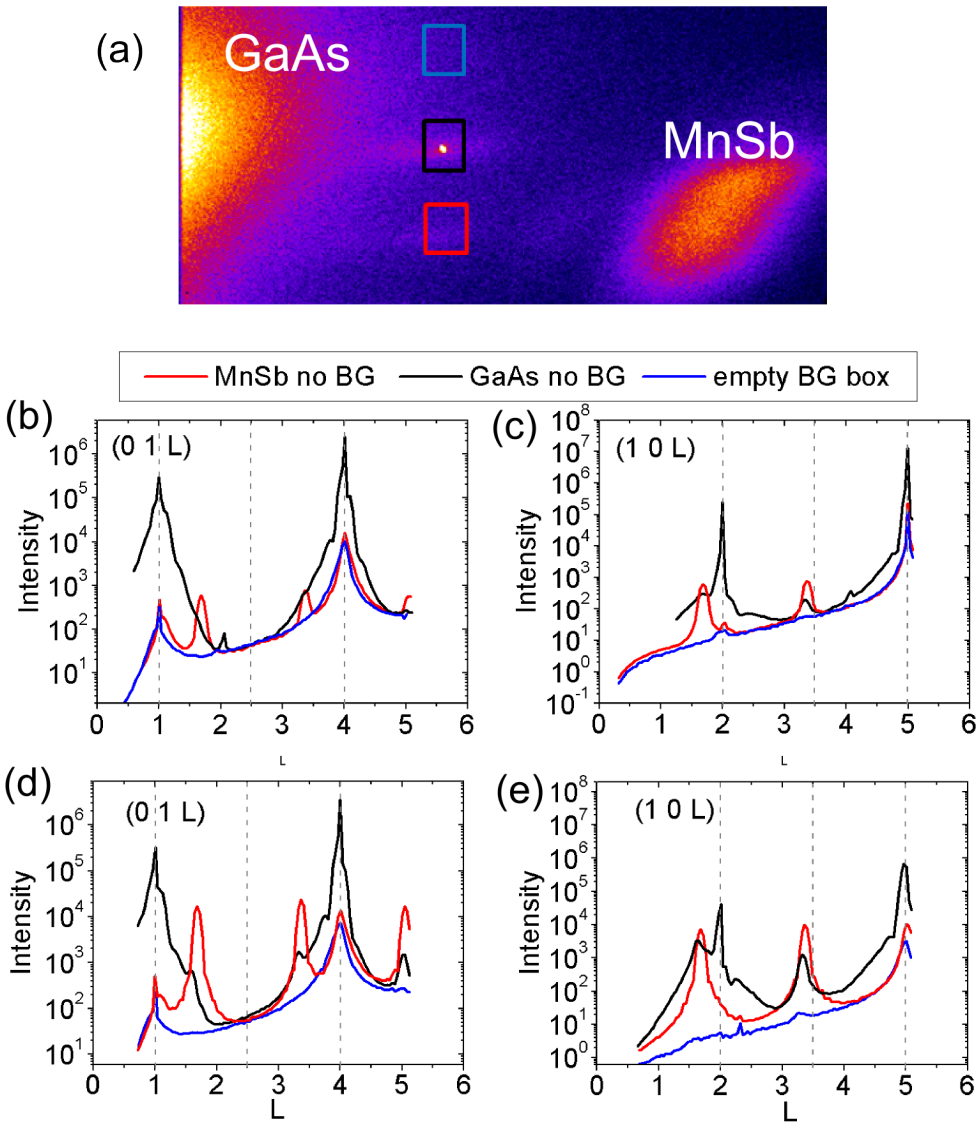

Figure 5.26: (a)Example detector image showing the three different regions of interest (ROI) used for the separate line analysis. The black box is centered on GaAs, the red box is centered on MnSb, and the blue box is centered on background. Example results of CTR data analysis using this separate line technique are shown for (b,c) sample 5-B, and (d,e) sample 5-A1.

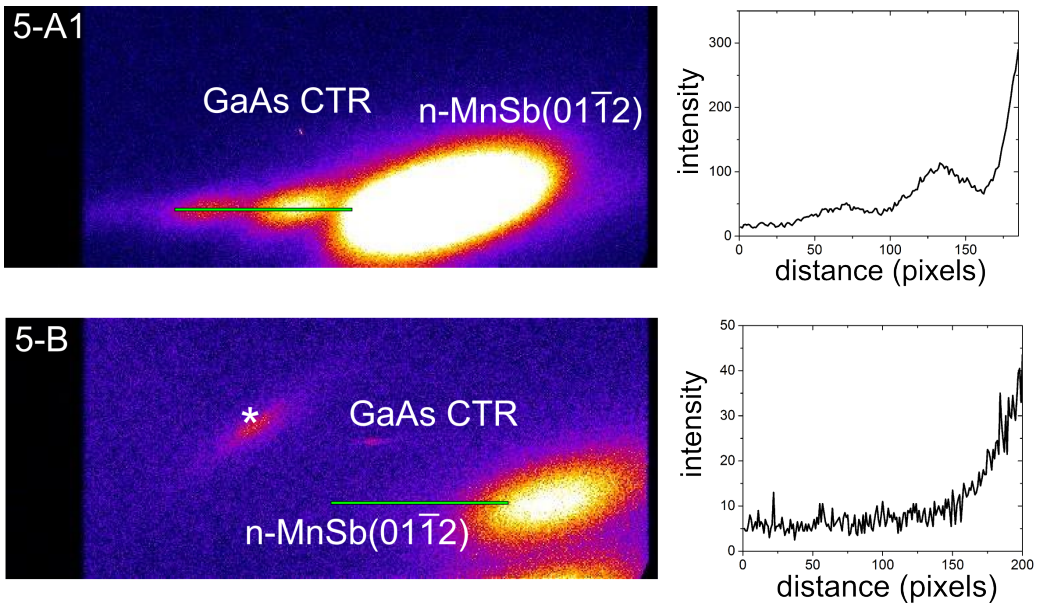

Figure 5.27: Detector images from the (01L) CTR for samples (*Top*)5-A1, and (*Bottom*) 5-B

CTR 3D visualisations

Following on from the separate line analysis, CTR data was analysed further using 3D visualisations and taking slices through reciprocal space. CTR scans showed that for all 6 inner CTRs (H or K $\leq$ 1) there are extra signals only seen in data from sample 5-B at approximately L=2.24 and 4.20. Examples of these weak signals are shown in figure 5.28, with identical data from samples 5-A1, 100-A and 100-B shown for comparison. 3D visualisations of two CTRs from 5-B which possess these extra signals are shown in figure 5.29, with the extra signals labelled with an asterisk (*). These extra signals are currently unidentified and could be an anomalous signal from sample contamination. Identification would require further investigation in order to see if these signals are reproducible.

From slices taken through these 3D visualisations shown in figure 5.29, it can also be seen that there is the start of a second signal appearing at the edge of the scanned areas. The existence of these dual signals at MnSb positions suggest that there are two distinct in-plane strain states for the MnSb layer. A second strain

state could arise from domains of strained MnSb growing on top of areas of the $In_{1-x}Ga_xSb$ alloyed layer which have a high Sb substitution, and therefore are closer to the in-plane lattice spacing of GaSb.

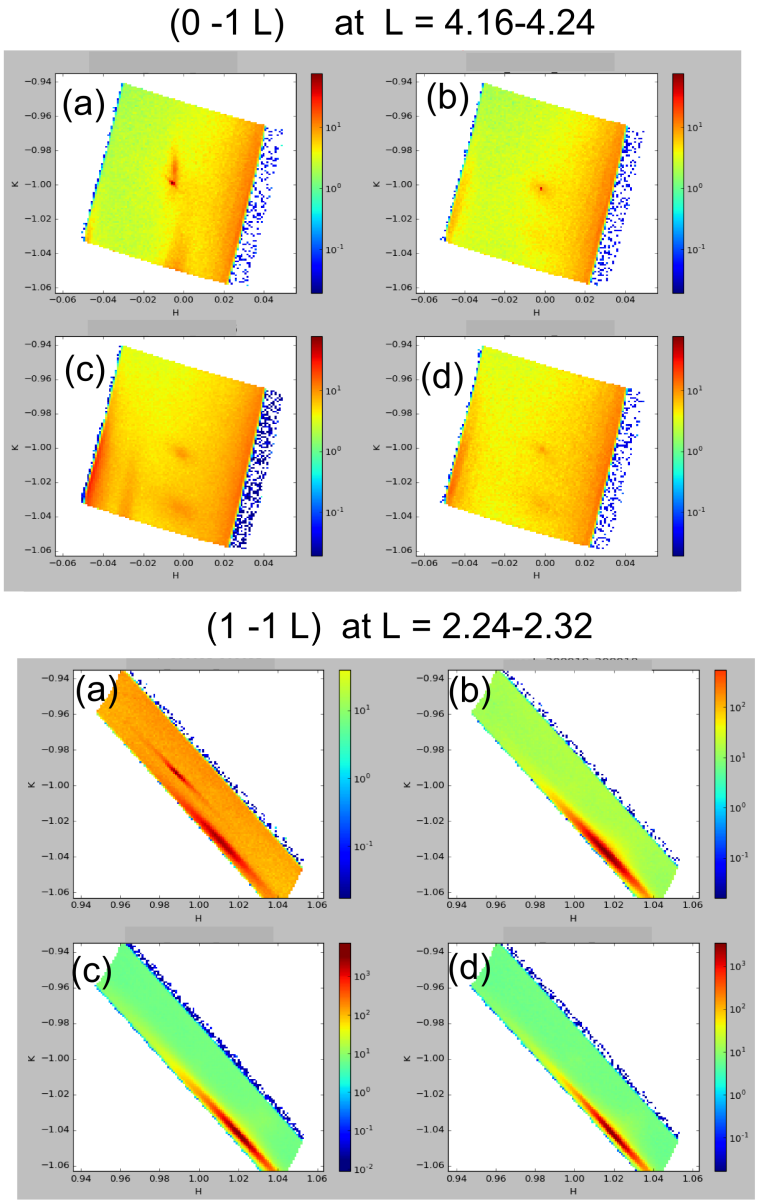

Figure 5.28: Slices through the HK plane from 3D CTR datasets. Showing slices through (0 -1 L) CTRs averaged for L= 4.16-4.24 and slices through (1 -1 L) CTRs averaged for L=2.24-2.32 ,from sample (a) 5-B , (b) 5-A1, (c) 100-B1, and (d) 100-A.

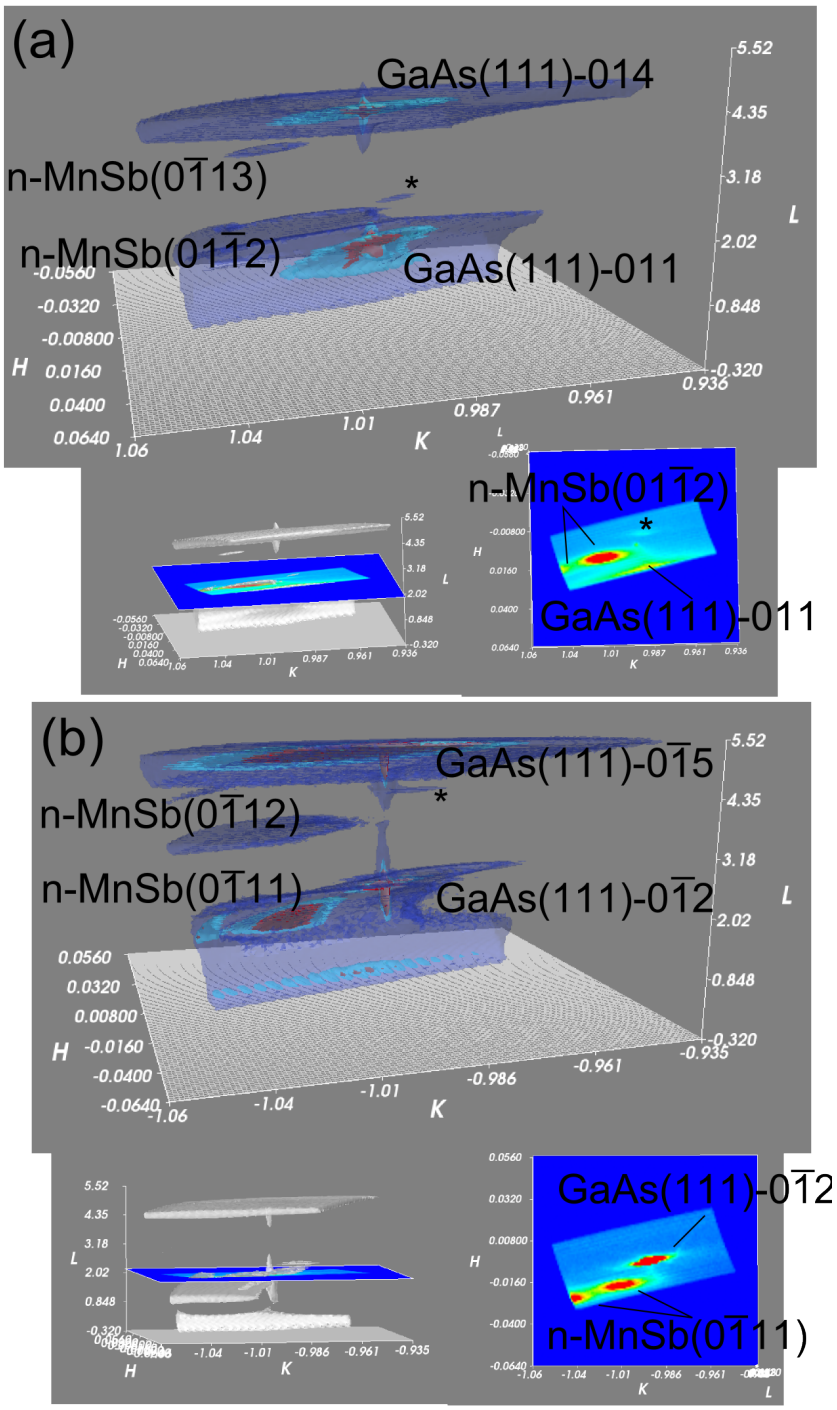

Figure 5.29: Full 3D visualisations of (a) 01L and (b) 0$\bar{1}$L CTR data from 5-B with corresponding slices in the HK plane. Two signals can be seen for the n-MnSb reflections.

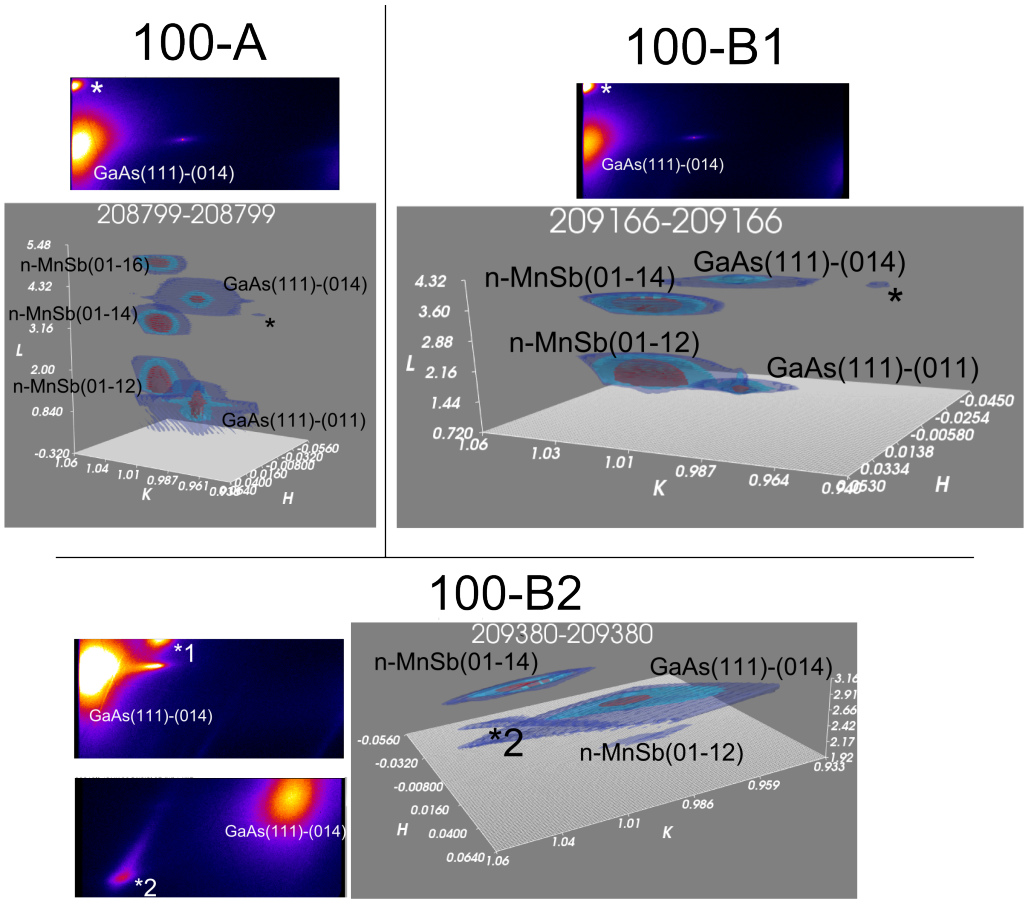

Figure 5.30: Examples of extra signal observed in thick samples. 3D (01L) CTR visualisations and detector images for samples 100-A (*Top Left*), 100-B1 (*Top Right*), and 100-B2 (*Bottom*).

For all 100nm samples there was an extra unidentified signal present near the GaAs(111)-014 position, with the 3D visualisations in figure 5.30 showing this extra signal labelled with an asterisk (*). The lowest section of figure 5.30 shows a section from a CTR collected using a n-MnSb UB matrix, and a second unidentified signal (*2) can be seen close to the first (*1) at a slightly higher L value. The change in position of signal *1 for 100-B2, when compared with the positions of the * signals present in both 100-A and 100-B1, suggest that this signal is linked to the surface preparation technique because sample 100-B2 was the only sample indium bonded

whilst in an inert atmosphere, and both 100-A and 100-B1 were not Sb-capped.

5.3.6 AFM

Ex-situ AFM was collected from decapped 5 nm samples grown on both GaAs(111)A and GaAs(111)B (figure 5.31). The RMS roughness values from ($1\mu m \times 1\mu m$) images were calculated to be 1.391 nm for 5-A1 and 1.045 nm for 5-B. The surfaces have almost identical morphology and very similar RMS values. This suggests that the increased layer quality evidenced by thickness oscillations for samples grown on GaAs(111)A is primarily due to a much sharper interface between the GaAs and MnSb.

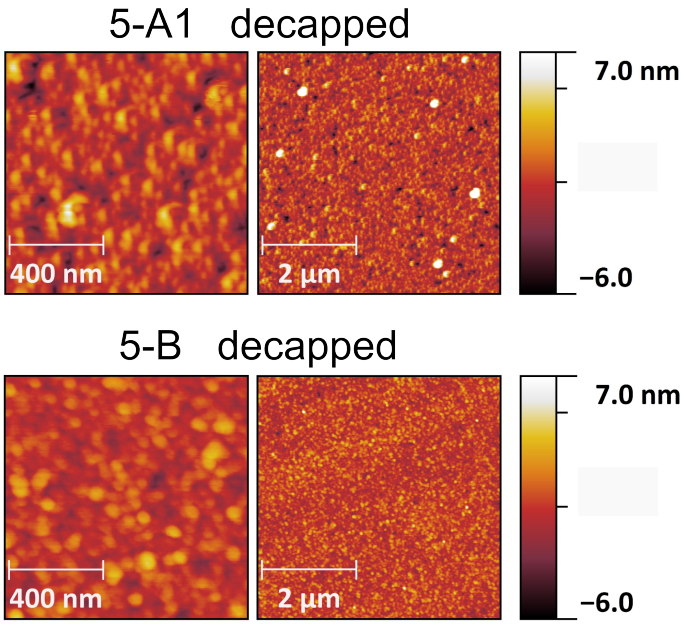

Figure 5.31: Ex-situ AFM images collected from decapped 5 nm samples. Sample 5-A1 (*Top*), and 5-B (*Bottom*)

5.4 Summary

Growth of MnSb films of thicknesses 5 nm and 100 nm on both GaAs(111)A and (111)B surfaces was investigated using RHEED, XPS, SXRD and AFM. RHEED observations during the start of deposition indicated that initial stages of growth on

GaAs(111)A proceeds by layer-by-layer processes, whereas initial stages of growth on GaAs(111)B were found to proceed by 3D island processes. For both substrate polarities a strong and sharp (2×2) signal was obtained after 100 nm, suggesting that the difference in growth process only occurs in the initial stages of deposition. XPS data showed that the Sb capping procedure was less efficient at preventing oxidation for thin films on GaAs(111)B. Out-of-plane symmetric diffraction data and CTR data both show oscillation fringes present only for samples grown on GaAs(111)A. Combining these oscillations with AFM measurements showed that the increase in crystalline quality of the films on GaAs(111)A was due to an increased interface quality. Fitting of [00L] CTRs showed that an alloyed interface layer of $GaAs_{1-x}Sb_x$ was formed in all samples, with GaAs(111)A substrates having thicker alloyed layers with lower Sb content. These results mean that for growth of devices utilising MnSb/GaAs(111) interfaces, the use of (111)A substrates is recommended due to the improved interface quality, and lower amount of Sb substitution and associated lattice expansion.

Chapter 6

SXRD investigation of GaAs/MnSb/Ga(In)As

6.1 Introduction

Many spintronic applications, in particular vertical transport devices [150], require the use of multi-layer structures [1]. For this reason, in material systems where single layer epitaxial growth has been successful, studies sometimes progress to investigate the growth of multi-layer heterostructures. However, for two materials A and B, if elastic strain energies result in layer-by-layer growth for A-on-B deposition, then layer-by-layer growth is prohibited for B-on-A deposition. This gives rise to a fundamental challenge in obtaining high-quality films and interfaces during multi-layer heterostructure growth of two dissimilar materials.

MnSb/Bi/MnSb heterostructures have been grown on GaAs(111)B using pulsed laser deposition [151], with RHEED patterns indicating that these multi-layers were polycrystalline. MnSb/MnAs/$MnAs_{1-x}Sb_x$ heterostructures were grown via MBE on GaAs(001) [152], and XRD showed that the growth direction of MnAs, $MnAs_{1-x}Sb_x$ and MnSb was primarily [$\bar{1}$101]. RHEED showed streaky patterns for the MnAsSb and MnAs layers, however the third MnSb layer pattern altered to trans-

mission spots indicating a transition to 3D island growth. More recently the growth of NiMnSb/ZnTe/NiMnSb multi-layers on InGaAs(001) has been investigated for applications in spin-torque devices [153]. This growth utilised a combination of MBE for NiMnSb layers and atomic layer epitaxy for the ZnTe layer. For the upper NiMnSb layer pronounced dots in RHEED observations showed that initial stages of deposition onto the ZnTe spacer layer involved 3D island growth.

Whilst metal-on-semiconductor heteroepitaxy is fairly common, the study of semiconductor-on-metal heteroepitaxy is a lot less widespread. This is due to the fact that deposition of a single-crystal semiconductor thin film onto a metal surface is difficult, with most results often being a polycrystalline thin film [154] or single-crystal nanostructures [155]. MnSb is a ferromagnetic metal which has similar bonding and surface reconstructions compared to III-V semiconductors. These properties prompt an interesting question - would crystalline III-V semiconductor thin films grow more readily on MnSb surfaces?

Following on from successful epitaxy of MnSb layers on Ga(In)As(111) presented in earlier chapters, as well as MnSb layer growth on GaAs(001) substrates published by others [58] [144], a SXRD experiment was conducted to investigate the growth of multi-layer heterostructures incorporating MnSb layers. The results of this experiment will be presented in this chapter as follows; sample structure and experimental details will be outlined in section 6.2, RHEED and SXRD data will be presented in section 6.3, and a summary will be given in section 6.4.

6.2 Experimental details

Virtual substrates were grown at Warwick University following almost identical procedures to the MnSb/InGaAs(111)A samples detailed in previously. An additional capping layer of Sb was deposited prior to removal from the UHV system in order to protect the MnSb layer while it was transported to the UHV system in Japan.

GaAs(111)A and InGaAs(111)A substrates were both used because even though InGaAs(111)A was expected to give rougher films, it was also expected to produce MnSb with a lower misfit strain which could improve GaAs overlayer deposition. On arrival in Japan the samples were bonded to the BL11 XU sample holders using indium eutectic, and once loaded inside the UHV system they were annealed to 500°C in order to remove the Sb capping layer and reveal the MnSb surface. Following decapping a layer of GaAs was was deposited using settings described in table 6.1. The total thickness of GaAs overlayer grown was 30 nm (10 nm) for the GaAs(111)A (InGaAs(111)A) substrate 6.1. Whilst technically the term 'virtual substrate' is referring to the MnSb layer, for brevity these samples are hereafter referred to as the GaAs(111) virtual substrate, InGaAs(111) virtual substrate, and GaAs(001) virtual substrate.

Sample	T_{sub} (°C)	Deposition time (minutes)	Growth rate(nm.hour^{-1})
GaAs(111)	430	60	10
InGaAs(111)	370	81	10
	370	16	60
GaAs(001)	425	35	60

Table 6.1: Growth settings used for GaAs overlayer deposition.

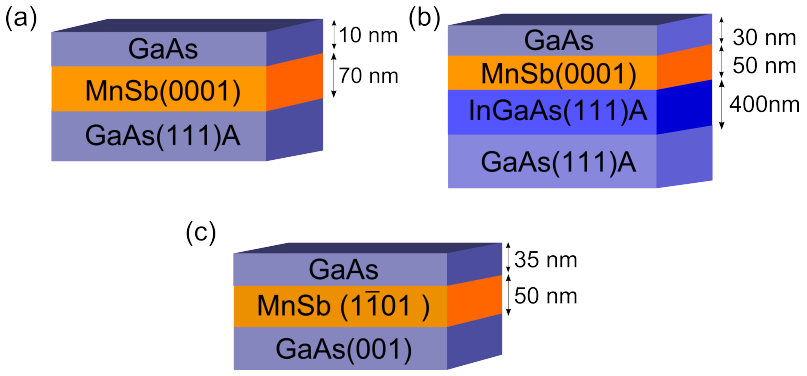

Figure 6.1: Schematic structure diagrams of samples grown on three different MnSb virtual substrates:(a)GaAs(111)A, (b)InGaAs(111)A, and (c) GaAs(001)

6.3 Results

6.3.1 Transmission Electron Microscopy

Ex-situ transmission electron microscopy (TEM) images were collected from all samples, and are shown in figure 6.2. All samples show a highly disrupted GaAs overlayer, with images for the InGaAs(111) and GaAs(001) virtual substrates also showing an absence of the MnSb layer material. This loss of material is due to delamination of the MnSb layer during TEM sample preparation, which has been observed before on previous samples. Post-decapping RHEED observations showed that the surface perparation was not optimal for both n-MnSb(0001) and $(1\bar{1}01)$. The poor surface preparation is attributed to a heating step in air used during indium bonding, which most likely damaged the protective Sb caps. Also this was the first attempt at growing these multi-layer heterostructures, which means that the GaAs deposition settings were not optimised. However, despite the poor quality of the overlayer, epitaxy was observed with SXRD providing information on both the GaAs overlayers and the MnSb layers.

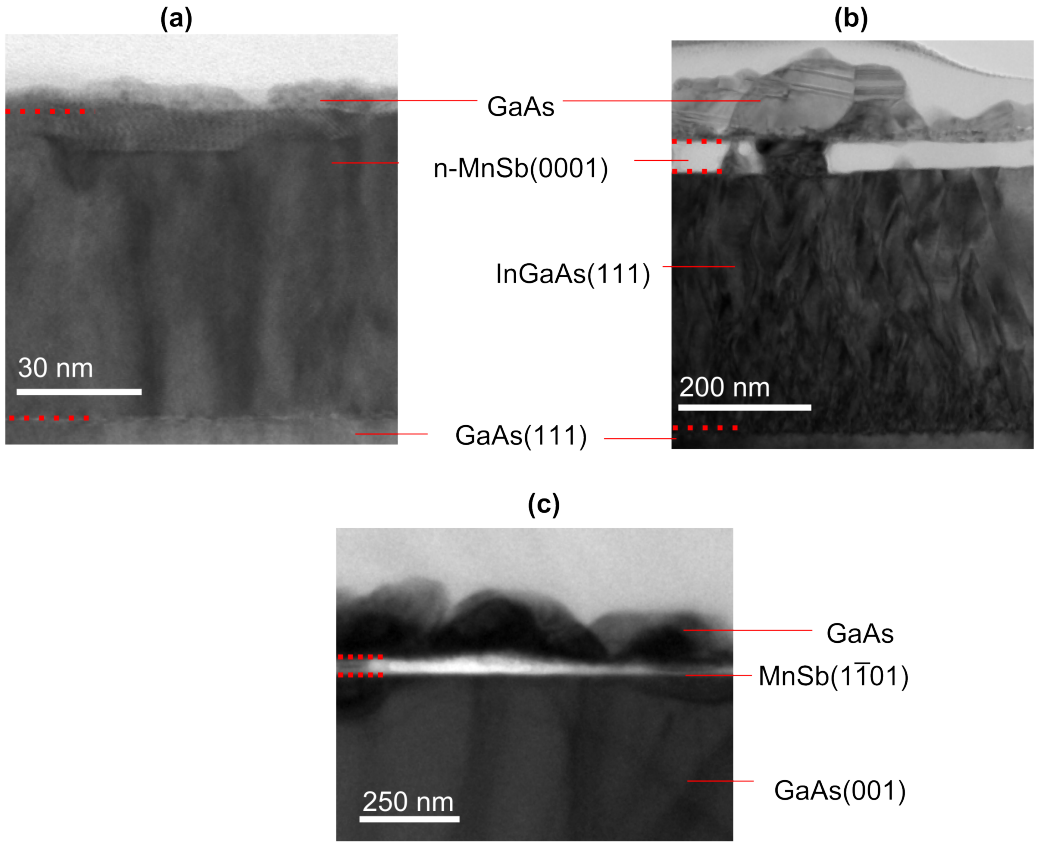

Figure 6.2: TEM images from (a)GaAs(111) virtual substrate,(b) InGaAs(111) virtual substrate, and (c) GaAs(001) virtual substrate. Red dotted lines show the rough position of interfaces between layers.

6.3.2 X-ray Diffraction: (111)A virtual substrates

XRD experiments were conducted using 20 keV (0.6199 Å) photons and a 2D detector to image scattered x-rays. Symmetric diffraction data was obtained from samples before, during and after growth. For the (111)-type samples some CTR scans were measured before and after growth, along with the accompanying RHEED patterns.

$\theta - 2\theta$ symmetric diffraction

Out-of-plane symmetric $\theta - 2\theta$ measurements were collected during growth for GaAs deposition on both(111)A virtual substrates (figure 6.3). These showed strong signals

from the substrates (InGaAs(111) and/or GaAs(111)), along with a n-MnSb(0002) peak. The position of these diffraction features hardly changed throughout GaAs overgrowth, which was to be expected due to the lack of surface specificity for this diffraction geometry.

The n-MnSb(0002) signal position is at a slightly higher Q_z value for the InGaAs(111) virtual substrate, which is to be expected due to the substrate having a larger in-plane lattice parameter. The increased bi-axial tensile strain will result in the MnSb layer have a larger in-plane lattice parameter, and consequently a smaller out-of-plane lattice parameter. For the GaAs(111) virtual substrate there is an unassigned peak labelled with ' * ', which matches the expected position for GaAs(002). This could arise due to contamination from cleaving debris or possibly crystallites formed at the edge of semiconductor wafer.

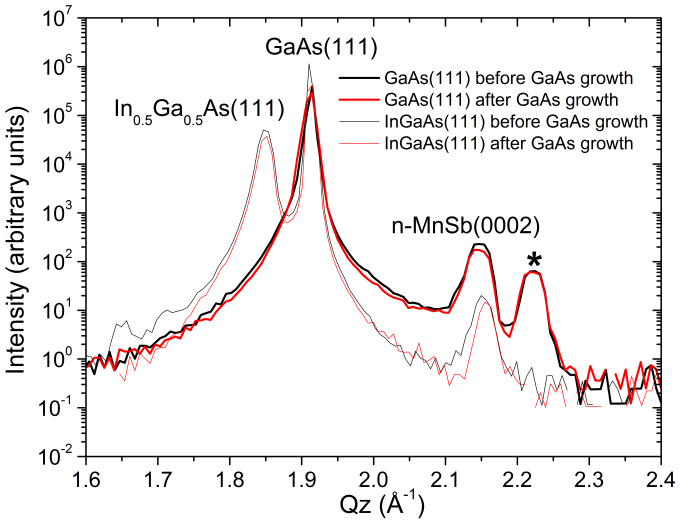

Figure 6.3: Symmetric out-of-plane diffraction data for GaAs/ MnSb(0001)/Ga(In)As(111) samples before and after GaAs growth. Q_z refers to the [0001] direction.

CTR separate line analysis: MnSb signal

CTR measurements were measured from the virutal substrate samples both before and after GaAs overlayer deposition. These scans could not be used in full CTR

profile analysis due to the CTR signals disappearing away from the vicinity of Bragg positions. However, analysis of the individual images close to the Bragg peaks could still be conducted, and provided information about the change in strain state of the MnSb layers that occurs due to the deposition of the GaAs overlayer.

The InGaAs(111) virtual substrate moved on the sample holder during GaAs deposition, and required realignment. This new sample position meant that the [01L] CTR was not suitable for the diffractometer, therefore the symmetrically equivalent [$1\bar{1}$L] CTR was measured instead. Detector images from these [01L] CTR scans are shown in figure 6.4, highlighting the positions of the n-MnSb(000n) peaks (n=2,4,6) before and after GaAs deposition onto the GaAs(111) virtual substrate. For these images the x-axis positions gives information on relative L-values, however it is not a direct mapping. The y-axis represents a combination of the H and K direction, which depends upon the position of the detector. In images before deposition the n-MnSb signals are in the lower third, but for images after deposition the n-MnSb are in the upper third. This indicates that there has been a shift in the HK position of the n-MnSb CTR. The signal has also shifted slightly to the left of the image, indicating an increase in the signals L position. To quantify this shift in L position, separate line analysis was conducted in a similar manner to the previous chapter, with profiles extracted using two different region of interest (ROI) boxes: either centred on the GaAs signal, or centred on the MnSb signal. Due to these not having any background removed these will be referred to as scan profiles, rather than CTRs.

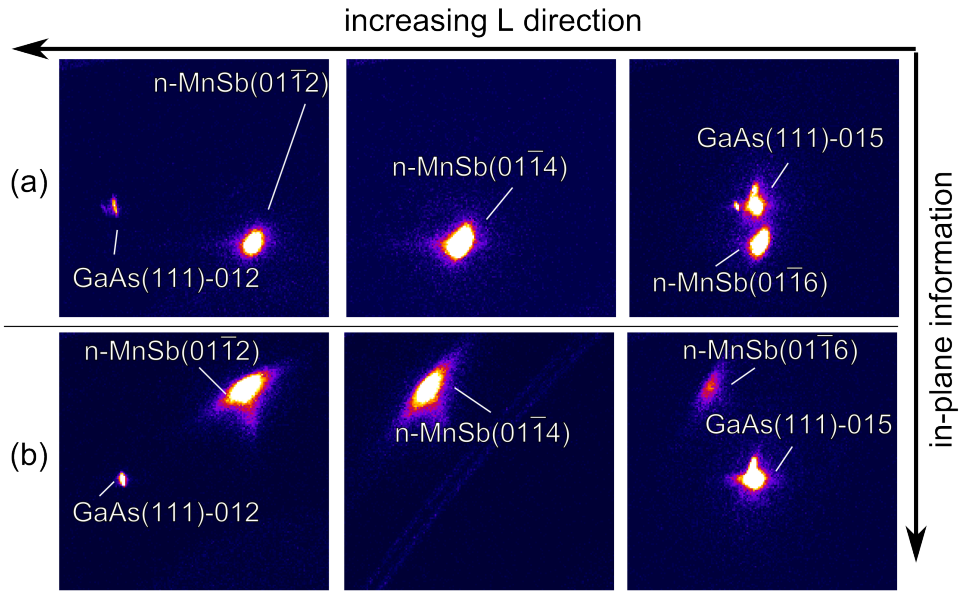

Figure 6.4: 2D detector images from <01L> CTR scans, showing the positions of n-MnSb(01$\bar{1}$n) signals from GaAs(111)A virtual substrate (a) before, and (b) after GaAs deposition

Figure 6.5 shows the scan profiles obtained using a ROI box centered on the n-MnSb signals for the GaAs virtual substrate, after *L*-shift correction. The n-MnSb(01$\bar{1}$n) peaks after GaAs deposition show a shift in L position. The magnitudes of these shifts in L position were calculated from peak fitting to the MnSb line profiles. The in-plane H and K shifts were calculated from individual detector images using the methodology detailed by Hu *et al.* [156].

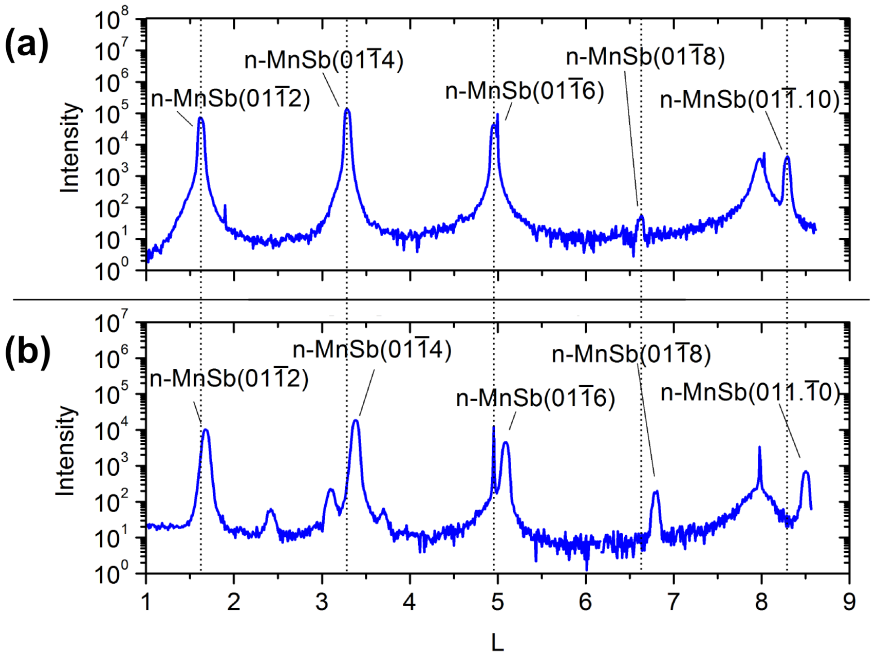

Figure 6.5: Line profiles obtained from <01L> CTR scans on GaAs(111)A virtual substrate sample (a) before, and (b) after GaAs deposition. Obtained using a region of interest centered on n-MnSb signals, with no back ground removal. Unlabelled peaks are due to background contributions from nearby signals at different x-positions.

The calculated values of these shifts are shown in figure 6.6a, and correspond to an increase in the out-of-plane reciprocal lattice value and a decrease in the in plane reciprocal lattice value. There is an increase in magnitude for the shift in L with increasing order of reflection. Whereas the magnitude of in-plane shifts remains relatively constant with increasing order of reflection. This shows that these shifts are caused by changes to the out-of-plane lattice strain of the MnSb layer. The strain values for the MnSb layer in the GaAs(111) virtual substrate are summarised in the first column of table 6.2. These values are relative to the average lattice constant measured on MnSb/GaAs(111)B samples previously grown at Warwick (c=5.797 Å). The uncertainty on these measurements, based on the L step-size used in the CTR scan, is approximately $\pm 0.15\%$.

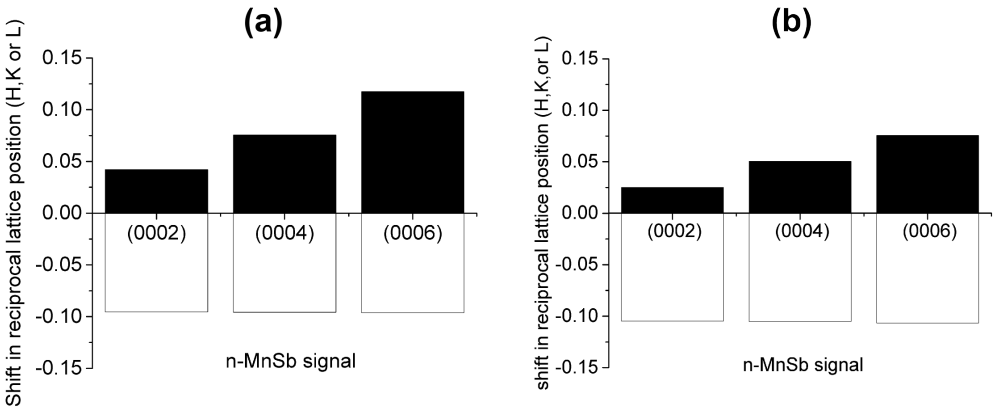

Figure 6.6: Magnitudes of shifts of the first three MnSb signals, in out-of-plane (black bars) and in-plane (white bars) directions, for (a) GaAs(111)A virtual substrate, and (b) InGaAs(111)A virtual substrate.

Stage	GaAs(111)	InGaAS(111)
before GaAs deposition	1.66	0.82
After GaAs deposition	-0.67	-0.67

Table 6.2: Out-of-plane strain values for n-MnSb relative to 5.797 Å. Errors on values are described in text.

Detector images in figure 6.7 show the positions of the n-MnSb(000n) peaks (n=2,4,6) before and after GaAs deposition onto the InGaAs(111) virtual substrate. The type of information represented by the x-axis and y-axis in these images is the same as that described previously for the GaAs(111) virtual substrate. The images show a similar movement of the n-MnSb CTR, with the signals moving from the lower third to the upper third of the image, as well as having a small shift to higher L-values.

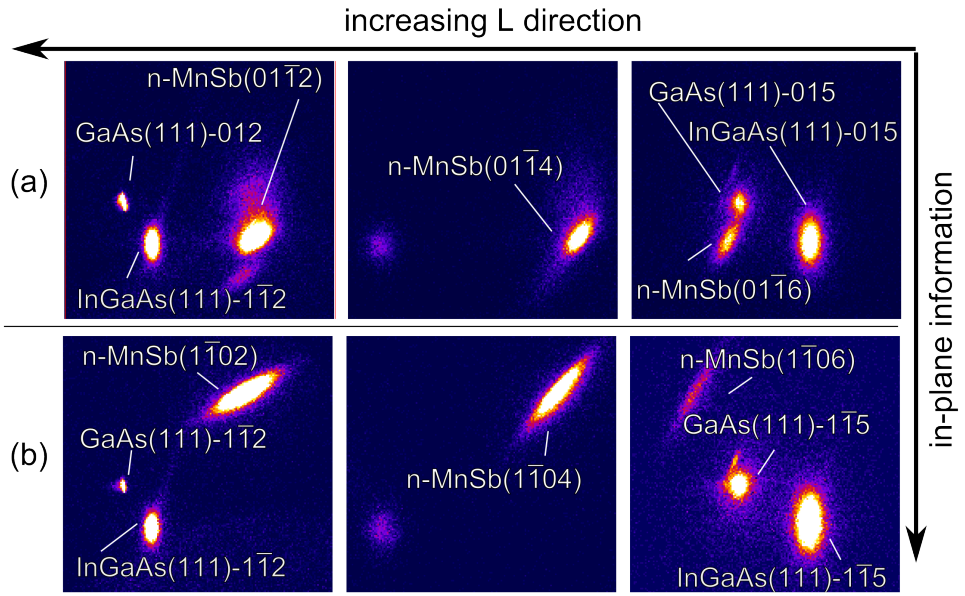

Figure 6.7: 2D detector images from <01L> CTRs, showing the positions of n-MnSb(01$\bar{1}$n) signals from InGaAs(111)A virtual substrate (a) before, and (b) after GaAs deposition

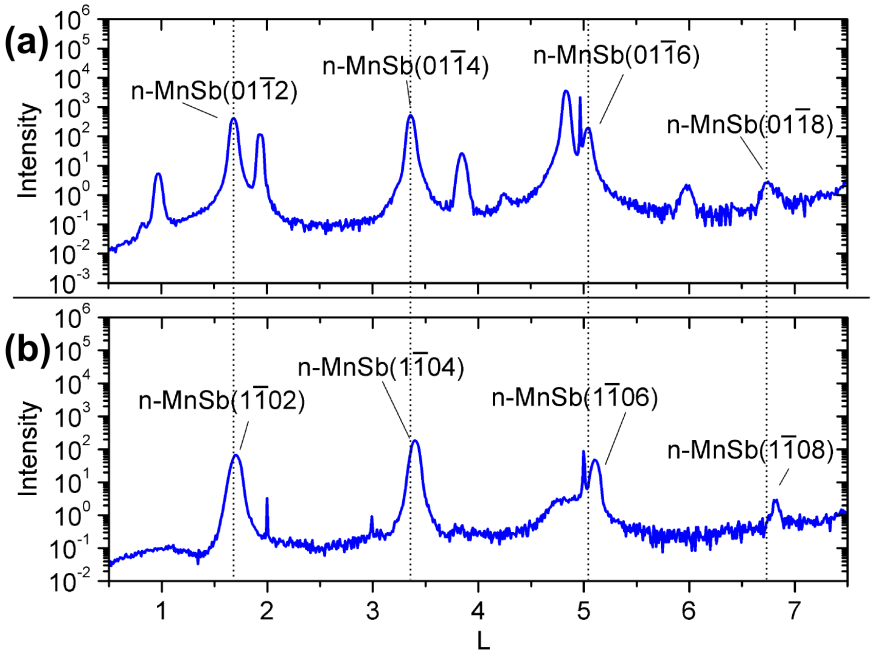

Figure 6.8: Line profiles obtained from <01L> CTR scans on InGaAs(111)A virtual substrate sample (a) before, and (b) after GaAs deposition. Obtained using a region of interest centered on n-MnSb signals, with no background removal. Unlabelled peaks are due to background contributions from nearby signals at different x-positions.

Figure 6.8 shows the scan profiles obtained using a ROI box centered on the n-MnSb signals for the InGaAs virtual substrate, after L-shift correction. The calculated values of these peak movements are shown in figure 6.6b. Similar to the GaAs(111) virtual substrate, the magnitudes of the movements show the trend expected for a change to the out-of-plane lattice parameter, corresponding to an increase of the out-of-plane L value and a decrease of the in-plane H and K values.

CTR separate line analysis: GaAs signal

Detector images in figure 6.9 are from the [01L] scans, obtained before and after GaAs deposition. These images show the appearance of a signal around L=1 in scans taken after GaAs deposition, which appears at the same y-axis position as the GaAs(111) substrate signals. A signal from GaSb(111) can also be seen in the scan from the

InGaAs(111)A virtual substrate prior to GaAs deposition, which matches with the interdiffusion results presented in Chapter 4. Scan profiles obtained using a signal ROI box centred on the GaAs(111) signals are shown in figures 6.10 and 6.11. These show the appearence of extra signals at L=1,4 and 7. These have been attributed to GaAs(111) signals occurring due to parts of the deposited GaAs(111) overlayer adopting a stacking structure which is twinned relative to the bulk substrate.

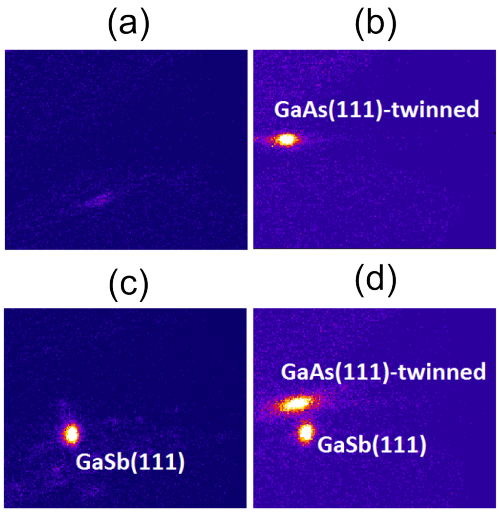

Figure 6.9: Detector images from [01L] scans near L=1.0, for the GaAs(111) virtual substrate (a) before and (b) after GaAs deposition, and the InGaAs(111) virtual substrate (c) before and (d) after GaAs deposition.

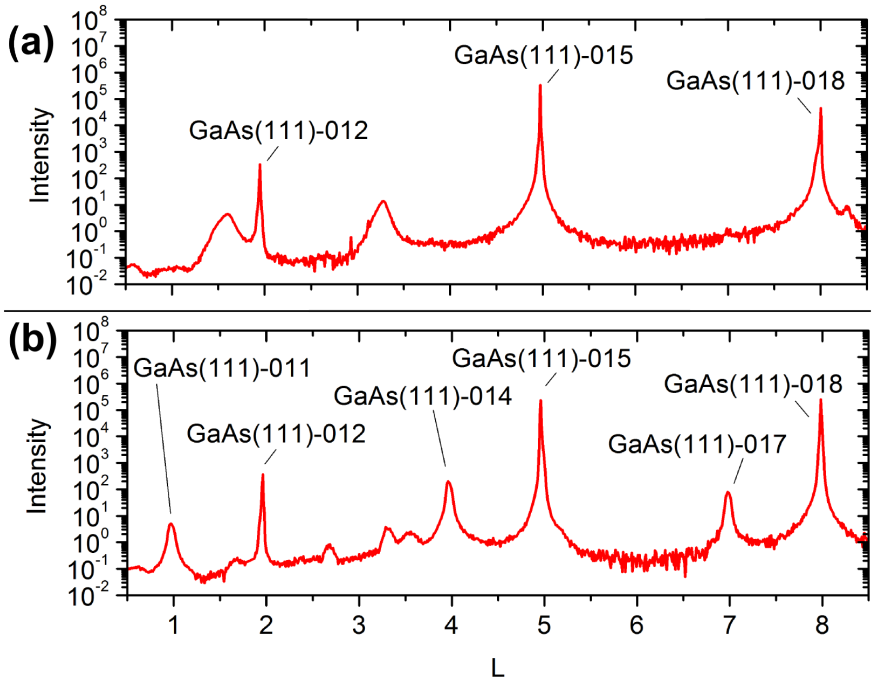

Figure 6.10: Line profiles obtained from <01L> CTR scans on GaAs(111)A virtual substrate sample (a) before, and (b) after GaAs deposition. Obtained using a region of interest centered on GaAs signals, with no back ground removal. Unlabelled peaks are due to background contributions from nearby signals at different x-positions.

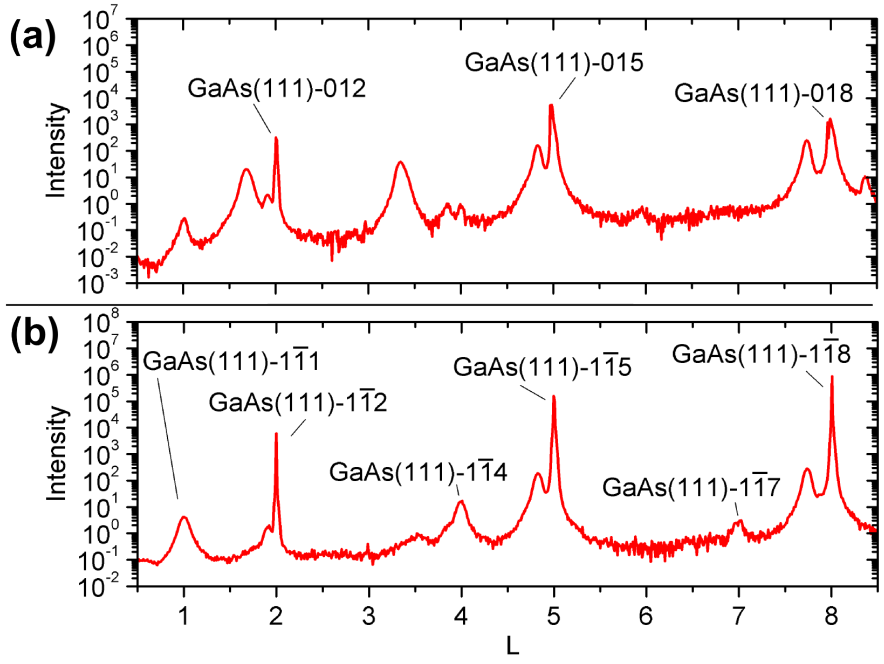

Figure 6.11: Line profiles obtained from <01L> CTR scans on InGaAs(111)A virtual substrate sample (a) before, and (b) after GaAs deposition. Obtained using a region of interest centered on GaAs signals, with no back ground removal. Unlabelled peaks are due to background contributions from nearby signals at different x-positions.

In-plane scans

To provide extra information about the in-plane properties of the sample layers, in-plane scans were recorded. Due to time restrictions of the experiment it was not possible to obtain a full in-plane dataset, but useful information was still obtainable from the smaller dataset. The in-plane scans obtained from the GaAs(111) and InGaAs(111) virtual substrates are shown in figures 6.12 and 6.13 respectively. The $[H\,K\,0]$ scans show signals around H (and K)= 1.09, and the $[H00]$ and $[0K0]$ scans show a signal at H (or K) = 2.17. The most likely identities of these signals are n-MnAs(11$\bar{2}$0) (Q_z= 1.093) and n-MnAs(20$\bar{2}$0)(Q_z= 2.186).

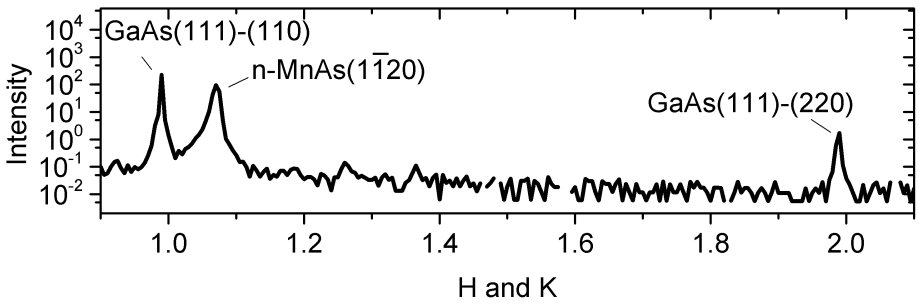

Figure 6.12: In-plane [H K 0] scan measured from GaAs(111)A virtual substrate after GaAs deposition

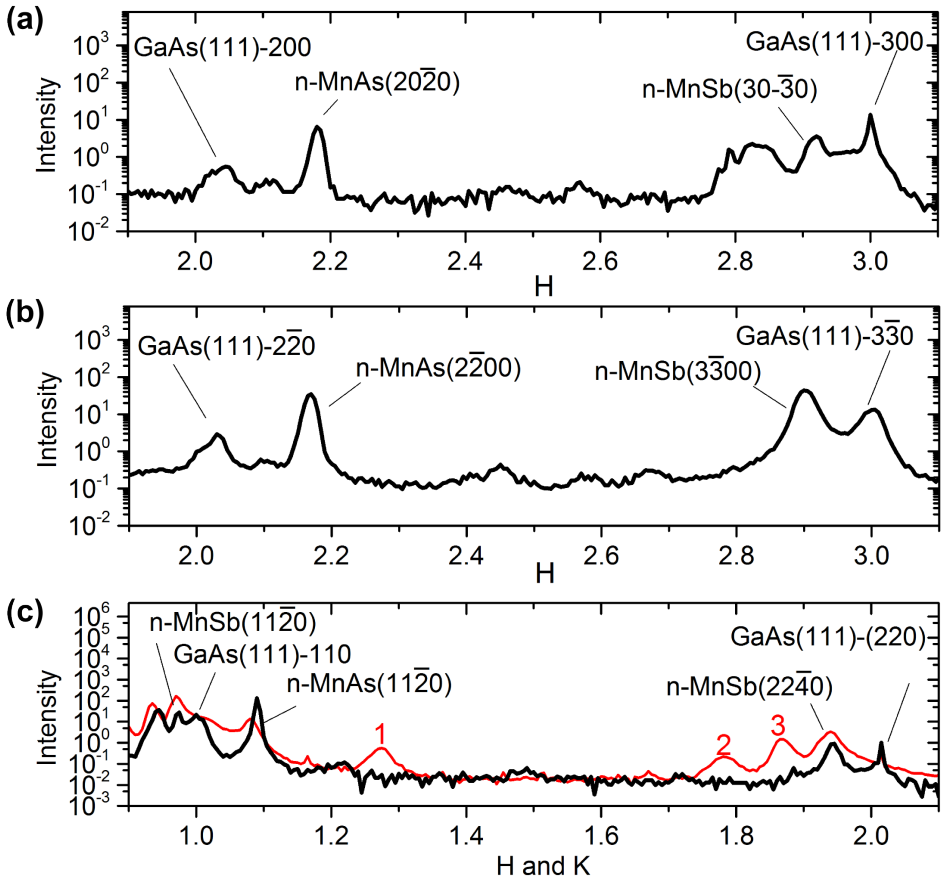

Figure 6.13: (a)[H 0 0], (b) [H -K 0], and [H K 0] scans taken from InGaAs(111)A virtual substrate. Red(Black) lines are scans taken before(after) GaAs deposition.

The Materials project database contains the elastic stiffness matrix for both GaAs and MnSb (codes mp-2534 and mp-786 respectively), which were calculated

as described by DeJong et al [157]. These stiffness matrices were analysed using the online tool ELATE [158], which produced Voigt averaged elastic values shown in table 6.3. The larger Youngs modulus for MnSb shows that stresses on this material cause a smaller linear change in lattice parameter. The smaller Poisson ratio shows that for in-plane lattice deformations MnSb has a smaller corresponding out-of-plane lattice deformation.

	GaAs	MnSb
Young modulus (GPa)	100.85	102.66
Poisson ratio	0.216	0.187

Table 6.3: Average elastic values for GaAs and MnSb, calculated using the ELATE online analysis tool with a Voigt averaging scheme

These elastic properties demonstrate that MnSb is less susceptible to stress forces when compared to GaAs. and when combined with the finding of potential MnAs signals in the samples after GaAs deposition indicates that the shift in n-MnSb out-of-plane lattice parameter observed for both (111) virtual substrates could be related to the formation of MnAs at the MnSb surface. These MnAs inclusions would form via the substitution of As onto the Sb sites within MnSb. As well as the formation of MnAs inclusions, the formation of alloyed areas of $MnAs_{1-x}Sb_x$ could also be a contributing factor to the change in lattice parameter.

6.3.3 GaAs(001) virtual substrate

RHEED

The MnSb($1\bar{1}01$) is a low symmetry surface, which means that for GaAs overlayer growth in a single orientation a low symmetry RHEED pattern would be expected. Typical RHEED patterns recorded during GaAs deposition along the [110] and the [$1\bar{1}0$] are shown in figure 6.14. The spotty pattern seen in both images is due to transmission diffraction occurring through epitaxial GaAs islands. These two almost identical patterns were collected with a difference in sample rotation of 90°, which

shows that the GaAs overlayer is four-fold symmetric. A plausible explanation for this would be the epitaxial relation GaAs(001)‖MnSb(1$\bar{1}$01), which is discussed in the next section.

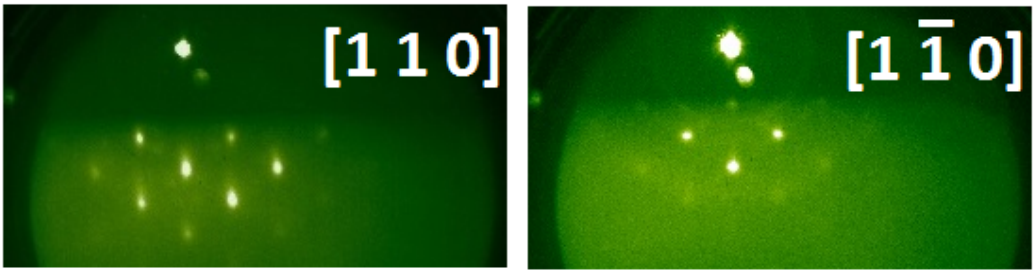

Figure 6.14: RHEED patterns for directions separated by 90°, recorded after GaAs deposition onto GaAs(001) virtual substrate

GaAs(001)‖ MnSb(1$\bar{1}$01) epitaxial relationship considerations

The surface of GaAs(001) is a square lattice with parameter b = 4.00 Å. In terms of bonding, GaAs(001) has 180° rotational symmetry due to the directionality of the surface dangling bonds. For successful epitaxy this square array needs to be matched with the oblique surface unit mesh of MnSb(1$\bar{1}$01). Using bulk n-MnSb lattice parameters ($a = 4.128$Å, $c = 5.789$Å) the relative mismatches can be calculated between the n-MnSb(1$\bar{1}$01) and GaAs(001). The in-plane mismatch is between the GaAs b and n-MnSb[$\bar{1}$102] , $y = \sqrt{c^2 + \frac{3a^2}{4}} = 6.804$ Å(figure 6.15).

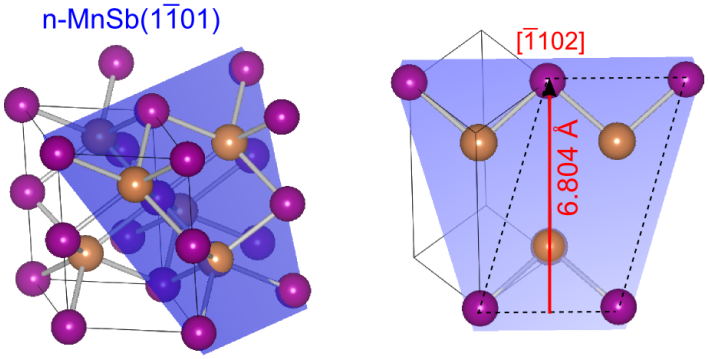

Figure 6.15: (left) MnSb (1$\bar{1}$01) plane relative to the n-MnSb unit cell (right) top down view of the MnSb (1$\bar{1}$01) plane

Comparing integer multiples of these two distances gives the first approximate match, allowing for a few % distortion, as $3y \approx 5b$. However using this a surface mesh would mean that Ga atoms are left midway between the surface Sb atoms. Doubling the distance along n-MnSb[$\bar{1}\bar{1}$02] gives a closer possible match as shown in figure 6.16. The common interface area [76] is $10b^2 = 160$ Å^2, which when using the GaAs(001) primitive mesh as the basis gives an interfacial superlattice of:

$$\begin{pmatrix} 10 & 3 \\ 0 & 1 \end{pmatrix}$$

There are four possible terminations for the n-MnSb(1$\bar{1}$01) surface [159], and density functonal theory (DFT) calculations indicate that the Sb-termination shown in the upper panel of figure 6.16 is the most stable [160]. Metal-pnictogen bonds have been shown to be favourable in all of our groups on-going MnSb/III-V interface DFT calculations [161]. Based on these considerations a possible interfacial relation is presented in the lower panel of figure 6.16. This allows Ga atoms to attach in rows to the terminating Sb atomic rows along n-MnSb[11$\bar{2}$0]. It seems possible that this interface could also allow Ga-Sb bonding to occur at several points adjacent to the third layer row of MnSb (Sb atoms labelled 3 in figure 6.16). Based on the GaAs-on-MnSb(0001) results present earlier in this chapter, it seems likely that

most of the interfacial strain is absorbed in the MnSb rather than GaAs. This would lead to MnSb experiencing compressive distortion along $[11\bar{2}0]$(-3.20%) and tensile distortion along the $[\bar{1}102]$(+2.06%).

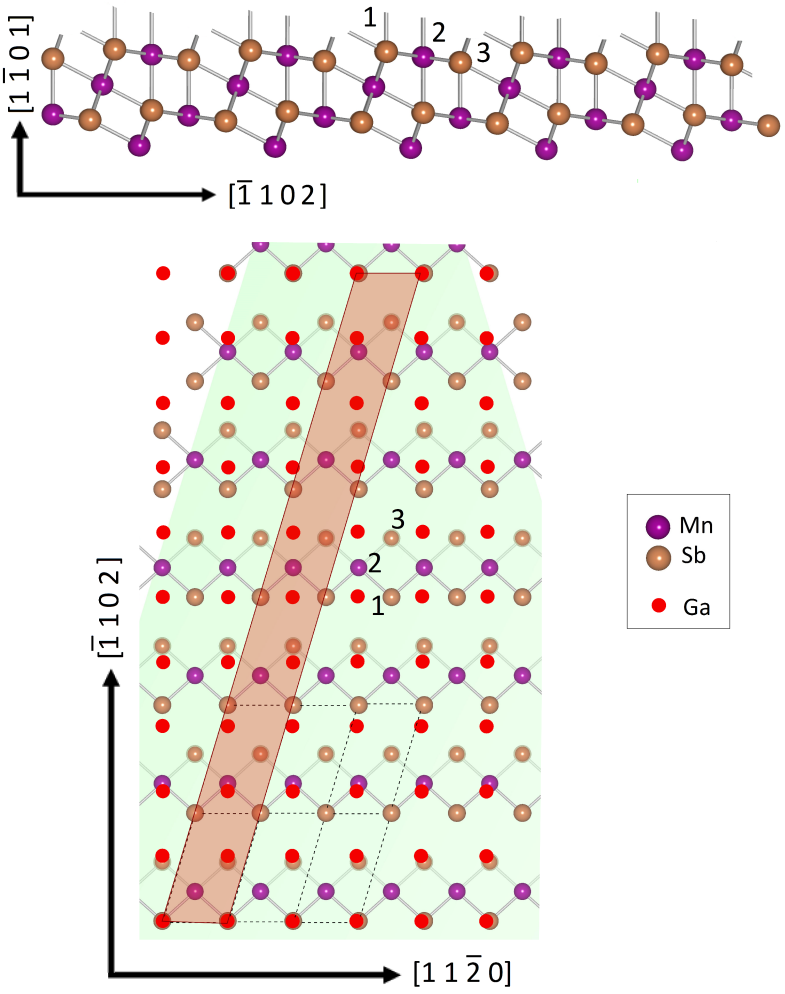

Figure 6.16: Plausible epitaxy for GaAs(001) on MnSb(1101). (upper) a side view of Sb-terminated MnSb(1101) projected on to the (1100) plane. (lower) plan view includes the top three atomic layers of MnSb (labeled as 1, 2, and 3 in both panels) and, to scale, a layer of Ga atoms (red) on GaAs(001). Crystallographic directions refer to the MnSb substrate.

6.4 Summary

This chapter presented results on the growth of tri-layer heterostructures, via the deposition of GaAs onto MnSb/$In_{1-x}Ga_xAs$ virtual substrates. This data shows that even with sub-optimal MnSb growth and surface preparation, GaAs overlayers can be grown onto the MnSb virtual substrates. For both MnSb(0001)/GaAs(111)A and MnSb/InGaAs(111)A virtual substrates it was found that upon deposition the MnSb layer undergoes a compression along the out-of-plane direction and a extension along the in plane direction. It was also found that the deposited GaAs overlayer for both virtual substrates contains twinned domains. A potential cause of the change in strain state to a smaller out-of-plane lattice parameter could be the formation of MnAs at the MnSb surface. For GaAs overlayer deposition onto the MnSb($1\bar{1}01$)/GaAs(001) virtual substrate it was shown that growth proceeds via 3D islands. Using a common matching interface area, a possible epitaxial relation between the MnSb($1\bar{1}01$) and the GaAs(001) surfaces is proposed.

Chapter 7

Conclusions and future work

7.1 Summary

In this thesis surface x-ray diffraction, along with a range of other complementary techniques, has been used to investigate the deposition of spintronic thin films onto $In_{1-x}Ga_xAs$ substrates. The first experimental chapter focussed on the early stages of deposition for ultra-thin Sb films onto InAs(111)B. It was shown that smooth layers of Sb with good interfaces to the InAs(111)A substrate can be grown, with CTR profile fitting revealing several growth features. For deposition at high temperature Sb layer deposition does not occur, however the top layer of As is mostly substituted for Sb. A substrate temperature of room temperature was found to enable Sb layer-by-layer deposition, which means that the Sb/InAs(111) system is highly applicable for further thin Sb film fundamental research as well as integration into novel electronic devices.

The second experimental chapter presented results of a growth study of MnSb on InGaAs(111)A, and showed that film growth can be strongly influenced by small changes to growth settings, with the flattest surface and a sharpest interface requiring slightly different growth conditions. This indicates that the optimum growth conditions are somewhere between the two, and differ from those found previously

for growth of MnSb on GaAs(111). The use of a two-stage growth process was found to improve the quality of the MnSb layer, but some intermixing at the interface was still observed. This suggests that a slightly longer initial low-temperature deposition stage is required to prevent interactions between the interface region and the growing overlayer.

The third experimental chapter compared the growth of MnSb on GaAs(111)A to growth on GaAs(111)B. It was found that initial stages of MnSb deposition proceeds by layer-by-layer growth on GaAs(111)A, but via 3D island processes on GaAs(111)B. XRD showed that this difference in initial growth led to higher quality films on (111)A surfaces. Fitting of CTR sections showed that films on both substrates formed an alloyed $GaAs_{1-x}Sb_x$ layer at the interface, which suggests that the growth conditions used do not lead to ideal interface formation. Evidence was found of a possible second strain state for n-MnSb within a 5 nm MnSb/GaAs(111)B sample.

The fourth and final experimental chapter showed initial results for the growth of multilayer heterostructures involving MnSb layers. It was shown that growth of epitaxial GaAs/MnSb/$In_{1-x}Ga_xAs$ was possible, and that the GaAs overlayer causes a change in the strain state of the MnSb layer. The change in strain state was attributed to the formation of MnAs at the MnSb surface. It was shown that crystalline growth of GaAs onto MnSb($1\bar{1}01$) was possible, and a plausible epitaxial relation was proposed.

7.2 Future Work

7.2.1 Sb/InAs(111)B

For this work an initial extension would be a comparison to Sb deposition onto InAs(111)A surfaces, to highlight what effects the surface termination has on the structure of the Sb layer and consequently the transport properties. Also an in-depth

study of transportation properties of these films would be useful in pin-pointing the key features of growth which can be linked to the anomalous transport measurements. Crystal structures obtained from SXRD data fitting can also now be used in future DFT calculations.

7.2.2 MnSb/InGaAs(111)A

A further investigation is needed to find the optimum growth conditions (i.e. smooth surface and sharp interface without interdiffusion) for MnSb growth on InGaAs(111)A, concentrating on fluxes between $J_{Sb/Mn} = 3.5 - 6.5$ using a growth temperature of $T_{sub} = 415°C$.Also a study of the effect that the duration of the low temperature deposition stage has for two-stage growth samples would be useful. The hexagonal morphology growth observed raises the possibility of incorporating MnSb layers into hexagonal InGaAs/GaAs nanopillars similar to those reported by Yang *et al.* [162]. Another possibility is an investigation looking at growth using higher quality InGaAs(111) virtual substrates which incorporate an InAs interlayer as described recently by Manoe *et al.* [163]. A detailed comparison to growth of MnSb on InGaAs(001) would also improve the understanding of interface dynamics between these two materials.

7.2.3 MnSb/GaAs(111)A Vs (111)B

Further analysis of the decapping procedure used to remove Sb caps is needed, highlighting any differences between settings required for (111)A and (111)B surfaces. Improved surface decapping procedures would allow the possibility to carry out a (111)A Vs (111)B SXRD comparison of the MnSb surface reconstructions. A possible extension of the MnSb deposition could be to study multiple additional thicknesses between 5 nm and 100 nm, to see if the differences observed are consistent at different thickness. The use of As flux during surface preparation, as well as a GaAs buffer layer, could be investigated to try to minimise the interdiffusion at the interface.

7.2.4 GaAs/MnSb/Ga(In)As

Similar to work on GaAs(111), there needs to be further analysis on the decapping procedure required for capped samples grown on Ga(In)As(111)A and GaAs(001). Once the decapping procedure has been perfected this will allow further studies of more complex multilayer samples. To better understand the interface between MnSb($1\bar{1}01$) and GaAs(001) a growth study of MnSb/GaAs(001) would be beneficial. Growth of multi-layer structures could also be extended to the (111)B surface terminations.

Bibliography

[1] Igor Žutić, Jaroslav Fabian, and S. Das Sarma. Spintronics: Fundamentals and applications. *Reviews of Modern Physics*, 76(2):323–410, apr 2004. doi: 10.1103/revmodphys.76.323. URL https://doi.org/10.1103/revmodphys.76.323.

[2] Atsufumi Hirohata and Koki Takanashi. Future perspectives for spintronic devices. *Journal of Physics D: Applied Physics*, 47(19):193001, apr 2014. doi: 10.1088/0022-3727/47/19/193001. URL https://doi.org/10.1088/0022-3727/47/19/193001.

[3] G. A. Prinz. Magnetoelectronics. *Science*, 282(5394):1660–1663, nov 1998. doi: 10.1126/science.282.5394.1660. URL https://doi.org/10.1126/science.282.5394.1660.

[4] S. A. Wolf. Spintronics: A spin-based electronics vision for the future. *Science*, 294(5546):1488–1495, nov 2001. doi: 10.1126/science.1065389. URL https://doi.org/10.1126/science.1065389.

[5] M. Johnson. Magnetoelectronic memories last and last. *IEEE Spectrum*, 37 (2):33–40, 2000. doi: 10.1109/6.819927. URL https://doi.org/10.1109/6.819927.

[6] M. N. Baibich, J. M. Broto, A. Fert, F. Nguyen Van Dau, F. Petroff, P. Etienne, G. Creuzet, A. Friederich, and J. Chazelas. Giant magne-

toresistance of (001)fe/(001)cr magnetic superlattices. *Physical Review Letters*, 61(21):2472–2475, nov 1988. doi: 10.1103/physrevlett.61.2472. URL https://doi.org/10.1103/physrevlett.61.2472.

[7] Jagadeesh S. Moodera and George Mathon. Spin polarized tunneling in ferromagnetic junctions. *Journal of Magnetism and Magnetic Materials*, 200 (1-3):248–273, oct 1999. doi: 10.1016/s0304-8853(99)00515-6. URL https://doi.org/10.1016/s0304-8853(99)00515-6.

[8] Sining Mao, Yonghua Chen, Feng Liu, Xingfu Chen, Bin Xu, Puling Lu, M. Patwari, Haiwen Xi, Clif Chang, B. Miller, D. Menard, B. Pant, J. Loven, K. Duxstad, Shaoping Li, Zhengyong Zhang, A. Johnston, R. Lamberton, M. Gubbins, T. McLaughlin, J. Gadbois, Juren Ding, B. Cross, Song Xue, and P. Ryan. Commercial TMR heads for hard disk drives: characterization and extendibility at 300 gbit/in/sup 2/. *IEEE Transactions on Magnetics*, 42(2):97–102, feb 2006. doi: 10.1109/tmag.2005.861788. URL https://doi.org/10.1109/tmag.2005.861788.

[9] Zhi Gang Wang and Y. Nakamura. Spin tunneling random access memory (STram). *IEEE Transactions on Magnetics*, 32(5):4022–4024, 1996. doi: 10.1109/20.539250. URL https://doi.org/10.1109/20.539250.

[10] J. Akerman. APPLIED PHYSICS: Toward a universal memory. *Science*, 308 (5721):508–510, apr 2005. doi: 10.1126/science.1110549. URL https://doi.org/10.1126/science.1110549.

[11] Alexander Makarov, Thomas Windbacher, Viktor Sverdlov, and Siegfried Selberherr. CMOS-compatible spintronic devices: a review. *Semiconductor Science and Technology*, 31(11):113006, oct 2016. doi: 10.1088/0268-1242/31/11/113006. URL https://doi.org/10.1088/0268-1242/31/11/113006.

[12] R Jansen, S P Dash, S Sharma, and B C Min. Silicon spintronics with

ferromagnetic tunnel devices. *Semiconductor Science and Technology*, 27 (8):083001, jul 2012. doi: 10.1088/0268-1242/27/8/083001. URL https://doi.org/10.1088/0268-1242/27/8/083001.

[13] L. N. Liebermann, D. R. Fredkin, and H. B. Shore. Two-dimensional "ferromagnetism" in iron. *Physical Review Letters*, 22(11):539–541, mar 1969. doi: 10.1103/physrevlett.22.539. URL https://doi.org/10.1103/physrevlett.22.539.

[14] Charles Kane and Joel Moore. Topological insulators. *Physics World*, 24(02): 32–36, feb 2011. doi: 10.1088/2058-7058/24/02/36. URL https://doi.org/10.1088/2058-7058/24/02/36.

[15] Binghai Yan and Shou-Cheng Zhang. Topological materials. *Reports on Progress in Physics*, 75(9):096501, aug 2012. doi: 10.1088/0034-4885/75/9/096501. URL https://doi.org/10.1088/0034-4885/75/9/096501.

[16] Joel E. Moore. The birth of topological insulators. *Nature*, 464(7286):194–198, mar 2010. doi: 10.1038/nature08916. URL https://doi.org/10.1038/nature08916.

[17] R. A. de Groot, F. M. Mueller, P. G. van Engen, and K. H. J. Buschow. New class of materials: Half-metallic ferromagnets. *Physical Review Letters*, 50(25):2024–2027, jun 1983. doi: 10.1103/physrevlett.50.2024. URL https://doi.org/10.1103/physrevlett.50.2024.

[18] M. Fonin, Yu. S. Dedkov, R. Pentcheva, U. Rüdiger, and G. Güntherodt. Magnetite: a search for the half-metallic state. *Journal of Physics: Condensed Matter*, 19(31):315217, jul 2007. doi: 10.1088/0953-8984/19/31/315217. URL https://doi.org/10.1088/0953-8984/19/31/315217.

[19] H Kino. Gw study of half-metallic electronic structure of la0.7sr0.3mno3. *Physica B: Condensed Matter*, 329-333:858–859, may 2003. doi: 10.1016/

s0921-4526(02)02573-5. URL https://doi.org/10.1016/s0921-4526(02)02573-5.

[20] Ph Mavropoulos and I Galanakis. A review of the electronic and magnetic properties of tetrahedrally bonded half-metallic ferromagnets. *Journal of Physics: Condensed Matter*, 19(31):315221, jul 2007. doi: 10.1088/0953-8984/19/31/315221. URL https://doi.org/10.1088/0953-8984/19/31/315221.

[21] J S Kang, J G Park, C G Olson, S J Youn, and B I Min. Valence band and sb 4d core level photoemission of the XMnSb-type heusler compounds (x=pt, pd, ni). *Journal of Physics: Condensed Matter*, 7(19):3789–3800, may 1995. doi: 10.1088/0953-8984/7/19/013. URL https://doi.org/10.1088/0953-8984/7/19/013.

[22] M. I. Katsnelson, V. Yu. Irkhin, L. Chioncel, A. I. Lichtenstein, and R. A. de Groot. Half-metallic ferromagnets: From band structure to many-body effects. *Reviews of Modern Physics*, 80(2):315–378, apr 2008. doi: 10.1103/revmodphys.80.315. URL https://doi.org/10.1103/revmodphys.80.315.

[23] K. E. H. M. Hanssen, P. E. Mijnarends, L. P. L. M. Rabou, and K. H. J. Buschow. Positron-annihilation study of the half-metallic ferromagnet NiMnSb: Experiment. *Physical Review B*, 42(3):1533–1540, jul 1990. doi: 10.1103/physrevb.42.1533. URL https://doi.org/10.1103/physrevb.42.1533.

[24] D. J. Huang, L. H. Tjeng, J. Chen, C. F. Chang, W. P. Wu, S. C. Chung, A. Tanaka, G. Y. Guo, H.-J. Lin, S. G. Shyu, C. C. Wu, and C. T. Chen. Anomalous spin polarization and dualistic electronic nature ofCrO2. *Physical Review B*, 67(21), jun 2003. doi: 10.1103/physrevb.67.214419. URL https://doi.org/10.1103/physrevb.67.214419.

[25] K. A. Yates, W. R. Branford, F. Magnus, Y. Miyoshi, B. Morris, L. F. Cohen, P. M. Sousa, O. Conde, and A. J. Silvestre. The spin polarization of CrO2

revisited. *Applied Physics Letters*, 91(17):172504, oct 2007. doi: 10.1063/1.2801693. URL https://doi.org/10.1063/1.2801693.

[26] S.V. Chekmazov, S.I. Bozhko, A.A. Smirnov, A.M. Ionov, and A.A. Kapustin. STM/STS study of the sb (111) surface. *Physics Procedia*, 71:323–326, 2015. doi: 10.1016/j.phpro.2015.08.342. URL https://doi.org/10.1016/j.phpro.2015.08.342.

[27] Anubhav Jain, Shyue Ping Ong, Geoffroy Hautier, Wei Chen, William Davidson Richards, Stephen Dacek, Shreyas Cholia, Dan Gunter, David Skinner, Gerbrand Ceder, and Kristin A. Persson. Commentary: The materials project: A materials genome approach to accelerating materials innovation. *APL Materials*, 1(1):011002, jul 2013. doi: 10.1063/1.4812323. URL https://doi.org/10.1063/1.4812323.

[28] C. S. Barrett, P. Cucka, and K. Haefner. The crystal structure of antimony at 4.2, 78 and 298°k. *Acta Crystallographica*, 16(6):451–453, jun 1963. doi: 10.1107/s0365110x63001262. URL https://doi.org/10.1107/s0365110x63001262.

[29] S. Bengió, J.W. Wells, T.K. Kim, G. Zampieri, L. Petaccia, S. Lizzit, and Ph. Hofmann. The structure of sb(111) determined by photoelectron diffraction. *Surface Science*, 601(14):2908–2911, jul 2007. doi: 10.1016/j.susc.2007.04.251. URL https://doi.org/10.1016/j.susc.2007.04.251.

[30] Kristin Persson. Materials data on sb (sg:166) by materials project, 1 2015.

[31] J. C. Woicik, T. Kendelewicz, K. E. Miyano, P. L. Cowan, C. E. Bouldin, B. A. Karlin, P. Pianetta, and W. E. Spicer. Determination of the sb/si(111) interfacial structure by back-reflection x-ray standing waves and surface extended x-ray-absorption fine structure. *Physical Review B*, 44(7):3475–3478, aug 1991.

doi: 10.1103/physrevb.44.3475. URL https://doi.org/10.1103/physrevb.44.3475.

[32] T. Kendelewicz, J. C. Woicik, K. E. Miyano, S. A. Yoshikawa, P. Pianetta, and W. E. Spicer. Structural study of monolayers of sb on ge(111) with different surface reconstructions. *Journal of Vacuum Science & Technology A: Vacuum, Surfaces, and Films*, 12(4):1843–1847, jul 1994. doi: 10.1116/1.579015. URL https://doi.org/10.1116/1.579015.

[33] P. Moriarty. Island, trimer, and chain formation on the sb-terminated GaAs(111)b surface. *Journal of Vacuum Science & Technology B: Microelectronics and Nanometer Structures*, 14(2):1024, mar 1996. doi: 10.1116/1.588447. URL https://doi.org/10.1116/1.588447.

[34] J.R. Power and J.F. McGilp. Optical second harmonic generation from the si(111)-sb interface. *Applied Surface Science*, 63(1-4):111–114, jan 1993. doi: 10.1016/0169-4332(93)90073-k. URL https://doi.org/10.1016/0169-4332(93)90073-k.

[35] H. Jorke. Surface segregation of sb on si(100) during molecular beam epitaxy growth. *Surface Science*, 193(3):569–578, jan 1988. doi: 10.1016/0039-6028(88)90454-2. URL https://doi.org/10.1016/0039-6028(88)90454-2.

[36] M. Copel, M. C. Reuter, Efthimios Kaxiras, and R. M. Tromp. Surfactants in epitaxial growth. *Physical Review Letters*, 63(6):632–635, aug 1989. doi: 10.1103/physrevlett.63.632. URL https://doi.org/10.1103/physrevlett.63.632.

[37] Sabrina Oppo, Vincenzo Fiorentini, and Matthias Scheffler. Theory of adsorption and surfactant effect of sb on ag(111). *Physical Review Letters*, 71(15):2437–2440, oct 1993. doi: 10.1103/physrevlett.71.2437. URL https://doi.org/10.1103/physrevlett.71.2437.

[38] C. Nowak, A. Chassé, W. Braun, W. Richter, I.T. McGovern, and D.R.T. Zahn. Antimony adsorption on III–v(110) surfaces: Growth and structure studied by photoemission and photoelectron diffraction. *Journal of Electron Spectroscopy and Related Phenomena*, 80:143–146, may 1996. doi: 10.1016/0368-2048(96)02942-8. URL https://doi.org/10.1016/0368-2048(96)02942-8.

[39] T. Kendelewicz, J. C. Woicik, A. Herrera-Gomez, K. E. Miyano, P. L. Cowan, B. A. Karlin, P. Pianetta, and W. E. Spicer. X-ray standing wave study of the sb/GaAs(110) interface structure. *Journal of Vacuum Science & Technology A: Vacuum, Surfaces, and Films*, 11(4):2351–2353, jul 1993. doi: 10.1116/1.578331. URL https://doi.org/10.1116/1.578331.

[40] T. Kendelewicz. Structure of sb monolayers on ge(111)2x1: A combined study using core-level photoemission, x-ray standing waves, and surface extended x-ray absorption fine structure. *Journal of Vacuum Science & Technology B: Microelectronics and Nanometer Structures*, 11(4):1449, jul 1993. doi: 10.1116/1.586958. URL https://doi.org/10.1116/1.586958.

[41] W. C. Wang, J. A. Dura, J. T. Zborowski, A. Vigliante, H. C. Chen, T. D. Golding, and J. R. Meyer. Preparation of sb/gasb(111)-oriented multilayer structures using molecular-beam epitaxy and migration enhanced epitaxy. *Journal of Vacuum Science & Technology A: Vacuum, Surfaces, and Films*, 11(4):1001–1005, jul 1993. doi: 10.1116/1.578803. URL https://doi.org/10.1116/1.578803.

[42] Toshiyuki Kaizu, Masamitu Takahasi, Koichi Yamaguchi, and Jun'ichiro Mizuki. In situ determination of sb distribution in sb/GaAs(001) layer for high-density InAs quantum dot growth. *Journal of Crystal Growth*, 310 (15):3436–3439, jul 2008. doi: 10.1016/j.jcrysgro.2008.05.008. URL https://doi.org/10.1016/j.jcrysgro.2008.05.008.

[43] M.R Pillai, Scott C Theiring, S.A Barnett, Bruce W Wessels, Arvind Desikan, and Eric P. Kvam. Effect of sb pre-deposition on the compositional profiles in MOVPE-grown InAsSb/InAs(111) multi-quantum wells. *Journal of Crystal Growth*, 208(1-4):79–84, jan 2000. doi: 10.1016/s0022-0248(99)00452-2. URL https://doi.org/10.1016/s0022-0248(99)00452-2.

[44] Awadhesh Narayan, Ivan Rungger, and Stefano Sanvito. Topological surface states scattering in antimony. *Physical Review B*, 86(20), nov 2012. doi: 10.1103/physrevb.86.201402. URL https://doi.org/10.1103/physrevb.86.201402.

[45] Davide Campi, Marco Bernasconi, and Giorgio Benedek. Phonons and electron-phonon interaction at the sb(111) surface. *Physical Review B*, 86 (7), aug 2012. doi: 10.1103/physrevb.86.075446. URL https://doi.org/10.1103/physrevb.86.075446.

[46] Feng-Chuan Chuang, Chia-Hsiu Hsu, Chia-Yu Chen, Zhi-Quan Huang, Vidvuds Ozolins, Hsin Lin, and Arun Bansil. Tunable topological electronic structures in sb(111) bilayers: A first-principles study. *Applied Physics Letters*, 102 (2):022424, jan 2013. doi: 10.1063/1.4776734. URL https://doi.org/10.1063/1.4776734.

[47] Dongchao Wang, Li Chen, Hongmei Liu, and Xiaoli Wang. Topological phase transitions in sb(111) films driven by external strain and electric field. *EPL (Europhysics Letters)*, 104(5):57011, dec 2013. doi: 10.1209/0295-5075/104/57011. URL https://doi.org/10.1209/0295-5075/104/57011.

[48] Chi-Hsuan Lee and Chih-Kai Yang. Topological surface states revealed by sb thin films adsorbed with impurity atoms. *Physical Review B*, 87(11), mar 2013. doi: 10.1103/physrevb.87.115306. URL https://doi.org/10.1103/physrevb.87.115306.

[49] PengFei Zhang, Zheng Liu, Wenhui Duan, Feng Liu, and Jian Wu. Topological and electronic transitions in a sb(111) nanofilm: The interplay between quantum confinement and surface effect. *Physical Review B*, 85(20), may 2012. doi: 10.1103/physrevb.85.201410. URL https://doi.org/10.1103/physrevb.85.201410.

[50] A. A. Burkov. Topological semimetals. *Nature Materials*, 15(11):1145–1148, oct 2016. doi: 10.1038/nmat4788. URL https://doi.org/10.1038/nmat4788.

[51] M Mayrhofer-Reinhartshuber, A Tamtögl, P Kraus, and W E Ernst. Helium atom scattering investigation of the sb(111) surface. *Journal of Physics: Condensed Matter*, 25(39):395002, aug 2013. doi: 10.1088/0953-8984/25/39/395002. URL https://doi.org/10.1088/0953-8984/25/39/395002.

[52] Anton Tamtögl, Michael Mayrhofer-Reinhartshuber, Patrick Kraus, and Wolfgang E. Ernst. Surface debye temperature and vibrational dynamics of antimony(111) from helium atom scattering measurements. *Surface Science*, 617:225–228, nov 2013. doi: 10.1016/j.susc.2013.08.001. URL https://doi.org/10.1016/j.susc.2013.08.001.

[53] Guanggeng Yao, Ziyu Luo, Feng Pan, Wentao Xu, Yuan Ping Feng, and Xue sen Wang. Evolution of topological surface states in antimony ultra-thin films. *Scientific Reports*, 3(1), jun 2013. doi: 10.1038/srep02010. URL https://doi.org/10.1038/srep02010.

[54] T. Kadono, K. Miyamoto, R. Nishimura, K. Kanomaru, S. Qiao, K. Shimada, H. Namatame, A. Kimura, and M. Taniguchi. Direct evidence of spin-polarized band structure of sb(111) surface. *Applied Physics Letters*, 93(25):252107, dec 2008. doi: 10.1063/1.3049610. URL https://doi.org/10.1063/1.3049610.

[55] K. Sugawara, T. Sato, S. Souma, T. Takahashi, M. Arai, and T. Sasaki. Fermi

surface and anisotropic spin-orbit coupling of sb(111) studied by angle-resolved photoemission spectroscopy. *Physical Review Letters*, 96(4), feb 2006. doi: 10.1103/physrevlett.96.046411. URL https://doi.org/10.1103/physrevlett.96.046411.

[56] D Hsieh, L Wray, D Qian, Y Xia, J H Dil, F Meier, L Patthey, J Osterwalder, G Bihlmayer, Y S Hor, R J Cava, and M Z Hasan. Direct observation of spin-polarized surface states in the parent compound of a topological insulator using spin- and angle-resolved photoemission spectroscopy in a mott-polarimetry mode. *New Journal of Physics*, 12(12):125001, dec 2010. doi: 10.1088/1367-2630/12/12/125001. URL https://doi.org/10.1088/1367-2630/12/12/125001.

[57] A Takayama, T Sato, S Souma, and T Takahashi. Rashba effect in antimony and bismuth studied by spin-resolved ARPES. *New Journal of Physics*, 16 (5):055004, may 2014. doi: 10.1088/1367-2630/16/5/055004. URL https://doi.org/10.1088/1367-2630/16/5/055004.

[58] Kanta Ono, Masaki Shuzo, Masaharu Oshima, and Hiro Akinaga. Ga segregation in MnSb epitaxial growth on GaAs (100) and (111)bsubstrates. *Physical Review B*, 64(8), aug 2001. doi: 10.1103/physrevb.64.085328. URL https://doi.org/10.1103/physrevb.64.085328.

[59] J D Aldous, C W Burrows, I Maskery, M S Brewer, T P A Hase, J A Duffy, M R Lees, C Sánchez-Hanke, T Decoster, W Theis, A Quesada, A K Schmid, and G R Bell. Depth-dependent magnetism in epitaxial MnSb thin films: effects of surface passivation and cleaning. *Journal of Physics: Condensed Matter*, 24(14):146002, mar 2012. doi: 10.1088/0953-8984/24/14/146002. URL https://doi.org/10.1088/0953-8984/24/14/146002.

[60] Masaaki Tanaka. Ferromagnet (MnAs)/III v semiconductor hybrid structures.

Semiconductor Science and Technology, 17(4):327–341, mar 2002. doi: 10.1088/0268-1242/17/4/306. URL https://doi.org/10.1088/0268-1242/17/4/306.

[61] Wen-Hui Xie, Bang-Gui Liu, and D. G. Pettifor. Half-metallic ferromagnetism in transition metal pnictides and chalcogenides with wurtzite structure. *Physical Review B*, 68(13), oct 2003. doi: 10.1103/physrevb.68.134407. URL https://doi.org/10.1103/physrevb.68.134407.

[62] J. E. Pask, L. H. Yang, C. Y. Fong, W. E. Pickett, and S. Dag. Six low-strain zinc-blende half metals: anab initioinvestigation. *Physical Review B*, 67(22), jun 2003. doi: 10.1103/physrevb.67.224420. URL https://doi.org/10.1103/physrevb.67.224420.

[63] Jin-Cheng Zheng and James W. Davenport. Ferromagnetism and stability of half-metallic MnSb and MnBi in the strained zinc-blende structure: predictions from full potential and pseudopotential calculations. *Physical Review B*, 69(14), apr 2004. doi: 10.1103/physrevb.69.144415. URL https://doi.org/10.1103/physrevb.69.144415.

[64] James D. Aldous, Christopher W. Burrows, Ana M. Sánchez, Richard Beanland, Ian Maskery, Matthew K. Bradley, Manuel dos Santos Dias, Julie B. Staunton, and Gavin R. Bell. Cubic MnSb: Epitaxial growth of a predicted room temperature half-metal. *Physical Review B*, 85(6), feb 2012. doi: 10.1103/physrevb.85.060403. URL https://doi.org/10.1103/physrevb.85.060403.

[65] M Nishida. Surface relaxation effects on the electronic structure of (111) and (111) surfaces of GaP, GaAs, and GaSb. *Journal of Physics C: Solid State Physics*, 14(4):535–552, feb 1981. doi: 10.1088/0022-3719/14/4/025. URL https://doi.org/10.1088/0022-3719/14/4/025.

[66] G. M. Sipahi, S. C. P. Rodrigues, L. M. R. Scolfaro, and I. C. da Cunha Lima. Charge and spin distribution in ferromagnetic mn-doped InGaAsâĹŢGaAs multilayers. *Applied Physics Letters*, 85(25):6209–6211, dec 2004. doi: 10.1063/1.1840121. URL https://doi.org/10.1063/1.1840121.

[67] P. Barate, S. Liang, T. T. Zhang, J. Frougier, M. Vidal, P. Renucci, X. Devaux, B. Xu, H. Jaffrès, J. M. George, X. Marie, M. Hehn, S. Mangin, Y. Zheng, T. Amand, B. Tao, X. F. Han, Z. Wang, and Y. Lu. Electrical spin injection into InGaAs/GaAs quantum wells: A comparison between MgO tunnel barriers grown by sputtering and molecular beam epitaxy methods. *Applied Physics Letters*, 105(1):012404, jul 2014. doi: 10.1063/1.4887347. URL https://doi.org/10.1063/1.4887347.

[68] S. H. Liang, T. T. Zhang, P. Barate, J. Frougier, M. Vidal, P. Renucci, B. Xu, H. Jaffrès, J.-M. George, X. Devaux, M. Hehn, X. Marie, S. Mangin, H. X. Yang, A. Hallal, M. Chshiev, T. Amand, H. F. Liu, D. P. Liu, X. F. Han, Z. G. Wang, and Y. Lu. Large and robust electrical spin injection into GaAs at zero magnetic field using an ultrathin CoFeB/MgO injector. *Physical Review B*, 90 (8), aug 2014. doi: 10.1103/physrevb.90.085310. URL https://doi.org/10.1103/physrevb.90.085310.

[69] P. J. Simmonds, S. N. Holmes, H. E. Beere, I. Farrer, F. Sfigakis, D. A. Ritchie, and M. Pepper. Molecular beam epitaxy of high mobility in[sub 0.75]ga[sub 0.25]as for electron spin transport applications. *Journal of Vacuum Science & Technology B: Microelectronics and Nanometer Structures*, 27(4):2066, 2009. doi: 10.1116/1.3156736. URL https://doi.org/10.1116/1.3156736.

[70] A.Y. Cho and J.R. Arthur. Molecular beam epitaxy. *Progress in Solid State Chemistry*, 10:157–191, jan 1975. doi: 10.1016/0079-6786(75)90005-9. URL https://doi.org/10.1016/0079-6786(75)90005-9.

[71] D. J Dunstan. Strain and strain relaxation in semiconductors. *Journal of Materials Science Materials in Electronics*, 8(6):337–375, 1997. doi: 10.1023/a:1018547625106. URL https://doi.org/10.1023/a:1018547625106.

[72] John Ayers. *Heteroepitaxy of semiconductors : theory, growth, and characterization*. CRC Press, Boca Raton, 2007. ISBN 978-1-4200-0664-3.

[73] Vladimir Dubrovskii. *Nucleation theory and growth of nanostructures*. Springer, Berlin, Heidelberg, 2014. ISBN 978-3-642-39659-5.

[74] Christopher William Burrows. *Growth and Characterisation of MnSb Thin Films and Interfaces*. PhD thesis, Unviersity of Warwick, 2012. URL http://wrap.warwick.ac.uk/55927/.

[75] I K Robinson and D J Tweet. Surface x-ray diffraction. *Reports on Progress in Physics*, 55(5):599–651, may 1992. doi: 10.1088/0034-4885/55/5/002. URL https://doi.org/10.1088/0034-4885/55/5/002.

[76] A. Zur and T. C. McGill. Lattice match: An application to heteroepitaxy. *Journal of Applied Physics*, 55(2):378–386, jan 1984. doi: 10.1063/1.333084. URL https://doi.org/10.1063/1.333084.

[77] D. P. Woodruff. *Modern techniques of surface science*. Cambridge University Press, Cambridge New York, 1994. ISBN 0521424984.

[78] J Nielsen. *Elements of modern X-ray physics*. John Wiley, Chichester, West Sussex, 2011. ISBN 978-1-119-97015-6.

[79] E. Vlieg. A (2+3)-type surface diffractometer: Mergence of the z-axis and (2+2)-type geometries. *Journal of Applied Crystallography*, 31(2):198–203, apr 1998. doi: 10.1107/s0021889897009990. URL https://doi.org/10.1107/s0021889897009990.

[80] Chris Nicklin, Tom Arnold, Jonathan Rawle, and Adam Warne. Diamond beamline i07: a beamline for surface and interface diffraction. *Journal of Synchrotron Radiation*, 23(5):1245–1253, jul 2016. doi: 10.1107/s1600577516009875. URL https://doi.org/10.1107/s1600577516009875.

[81] Masamitu Takahasi, Yasuhiro Yoneda, Hirotane Inoue, Naomasa Yamamoto, and Jun'ichiro Mizuki. X-ray diffractometer for studies on molecular-beam-epitaxy growth of III–v semiconductors. *Japanese Journal of Applied Physics*, 41(Part 1, No. 10):6247–6251, oct 2002. doi: 10.1143/jjap.41.6247. URL https://doi.org/10.1143/jjap.41.6247.

[82] W. R. Busing and H. A. Levy. Angle calculations for 3- and 4-circle x-ray and neutron diffractometers. *Acta Crystallographica*, 22(4):457–464, apr 1967. doi: 10.1107/s0365110x67000970. URL https://doi.org/10.1107/s0365110x67000970.

[83] C. M. Schlepütz, R. Herger, P. R. Willmott, B. D. Patterson, O. Bunk, Ch. Brönnimann, B. Henrich, G. Hülsen, and E. F. Eikenberry. Improved data acquisition in grazing-incidence x-ray scattering experiments using a pixel detector. *Acta Crystallographica Section A Foundations of Crystallography*, 61(4):418–425, jun 2005. doi: 10.1107/s0108767305014790. URL https://doi.org/10.1107/s0108767305014790.

[84] Vladimir M. Kaganer. Crystal truncation rods in kinematical and dynamical x-ray diffraction theories. *Physical Review B*, 75(24), jun 2007. doi: 10.1103/physrevb.75.245425. URL https://doi.org/10.1103/physrevb.75.245425.

[85] E. Vlieg. Integrated intensities using a six-circle surface x-ray diffractometer. *Journal of Applied Crystallography*, 30(5):532–543, oct 1997. doi: 10.1107/s0021889897002537. URL https://doi.org/10.1107/s0021889897002537.

[86] D.Kaminski. Winrod for surface diffraction modeling, 2010. URL http://www.kaminski.up.lublin.pl/WinRod.html.

[87] Elias Vlieg. ROD: a program for surface x-ray crystallography. *Journal of Applied Crystallography*, 33(2):401–405, apr 2000. doi: 10.1107/s0021889899013655. URL https://doi.org/10.1107/s0021889899013655.

[88] Sander Roobol, Willem Onderwaater, Jakub Drnec, Roberto Felici, and Joost Frenken. BINoculars: data reduction and analysis software for two-dimensional detectors in surface x-ray diffraction. *Journal of Applied Crystallography*, 48 (4):1324–1329, jun 2015. doi: 10.1107/s1600576715009607. URL https://doi.org/10.1107/s1600576715009607.

[89] P. Ramachandran and G. Varoquaux. Mayavi: 3D Visualization of Scientific Data. *Computing in Science & Engineering*, 13(2):40–51, 2011. ISSN 1521-9615.

[90] Ayahiko Ichimiya. *Reflection high-energy electron diffraction*. Cambridge University Press, Cambridge, U.K. New York, 2004. ISBN 0521453739.

[91] John E. Mahan, Kent M. Geib, G. Y. Robinson, and Robert G. Long. A review of the geometrical fundamentals of reflection high-energy electron diffraction with application to silicon surfaces. *Journal of Vacuum Science & Technology A: Vacuum, Surfaces, and Films*, 8(5):3692–3700, sep 1990. doi: 10.1116/1.576481. URL https://doi.org/10.1116/1.576481.

[92] P. Laukkanen, J. Sadowski, and M. Guina. Surface studies by low-energy electron diffraction and reflection high-energy-electron diffraction. In *Semiconductor Research*, pages 1–21. Springer Berlin Heidelberg, 2012. doi: 10.1007/978-3-642-23351-7_1. URL https://doi.org/10.1007/978-3-642-23351-7_1.

[93] David Nečas and Petr Klapetek. Gwyddion: an open-source software for SPM data analysis. *Open Physics*, 10(1), jan 2012. doi: 10.2478/s11534-011-0096-2. URL https://doi.org/10.2478/s11534-011-0096-2.

[94] Jingyue Liu. High-resolution scanning electron microscopy. In *Handbook of Microscopy for Nanotechnology*, pages 325–359. Kluwer Academic Publishers. doi: 10.1007/1-4020-8006-9_11. URL https://doi.org/10.1007/1-4020-8006-9_11.

[95] W.F.J. Slijkerman, P.M. Zagwijn, J.F. van der Veen, D.J. Gravesteijn, and G.F.A. van de Walle. The interaction of sb overlayers with si(001). *Surface Science*, 262(1-2):25–32, feb 1992. doi: 10.1016/0039-6028(92)90456-g. URL https://doi.org/10.1016/0039-6028(92)90456-g.

[96] R. Hunger, N. Blick, N. Esser, M. Arens, W. Richter, V. Wagner, and J. Geurts. Growth of sb on si(111) studied by raman scattering. *Surface Science*, 307-309:1061–1065, apr 1994. doi: 10.1016/0039-6028(94)91540-7. URL https://doi.org/10.1016/0039-6028(94)91540-7.

[97] G. Bian, T. Miller, and T.-C. Chiang. Passage from spin-polarized surface states to unpolarized quantum well states in topologically nontrivial sb films. *Physical Review Letters*, 107(3), jul 2011. doi: 10.1103/physrevlett.107.036802. URL https://doi.org/10.1103/physrevlett.107.036802.

[98] Strozak. Early stage of sb ultra-thin film growth: Crystal structure and electron band structure. *Condensed Matter*, 1(1):11, dec 2016. doi: 10.3390/condmat1010011. URL https://doi.org/10.3390/condmat1010011.

[99] Hartmut Höchst and Christian R Ast. The fermi surfaces of thin sb(111) films. *Journal of Electron Spectroscopy and Related Phenomena*, 137-140:441–444, jul 2004. doi: 10.1016/j.elspec.2004.02.057. URL https://doi.org/10.1016/j.elspec.2004.02.057.

[100] R. Strümpler and H. Lüth. Growth of sb overlayers on GaAs(110). *Surface Science*, 182(3):545–556, apr 1987. doi: 10.1016/0039-6028(87)90019-7. URL https://doi.org/10.1016/0039-6028(87)90019-7.

[101] A.A. Cafolla, C. McGinley, E. McLoughlin, G. Hughes, P. Moriarty, A.W. Dunn, Y.-R. Ma, D. Teehan, B. Murphy, S. Downes, and D.A. Woolf. Adsorption of sb on GaAs(111)b studied by photoemission and low energy electron diffraction. *Surface Science*, 377-379:130–134, apr 1997. doi: 10.1016/s0039-6028(96)01379-9. URL https://doi.org/10.1016/s0039-6028(96)01379-9.

[102] J. Carelli and A. Kahn. LEED-AES-TDS characterization of sb overlayers on GaAs(110). *Surface Science*, 116(2):380–390, apr 1982. doi: 10.1016/0039-6028(82)90441-1. URL https://doi.org/10.1016/0039-6028(82)90441-1.

[103] S. Srinivasan, L. Geng, R. Liu, F. A. Ponce, Y. Narukawa, and S. Tanaka. Slip systems and misfit dislocations in InGaN epilayers. *Applied Physics Letters*, 83(25):5187–5189, dec 2003. doi: 10.1063/1.1633029. URL https://doi.org/10.1063/1.1633029.

[104] S. Ichikawa, N. Sanada, N. Utsumi, and Y. Fukuda. Surface structures and electronic states of clean and (NH4)2sx-treated InAs(111)a and (111)b. *Journal of Applied Physics*, 84(7):3658–3663, oct 1998. doi: 10.1063/1.368594. URL https://doi.org/10.1063/1.368594.

[105] Anna Bergamaschi. Experience and results from the 6 megapixel pilatus system. In *Vertex 2007*, 2007.

[106] Christian Chatillon and Dominique Chatain. Congruent vaporization of GaAs(s) and stability of ga(l) droplets at the GaAs(s) surface. *Journal of Crys-*

tal Growth, 151(1-2):91–101, may 1995. doi: 10.1016/0022-0248(95)00044-5. URL https://doi.org/10.1016/0022-0248(95)00044-5.

[107] Songphol Kanjanachuchai and Pat Photongkam. Dislocation-guided self-running droplets. *Crystal Growth & Design*, 15(1):14–19, jan 2015. doi: 10.1021/cg5013704. URL https://doi.org/10.1021/cg5013704.

[108] Yongjun Hu, M. B. Jost, T. J. Wagener, and J. H. Weaver. Long-range ordering of sb multilayers on GaAs(110): Evolution of resonant inverse photoemission. *Physical Review B*, 42(11):7050–7057, oct 1990. doi: 10.1103/physrevb.42.7050. URL https://doi.org/10.1103/physrevb.42.7050.

[109] Chong-Yun Park, Tadashi Abukawa, Toyohiko Kinoshita, Yoshiharu Enta, and Shozo Kono. Low energy electron diffraction and x-ray photoelectron spectroscopy studies of the formation of submonolayer interfaces of sb/si(111). *Japanese Journal of Applied Physics*, 27(Part 1, No. 1):147–148, jan 1988. doi: 10.1143/jjap.27.147. URL https://doi.org/10.1143/jjap.27.147.

[110] Ki-Seok An, Chan-Cuk Hwang, Chong-Yun Park, and Akito Kakizaki. Low-energy electron diffraction and x-ray photoelectron spectroscopy studies of sb-induced reconstruction on si(113)3x2 surface. *Japanese Journal of Applied Physics*, 39(Part 1, No. 5A):2771–2774, may 2000. doi: 10.1143/jjap.39.2771. URL https://doi.org/10.1143/jjap.39.2771.

[111] K.S An, C.C Hwang, Y.K Kim, E.S Cho, C.-Y Park, and A Kakizaki. Epitaxial growth of sb thin film and chemical reaction of sb-induced surface reconstruction on si(113)3x2. *Surface Science*, 492(1-2):L705–L710, oct 2001. doi: 10.1016/s0039-6028(01)01441-8. URL https://doi.org/10.1016/s0039-6028(01)01441-8.

[112] C.B.M. Andersson, U.O. Karlsson, M.C. Håkansson, L.Ö. Olsson, L. Ilver, J. Kanski, P.-O. Nilsson, and P.E.S. Persson. Sputtered and annealed

InAs() : an unreconstructed surface. *Surface Science*, 307-309:885–889, apr 1994. doi: 10.1016/0039-6028(94)91509-1. URL https://doi.org/10.1016/0039-6028(94)91509-1.

[113] Fumihiko Maeda, Yoshio Watanabe, and Masaharu Oshima. Surface termination of GaAs(001) by sb dimers. *Surface Science*, 357-358:540–544, jun 1996. doi: 10.1016/0039-6028(96)00219-1. URL https://doi.org/10.1016/0039-6028(96)00219-1.

[114] M. W. Wang. X-ray photoelectron spectroscopy investigation of the mixed anion GaSb/InAs heterointerface. *Journal of Vacuum Science & Technology B: Microelectronics and Nanometer Structures*, 11(4):1418, jul 1993. doi: 10.1116/1.586952. URL https://doi.org/10.1116/1.586952.

[115] Fumihiko Maeda, Yoshio Watanabe, and Masaharu Oshima. Sb-induced surface reconstruction on GaAs(001). *Physical Review B*, 48(19):14733–14736, nov 1993. doi: 10.1103/physrevb.48.14733. URL https://doi.org/10.1103/physrevb.48.14733.

[116] H. Kosaka, A.A. Kiselev, F.A. Baron, Ki Wook Kim, and E. Yablonovitch. Electron g factor engineering in III-v semiconductors for quantum communications. *Electronics Letters*, 37(7):464, 2001. doi: 10.1049/el:20010314. URL https://doi.org/10.1049/el:20010314.

[117] Tomohiro Amemiya, Yusuke Ogawa, Hiromasa Shimizu, Hiro Munekata, and Yoshiaki Nakano. Semiconductor waveguide optical isolator incorporating ferromagnetic epitaxial MnSb for high temperature operation. *Applied Physics Express*, 1:022002, jan 2008. doi: 10.1143/apex.1.022002. URL https://doi.org/10.1143/apex.1.022002.

[118] GAVIN R. BELL, CHRISTOPHER W. BURROWS, THOMAS P. A. HASE, MARK J. ASHWIN, SEAN R. C. MCMITCHELL, ANA M. SANCHEZ,

and JAMES D. ALDOUS. EPITAXIAL GROWTH OF CUBIC MnSb ON GaAs AND InGaAs(111). *SPIN*, 04(04):1440025, dec 2014. doi: 10.1142/s2010324714400256. URL https://doi.org/10.1142/s2010324714400256.

[119] Akihiro Ohtake and Toru Akiyama Tomonori Ito. As-rich (2x2) surface reconstruction on GaAs(111)a. *Surface Science*, 606(23-24):1864–1870, dec 2012. doi: 10.1016/j.susc.2012.07.029. URL https://doi.org/10.1016/j.susc.2012.07.029.

[120] K. W. Haberern and M. D. Pashley. GaAs(111)a-(2x2) reconstruction studied by scanning tunneling microscopy. *Physical Review B*, 41(5):3226–3229, feb 1990. doi: 10.1103/physrevb.41.3226. URL https://doi.org/10.1103/physrevb.41.3226.

[121] E. Kaxiras, Y. Bar-Yam, J. D. Joannopoulos, and K. C. Pandey. Ab initiotheory of polar semiconductor surfaces. i. methodology and the (2x2) reconstructions of GaAs(111). *Physical Review B*, 35(18):9625–9635, jun 1987. doi: 10.1103/physrevb.35.9625. URL https://doi.org/10.1103/physrevb.35.9625.

[122] L. Ö. Olsson, L. Ilver, J. Kanski, P. O. Nilsson, C. B. M. Andersson, U. O. Karlsson, and M. C. Håkansson. Core level and valence-band studies of the (111)2x2 surfaces of InSb and InAs. *Physical Review B*, 53(8):4734–4740, feb 1996. doi: 10.1103/physrevb.53.4734. URL https://doi.org/10.1103/physrevb.53.4734.

[123] C. B.M. Andersson, L. Ö. Olsson, M. C. Håkansson, L. Ilver, U. O. Karlsson, and J. Kanski. Core level photoemission from (111)-type InAs surfaces. *Le Journal de Physique IV*, 04(C9):C9–209–C9–212, nov 1994. doi: 10.1051/jp4:1994937. URL https://doi.org/10.1051/jp4:1994937.

[124] J.W. Matthews and A.E. Blakeslee. Defects in epitaxial multilayers. *Journal*

of Crystal Growth, 27:118–125, dec 1974. doi: 10.1016/s0022-0248(74)80055-2. URL https://doi.org/10.1016/s0022-0248(74)80055-2.

[125] Stuart Andrew Hatfield. *Heteroepitaxial growth of MnSb on III-V semiconductor substrates*. PhD thesis, Unviersity of Warwick, 2006.

[126] James Douglas Aldous. *Growth, Characterisation and Surface Structures of MnSb and NiSb Thin Films*. PhD thesis, Unviersity of Warwick, 2011. URL http://wrap.warwick.ac.uk/47091/.

[127] Kiyoko Kato, Toshihiro Kusunoki, Chisato Takenaka, Toshiyuki Tanahashi, and Kazuo Nakajima. Reduction of dislocations in InGaAs layer on GaAs using epitaxial lateral overgrowth. *Journal of Crystal Growth*, 115(1-4):174–179, dec 1991. doi: 10.1016/0022-0248(91)90734-m. URL https://doi.org/10.1016/0022-0248(91)90734-m.

[128] Y. Hayakawa, S. Iida, T. Sakurai, H. Yanagida, M. Kikuzawa, T. Koyama, and M. Kumagawa. Epitaxial lateral overgrowth of InGaAs on patterned GaAs substrates by liquid phase epitaxy. *Journal of Crystal Growth*, 169(4):613–620, dec 1996. doi: 10.1016/s0022-0248(96)00491-5. URL https://doi.org/10.1016/s0022-0248(96)00491-5.

[129] S. Iida, Y. Hayakawa, T. Koyama, and M. Kumagawa. Effect of trench structure on the quality of InGaAs layers grown on patterned GaAs (111) a substrates. *Journal of Crystal Growth*, 200(3-4):368–374, apr 1999. doi: 10.1016/s0022-0248(99)00014-7. URL https://doi.org/10.1016/s0022-0248(99)00014-7.

[130] Kazuhiko Nozawa and Yoshiji Horikoshi. Low threading dislocation density GaAs on si(100) with InGaAs/GaAs strained-layer superlattice grown by migration-enhanced epitaxy. *Journal of Electronic Materials*, 21(6):641–

645, jun 1992. doi: 10.1007/bf02655433. URL https://doi.org/10.1007/bf02655433.

[131] T. Walther, A. G. Cullis, D. J. Norris, and M. Hopkinson. Nature of the stranski-krastanow transition during epitaxy of InGaAs on GaAs. *Physical Review Letters*, 86(11):2381–2384, mar 2001. doi: 10.1103/physrevlett.86.2381. URL https://doi.org/10.1103/physrevlett.86.2381.

[132] K Hricovini, P De Padova, C Quaresima, P Perfetti, R Brochier, C Richter, V Ilakovac, O Heckmann, L Lechevallier, P Bencok, P Le Fevre, and C Teodorescu. Atomic structure and magnetic properties of mn on InAs(100). *Applied Surface Science*, 212-213:17–25, may 2003. doi: 10.1016/s0169-4332(03)00013-8. URL https://doi.org/10.1016/s0169-4332(03)00013-8.

[133] S.A. Hatfield and G.R. Bell. Growth by molecular beam epitaxy and interfacial reactivity of MnSb on InP(001). *Journal of Crystal Growth*, 296(2):165–173, nov 2006. doi: 10.1016/j.jcrysgro.2006.08.031. URL https://doi.org/10.1016/j.jcrysgro.2006.08.031.

[134] R. D. Bringans and R. Z. Bachrach. Comparison between the electronic structures of GaAs(111) andGaAs(1$\bar{1}\bar{1}\bar{1}$)from angle-resolved photoemission. *Physical Review Letters*, 53(20):1954–1957, nov 1984. doi: 10.1103/physrevlett.53.1954. URL https://doi.org/10.1103/physrevlett.53.1954.

[135] J. W. Yang, J. N. Kuznia, Q. C. Chen, M. Asif Khan, T. George, M. De Graef, and S. Mahajan. Temperature-mediated phase selection during growth of GaN on (111)a and (111)b GaAs substrates. *Applied Physics Letters*, 67(25):3759–3761, dec 1995. doi: 10.1063/1.115374. URL https://doi.org/10.1063/1.115374.

[136] C. H. Hong, K. Wang, and D. Pavlidis. Epitaxial growth of cubic GaN on (111) GaAs by metalorganic chemical vapor deposition. *Journal of Electronic*

Materials, 24(4):213–218, apr 1995. doi: 10.1007/bf02659677. URL https://doi.org/10.1007/bf02659677.

[137] T. Scimeca, Y. Muramatsu, M. Oshima, H. Oigawa, and Y. Nannichi. Interfacial chemistry and stability of sulfur-treated GaAs(111)a, 100 and (111)b. *Applied Surface Science*, 60-61:256–259, jan 1992. doi: 10.1016/0169-4332(92)90426-x. URL https://doi.org/10.1016/0169-4332(92)90426-x.

[138] B. Murphy, P. Moriarty, L. Roberts, T. Cafolla, G. Hughes, L. Koenders, and P. Bailey. Chemical and structural studies of the interactions of molecular sulfur with the GaAs(111)a and GaAs(111)b surfaces. *Surface Science*, 317 (1-2):73–83, sep 1994. doi: 10.1016/0039-6028(94)90254-2. URL https://doi.org/10.1016/0039-6028(94)90254-2.

[139] K Ono, T Uragami, M Mizuguchi, H Fujioka, M Oshima, M Tanaka, and H Akinaga. Molecular beam epitaxy of MnSb/MnAs multilayers on GaAs. *Journal of Crystal Growth*, 209(2-3):556–560, feb 2000. doi: 10.1016/s0022-0248(99)00619-3. URL https://doi.org/10.1016/s0022-0248(99)00619-3.

[140] M Oshima, M Shuzo, K Ono, H Fujioka, Y Watanabe, S Miyanishi, and H Akinaga. Initial stage of schottky barrier formation of ferromagnetic MnSb(0001) films on GaAs(111)b. *Applied Surface Science*, 130-132:892–898, jun 1998. doi: 10.1016/s0169-4332(98)00172-x. URL https://doi.org/10.1016/s0169-4332(98)00172-x.

[141] T. Manago, S. Miyanishi, H. Akinaga, W. Van Roy, R. F. B. Roelfsema, T. Sato, E. Tamura, and S. Yuasa. Schottky barrier height of MnSb(0001)/GaAs(111)b contacts: Influence of interface structure. *Journal of Applied Physics*, 88(4):2043–2047, aug 2000. doi: 10.1063/1.1305835. URL https://doi.org/10.1063/1.1305835.

[142] H. Akinaga, S. Miyanishi, W. Van Roy, and L. H. Kuo. Structural and mag-

netic properties of epitaxial (0001) MnSb thin films grown on (111) b GaAs: Influence of interface quality. *Applied Physics Letters*, 70(18):2472–2474, may 1997. doi: 10.1063/1.118860. URL https://doi.org/10.1063/1.118860.

[143] S.A. Hatfield, J.D. Aldous, and G.R. Bell. Stoichiometry, contamination and microstructure of MnSb(0001) surfaces. *Applied Surface Science*, 255(6):3567–3575, jan 2009. doi: 10.1016/j.apsusc.2008.09.082. URL https://doi.org/10.1016/j.apsusc.2008.09.082.

[144] Krystyna Lawniczak-Jablonska, Anna Wolska, Jadwiga Bak-Misiuk, Elzbieta Dynowska, and et al. Structural and magnetic properties of the molecular beam epitaxy grown MnSb layers on GaAs substrates. *Journal of Applied Physics*, 106(8):083524, oct 2009. doi: 10.1063/1.3246806. URL https://doi.org/10.1063/1.3246806.

[145] Krystyna Lawniczak-Jablonska, Anna Wolska, Marcin T. Klepka, Slawomir Kret, Jacek Gosk, Andrzej Twardowski, Dariusz Wasik, Adam Kwiatkowski, Boguslawa Kurowska, Bogdan J. Kowalski, and Janusz Sadowski. Magnetic properties of MnSb inclusions formed in GaSb matrix directly during molecular beam epitaxial growth. *Journal of Applied Physics*, 109(7):074308, apr 2011. doi: 10.1063/1.3562171. URL https://doi.org/10.1063/1.3562171.

[146] H. Tatsuoka, H. Kuwabara, M. Oshita, T. Nakamura, H. Fujiyasu, and Y. Nakanishi. Growth of MnSb and mn2sb epitaxial layers on GaAs substrates by hot-wall epitaxy. *Thin Solid Films*, 281-282:499–502, aug 1996. doi: 10.1016/0040-6090(96)08684-1. URL https://doi.org/10.1016/0040-6090(96)08684-1.

[147] W. Van Roy, G. Borghs, and J. De Boeck. Epitaxial growth of NiMnSb on GaAs(111)a and b. *Journal of Magnetism and Magnetic Materials*, 242-245:

489–491, apr 2002. doi: 10.1016/s0304-8853(01)01054-x. URL https://doi.org/10.1016/s0304-8853(01)01054-x.

[148] D. A. Woolf, D. I. Westwood, and R. H. Williams. Surface reconstructions of GaAs(111)a and (111)b: A static surface phase study by reflection high-energy electron diffraction. *Applied Physics Letters*, 62(12):1370–1372, mar 1993. doi: 10.1063/1.108682. URL https://doi.org/10.1063/1.108682.

[149] Odile Robach. Appendix to the manual of the rod program (experimental version): Robach's extension, September 2007. URL http://www.esrf.eu/computing/scientific/joint_projects/ANA-ROD/binaries/rodmanual_robach.pdf.

[150] S Sakai, M Kawano, M Ikawa, H Sato, S Yamada, and K Hamaya. Low-temperature growth of fully epitaxial CoFe/ge/fe3si layers on si for vertical-type semiconductor spintronic devices. *Semiconductor Science and Technology*, 32(9):094005, aug 2017. doi: 10.1088/1361-6641/aa7886. URL https://doi.org/10.1088/1361-6641/aa7886.

[151] M.L Reed, S.X Liu, J.C Roberts, H.H Stadelmaier, S.M Bedair, and N.A El-Masry. The planar hall effect in MnSb films and MnSb-based multilayer structures grown on (111)b GaAs. *Journal of Magnetism and Magnetic Materials*, 218(2-3):177–181, aug 2000. doi: 10.1016/s0304-8853(00)00403-0. URL https://doi.org/10.1016/s0304-8853(00)00403-0.

[152] N Uchitomi, Y Nakayama, M Yamazaki, and Y Jinbo. Growth of ferromagnetic MnAs1-xSbx films and MnSb/MnAs/MnAs1-xSbx multilayers on GaAs (001) by molecular beam epitaxy. *Journal of Crystal Growth*, 268(1-2):96–102, jul 2004. doi: 10.1016/j.jcrysgro.2004.04.114. URL https://doi.org/10.1016/j.jcrysgro.2004.04.114.

[153] F. Gerhard, T. Naydenova, M. Baussenwein, C. Schumacher, C. Gould, and

L.W. Molenkamp. Growth and characterization of epitaxial NiMnSb/ZnTe/NiMnSb magnetic multilayers. *Journal of Crystal Growth*, 435:46–49, feb 2016. doi: 10.1016/j.jcrysgro.2015.11.015. URL https://doi.org/10.1016/j.jcrysgro.2015.11.015.

[154] Ming Wu, Kiran Pangal, J. C. Sturm, and Sigurd Wagner. High electron mobility polycrystalline silicon thin-film transistors on steel foil substrates. *Applied Physics Letters*, 75(15):2244–2246, oct 1999. doi: 10.1063/1.124978. URL https://doi.org/10.1063/1.124978.

[155] Junce Zhang, Min Wei, David M. Fryauf, Juan J. Diaz Leon, Kate J. Norris, Hong Deng, and Nobuhiko P. Kobayashi. Single-crystal indium phosphide nanowires grown on polycrystalline copper foils with an aluminum-doped zinc oxide template. *Journal of Materials Science*, 50(14):4926–4932, apr 2015. doi: 10.1007/s10853-015-9038-5. URL https://doi.org/10.1007/s10853-015-9038-5.

[156] Wen Hu, Hidetoshi Suzuki, Takuo Sasaki, Miwa Kozu, and Masamitu Takahasi. High-speed three-dimensional reciprocal-space mapping during molecular beam epitaxy growth of InGaAs. *Journal of Applied Crystallography*, 45(5):1046–1053, sep 2012. doi: 10.1107/s0021889812036175. URL https://doi.org/10.1107/s0021889812036175.

[157] Maarten de Jong, Wei Chen, Thomas Angsten, Anubhav Jain, Randy Notestine, Anthony Gamst, Marcel Sluiter, Chaitanya Krishna Ande, Sybrand van der Zwaag, Jose J Plata, Cormac Toher, Stefano Curtarolo, Gerbrand Ceder, Kristin A. Persson, and Mark Asta. Charting the complete elastic properties of inorganic crystalline compounds. *Scientific Data*, 2:150009, mar 2015. doi: 10.1038/sdata.2015.9. URL https://doi.org/10.1038/sdata.2015.9.

[158] Romain Gaillac, Pluton Pullumbi, and François-Xavier Coudert. ELATE: an

open-source online application for analysis and visualization of elastic tensors. *Journal of Physics: Condensed Matter*, 28(27):275201, may 2016. doi: 10.1088/0953-8984/28/27/275201. URL https://doi.org/10.1088/0953-8984/28/27/275201.

[159] S.A. Hatfield and G.R. Bell. Mapping the surface reconstructions of MnSb(0001) and (1-101). *Surface Science*, 601(23):5368–5377, dec 2007. doi: 10.1016/j.susc.2007.09.002. URL https://doi.org/10.1016/j.susc.2007.09.002.

[160] Haiyuan Wang. *Density Functional Theory Investigations of MnSb(0001)/GaAs(111)B*. PhD thesis, Unviersity of Warwick, 2017. URL http://wrap.warwick.ac.uk/90101/.

[161] Ebiyibo Collins Ouserigha. *First-Principles Simulation of Functional Materials Interfaces*. PhD thesis, University of Warwick, 2017.

[162] L. Yang, J. Motohisa, J. Takeda, K. Tomioka, and T. Fukui. Size-dependent photoluminescence of hexagonal nanopillars with single InGaAsâĹŢGaAs quantum wells fabricated by selective-area metal organic vapor phase epitaxy. *Applied Physics Letters*, 89(20):203110, nov 2006. doi: 10.1063/1.2372710. URL https://doi.org/10.1063/1.2372710.

[163] Takaaki Mano, Kazutaka Mitsuishi, Neul Ha, Akihiro Ohtake, Andrea Castellano, Stefano Sanguinetti, Takeshi Noda, Yoshiki Sakuma, Takashi Kuroda, and Kazuaki Sakoda. Growth of metamorphic InGaAs on GaAs (111)a: Counteracting lattice mismatch by inserting a thin InAs interlayer. *Crystal Growth & Design*, 16(9):5412–5417, sep 2016. doi: 10.1021/acs.cgd.6b00899. URL https://doi.org/10.1021/acs.cgd.6b00899.

Appendix A

Matlab code sections

Listings

Listing A.1: Example code used for calculating L-shift in CTR signal

```
[data,path] = uigetfile('*.csv');
%break up array into individual columns
M = importdata([path data]);
H = round(M(:,1));
K= round(M(:,2));
L = M(:,3);
I =M(:,4);
dI =M(:,5);
columns = length(M(1,:));
if columns==11
sigpix_x=M(:,6);
sigpix_y=M(:,7);
alp=M(:,8);
gam=M(:,9);
del=M(:,10);
om =M(:,11);
elseif columns==10
sigpix_x=M(:,6);
alp=M(:,7);
gam=M(:,8);
del=M(:,9);
om =M(:,10);
end
%------define experiment and detector setup------
deg_pp = 0.01095;%radians per pixel on pilatus detector
cen_px =240; %central pixel in x
cen_py = 96; %central pixel in y
k = (2*pi)/0.61991; %wavevector of x-rays used in scan

Lshifted = zeros(length(M),1);
deg_hor=zeros(length(M),1);
```

```
for n=(1:length(L))
deg_hor(n) = ( sigpix_x(n)- cen_px)*deg_pp; %degree shift away from
    defined centre of detector
inc_qz_cen = k*sin(deg2rad(alp(n)));
exit_qz_cen = k*sin(deg2rad(gam(n)-alp(n)));
exit_qz_sig = k*sin(deg2rad(gam(n)-alp(n)-deg_hor(n)));
total_cen_qz = inc_qz_cen + exit_qz_cen;
total_sig_qz = inc_qz_cen + exit_qz_sig;
Lshifted(n)= L(n)*(total_sig_qz/total_cen_qz);
end

%plot CTR line profiles for comparison
x1=L;
y1=I;
x2=Lshifted;
y2=I;
fig = gcf;
figure(fig);
semilogy(x1,y1,'-o',x2,y2,'-*'), ylabel('Intensity'),xlabel('L'),title
    ([data(1:6) ' Lshifted']),legend('L from scananlysis','L shifted'),
    grid 'on';

%save Lshifted dataset
outfilename = [path data(1:7) '_MnSb-Cen_Lshifted.dat'];
fid = fopen(outfilename,'w');
outfile = [H, K, Lshifted, I, dI];
outfile = transpose(outfile);
fprintf(fid,'%11.6f %11.6f %11.6f %15.8g %15.8g\n',outfile);
fclose(fid);
```

Listing A.2: Example code used to convert .hdf5 files to .VTK files

```
%script to read in hdf5 files and save to VTK file for use in mayavi 3d
%plotting software
scan1 = '209404';
scan2 = '209404';

filename = ['C:\my-www\binoculars\scripts\mesh_' scan1 '_' scan2 '.hdf5
    '];
Hdatasetname = '/binoculars/axes/H';
Hdata = h5read(filename,Hdatasetname);
Kdatasetname = '/binoculars/axes/K';
Kdata = h5read(filename,Kdatasetname);
Ldatasetname = '/binoculars/axes/L';
Ldata = h5read(filename,Ldatasetname);
countdata = h5read(filename,'/binoculars/counts');
```

```
14
15 %normalise countdata to its maximum value then *10000
16 countdata_max = max(max(max(countdata)));
17 countdata_norm = countdata./countdata_max;
18 countdata_norm = countdata_norm.*10000;
19
20 %save ranges of H K L into python file for running in Mayavi
21 FID = fopen(['C:\Anaconda2/' scan1 '_' scan2 '_ranges.py'],'w');
22 fprintf(FID,'axes.axes.ranges = array([ %d ,  %d ,  %d,  %d   ,  %d   ,
       %d  ])\n',Ldata(2), Ldata(3),Kdata(2),Kdata(3),Hdata(2),Hdata(3))
    ;
23 fprintf(FID,'text.text = u''%s''\n',[scan1 '—' scan2]);
24 fclose(FID);
25 %save copy of ranges for image plane slicing
26 FID = fopen(['C:\Anaconda2/' scan1 '_' scan2 '_ranges1.py'],'w');
27 fprintf(FID,'axes1.axes.ranges = array([ %d ,  %d ,  %d,  %d   ,  %d
    ,  %d  ])\n',Ldata(2), Ldata(3),Kdata(2),Kdata(3),Hdata(2),Hdata(3)
    );
28 fprintf(FID,'text.text = u''%s''\n',[scan1 '—' scan2]);
29 fclose(FID);
30 %create structured point VTK file
31 Mat2VTK([scan1 '_' scan2 '_M2_norm.vtk'],countdata_norm,'binary');
```